



Advanced strategies for ultra-high PV efficiency

Joya Zeitouny

► To cite this version:

Joya Zeitouny. Advanced strategies for ultra-high PV efficiency. Other. Université de Perpignan, 2018. English. NNT: 2018PERP0056 . tel-03270910

HAL Id: tel-03270910

<https://theses.hal.science/tel-03270910>

Submitted on 25 Jun 2021

HAL is a multi-disciplinary open access archive for the deposit and dissemination of scientific research documents, whether they are published or not. The documents may come from teaching and research institutions in France or abroad, or from public or private research centers.

L'archive ouverte pluridisciplinaire **HAL**, est destinée au dépôt et à la diffusion de documents scientifiques de niveau recherche, publiés ou non, émanant des établissements d'enseignement et de recherche français ou étrangers, des laboratoires publics ou privés.

THÈSE

Pour obtenir le grade de Docteur

Délivrée par
UNIVERSITÉ DE PERPIGNAN VIA DOMITIA

Préparée au sein de l'école doctorale
Énergie et Environnement ED 305

Et de l'unité de recherche
PROMES-CNRS UPR 8521

Spécialité :
**Sciences de l'Ingénieur - Énergétique et Génie des
Procédés**

Présentée par :
Joya ZEITOUNY

Advanced strategies for ultra-high PV efficiency

Soutenue le 14 Décembre 2018 devant le jury composé de :

M. Carlos ALGORA, Professeur, Instituto de Energia Solar	Examinateur
M. Alain DOLLET, Directeur de Recherche, PROMES - CNRS	Directeur de thèse
M. Jean-François GUILLEMOLES, Directeur de Recherche, IPVF	Rapporteur
Mme. Stéphanie PAROLA, Maître de Conférences, IES	Examinateur
M. Abdelilah SLAOUI, Directeur de Recherche, ICUBE	Examinateur
M. Rodolphe VAILLON, Directeur de Recherche, CETHIL	Rapporteur
M. Philippe VOARINO, Ingénieur R&D, CEA	Examinateur
M. Alexis VOSSIER, Chargé de Recherche, PROMES - CNRS	Directeur de thèse



Acknowledgement

The work presented in this thesis would not have been possible without the presence of several people by my side. I extend my sincere gratitude and appreciation to all those who made this work possible.

I had the privilege of being supervised by two directors Alain Dollet and Alexis Vossier. Each of you has, in one way or another, guided me through this journey from its beginning till its end. There are no proper words to express my deep gratitude and respect for you.

Alain, I really appreciate the trust you gave me, your support, your advices and your encouragements. Thank you for the discussions we had to achieve such interesting projects and for the opportunities you gave me including attending conferences and summer schools. I am really grateful for defending me in critical situations and for facilitating the requirements to accomplish this work.

Alexis, I am really honored and lucky to be your first PhD student. You are the best supervisor one can ask for. I'm really grateful for the trust you gave me since day 1, for always considering me like a colleague, and for all the projects and papers opportunities we accomplished together. You helped me become an independent researcher: you allow me to animate meetings, to supervise interns, to review an article and to develop critical reasoning. You made me discover the research field with all its beauties and difficulties. Thank you for the discussions we had and for your continuous encouragement and appreciations. Those little words helped me improve my technical skills, overcome my fears of speaking in front of people and stop hating writing. Your advices on both research and my future career have been priceless. You really are a great person scientifically and humanely. I really appreciate your humanity, your kindness and your presence. Even if you won't be my Boss anymore, you will always be my mentor. I hope that future students will enjoy working with you as much as I did.

Thank you for the jury members: Mr. Carlos Algora, Mr. Jean-François Guillemoles, Mrs. Stéphanie Parola, Mr. Abdelilah Slaoui, Mr. Rodolphe Vaillon, and Mr. Philippe Voarino for accepting to read and assess this work. The discussions were rewarding and interesting to reach new perspectives and ideas.

My sincere thanks must also go to the members of my thesis exam committee (CST): Mr. Stéphane Collin and Mr. Laurent Thomas.

Thank you for our collaborators: Mr. Stéphane Collin, Mr. Gilles Flamant, Mr. Jeffrey M. Gordon, Mr. Eugene A. Katz and Mrs. Françoise Massines for all the interesting exchanges and papers we published together.

A special thanks to Paul André, a 6-month intern with whom I had the chance to work and who had the responsibilities of finishing my experiments when I was loaded with writing. We accomplished a nice work together. I wish you all the best for your next chapter in life.

My sincere gratitude goes to Nicolas Boulet and Emmanuel Guillot for providing explanations and help regarding experiments.

I would also like to thank Susan Vossier for proofreading parts of this thesis.

Sometimes life puts people in your way to brighten your days and give a better taste for your life. Lucile, Hélène, Chloé and Srirat I really don't know what life in Font Romeu would be if I didn't meet you!! You became family real quick and made me feel home whenever you are around. Thank you for all the memories we shared and to many more to come!

Lucile, my "acolyte", my partner in crime who never let me do crazy and foolish activities alone! I will never forget the hikes, the great meals we shared, the sport activities we did together, the funny 'snow' situations and all the gossips we had. Even during the stressful writing period and the late-night writing, we managed to have fun and to appreciate these moments. To a friendship that started because of our love for shopping to a friendship that I hope will last forever!

Hélène, I am really grateful for all the activities we shared together, the parties, the meals and the typical French interests you made me discover like finding and cooking mushrooms. You were here whenever I needed someone by my side even without me asking! Thank you for all the nights you spent with me in the lab, so I don't stay late alone writing, all the meals you prepared so I don't lose time preparing them. You are such an amazing friend!

Chloé, my little soul sister, thank you for the amazing quality time we spent together! All the activities we did and the invaluable moments we shared will always be engraved in my memories. I was really thrilled by your presence!

Srirat, I will never forget the sports sessions, all the activities we shared and your continuous encouragements. You were always here whenever I needed to talk, always ready to help whenever the situation was, including assisting me with my car.

A special thanks to all the people in the lab for the great working environment, especially to all the PhD students and the interns I met. Besides being a workplace, this lab is a family where we all shared amazing moments. I really appreciated the Christmas meals, the "rifles", pétanques competitions, carnivals and all the activities we did. A special thought for the people with whom I spent priceless times: Myriam Bruno, Tony Gebrayel, Emmanuel Guillot, Sylvie du Homet (and your delicious cakes), Renée Lestrades, Laurène Parent, Pépita and Antoine Pozzobon, Reyes Rodriguez, and Léa and Laurent Thomas.

I cannot but acknowledge a very special person to my heart, Michel Khalaf, for his eternal support. You were by my side for the last 8 years, including 4 years being separated by oceans and continents. Thank you for accepting this distance and for sharing this adventure with me! You were always here to cheer me up, to encourage me and to motivate me. I really appreciate that you are always proud of all my achievements, and that you always push me to accomplish even higher goals. I hope we will share a long and beautiful journey together.

And last but not least, a particular appreciation to my small family who supported me since day 1 for any decision I made and was always here to back me up whenever I needed. This thesis is the fruit of your support and guidance. Dad, I don't know what I would do without your help, your advices and the long discussion we had especially when difficult decisions were to be made. Mum, thank you for your prayers, for correcting all my presentations (even though you didn't understand a word), for listening to my continuous nagging, and for just being here! Léa and Yara, my lovely little sisters, your presence in my life is the best gift I can ever ask for! Thank you for all the hours we spent talking to relieve our stresses and to update me with all the beautiful and sad news I should be aware of.

Well, even though in the first place I said that "I applied for an internship at a place where I will never go", and of course I ended up coming there, I will never regret moving to this amazing place, where I spent the best 4 years of my life!

To all of you, THANK YOU!

Table of content

Acknowledgement	i
List of Figures	xii
List of Tables	xviii
Nomenclature	xix
Introduction.....	xxiv
Chapter I: General introduction to solar energy conversion	1
I. Solar energy	2
II. Photovoltaic electricity	4
A. History of solar cells	5
B. Operating principle	6
1. Direct and indirect semiconductors	6
2. Doping.....	7
3. Photovoltaic effect	7
4. <i>pn</i> -junction	7
a) In the dark	8
b) Under illumination.....	8
5. Recombination	9
a) Radiative Recombination.....	9
i. Quantum Efficiency	10
a. External Quantum Efficiency	10
b. Internal Quantum Efficiency	10
ii. Radiative Efficiency.....	10
a. External Radiative Efficiency.....	10
b. Internal Radiative Efficiency	11
b) Auger Recombination	11
c) Shockley Read-Hall Recombination.....	11
d) Surface Recombination.....	12
e) Mobility.....	12
f) Lifetime.....	12
g) Diffusion length	12
6. Electrical characteristics	12
a) Equivalent circuit	12
b) Dark current	14
c) Photo-generated current.....	15

d) I-V curve	15
i. Short-circuit current	16
ii. Open-circuit voltage	16
iii. Maximum power point	16
iv. Fill factor	16
v. Conversion efficiency	16
e) Ideality factor	17
f) Parasitic Resistances	17
i. Series Resistances	17
ii. Shunt Resistances	17
g) Effect of irradiance	17
h) Effect of temperature	18
C. Photovoltaic technologies	18
1. Silicon technologies	20
2. Thin film solar cells	20
3. III-V materials.....	21
4. Concentrated photovoltaics (CPV)	21
5. Emerging PV.....	22
a) Multi-junction solar cells	22
b) Intermediate band solar cells	22
c) Quantum dots solar cells.....	23
d) Hot carriers solar cells	23
e) Up and down conversions.....	23
f) Dye sensitized solar cells	24
g) Organic PV.....	24
h) Perovskite solar cells.....	25
III. Solar thermal electricity	27
A. CSP Technologies	27
1. Line focus collectors	27
a) Parabolic trough	27
b) Linear Fresnel	28
2. Point focus collectors	29
a) Solar tower	29
b) Parabolic dish.....	30
B. Thermal Energy Storage	31

IV. References.....	33
Chapter II: Literature review	39
I. Photovoltaic technology.....	40
A. Shockley-Queisser formalism.....	40
B. Fundamental losses in solar cells	41
C. Multi-junction solar cells	44
D. Concentrated Photovoltaics (CPV)	47
1. History.....	47
2. Concentration factor.....	48
3. Interest.....	49
4. Operating principle	49
5. Optical concentrators	49
a) Parabolic mirrors.....	50
b) Compound parabolic concentrator	50
c) Fresnel lenses	51
6. Tracking system.....	52
a) Single axis tracking.....	53
b) Dual axis tracking	53
c) Static concentrator	53
7. Concentrator cell designs and materials	54
8. Solar concentration and cell performances	54
a) Short-circuit current and solar concentration.....	54
b) Open-circuit voltage and solar concentration	54
c) Conversion efficiency and solar concentration	55
9. Limiting mechanisms.....	55
a) Series resistances	55
b) Tunnel junctions (for multi-junction cells)	56
c) High operating temperatures.....	56
d) Accuracy of tracking systems	56
e) Diffuse light	56
10. Cooling Systems	56
a) Passive cooling.....	57
i. Heat pipe cooling	57
ii. Phase change material	58
b) Active cooling.....	58

i.	Forced air cooling	58
ii.	Water cooling	58
iii.	Micro-channel heat sink cooling	58
iv.	Jet impingement cooling	59
v.	Two-phase forced convection cooling	59
E.	Emission angular restriction	59
1.	Interest.....	59
2.	Optical path length.....	60
3.	Light extraction.....	60
4.	Photon recycling	61
5.	Light trapping.....	62
a)	Surface texturization	62
6.	Emission angular confinement.....	63
a)	Cell design and requirements.....	63
b)	Angular restriction and cell performances	64
c)	Optical devices for angular confinement	65
i.	Compound parabolic concentrators	65
ii.	Domes for external confinement	66
iii.	Angular selective filters	67
a.	Rugate filters.....	67
b.	Bragg filters	68
c.	3D photonic structure	68
d)	Limitations	68
i.	Low ERE.....	69
ii.	Non-ideal back mirror	69
iii.	Cell thickness	69
F.	Combining CPV and angular restriction.....	70
II.	Hybrid PV-CSP Systems	71
A.	Interest.....	71
B.	Hybrid PV/CSP approaches.....	72
1.	“One-sun PV” Approach.....	72
2.	“Spectrum Splitting” Approach	73
3.	“High temperature PV” approach	75
a)	Operating Principle	75
b)	Effect of high temperatures on solar cells.....	76

i.	Short-circuit current	77
ii.	Open-circuit voltage	77
iii.	Conversion efficiency	78
iv.	EQE	78
C.	Energy Analysis	79
1.	Absorber heat loss	79
2.	Thermal converter efficiency	79
3.	Hybrid efficiency	80
D.	Economical review	80
III.	References	81
Chapter III: Concentrated multi-junction solar cells		90
I.	Methodology and Assumptions	91
A.	Objectives	91
B.	Methodology	91
1.	Series Resistances	91
a)	General considerations	91
b)	Series Resistance Scenario	94
2.	Description of the Algorithm	95
3.	Genetic Algorithm	96
II.	Results	97
A.	Effect of concentration on real solar cells	97
B.	Effect of series resistances	99
C.	Discussion	103
III.	Conclusion	110
IV.	References	112
Chapter IV: Combining CPV and angular restriction		115
I.	Methodology and Assumptions	117
A.	Objectives	117
B.	Methodology	117
II.	Results	119
A.	Ideal Solar Cells	119
B.	Effect of series resistances	120
C.	Effect of non-radiative recombination	121
D.	Effect of series resistances and non-radiative recombination	125
E.	Extended model	129

III.	Conclusions.....	139
IV.	References.....	139
Chapter V: Hybrid PV/CSP Systems.....		141
I.	Comparison of the performances of the hybrid approaches	142
A.	Methodology and assumptions	142
1.	Objectives	142
2.	Assumptions.....	143
a)	One-sun PV approach	143
b)	Spectrum Splitting Approach.....	143
c)	High-temperature PV approach	143
d)	Thermal receiver	144
e)	General hypotheses	144
3.	Description of the Algorithm	145
B.	Results.....	146
1.	Ideal solar cells	146
2.	Realistic solar cells	147
3.	Two-cut-off energies.....	149
C.	Conclusion	150
II.	High Temperature PV approach	151
A.	Methodology and assumptions	151
1.	Objectives	151
2.	Assumptions.....	151
a)	Solar cells.....	151
b)	Hybrid system	153
3.	Description of the algorithm	154
B.	Results.....	154
1.	Single junction solar cells	154
a)	SQ limit at high temperatures	154
b)	Electrical parameters variations	156
2.	Multi-junction solar cells	158
a)	Bandgap optimization	158
b)	Electrical parameter variation	161
c)	Sensitivity study.....	166
3.	Hybrid system performances	167
III.	Conclusions.....	170

IV. References.....	172
General Conclusions and Perspectives	175
References.....	181
Appendices.....	183
Appendix A: Variation of the different electrical parameters for single, double and triple junction solar cells, for bandgaps optimized at 973K.....	184
Appendix B: I-V curves for single and double junction solar cells for varying temperatures and concentration levels.....	186
Appendix C: Experimental preliminary results on solar cells operating at high temperature	189
A. Experimental set-up	189
B. Experimental results.....	192
1. Cell design resistance to high operating temperatures.....	192
2. Main electrical parameters at high operating temperatures	195
C. Reference	199
Appendix D: Résumé en Français.....	200
A. Introduction.....	200
B. Cellules multi-jonction à concentration	200
1. Objectifs et méthodologie	201
a) Objectifs	201
b) Méthodologie	201
2. Résultats.....	202
a) Effet de la concentration sur les cellules réelles	202
b) Effet de la résistance série.....	203
3. Discussion	205
C. Combinaison de la concentration et de la restriction angulaire	207
4. Objectifs et méthodologie	208
a) Objectifs	208
b) Méthodologie	208
5. Résultats	209
a) Cellules Solaires Idéales	209
b) Effet des résistances série	209
c) Effet des recombinaisons non-radiatives	211
d) Effet des pertes résistives et des recombinaisons non-radiatives.....	212
D. Systèmes hybrides PV/CSP	214
1. Comparaison des performances des différentes approches	215

a) Objectifs et méthodologie	215
i. Objectifs	215
ii. Méthodologie	215
iii. Hypothèses	215
b) Résultats	216
2. Approche PV haute température	218
a) Objectifs et Méthodologie.....	218
i. Objectifs	218
ii. Méthodologie	218
b) Résultats	219
i. Cellules solaires simple-jonction	219
ii. Cellules Multi-jonctions	220
iii. Systèmes hybrides	222
E. Conclusions.....	223
F. Références.....	224
Appendix E: List of publications and communications	226
A. Publications.....	226
B. Conferences.....	226

List of Figures

FIGURE I-1 Representation of the zenith angle needed to compute the air mass coefficient [3].....	2
FIGURE I-2 Irradiance of five different solar spectra [4].....	3
FIGURE I-3 Schematic representation of direct, diffuse and reflected solar radiation [2].....	4
FIGURE I-4 Difference between direct and indirect semiconductor bandgaps [17].....	7
FIGURE I-5 Three main types of recombination. From left to right: Radiative recombination, Shockley-Read-Hall recombination and Auger recombination.....	9
FIGURE I-6 Equivalent circuit of an ideal solar cell [29].....	13
FIGURE I-7 Equivalent circuits of realistic solar cells, accounting for series resistances alone (a), and for both series and shunt resistances (b) [29].	14
FIGURE I-8 I-V curve and corresponding P-V curve along with the main electrical parameters of a solar cell [31].....	15
FIGURE I-9 Evolution of the different solar cells' technologies since 1976 [32].....	19
FIGURE I-10 Summary of the third PV generation: (a) Intermediate band, (b) Quantum dot, (c) Up conversion, (d) Down conversion (e) Hot carrier, (f) Dye sensitized solar cells, (g) Organic solar cells, and (h) Perovskite solar cells [34, 66-68].	26
FIGURE I-11 Operating Principle of a Concentrated Solar Power System (CSP) [70].....	27
FIGURE I-12 Operating principle of a parabolic trough power plant. Source: EERE, Energy Efficiency and Renewable Energy, U.S. Department of Energy [73].	28
FIGURE I-13 Micro-Sol-R, PROMES-CNRS, Odeillo, France [74].....	28
FIGURE I-14 Operating principle of a linear Fresnel reflector solar plant. Source: EERE, Energy Efficiency and Renewable Energy, U.S. Department of Energy [75].....	29
FIGURE I-15 Areva Solar's Linear Fresnel Reflector, Bakersfield, CA, USA [76].	29
FIGURE I-16 Operating principle of a solar tower power plant. Source: EERE, Energy Efficiency and Renewable Energy, U.S. Department of Energy [78].	30
FIGURE I-17 THEMIS Solar Tower, PROMES-CNRS, Targassonne, France [79].	30
FIGURE I-18 Operating principle of parabolic dish power plants. Source: EERE, Energy Efficiency and Renewable Energy, U.S. Department of Energy [80].	31
FIGURE I-19 Stirling EuroDish, PROMES-CNRS, Odeillo, France [81].....	31
FIGURE II-1 Shockley-Queisser limit as a function of the bandgap [5].	41
FIGURE II-2 Fundamental losses in single-junction solar cells [8].....	42
FIGURE II-3 Schematic illustration of the thermalization and below- E_g losses.....	43
FIGURE II-4 Schematic showing the asymmetry between the angles of absorption and emission responsible for the Boltzmann losses.	44
FIGURE II-5 Comparison of solar spectrum absorption for a single-junction cell and a triple-junction cell [16].....	45
FIGURE II-6 Fundamental losses in multi-junction solar cells [8].....	46
FIGURE II-7 Operating principle scheme of concentrated photovoltaic systems [25].....	49
FIGURE II-8 Parabolic mirror CPV [26].	50
FIGURE II-9 Schematic of a CPC [27].	51
FIGURE II-10 (a) Scheme of a Fresnel lens, (b) scheme of a normal lens [31].	52
FIGURE II-11 (a) Fresnel module (b) Fresnel cell [25,32].	52

FIGURE II-12 Angle subtended by the sun between two tracking movements.....	53
FIGURE II-13 Conversion efficiency as a function of the concentration ratio.....	55
FIGURE II-14 Ultra-light trapping operating principle [55].....	62
FIGURE II-15 Different CPCs designs suggested by Kosten et al. [54].....	65
FIGURE II-16 Schematic of a mirrored dome for angular confinement [49].	67
FIGURE II-17 Comparison of cost and dispatchability for PV or CSP used alone or combined as a hybrid system [88].	72
FIGURE II-18 Schematic of the one-sun PV developed at Arizona state university (a) and diagram of the spectrum splitting showing the fraction of light transmitted to the cells and the one concentrated onto the thermal receiver (b). Courtesy of Dr. Zachary Holman [93].	73
FIGURE II-19 Schematic of a spectrum splitting strategy assuming a spectral splitting device with 2 cut-off energies, with E_L and E_H the low and high cut-off energies respectively [99].	74
FIGURE II-20 Schematic of the “HEATS” receiver, based on spectrum splitting hybrid strategy [107].	75
FIGURE II-21 Schematic of the high temperature PV approach [110].....	76
FIGURE III-1 The different components of the series resistance in a single-junction solar cell [6].....	92
FIGURE III-2 Iso-efficiency curves for a triple-junction solar cell with a total series resistance of $0.01 \Omega \text{ cm}^2$, assuming a 0.7eV bottom cell bandgap under concentration levels of (a) 1 sun, (b) 1000suns, (c) 5000 suns and (d) 10000 suns.	98
FIGURE III-3 Iso-efficiency curves for a triple-junction solar cell with a total series resistance of $0.05 \Omega \text{ cm}^2$, assuming a 0.7eV bottom cell bandgap under concentration levels of (a) 1 sun, (b) 1000suns, (c) 5000 suns and (d) 10000 suns.	99
FIGURE III-4 Iso-efficiency curves for a triple-junction solar cell under a concentration of 1000 suns, with different values of the total series resistance (a) $0 \Omega \text{ cm}^2$, (b) $0.01 \Omega \text{ cm}^2$, (c) $0.05 \Omega \text{ cm}^2$ and (d) $0.1 \Omega \text{ cm}^2$	100
FIGURE III-5 Iso-efficiency curves for a triple-junction solar cell under a concentration of 2500 suns, with different values of the total series resistance (a) $0.01 \Omega \text{ cm}^2$ and (b) $0.05 \Omega \text{ cm}^2$	100
FIGURE III-6 I-V curves for triple-junction cells (a) as well as for each junction alone: top junction (b), middle junction (c) and bottom junction (d), for ideal cases, evenly distributed resistance and non-evenly distributed resistance assuming a concentration factor of 1000 suns.	101
FIGURE III-7 Ratio between the optimized and non-optimized bandgaps of each sub-cell for a triple-junction cell, and their corresponding efficiencies, as a function of the series resistance value, assuming a concentration ratio of 5000 suns.....	105
FIGURE III-8 J_{sc} and V_{oc} computed assuming 1 sun illumination for triple-junction solar cells for different combinations of bandgaps taken from Table III-2.	105
FIGURE III-9 I-V curve of a triple-junction solar cells having a total series resistance of $0.05 \Omega \text{ cm}^2$ assuming an illumination level of 5000 suns for non-optimized (a) and optimized bandgap combination (b).	107
FIGURE III-10 Conversion efficiency (a) and relative efficiency variation (b) as a function of the concentration factors for a triple-junction solar cell having a fixed series resistance value of $0.01 \Omega \text{ cm}^2$	108

FIGURE III-11 Conversion efficiency (a) and relative efficiency variation (b) as a function of the concentration factors for a triple-junction solar cell having a fixed series resistance value of $0.05 \Omega \text{ cm}^2$	109
FIGURE IV-1 Sketch illustrating the broad discrepancies between the angles of emission and absorption (a) and the solutions used to decrease this asymmetry: solar concentration (b) and angular restriction (c) [5].	116
FIGURE IV-2 Schematic of the combination of solar concentration with angular restriction.	117
FIGURE IV-3 Iso-efficiency curves for an ideal single-junction solar cell characterized by a bandgap of 1.4eV, as a function of the solar angles of emission and absorption, assuming no series resistances and an ERE of 100%	119
FIGURE IV-4 Iso-efficiency curves for single-junction solar cells characterized by a bandgap of 1.4eV, as a function of the solar angles of emission and absorption, assuming an ERE of 100% and series resistances of $0.001 \Omega \text{ cm}^2$ (a) and $0.01 \Omega \text{ cm}^2$ (b).	121
FIGURE IV-5 Iso- V_{oc} curves for ideal single-junction solar cells assuming a bandgap of 1.4eV, no series resistances and ERE values of 100% (a), 24.5% (b) and 1% (c).	123
FIGURE IV-6 V_{oc} and V_{oc} relative variation with respect to ideal conventional cells as a function of the angles of emission and for different ERE values, assuming an angle of absorption equal to 4.65 mrad (equivalent to 1 sun illumination) and a bandgap of 1.4 eV. 124	
FIGURE IV-7 Iso-efficiency curves for single-junction solar cells, characterized by a bandgap of 1.4eV as a function of the solar angles of emission and absorption, assuming no series resistances and an ERE of 1% (a) and 30% (b).	125
FIGURE IV-8 Iso-efficiency curves for a single-junction solar cell characterized by a bandgap of 1.4eV, as a function of the solar angles of emission and absorption, assuming an ERE of 1% and a R_s of $0.001\Omega \text{ cm}^2$ (a) an ERE of 30% and a R_s of $0.001\Omega \text{ cm}^2$ (b) and an ERE of 30% and a R_s of $0.01\Omega \text{ cm}^2$ (c).	127
FIGURE IV-9 Variation of the IRE (equivalent to the internal fluorescent efficiency) as a function of the applied voltage for Ge, Si and GaAs semiconductors.....	133
FIGURE IV-10 Minority carrier lifetime and internal fluorescence efficiency as a function of the excess carrier concentration for three semiconductor materials: Ge (a), Si (b) and GaAs (c) [7].	134
FIGURE IV-11 Variation of the ERE as a function of the applied voltage for Si (a) and GaAs (b) semiconductors assuming thicknesses of $100\mu\text{m}$ for Si and of $1\mu\text{m}$ for GaAs.	136
FIGURE IV-12 Iso-efficiency curve for a single-junction solar cell, characterized by a bandgap of 1.4eV as a function of the solar angles of emission and absorption, assuming no series resistances and an ERE varying with the degree of angular restriction.....	137
FIGURE IV-13 Iso-efficiency curve for a single-junction solar cell, characterized by a bandgap of 1.4eV as a function of the angles of absorption and emission, assuming a series resistance of $0.001 \Omega \text{ cm}^2$ and an ERE varying with the degree of angular restriction.....	138
FIGURE IV-14 Efficiency as a function of the angles of absorption and emission (assumed to be equal) for different combinations of ERE and series resistance values.	138
FIGURE V-1 Schematic of the 3 PV/CSP hybrid strategies investigated: (a) “high temperature PV”, (b) “spectrum splitting” and (c) “one-sun PV” approaches.	142

FIGURE V-2 Overall hybrid conversion efficiency (left) and PV contribution to total electricity generated (right) as function of the electronic energy gap for the three hybrid systems with ideal solar cell at a concentration level of 1000 suns operating at the radiative limit (a), solar cells with $R_s = 0.01 \Omega\text{-cm}^2$ (b) and solar cells with ERE= 1% (c).....	146
FIGURE V-3 Overall hybrid conversion efficiency (left) and PV contribution to total electricity generated (right) as function of the electronic energy gap, with two cut-off energies in the spectrum splitting device, for the three hybrid systems with ideal solar cell at a concentration level of 1000 suns operating at the radiative limit (a), solar cells with $R_s = 0.01 \Omega\text{-cm}^2$ (b) and solar cells with ERE = 1% (c).....	150
FIGURE V-4 Material specific temperature dependent bandgaps as a function of temperature.	153
FIGURE V-5 Maximal theoretical achievable PV efficiency for a single-junction cell as a function of the gap for temperatures between 298 and 973K and for concentration level of 1 (a), 100(b) and 1000 (c) suns.	155
FIGURE V-6 (a) η_{PV} , (b) V_{oc} , (c) variation of J_{sc} and (d) FF, as a function of T for a single-junction cell optimized at $T = 523$ K (see Table V-6), for $X= 1, 100$ and $1,000$ suns.	156
FIGURE V-7 (a) η_{PV} , (b) V_{oc} , (c) variation of J_{sc} and (d) FF, as a function of T for a single-junction cell optimized at $T = 773$ K (see Table V-6), for $X= 1, 100$ and $1,000$ suns.	157
FIGURE V-8 Iso-efficiency curves for tandem junction solar cells under 100 suns and for temperatures of 298K (a), 523K (b), 773K (c), and 973K (d).	159
FIGURE V-9 Iso-efficiency curves for tandem junction solar cells under 1000 suns and for temperatures of 298K (a), 523K (b), 773K (c), and 973K (d).	159
FIGURE V-10 (a) η_{PV} , (b) V_{oc} , (c) variation of J_{sc} and (d) FF, as a function of T for double-junction cells optimized at $T = 523$ K (see Table V-6), for $X= 1, 100$ and $1,000$ suns.....	161
FIGURE V-11 (a) η_{PV} , (b) V_{oc} , (c) variation of J_{sc} and (d) FF, as a function of T for double-junction cells optimized at $T = 773$ K (see Table V-6), for $X= 1, 100$ and $1,000$ suns.....	162
FIGURE V-12 I-V curve for tandem cells at 1000 suns and for cells optimized at 773K at the point of 773K (a) and 823K (b).	163
FIGURE V-13 (a) η_{PV} , (b) V_{oc} , (c) variation of J_{sc} and (d) FF, as a function of T for triple-junction cells optimized at $T = 523$ K (see Table V-6), for $X= 1, 100$ and $1,000$ suns.....	164
FIGURE V-14 (a) η_{PV} , (b) V_{oc} , (c) variation of J_{sc} and (d) FF, as a function of T for triple-junction cells optimized at $T = 773$ K (see Table V-6), for $X= 1, 100$ and $1,000$ suns.....	165
FIGURE V-15 Conversion efficiency as a function of temperature for single (a), double (b) and triple (c) junction solar cells at concentrations of 100 and 1000 suns and bandgap optimization temperatures of 523 and 973K.....	166
FIGURE V-16 PV, thermal and overall hybrid efficiencies as well as the associated thermal losses as a function of the operating temperature, for solar cells at the radiative limit under a concentration of 100 suns (a), at the radiative limit under 1000 suns (b) and for more realistic solar cells under 1000 suns (c).....	168
FIGURE V-17 PV, thermal and overall hybrid efficiencies as well as the associated thermal losses as a function of the operating temperature, for a concentration of 1000 suns, for solar cells at the radiative limit (a), and for more realistic solar cells (b).	169

FIGURE A-1 (a) η_{PV} , (b) V_{oc} , (c) variation of J_{sc} and (d) FF, as a function of temperature for a single-junction cell optimized at $T = 973$ K (see Table V-6), for concentration factors of 1, 100 and 1,000 suns.....	184
FIGURE A-2 (a) η_{PV} , (b) V_{oc} , (c) variation of J_{sc} and (d) FF, as a function of temperature for a double-junction cell optimized at $T = 973$ K (see Table V-6), for concentration factors of 1, 100 and 1,000 suns.....	184
FIGURE A-3 (a) η_{PV} , (b) V_{oc} , (c) variation of J_{sc} and (d) FF, as a function of temperature for a triple-junction cell optimized at $T = 973$ K (see Table V-6), for concentration factors of 1, 100 and 1,000 suns.....	185
FIGURE B-1 I-V curves for single-junction solar cells for temperatures varying between 298 and 973 K and concentrations of (a) 1, (b) 100, and (c) 1000 suns	186
FIGURE B-2 I-V curves for double-junction solar cells for temperatures varying between 298 and 973 K and concentrations of (a) 1, (b) 100, and (c) 1000 suns	187
FIGURE C-1 Operating principle of the experimental set-up.....	189
FIGURE C-2 LINKAM HFS600E-PB4 device used to control the cell temperature.	190
FIGURE C-3 The solar cell positioned inside the heating device.	191
FIGURE C-4 Experimental set-up of the high-temperature solar cells characterization (a), the temperature control system installation (b), the positioning of the solar cell on the heating plate (c), the cell illuminated by the optical fiber (d), and the Keithley 2601 (e).....	191
FIGURE C-5 Temperature profile and corresponding heated cell at 290°C.	192
FIGURE C-6 Solar cells at 270° (left) and at 296°C (right).....	193
FIGURE C-7 Profile showing the effect of concentration which increases the operating temperature, up to 70°C.	195
FIGURE C-8 Profile of the temperature used to measure the different cells electrical parameters.....	196
FIGURE C-9 I-V curve plotted for different temperatures and for three concentration ratios (a) 500 suns, (b) 1100 suns and (c) 1800 suns.	197
FIGURE C-10 V_{oc} , FF and η as a function of concentration for different operating temperatures.....	198
FIGURE D-1 Courbes iso-rendements pour une cellule solaire triple-jonction ayant une résistance série de $0.01 \Omega \text{ cm}^2$, en fixant le gap de la jonction du bas à 0.7 eV, pour des facteurs de concentration de (a) 1, (b) 1000, (c) 5000 et (d) 10000 soleils.	203
FIGURE D-2 Courbes iso-rendements pour une cellule solaire triple-jonction, en fixant le gap de la jonction du bas à 0.7 eV, pour un facteur de concentration de 1000 soleils et différentes valeurs de la résistance série : (a) 0, (b) 0.01, (c) 0.05 et (d) $0.1 \Omega \text{ cm}^2$	204
FIGURE D-3 Rendement de conversion (a) et variation relative des rendements (b) en fonction de la concentration pour une cellule solaire triple-jonction ayant une résistance série de $0.05 \Omega \text{ cm}^2$	207
FIGURE D-4 Courbes iso-rendement pour une cellule solaire simple-jonction ayant un gap électronique de 1.4 eV en fonction des angles solides d'absorption et d'émission, en supposant des recombinaisons 100% radiatives et des résistances série $0.001 \Omega \text{ cm}^2$ (a) et $0.01 \Omega \text{ cm}^2$ (b).	210

FIGURE D-5 Courbes iso-rendement pour une cellule solaire simple jonction ayant un gap électronique de 1.4 eV en fonction des angles solides d'absorption et d'émission, en supposant des résistances série nulles et des recombinaisons radiatives de 1% (a) et 30% (b).	212
FIGURE D-6 Courbes iso-rendement pour une cellule solaire simple jonction ayant un gap électronique de 1.4 eV en fonction des angles solides d'absorption et d'émission, en supposant un ERE de 1% et R_s $0.001 \Omega \text{ cm}^2$ (a) ERE de 30% et R_s de $0.001\Omega \text{ cm}^2$ (b) et un ERE de 30% et R_s de $0.01\Omega \text{ cm}^2$ (c).	213
FIGURE D-7 Rendement de conversion hybride global (gauche) et contribution du PV à la production de l'électricité totale générée (droite) en fonction du gap électronique pour les trois approches étudiées. Les graphes supposent une concentration de 1000 soleils, et sont tracés pour des cellules solaires idéales (a) des cellules ayant des pertes résistives de 0.01 Ohm cm ² (b) et un ERE de 1% (c).....	217
FIGURE D-8 Rendement théorique maximal pour une cellule solaire simple-jonction en fonction du gap électronique, pour des températures comprises entre 298 et 973K et pour des concentrations de (a) 1 soleil, (b) 100 soleils (c) 1000 soleils.....	219
FIGURE D-9 (a) η_{PV} , (b) V_{oc} , (c) variation du J_{sc} et (d) FF, en fonction de la température pour une cellule simple-jonction optimisée pour $T=773K$, et pour des concentrations de 1, 100 et 1000 soleils.	220
FIGURE D-10 (a) η_{PV} , (b) V_{oc} , (c) variation du J_{sc} et (d) FF, en fonction de la température pour une cellule triple-jonction optimisée pour $T=773K$, et pour des concentrations de 1, 100 et 1000 soleils.	221
FIGURE D-11 Rendements de conversion PV, thermique et hybride en fonction de la température de fonctionnement ainsi que les pertes thermiques associées pour des cellules fonctionnant à la limite radiative sous une concentration de 100 soleils (a), à la limite radiative sous 1000 soleils (b) et pour des cellules solaires « réelles » sous 1000 soleils (c).	222

List of Tables

TABLE II-1 Optimum electronic energy gaps for multi-junction cells with up to 10 junctions and their efficiencies at 1 sun illumination [12].	47
TABLE III-1 Summary of the equations used in the program	95
TABLE III-2 Optimal bandgap combination for a 3J solar cell using genetic algorithm, for illumination levels ranging between 1 and 10000 suns and for two series resistance values 0.01 and 0.05 Ω cm ²	102
TABLE III-3 Main electrical parameters of a triple-junction solar cell with non-optimized and optimized bandgap combination.....	104
TABLE IV-1 List of the different equations used in the algorithm.....	118
TABLE IV-2 Comparison of open-circuit voltage, fill factor and conversion efficiency for five different cases of series resistances and radiative efficiencies, for equal solid angles of absorption and emission (4.65mrad for the maximum scenario, and $\pi/10$ for the minimum scenario).....	128
TABLE IV-3 Comparison of open-circuit voltage, fill factor and conversion efficiency for four different cases of series resistances, radiative efficiencies and solid angles of absorption and emission.....	129
TABLE IV-4 Main optical and electrical parameters of GaAs, Si and Ge.....	131
TABLE V-1 PV operating conditions for the 3 hybrid approaches considered in this study.	145
TABLE V- 2 Summary of the equations used in this chapter	145
TABLE V-3 Maximum efficiency (η) and PV fraction (PV _f) at the point of optimal efficiency computed for each hybrid strategy.....	148
TABLE V-4 Maximum system efficiency for the 3 hybrid strategies, based on ideal solar cells, for different concentration levels and two receiver temperatures, 666 and 823K, as well as the PV fraction.....	148
TABLE V-5 Bandgap temperature coefficient for III-V semiconductors.	153
TABLE V-6 Optimal bandgap for single, double and triple junction cells, optimized at 298, 523, 773 and 973K at 1, 100 and 1000 suns solar illuminations.	160
TABLE C-1 Properties and physical characteristics of the three tested cells before and after heating.....	194
TABLEAU D-1 Combinaison optimale des gaps électroniques d'une cellule solaire triple-jonction, calculée en utilisant l'algorithme génétique, pour des facteurs de concentration compris entre 1 et 10000 soleils et des résistances série de 0.01 et 0.05 Ω cm ²	205
TABLEAU D-2 Principaux paramètres électriques pour une cellule triple-jonction pour des combinaisons de gaps non-optimisées et optimisées.....	206

Nomenclature

Physical constants

c	Speed of light (2.998×10^8 m s ⁻¹)
h	Planck constant (6.626×10^{-34} J s)
σ	Stefan-Boltzmann constant (5.6704×10^{-8} Kg s ⁻³ K ⁻⁴)
q	Elementary charge ($1.60217653 \times 10^{-19}$ A s)
k	Boltzmann constant (1.38065×10^{-23} Kg m ² s ⁻² K ⁻¹)

Abbreviations

A _{cell}	Area of the cell (cm ²)
A _{conc}	Aperture area of the optical concentrator (cm ²)
AM	Air Mass
B _r	Radiative coefficient (cm ³ s ⁻¹)
C _{Auger}	Auger coefficient (cm ⁶ s ⁻¹)
C _n	Capture probability coefficient of an electron
C _p	Capture probability coefficient of a hole
CPC	Compound Parabolic Concentrator
CPV	Concentrated Photovoltaic
CSP	Concentrated Solar Power
DBC	Direct Bonded Copper
E	Energy at a given wavelength (eV)
e	Electron
E _{cut-off}	Cut-off energy (eV)
E _g	Bandgap (eV)
E _{g_opt}	Optimized bandgap (eV)
EQE	External Quantum Efficiency (%)
ERE	External Radiative Efficiency (%)
FF	Fill Factor
GaAs	Gallium Arsenide
Ge	Germanium

h	Hole
h_c	Convective heat transfer coefficient ($\text{W m}^{-2} \text{K}^{-1}$)
HOMO	Highest Occupied Molecular orbital
I	Current flowing through the cell (A)
I_0	Dark current (A)
I_{0_rad}	Dark current at the radiative limit (A)
I_{0_s}	Dark current accounting for angular restriction (A)
i_1	Angle of incidence (rad)
i_2	Angle of refraction (rad)
I_d	Current flowing through the diode (A)
I_{MPP}	Current at maximum power point (A)
I_{ph}	Photo-generated current (A)
IQE	Internal Quantum Efficiency (%)
IRE	Internal Radiative Efficiency (%)
I_{sc}	Short-circuit current (A)
J	Current density flowing through the cell (A cm^{-2})
J_0	Dark current density (A cm^{-2})
J_{0_s}	Dark current density accounting for angular restriction (A cm^{-2})
J_{Auger}	Auger recombination current density (A cm^{-2})
J_{ph}	Photo-generated current density (A cm^{-2})
J_{rad}	Radiative recombination current density (A cm^{-2})
J_{sc}	Short-circuit current density (A cm^{-2})
J_{SRH}	Shockley-Read-Hall recombination current density (A cm^{-2})
LCOE	Levelized cost of electricity
LUMO	Lowest Unoccupied Molecular Orbital
n	Ideality factor
n_1	Refractive index of medium 1
n_2	Refractive index of medium 2
N_a	Acceptor concentration (cm^{-3})

N_d	Donor concentration (cm^{-3})
n_e	Concentration of electrons (cm^{-3})
n_{e0}	Concentration of electrons at equilibrium (cm^{-3})
n_{ex}	Excess carrier concentration (cm^{-3})
n_h	Concentration of holes (cm^{-3})
n_{h0}	Concentration of holes at equilibrium (cm^{-3})
n_i	Intrinsic carrier concentration (cm^{-3})
n_r	Refractive index
n_t	Concentration of electrons in the impurities (cm^{-3})
N_t	Trap density (cm^{-3})
OPL	Optical Path Length
P_{abs}	Probability that radiatively emitted photons are reabsorbed
$\overline{P_{\text{abs}}}$	Averaged probability that radiatively emitted photons are reabsorbed
P_{conv}	Convective power density (W m^{-2})
P_{esc}	Probability that radiatively emitted photons escape from the cell
$\overline{P_{\text{esc}}}$	Averaged probability that radiatively emitted photons escape from the cell
P_{in}	Incident solar power density (W m^{-2})
P_{loss}	Resistive power density (W m^{-2})
P_{max}	Maximum power density extracted from the cell (W m^{-2})
P_{MPP}	Maximal power point (W m^{-2})
P_{PV}	Power density generated by the photovoltaic cell (W m^{-2})
P_{rad}	Radiative power density (W m^{-2})
p_t	Concentration of holes in the impurities (cm^{-3})
P_{turbine}	Power density generated by the turbine (W m^{-2})
PV	Photovoltaic
QE	Quantum Efficiency (%)
R	Reflectivity coefficient
R_{Auger}	Auger recombination rate

RE	Radiative Efficiency (%)
R_p	Shunt resistance ($\Omega \text{ cm}^2$)
R_{rad}	Radiative recombination rate
R_s	Series resistance ($\Omega \text{ cm}^2$)
R_{SRH}	Shockley-Read-Hall recombination rate
Si	Silicon
S_{opt}	Optical entropy
SQ	Shockley-Queisser
SRH	Shockley-Read-Hall
T	Operating temperature (K)
T_a	Ambient temperature (K)
T_c	Temperature of the solar cell (K)
T_{CSP}	Operating temperature of the thermal receiver (K)
T_{opt}	Temperature of optimization (K)
T_s	Temperature of the sun (K)
V	Voltage (V)
V_{MPP}	Voltage at maximal power point (V)
v_n	Thermal velocity for electrons (cm s^{-1})
V_{oc}	Open-circuit voltage (V)
$V_{\text{oc_opt}}$	Maximum open-circuit voltage (V)
V_{op}	Voltage at the operating point (V)
v_p	Thermal velocity for holes (cm s^{-1})
W	Thickness (cm)
X	Concentration ratio (sun)
α	Absorptivity
ε	Emissivity
η	Efficiency (%)
η_{Carnot}	Carnot efficiency (%)
η_{CSP}	Thermal efficiency (%)

η_{hybrid}	Hybrid efficiency (%)
η_{PV}	Photovoltaic efficiency (%)
η_{turbine}	Turbine efficiency (%)
θ	Zenith angle
θ_{abs}	Half-angle of absorption (rad)
θ_{em}	Half-angle of emission (rad)
λ	Wavelength (nm)
μ	Chemical potential (eV)
σ_n	Electron capture cross section (cm^2)
σ_p	Hole capture cross section (cm^2)
τ_{n0}	Lifetime of an electron (s)
τ_{p0}	Lifetime of a hole (s)
Ω	Solid angle (sr)
Ω_{abs}	Solid angle of emission (sr)
Ω_{sun}	Solid angle of the sun (6.8×10^{-5} sr)

Introduction

In an era where pollution has become a huge concern, sustainable development is more than ever a necessity to reduce greenhouse gas emissions and to find alternatives to conventional energy sources (oil, gas, petroleum, nuclear power, etc.), electricity production being a dominant polluting factor. To diminish environmental pollution and to satisfy the increasing human need for energy, and more particularly for electricity, renewable energies in general are being developed and currently instigate significant research efforts in the scientific community. Renewable energies take different forms such as wind, geothermal, biomass, hydropower and solar energies that are unevenly distributed on the planet. Accounting for the availability, abundance and price of harvesting these energies, two technologies offer particularly promising perspectives: solar and wind energies. However, solar energy remains a privileged resource due to its abundance and ability of meeting, by itself, the worldwide energy demand.

Research in the field of solar electricity principally aims at efficiently harvesting solar energy and converting it to electrical energy. Thermodynamic electricity is indirectly generated from solar energy, through concentrated solar power systems (CSP): photons are first converted to heat and then to electrical energy via a turbine. Such an approach offers the advantage of cheap energy storage allowing continuous electricity production, all day long. Alternatively, photovoltaic electricity is generated directly from the sun, through solar cells that are based on materials capable of directly converting incident photons to electrical energy by photoelectric effect. Photovoltaic cells currently offer low-cost energy and are probably the most promising path economically for solar electricity production. Nonetheless, their main drawback is the expensive, limited and complex storage, usually accomplished through electrochemical means, via batteries for instance.

The maximal attainable PV efficiency for single-junction solar cells is known to be slightly higher than 30%. On the other hand, the Carnot limit for conversion of sunlight energy into electricity foresees conversion efficiencies as high as 93%. The large gap between both limits is due to several fundamental limitations such as the discrepancy between the wide solar spectrum energy range and the narrow energy range that can be efficiently converted by solar cells, or to the asymmetry between the angular properties of the absorbed and emitted fluxes (*Boltzmann* losses).

Numerous innovative approaches exist to outweigh these intrinsic losses and surpass the Shockley-Queisser limit, such as multi-junction solar cells, up/down conversion, hot carriers, quantum dots, etc..., all capable of better harvesting the solar spectrum. This thesis focuses on three different strategies: 1) concentrated multi-junction solar cells reducing the spectral mismatch and the *Boltzmann* losses, 2) combination of solar concentration and angular restriction tackling the *Boltzmann* losses, and 3) hybrid PV/CSP systems reducing spectral mismatch and *Boltzmann* losses, as well as allowing the development of low-cost, dispatchable electricity all-day long.

These strategies are limited by various mechanisms such as series resistances, non-radiative recombination or high operating temperatures that deteriorate their performances. Consequently, the objective of this thesis is to better understand the extent to which strategies aiming at an improved conversion of solar energy into electricity are likely to be penalized by non-ideal loss mechanisms, and to optimize solar cells toward minimizing their effects. The solar cells architectures are optimized for a broad range of series resistance values, concentration factors and operating temperatures, for ideal (i.e. without any series resistance losses nor non-radiative recombination, and assuming ambient temperature and AM1.5 solar spectrum) and for more realistic solar cells. The angular properties of the absorbed and emitted fluxes are also tuned for both ideal and realistic cells accounting for series resistances and non-radiative recombination.

The first chapter of this manuscript is a general introduction addressing solar energy conversion. The first part considers photovoltaic conversion and recalls the operating principles, the *pn*-junction, the different recombination types, as well as the solar cells main electrical parameters. The second part provides an overview of the different photovoltaic technologies developed until today. Finally, the third section tackles thermodynamic solar energy conversion, the different CSP technologies and thermal storage.

The second chapter, after introducing the Shockley-Queisser formalism and the fundamental losses affecting PV cell operation, details three state-of-the-art innovative technologies used to efficiently convert solar energy into electricity and to overcome the Shockley-Queisser limit. It starts with a brief overview of multi-junction solar cells, before detailing concentrated photovoltaic systems: their interest, limit, operating principle, the different concentrator, tracking and cooling systems available and their main limiting mechanisms. Then, the angular restriction strategy (used to limit the photons' emission angle) is described, starting with some background on the optical path in solar cells, light extraction and light trapping in general. In a second time, we detail the angular restriction operating principle, its effect on the cell's electrical parameters, the different optical means employed to accomplish it, its limitations, and the interest of combining it with solar concentration. Finally, hybrid PV/CSP systems are presented along with the different approaches used to implement them. Detailed analysis addressing the effect of temperature on solar cells and an energy analysis for the overall hybrid system are also provided.

The third chapter is devoted to the theoretical study of concentrated multi-junction solar cells. It investigates the bandgap optimization for different series resistance values and for various concentration factors. A discussion explaining the different results obtained follows.

The fourth chapter considers theoretically, by using numerical modeling, the combination of angular restriction and solar concentration. Ideal solar cells are first studied before considering more realistic solar cells encompassing non-ideal loss mechanisms, such as series resistance losses and non-radiative recombination. Finally, the chapter is concluded with a discussion on how to improve the model; it mainly explains how to account for the effect of the angular restriction on the external radiative efficiency.

The fifth chapter focuses on hybrid PV/CSP systems. It starts by listing the main assumptions considered for each hybrid approach. After that, a comparison is made between the different strategies investigated based on their ability to efficiently perform and to provide a balance share between PV and CSP electricity. The comparison is done for ideal and more realistic solar cells, accounting for series resistances or non-radiative recombination, and considering single or two cut-off energies when a spectrum splitting device is used. The second part tackles the high temperature PV approach. It first examines the effect of temperature on single and multi-junction solar cells for a broad range of concentration factors. Then, the effect of temperature is described for different “high-temperature PV” hybrid systems, while varying the concentration ratio and the cell properties. Preliminary experimental results on the effect of temperature on solar cells, as well as on the behavior of the main electrical parameters with varying temperatures and concentration are provided in appendix C.

Chapter I: General introduction to solar energy conversion

Renewable energies, such as hydropower, geothermal, wind and solar energies, are currently seen as promising green alternative energies toward reducing greenhouse gas emissions and pollution. The use of such energies has increased tremendously in the past years, and there is currently a growing number of research works aiming at increasing their efficiency and reducing their cost. Wind and solar energies represent the two dominating sectors. This thesis only focuses on solar energy, which has the highest theoretical potential of the Earth's renewable energy sources, with a potential of 89300 TW [1].

I. Solar energy

Solar energy can meet the world's annual energy consumption in an hour, which is equivalent to the energy provided by all the other sources combined during a whole year [1].

Radiation emitted by any object depends to a very great extent on its temperature. To characterize the radiation emitted by a body at a given temperature, it is common to use the radiation emitted by a blackbody as a reference. In the limits of Planck's theory, a blackbody is a perfect emitter and a perfect absorber [2], absorbing all the incident radiation on its surface and emitting more energy than any other object; no radiations are reflected or transmitted through the body. The sun is assimilated to a blackbody object with a surface temperature of 5700K.

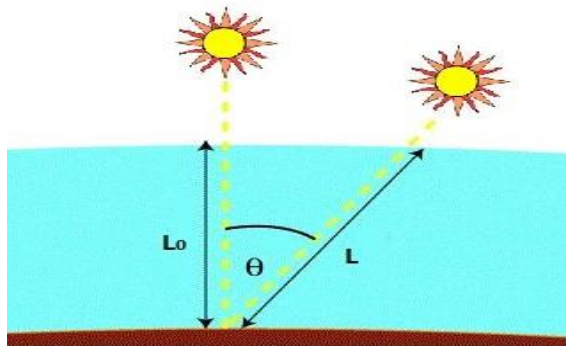


FIGURE I-1 Representation of the zenith angle needed to compute the air mass coefficient [3].

As solar radiation crosses the atmosphere to reach the Earth surface, the solar spectrum is modified since photons can be absorbed by dust, aerosols, or gases like ozone (O_3), water vapor (H_2O) or carbon dioxide (CO_2). The beams can also be scattered by clouds, air molecules, pollution or dust from the atmosphere, or reflected by clouds. The location, the seasons of the year as well as the time of the day affect the incident radiation on the Earth's surface. All these parameters alter the overall solar power received and the spectral distribution of the light.

To quantify the reduction in power and evaluate the amount of energy reaching the Earth surface, a coefficient called "air mass" (AM) is introduced. It quantifies the length of the light path through the atmosphere normalized to the shortest path, with the sun overhead, as illustrated by equation (I-1), with θ the zenith angle (Figure I-1).

$$AM = \frac{1}{\cos(\theta)} \quad (I-1)$$

Figure I-2 shows the spectral distribution for 4 different solar spectra, corresponding to different AM values, together with the spectral distribution of a 6000K blackbody. AM0 represents the solar spectral irradiance distribution measured outside the atmosphere, at normal incidence. AM1 denotes a zenith angle of 0° , the spectrum being measured at sea level with the sun overhead. It represents the spectral distribution at the tropical and the equatorial regions. The AM1.5 solar spectrum is measured at an angle of 48.2° and is representative of the spectral distribution of sunlight in mid-latitude regions (this spectrum is also used for standard test conditions for the tests/qualifications of solar systems/components). A distinction is made between the AM1.5G and the AM1.5D (global and direct respectively), the former considering both direct and diffuse radiations, with a power density of $1000W/m^2$, the latter only direct radiation, with an average of $900W/m^2$. For regions at higher latitudes, AM2 and AM3 may be used, measured at angles of 60 and 70° respectively.

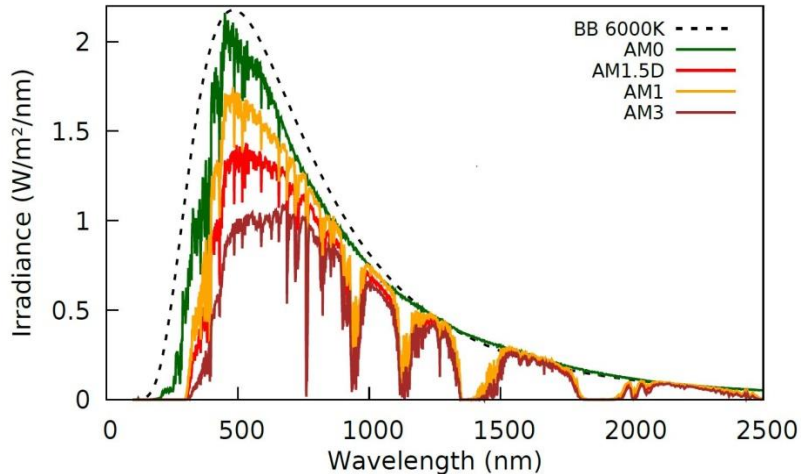


FIGURE I-2 Irradiance of five different solar spectra [4].

Diffuse light represents the incident light that reaches the surface of the Earth after being scattered by molecules, clouds and aerosols whereas direct light reaches the surface directly from the sun. Direct radiation has a defined path, going from the sun through the atmosphere directly to the receiver in a straight line. The solar radiation striking a receiver is a combination of both types of radiation as shown in Figure I-3.

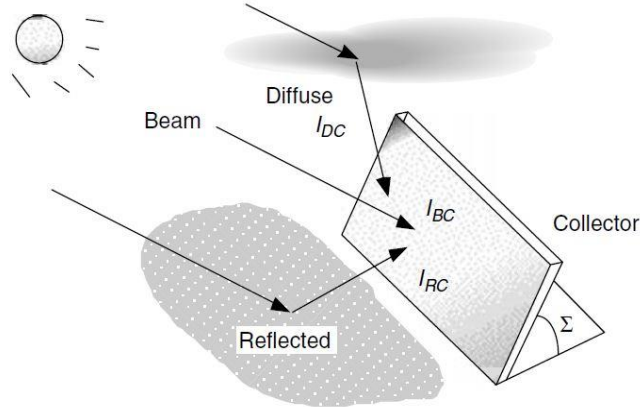


FIGURE I-3 Schematic representation of direct, diffuse and reflected solar radiation [2].

Sunlight is a very abundant source of free green energy, available and accessible to everyone, as long as the sun exists, and does not produce radioactive waste nor polluting greenhouse gas emissions. Converting solar energy into other forms of energy (electrical, thermal, mechanical, chemical) can be accomplished with very high efficiency, because of the high temperature of the sun (the Carnot efficiency for sunlight to electricity conversion being $\sim 93\%$ [5,6]). This source of energy, because of its abundance and the efficiency with which one may convert it into another form of useful energy, has instigated a large number of research works aiming at harvesting it by different means and for diverse applications (electricity generation, water heater, dryer, cooker, etc.). The scope of this thesis only considers electricity production.

Various methods exist to convert solar energy to electrical energy, such as photovoltaic conversion, thermal conversion, or solar fuels. Only the first two strategies are developed in this manuscript. Solar electricity may be generated directly by mean of photovoltaic cells, which consist of materials capable of converting the incident solar photons energy into electrical energy, or by thermodynamic energy conversion where incident photons are first converted to heat and then to electricity. Both approaches are detailed in this chapter.

II. Photovoltaic electricity

Photovoltaic converters involve direct conversion of sunlight into electricity using PV cells, and allow low-cost and environmentally friendly electricity generation.

Besides their advantages, photovoltaic cells struggle with some issues. Their efficiencies remain far from the Carnot limit, despite the large range of research activities performed over the last decades to improve the existing technologies and develop emerging ones. Another issue is related to the non-dispatchability of the electricity produced, since the current generation only occurs during the day, at sunny hours. Photovoltaic technology is weather-dependent (which makes electricity production difficult to predict), as well as highly location-dependent (due to the unequal worldwide repartition of the solar resource, as well as the differences in the thermal environment around the globe). Solar energy conversion happens during the day, and the production does not coincide with the peak electricity

demand. To tackle this issue, the energy produced can be stored electro-chemically, via batteries which are still expensive and rather complex devices.

A. History of solar cells

In 1839, A. Becquerel [7] discovered the photovoltaic effect by generating a current after illuminating two platinum electrodes coated with silver chloride, immersed in an electrolyte solution and separated by a thin membrane. 34 years later, in 1873, W. Smith observed an increase in the conductivity of a selenium rod when exposed to light. This observation represents the first description of photoconductivity [8]. In 1876, W. Adams and R. Day observed the photoconductive effect in selenium, by noticing a generation of current after exposing a selenium rod to light. This is the first study revealing the photovoltaic effect in solids [9, 10]. Seven years later, C. E. Fritts built the first solar module using selenium coated with a thin layer of gold. This device could generate continuous current when exposed to light with an efficiency of 1% [11]. Two decades later, in 1905, A. Einstein explained the photo-electrical phenomena using quantum physics assumptions and proposed the concept of photon (that he called *quanta*, independent particles of energy forming light) [12].

During the 1910's, a Polish scientist, Czochralski, produced good quality crystals of silicon that were used since the 1940's to produce the first generations of solar cells [9]. In 1954, the first attempt of practical solar cell development was realized by Bell Laboratories with a conversion efficiency of 6%, using a modified wafer of silicon.

In 1958, the first satellite using PVs as its main electrical power source, Vanguard I, was launched. Solar cells were very expensive, preventing solar electricity from being widely adopted as a source of energy. Meanwhile, researches were conducted to improve the manufacturing processes and the cells efficiency that increased to 14% by the end of the 1960's.

In the 1970's, the interest in alternative energies rose with the first oil crisis that increased the oil price by a factor of 4. Micro-electronics industries surfaced. From the silicon rejects from micro-chip production, Dr. Elliott Berman designed cheaper solar cells, with less pure silicon materials. This work allowed photovoltaic terrestrial applications.

In the 1976, H. Hovel and J. Woodall manufactured a GaAs solar cell with an efficiency of 21.9% [13], a higher record efficiency than the one obtained with silicon. In 1994, NREL developed a solar cell with a conversion efficiency of 30.2% by using a stack of different gaps on top of each other. In 2006, cells including three junctions, with efficiency over 40% were released by Spectrolab. The highest record cell nowadays was released in 2014, with 46% efficiency under concentrated light. The highest record for silicon single-junction reached 26.7% [14].

At the same time, the cost of solar cells decreased continuously, to reach an average of 9 ¢ per kilowatt-hour in 2017 [15]. Today's solar cells are employed worldwide, and their applications are extended beyond solar electricity: they can even power solar cars or solar planes.

B. Operating principle

PV cells basically include three principal parts: 1) a light absorber that absorbs the incident photons and transfers their energy to create free electrons and holes, 2) a carrier collector that captures the electrons and holes separately and 3) metal contacts that transport the electrons to the external circuit to generate a current flow. PV cell operation requires the use of specific semiconductor materials allowing the energy of solar photons to be transmitted to the charge carriers.

1. Direct and indirect semiconductors

The difference in energy between the valence and the conduction bands is known as the bandgap (E_g) and is a semiconductor's characteristic. The energy associated with the electronic energy gap is the minimum energy required for an electron to be propelled from the valence band to the conduction band, and hence the minimum energy a photon should possess to produce the aforementioned effect. The semiconductor gap can be either direct or indirect, as illustrated in Figure I-4.

Direct gap semiconductor materials refer to materials whose valence band maxima and conduction band minima occur at the same value of the wave-vector k (these two characteristic energies are aligned with respect to momentum). In this case, the absorption of a photon is sufficient to create an electron/hole pair, since no change in the momentum is required [16].

Indirect gap materials refer to materials whose valence band maxima and conduction band minima occur at different values of the wave-vector k . In this condition, photons with energy at least equal to the bandgap are not able to induce optical transitions from the valence band to the conduction band since the conservation of momentum is not satisfied. To ensure energy and momentum conservation, an extra-particle is required to provide the electron with the sufficient momentum value making the optical transition possible. This process involves a *phonon*, a quasi-particle associated with the vibration of the crystal lattice of the material, characterized by low energy and relatively high momentum (contrary to the photon which has high energy and low momentum). The phonon gives its momentum to the electron, modifying the momentum of the particle while conserving the energy and the momentum of the system. Since the transition from the valence band to the conduction band requires both the absorption of a photon and the emission or the absorption of a phonon, photon absorption in indirect gaps is weaker than in direct gap materials [16], and the thickness of material required to absorb most of the incoming light is, in turn, significantly larger.

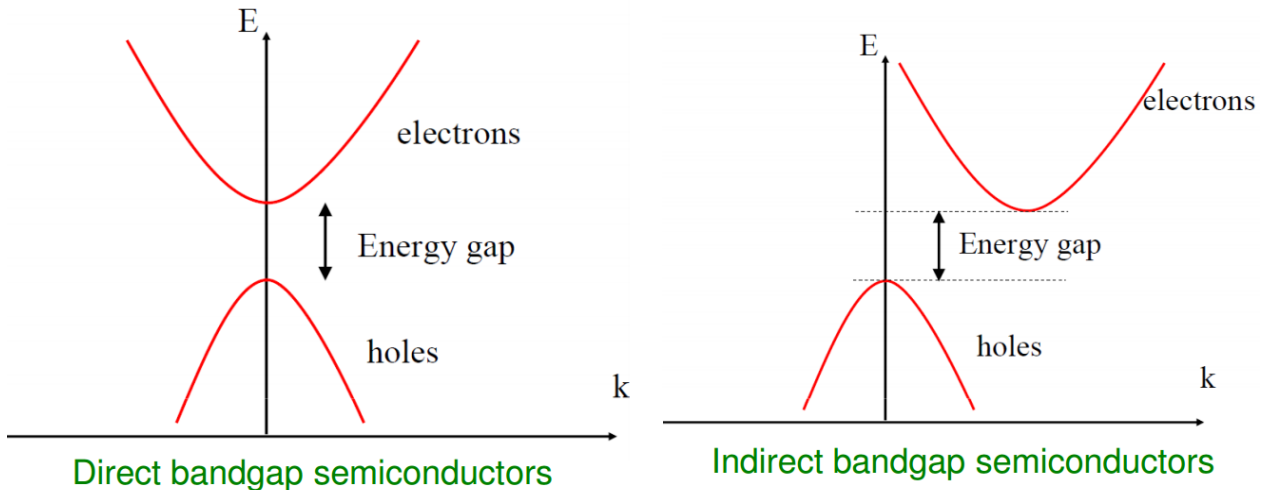


FIGURE I-4 Difference between direct and indirect semiconductor bandgaps [17].

2. Doping

Pure semiconductors are very weak electrical conductors. Introducing impurity atoms, known as *dopants*, in the semiconductor crystal changes the distribution of the electronic energy levels and alters the semiconductor electrical characteristics, leading to modified conductivity [16, 18]. Two types of doping are possible: *n*-type (negative) and *p*-type (positive) doping.

The *n*-type doping consists in increasing the concentration of electrons by introducing impurity atoms, known as *donors*, which can donate extra electrons able to move freely in the crystal. Increasing the total density of carriers increases the conductivity of the cell and the conduction in this type is mainly due to electrons [16,18,19].

The *p*-type doping consists in increasing the number of holes in the semi-conductor, by introducing impurity atoms, known as *acceptors*, which take valence electrons from another atom, leading to extra free holes. In this case, holes represent the majority carriers and electrons the minority carriers, so conduction is mainly due to holes [16].

3. Photovoltaic effect

Photons whose energy is higher than the semiconductor bandgap may be converted in the PV cell, creating electron-hole pairs able to move in the crystal network for a short period of time, before losing their energy and relaxing to the edge of their specific bands (conduction band for holes, valence band for electrons). For efficient photovoltaic devices, the carrier separation should be effective to ensure minimal recombination and efficient extraction of electrons on one electrode and holes on the other. It is commonly accomplished by generating an electric field inside the semiconductor material, at the *pn*-junction, a selective membrane transferring holes to the cathode and electrons to the anode [9].

4. *pn*-junction

The *pn*-junction is the basic structure of most solar cell technologies. It is created by associating two semiconductors of the same material but doped differently, one *p*-doped and

the other *n*-doped, creating an interface between the two semiconductors. Hence, a solar cell is assumed to have three distinct regions: a quasi-neutral *n*-type region, a quasi-neutral *p*-type region, and the *pn*-interface, named depletion region, between the two quasi-neutral regions.

As a result of doping, the *n*-side is mainly populated with electrons, while the *p*-side shows an excess of holes. By diffusion, and because of the concentration gradient between the different regions of the cell, the holes diffuse to the *n*-side and the electrons to the *p*-side. As they move toward the opposite side, charge carriers recombine in the vicinity of the junction, leaving positively charged dopant ions on the *n*-side and negatively charged ions on the *p*-side. Hence, at the *pn*-junction, the concentrations of electrons and holes balance, creating an equilibrium state with a zone having no free carriers, called *depletion* region or *space charge* region. The ions at the interface between the 2 quasi-neutral regions establish an intense built-in electric field preventing diffusion across the junction by pushing the free holes back toward the *p*-doped semiconductor and the free electrons to the *n*-doped layers. A differential potential between the *n* and *p* doped sides is induced by this electric field [9, 16, 18].

Consequently, two currents are distinguished in the *pn*-junction and contribute to the current flowing through the external circuit: the diffusion current generated by the carrier moving toward the *pn*-junction and the current flowing due to the built in electric field, pushing the carriers in the opposite direction. At equilibrium, these two currents cancel each other out.

The built-in electric field is a potential barrier between both quasi-neutral regions. In forward bias, a positive voltage being applied to the device, the applied electric field and the built-in electric field are in opposite direction in the depletion region. This reduces the net electric field and decreases the carrier diffusion barrier, allowing them to move from one side of the junction to the other, and increasing the diffusion current. Under reverse bias, a negative voltage being applied, the electric field and the built-in field are in the same direction resulting in higher net electric field, and increasing the diffusion barrier. The probability that carriers diffuse from one side of the junction to the other is reduced, leading to excessively small current flow in the circuit [9, 16, 18].

a) **In the dark**

At thermal equilibrium, a *pn*-junction in the dark cannot deliver any current or voltage in the absence of any external energy source. When an external voltage source is applied, the built-in differential potential shrinks and electrons that are injected to the *n*-type semiconductor move freely in the circuit and reach the *p*-side. The movement of electrons from *n* to *p* is balanced by the diffusion of holes from *p* to *n*. This diffusion current persists until an electrical potential difference arises for which the chemical energies of electrons and holes match. The driving force no longer exists, leading to the absence of any current flow in the circuit [9, 16, 18].

b) **Under illumination**

Three different processes occur when the *pn*-junction is exposed to light: carrier photo-generation, charge separation and carrier extraction.

Carrier photo-generation: Photons having energies higher than the bandgap may create an electron-hole pair, free to move in the crystalline network.

Charge separation: the *pn*-junction at the interface between the emitter and the base acts as a membrane, repelling electrons in the *n*-side and holes in the *p*-side.

Carrier extraction: If the cell's terminals are connected to an external circuit, the electrons move from the *n*-doped semiconductor through the external circuit to the *p*-side where they recombine with holes. The photo-generated carriers are collected by metallic contacts on both sides of the cell [9, 16, 18].

5. Recombination

The free carriers have a finite lifetime. The electrons in the conduction band tend to relax to lower energy levels in the valence band, where they recombine with holes, and lose their ability to move freely in the semiconductor material. This process is known as *recombination*.

The energy associated with any recombination event can be released through photon emission (radiative recombination) or through heat (non-radiative recombination). Based on these definitions, three major types of recombination processes are identified: *Radiative*, *Auger* and *Shockley-Read-Hall* (SRH) recombination, as illustrated in Figure I-5.

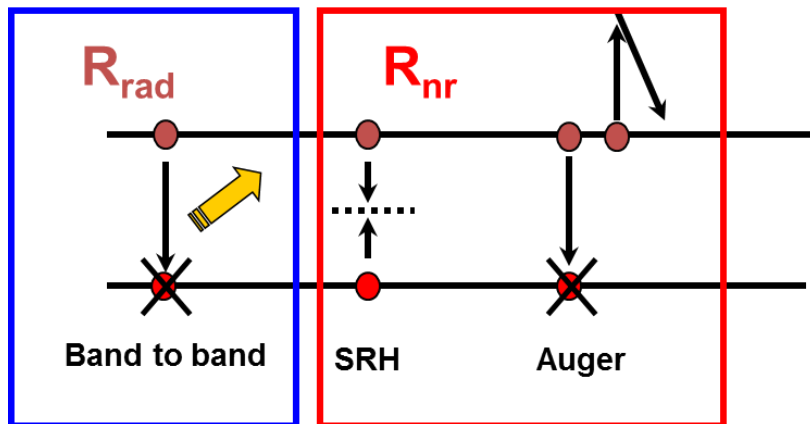


FIGURE I-5 Three main types of recombination. From left to right: Radiative recombination, Shockley-Read-Hall recombination and Auger recombination.

a) Radiative Recombination

Radiative recombination is an unavoidable and spontaneous recombination mechanism characterized by the annihilation of an *e-h* pair through emission of a photon with energy equal to the bandgap. Radiative recombination is the reverse process of photon absorption. Its rate increases with carriers' concentration and decreases with increasing temperature. It is the dominant recombination type in direct bandgap semiconductors [9, 16, 18].

The ability of a PV cell to emit a photon as a result of a recombination event was shown to significantly affect its efficiency. Several concepts are commonly used to quantify interactions between photons and electrons, such as quantum and radiative efficiencies. Because these terms are sometimes used interchangeably in the literature, creating confusion

since they represent different yields, some clarifications are made below to explain these differences.

i. Quantum Efficiency

The quantum efficiency (QE) is a spectral quantity representing the ratio between the number of electrons generated in the cell and the number of incident photons at a given wavelength. Two types of quantum efficiencies are distinguished: external and internal. Both types are usually formulated as a percentage as function of the wavelength [20].

a. External Quantum Efficiency

The external quantum efficiency (EQE) is the ratio between the number of photo-generated electrons that are extracted from the cell and the total incident photons at wavelength λ . It simply represents how efficiently a semiconductor converts a photon at a given wavelength. It is used by manufacturers as an indicator of the cell material quality, and for calibration of the cell efficiency to correct for the spectral mismatch between the reference spectrum and the test spectrum [20-22].

b. Internal Quantum Efficiency

The internal quantum efficiency (IQE) is the ratio between the number of carriers collected by the cell and the total number of absorbed photons at a given wavelength. The IQE is always higher than the EQE value since it only considers the *absorbed* photons and not the total incident photons. Both quantities are related by the reflectivity coefficient R , *photons in* denoting the total number of incident photons [20].

$$IQE = \frac{EQE}{(1 - R)} = \frac{\text{Electrons out}}{\text{Photons in} \times (1 - R)} \quad (\text{I-2})$$

ii. Radiative Efficiency

The radiative efficiency (RE) is a global ratio describing the percentage of radiative recombination occurring in the cell. It is an important indicator to estimate the performance of the cell material [22]. It can also be differentiated into external and internal radiative efficiencies.

a. External Radiative Efficiency

The external radiative efficiency (ERE) represents the ratio between the number of photons emitted radiatively that escapes from the cell (as a result of band-to-band recombination) and the total number of recombination occurring in the cell. To achieve the highest conversion efficiency possible, solar cells should exhibit an ERE of 100%. Nevertheless, the measured ERE is typically less than 1% for most of the manufactured cells nowadays. The ERE of direct bandgap semiconductors ranges between 1% and ~25% (as computed by Braun et al. [23] for the new GaAs AltaDevice with a record efficiency of 28.8% [24]). Low external radiative efficiency is a signature of large non-radiative recombination losses in the cell.

The ERE strongly depends on the applied voltage. The open-circuit voltage (V_{oc}) is considered as a reference voltage to measure ERE, given that the ERE is closely related to EQE at V_{oc} , as elaborated by Rau and Green [21, 22, 25, 26].

$$ERE = \frac{\exp\left(\frac{qV_{oc}}{kT}\right) \int_0^{\infty} \phi_B(E) EQE(E) dE}{I_{sc}} \quad (I-3)$$

$$\phi_B(E) = \frac{2\pi q}{h^3 c^2} \frac{E^2}{\exp\left(\frac{E}{kT}\right) - 1} \quad (I-4)$$

with I_{sc} the short-circuit current, q the elementary charge, k the Boltzmann constant, T the temperature in Kelvin, h the Planck's constant, c the speed of light and E the photon energy which depends on the wavelength.

b. Internal Radiative Efficiency

The internal radiative efficiency (IRE) represents the ratio between radiative recombination and total recombination in the bulk of the semiconductor. Its value is higher than the ERE, since it considers all the radiative recombination occurring in the cell, while ERE only accounts for photons generated by radiative recombination escaping from the cell. IRE reaches up to 99.7% in the case of GaAs [26], translating the predominance of radiative recombination in direct bandgap materials. The IRE value sets an upper bound on the ERE, and IRE should be $>> 90\%$ to ensure high external radiative efficiencies [22, 26].

External and internal radiative efficiencies are related using Geisz, et al. [27] formula, described in equation (I-5), with P_{esc} the probability that a photon emitted radiatively from the recombination of an electron and a hole escapes from the cell and P_{abs} the probability that a photon emitted radiatively is reabsorbed in the bulk of the semiconductor. $\overline{P_{esc}}$ and $\overline{P_{abs}}$ represent the averaged probabilities of these two parameters respectively.

$$ERE = \frac{IRE \times \overline{P_{esc}}}{1 - (IRE \times \overline{P_{abs}})} \quad (I-5)$$

b) Auger Recombination

Auger recombination is an unavoidable non-radiative recombination process where an electron or a hole interacts with a similar free carrier by transferring its energy as kinetic energy. The collision between 2 similar carriers results in 1) the relaxation of the first carrier which then recombines with an oppositely charged carrier, and 2) the excitation of a second carrier to higher energy levels. The excited carrier then relaxes back, losing its excess energy as heat. This type of recombination involves three particles: an electron and 2 holes (ehh configuration) or 2 electrons and a hole (eeh configuration).

Auger recombination rate is particularly significant for low bandgap materials, indirect semiconductors and heavily doped semiconductors (since it is proportional to the electron and hole concentrations) [9, 16, 18].

c) Shockley Read-Hall Recombination

Shockley-Read-Hall recombination is an avoidable non-radiative recombination mechanism caused by the presence of defects and impurities in the semiconductor. These defects form traps for free carriers by introducing new energy levels in the forbidden zone.

An empty trap may lead to the annihilation of an $e-h$ pair by simultaneously capturing an electron and a hole, the recombination energy being released as heat. The capture

probability of each type of charge carrier strongly depends on the position of the trap in the forbidden gap: if the traps happen to fall near the valence band or the conduction band, the probability of recombination is very low while the highest probability occurs for midway traps.

SRH recombination is non-negligible in materials with similar concentrations of electrons and holes (such as undoped or lightly-doped materials), and its amplitude is function of the material quality, the concentration of defects, and the temperature [9, 16, 18].

d) Surface Recombination

Surface recombination refers to SRH recombination occurring at the surface of the material, due to the high densities of defects as a result of broken bonds in the crystal, and extrinsic impurities. The surface recombination rate decreases for heavily doped semiconductors and increases with temperature. It is proportional to the density of traps per unit area [9, 16, 18].

e) Mobility

The carrier mobility is an important property of the semiconductor material. It illustrates how easily and rapidly a charge carrier moves in the bulk of the material when an electric field is applied.

f) Lifetime

The lifetime is the average time a free electron exists from its photo-generation until its recombination with a hole. Electron lifetime in direct semi-conductors is usually short (in nanoseconds) whereas the lifetime in indirect semiconductor is larger, ranging between microseconds and milliseconds.

Since the total recombination rate can be computed as the sum of the individual recombination rates, the inverse of the lifetime can be calculated as the sum of the inverse of each recombination lifetime.

g) Diffusion length

The diffusion length represents the average distance travelled by an electron from its generation to its recombination. Heavily doped semiconductors have a shorter diffusion length as a consequence of the higher recombination rate. High diffusion length denotes high carrier lifetime, a signature of higher material quality and a necessary condition for achieving better cell performance. The diffusion length depends on the type and magnitude of recombination occurring in the semiconductor material, as well as on the lifetime and carrier mobility.

6. Electrical characteristics

a) Equivalent circuit

Equivalent electrical models describe the electrical behavior of solar cells using basic electronic components, such as resistors, current generators, and diodes. The equivalent electrical circuit of an ideal photovoltaic cell, as shown in Figure I-6, comprises a current source which delivers a current proportional to the number of absorbed photons, and a parallel diode which models the *pn* junction and the recombination current [9, 28].

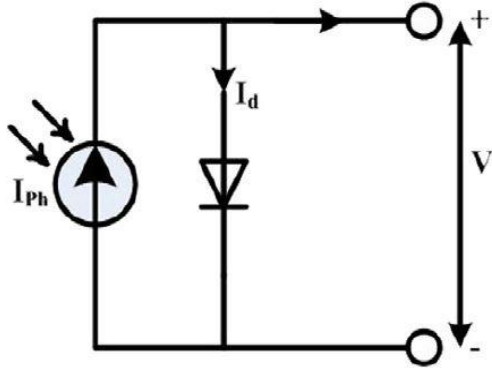


FIGURE I-6 Equivalent circuit of an ideal solar cell [29].

The current flowing through the terminal of the circuit can be expressed as eq.(I-6).

$$I = I_{ph} - I_d \quad (I-6)$$

with I_{ph} the photo-generated current and I_d the current flowing through the diode. This equation can be further developed to provide an explicit equation linking the current I and the voltage V .

$$I = I_{ph} - I_0 \left(e^{\frac{qV}{nkT}} - 1 \right) \quad (I-7)$$

$$V = \frac{k}{q} \times n \times T \times \ln\left(1 - \frac{I - I_{ph}}{I_0}\right) \quad (I-8)$$

where I_0 is the dark saturation current, and n is the diode ideality factor. q , k and T are the elementary charge, Boltzmann's constant, and cell operating temperature, respectively.

A more detailed and complex model is needed to describe realistic solar cells accounting for parasitic resistances inside the cell. Figure I-7 represents more realistic equivalent circuits accounting for series resistances alone (a) and series and shunt resistances (b). Series resistances occur due to the current flowing through the cell, the contacts and the metallic grid, while shunt resistances are due to current leakages through the cell. To better describe the recombination occurring in the cell, one may modify the value of the diode ideality factor n to account for non-ideal recombination or, alternatively, include a second diode describing additional recombination path occurring in parallel [28].

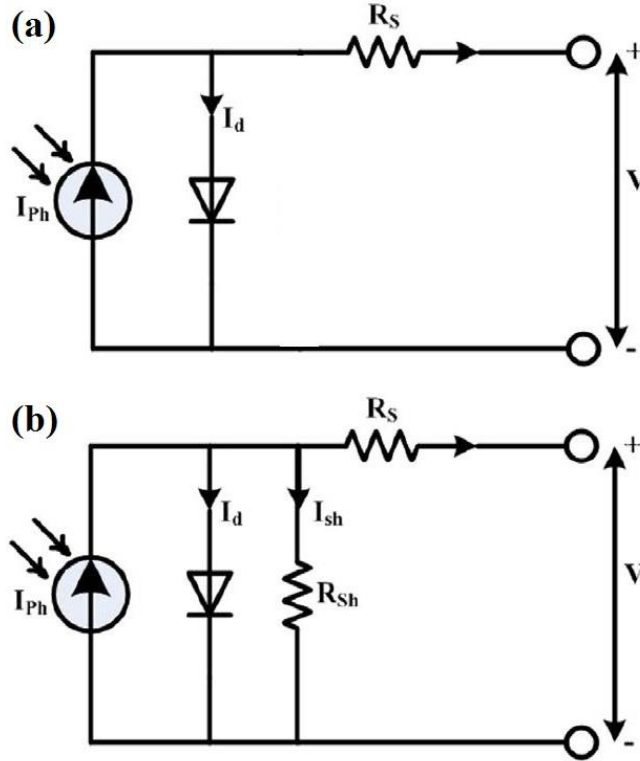


FIGURE I-7 Equivalent circuits of realistic solar cells, accounting for series resistances alone (a), and for both series and shunt resistances (b) [29].

Accounting for series resistances in the solar cell electrical model leads to a modification of equation (I-7) to deal with the voltage drop across the resistance, as described by equation (I-9), with R_s the series resistance:

$$I = I_{ph} - I_0 \left(e^{\frac{q(V+IR_s)}{nkT}} - 1 \right) \quad (I-9)$$

Series resistances induce power losses, P_{loss} , known as *Joule heating* or *Ohmic heating*, that are expressed by equation (I-10). These losses cause the degradation of the extracted power, and consequently, of the conversion efficiency.

$$P_{loss} = R_s I^2 \quad (I-10)$$

Equation (I-11) represents the behavior of the equivalent electrical circuit while accounting for both series and shunt resistances (with R_p the shunt resistance):

$$I = I_{ph} - I_0 \left(e^{\frac{q(V+IR_s)}{nkT}} - 1 \right) - \left(\frac{V + IR_s}{R_p} \right) \quad (I-11)$$

b) Dark current

The dark saturation current represents the current flowing through the cell when a bias voltage is applied in the dark [16]. At the radiative limit, it can be expressed as:

$$I_0 = \frac{q}{k} \times \frac{15\sigma}{\pi^4} \times T^3 \times \int_u^{\infty} \frac{x^2}{e^x - 1} dx \quad (I-12)$$

with $x = E/(kT)$, $u = E_g/(kT)$, and σ being the Stefan-Boltzmann constant.

It represents the recombination current density at thermal equilibrium [30] and increases as the recombination rate rises. It strongly depends on the minority carrier lifetime [30], on the temperature and the electronic energy gap [16].

c) **Photo-generated current**

It represents the current generated by the solar cell under illumination. It largely depends on the number of photons absorbed, on the spectral-distribution of the incoming light, the semiconductor bandgap and the quantum efficiency of the cell. I_{ph} increases as the bandgap decreases since more photons can be absorbed and converted.

$$I_{ph} = X \times q \int_{E_g}^{\infty} QE(E) \times f(E) dE \quad (\text{I-13})$$

where X is the concentration ratio and $f(E)$ is the photon flux distribution of the incident solar radiation. For instance, for a blackbody input,

$$f(E) = \frac{2\pi}{h^3 c^2} \frac{E^2}{\exp\left(\frac{E - \mu}{kT}\right) - 1} \quad (\text{I-14})$$

with h and c the Planck's constant and the speed of light respectively, E the photon energy, and μ the chemical potential.

d) **I-V curve**

In the radiative limit, the net current flowing through the cell is the difference between the absorbed and emitted flux. As the voltage increases, the net current decreases and vanishes as the absorbed and emitted currents cancel out.

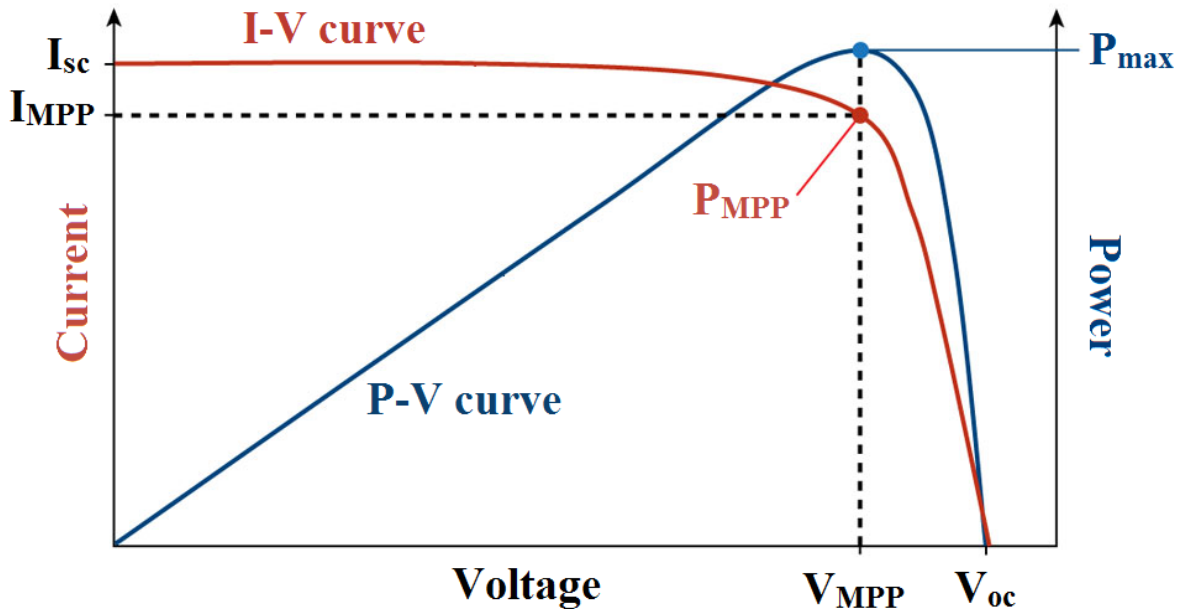


FIGURE I-8 I-V curve and corresponding P-V curve along with the main electrical parameters of a solar cell [31].

Equations (I-7), (I-9) and (I-11) illustrate the interdependence of voltage and current in a solar cell.

Figure I-8 illustrates the current-voltage characteristic of a solar cell in red, as well as the resultant power, in blue. Three important physical parameters are to be noted on the I-V curve: the open-circuit voltage (V_{oc}), the short-circuit current (I_{sc}) and the maximum power point (P_{MPP}) which corresponds to the maximum power that is extracted from the cell, P_{max} , at the point (V_{MPP} , I_{MPP}).

i. Short-circuit current

The short-circuit current, I_{sc} , represents the current flowing through a short-circuited cell, and is the maximal current generated by the cell. It is due to the generation and collection of light-generated carriers.

I_{sc} strongly depends on the number of absorbed photons and hence on the light intensity to which it is directly proportional, as well as on the solar spectrum. It is also dependent on the electron and hole diffusion lengths, the surface passivation and the cell area.

ii. Open-circuit voltage

The open-circuit voltage (V_{oc}) represents the voltage across a disconnected circuit and is the highest voltage that can be extracted from the cell. The generated carriers cannot leave the cells at this point, since they have no path to circulate, so they accumulate on both sides of the junctions and build up in density, increasing the differential potential between the electrical contacts. Because the photo-generated current and the dark current cancel out there is no net current flowing through the circuit [16], and the extracted power is zero. V_{oc} is given by:

$$V_{oc} = \frac{n k T}{q} \ln \left(\frac{I_{sc}}{I_0} \right) \quad (\text{I-15})$$

V_{oc} depends on the short-circuit as well as on the dark current. V_{oc} is especially sensitive to the cell temperature, as well as to the recombination mechanisms occurring in the cell, due to the strong temperature and recombination dependence of I_0 .

iii. Maximum power point

To optimize the power extracted from the cell, the device should operate at the maximal power point, P_{MPP} , where the maximal power is obtained for optimal current (I_{MPP} – current at maximal power point) and voltage (V_{MPP} – voltage at maximum power point).

iv. Fill factor

The fill factor, FF , represents the ratio of the maximum power extracted from the cell and the product of V_{oc} and I_{sc} . It is an indicator of the cell quality and should ideally be as close as possible to 1 to ensure high cell efficiency. It is computed using equation (I-16) with V_{MPP} and I_{MPP} the voltage and the current at maximum power point (P_{MPP}).

$$FF = \frac{V_{MPP} \times I_{MPP}}{V_{oc} \times I_{sc}} \quad (\text{I-16})$$

v. Conversion efficiency

The conversion efficiency, η_{pv} , represents the fraction of the incident power that is converted into electricity. It is the ratio between the maximum power extracted from the cell

and the incident solar power, as illustrated by equation (I-17), with P_{in} the incident solar power.

$$\eta_{PV} = \frac{FF \times V_{oc} \times I_{sc}}{P_{in}} = \frac{V_{MPP} \times I_{MPP}}{P_{in}} \quad (I-17)$$

e) Ideality factor

The diode ideality factor, n , defines the solar cell junction quality and provides indications concerning the types of recombination occurring in the cell. It describes how closely the diode behavior approaches ideality (a value of 1 corresponding to the ideal diode), and depends on the main recombination mechanism in the cell, the injection regime, and the region of the cell where recombination is predominant. n typically varies between 2/3 (Auger-limited in high injection, where the generated carrier density is higher than the doping) and 2 (SRH-limited in high-injection).

f) Parasitic Resistances

Parasitic resistances such as series and shunt resistances, represent power dissipation through electrical resistances or leakage currents respectively [16]. They affect different regions of the I-V curve and lower the fill factor.

i. Series Resistances

Series resistance losses stem from the current flowing through the emitter and base of the cell, the contact resistances between the metal and the semiconductor and the front and back contact resistances [16].

Resistive losses decrease the fill factor by modifying the I-V curve in the region near V_{oc} , without altering the V_{oc} value. Its effect increases as the resistance value increases, or with increasing current, since, as mentioned earlier, the losses are proportional to the square of the current.

ii. Shunt Resistances

Shunt resistances are due to current leakages through the cell, at the solar cell edges or between contacts of different polarities and are mainly due to manufacturing defects inside the material [16]. Small shunt resistances create an alternative current path in the circuit, which reduces the current flowing through the junctions of the solar cell. Shunt losses, which mainly affect the I-V curve close to I_{SC} , are more pronounced under low light intensity.

g) Effect of irradiance

The short-circuit current increases linearly with illumination intensity, while the open-circuit voltage is a logarithmic function of the incident power. Consequently, the conversion efficiency grows logarithmically with illumination intensity. In reality, several limiting mechanisms (cell over-heating, series resistance losses) may alter the cell ability to demonstrate a continuous increase in efficiency with increasing illumination intensity, giving rise to a “peak” intensity above which efficiency decreases [16]. The effect of irradiance will be further described in chapters II and III.

h) Effect of temperature

The temperature generally increases the short-circuit current and decreases the open-circuit voltage, as a result of decreasing the bandgap and increasing the dark saturation current. Those effects are further discussed in chapters II and V.

C. Photovoltaic technologies

A variety of solar cells are available today to harvest solar energy. Figure I-9 represents the evolution of the photovoltaic cells technologies since they were first manufactured, in 1976, accounting for the different emerging ideas to improve the cells performances.

Best Research-Cell Efficiencies

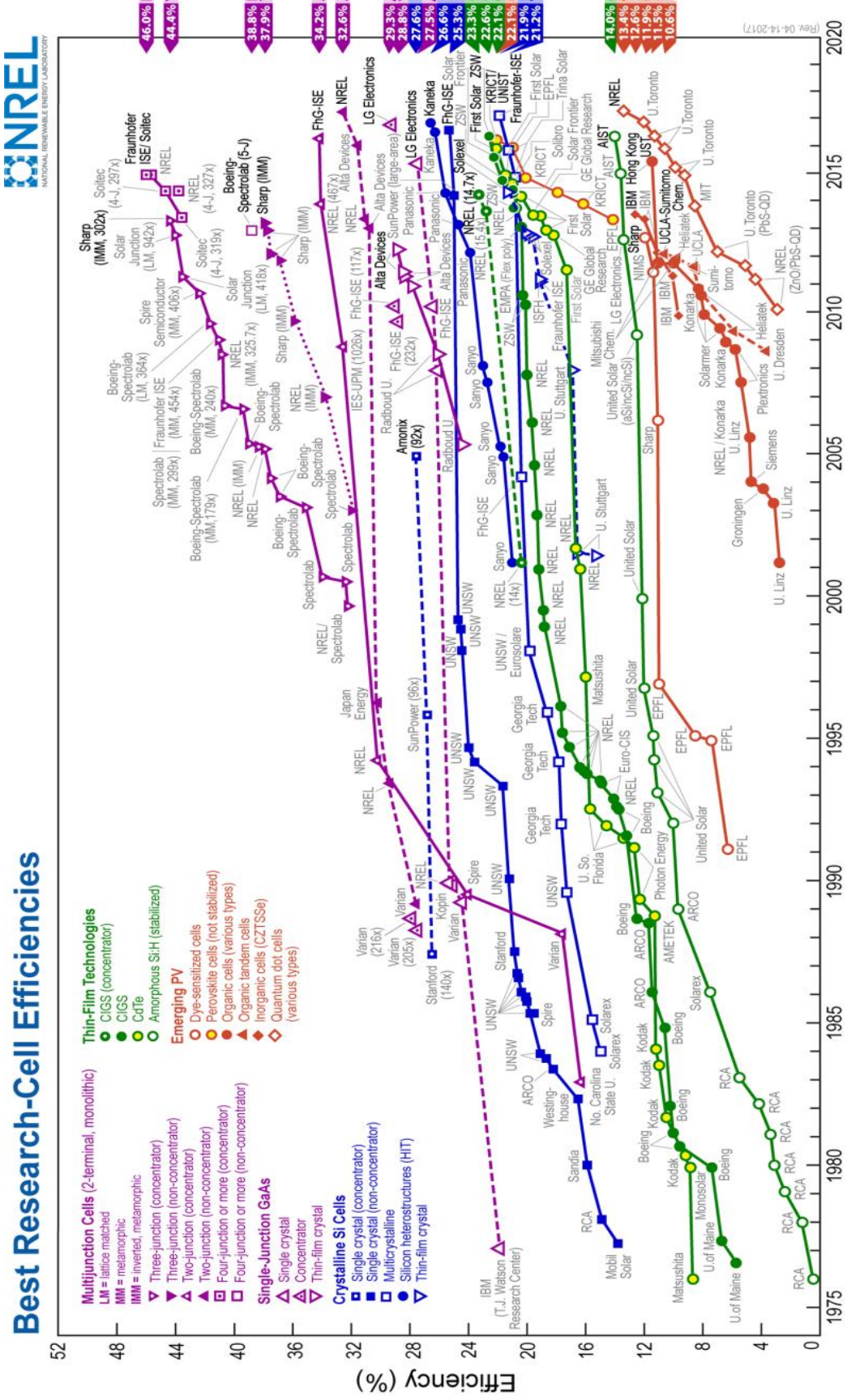


FIGURE I-9 Evolution of the different solar cells' technologies since 1976 [32].

1. Silicon technologies

Crystalline Silicon technology has been developed since 1954 and remains by far the most widely used PV technology worldwide accounting for almost 90% of the global photovoltaic market [33].

Silicon is the second most abundant element on Earth, after oxygen. Several types of Silicon are currently used in the PV industry: mono-crystalline, polycrystalline and amorphous [9, 33].

The cheapest and most widely used technique to elaborate mono-crystalline silicon wafers is known as Czochralski process. This method consists in melting Silicon in a Quartz container, in which a seed crystal mounted on a rod is dipped after the silicon has melted. The rod is spun while being slowly pulled up from the melt to ensure the crystallization of Silicon on the seed. Once the required size is obtained, the rod is withdrawn quickly to maintain its diameter. The size and diameter of the single crystal ingot is controlled by varying the melting temperature, the spinning speed and the withdraw rate. Thin silicon wafers are then cut from the formed ingot and polished. Today's record Silicon solar cells (with a conversion efficiency of 26.7% [9, 14, 33]) are obtained using such wafers.

Poly-crystalline cells show significantly smaller size of the crystal grains, compared to mono-crystalline wafers, [34]: despite their lower performances (primarily because of the inherently lower material quality), these cells offer a cheaper alternative to mono-crystalline Silicon. In both technologies, the cell thickness is typically comprised in the range 200-500 μm [9, 33].

2. Thin film solar cells

Thin film solar cells, commonly referred to as “second generation PV cells”, are characterized by their thickness which is in the order of 1 to 10 microns (1 or 2 orders of magnitude less than conventional Silicon cells). They are produced by depositing thin layers of a semiconductor on glass, metal or polymer. They require less semiconductor material than conventional Si-cells and hence are cheaper to manufacture. Their performances are still poor due to the challenging issues associated with high quality semiconductor film growth [33]. Three main successful types of thin film solar cells can be identified today: amorphous silicon, CdTe (Cadmium Telluride) and CIGS (Copper Indium Gallium Selenide).

Amorphous silicon cells are natural candidates for thin film solar cells, primarily because of the abundance and low toxicity of Silicon [35]. They are processed at low temperature, which allow the deposition on a low-cost substrate [36]: because of their good optical absorption properties, these cells only require a very thin layer of active material. Their relatively low performance mainly stems from the high concentration of impurities in the materials, as well as their tendency to degrade strongly when exposed to light [33, 34].

Cadmium Telluride (CdTe) solar cells are one of the most performing “thin film” technologies with a record efficiency of 21% [14]. This technology is cheaper than the others, however their manufacturing process requires high temperature, and CdTe is unstable and degrades quickly. Because of the toxicity of Cadmium, particular attention should be brought during the recycling of these cells at the end of their useful life [33, 34].

The last important technology to mention is Copper Indium Gallium Selenide (CIGS) which presents the highest efficiency among thin-film technologies, with a cell record of 21.7% [14]. It has a direct bandgap and a good light absorption with less degradation over time compared to the previous two technologies [34, 35].

Other thin-film technologies emerged more recently and are thus in the early stages of their development. They appeared subsequent to the thin-film second generation and are classified in the emerging third generation PV cells that will be described in the following sections.

3. III-V materials

While silicon dominates the solar cells market nowadays, there is however a broad range of research work aiming at improving PV efficiency well above the typical efficiency achievable with Silicon or “thin film” solar cells described above. Most of these cell concepts involve classes of materials known as III-V compounds, formed by elements from groups III and V of the periodic table. These compounds were first used for space applications and electronics, before being suggested as good candidates for terrestrial PV. III-V materials cover a wide range of bandgaps and are characterized by high absorption coefficients [37, 38]. They provide excellent performances, but their cost is significantly higher than that of Silicon or thin-film technologies, since these materials are not abundantly available [2]. The record conversion efficiency of any single-junction PV cell is currently held by a Gallium Arsenide (GaAs) cell, with a cell record of 28.8% [14,39]. This compound is formed with gallium, which is a scarce element (less abundant than gold), and arsenide which is a profuse but toxic element. It has a direct bandgap of 1.4 eV at ambient temperature, which lies in the range of optimal bandgap (1.1-1.5 eV) required for the highest performances. Until recently, the high cost of this material (mostly caused by the scarcity of Gallium) prevented a wide development of this cell technology [40], which was mainly implemented in *niche* markets (such as space applications, multi-junction and concentrator solar cells). Recent progress in epitaxial lift-off processes allowed the development of 1 sun GaAs cells offering both very high conversion efficiency and affordable price (as a result of the very low quantity of material required, and the possibility of re-using the wafer substrate up to ~1000 times).

The first two generations of solar cells, as well as III-V semiconductors, harvest small fractions of the solar spectrum, corresponding to photons with energies equal or slightly higher than their bandgap energy, whereas the remaining parts are lost (below E_g losses) or inefficiently converted (due to thermalization losses). This is due to the wide discrepancy between the large energy distribution of the solar spectrum and the narrow energy range that can be efficiently converted by solar cells. To deal with this issue, multi-junction solar cells have been developed.

4. Concentrated photovoltaics (CPV)

Concentrated photovoltaics involve optical elements collecting sunlight from a large area and concentrating it on a small receiver. In doing so, it is possible a) to reduce dramatically the area of PV cell required to produce a given amount of electricity and b) to improve significantly the solar to electricity conversion efficiency. The area of PV cell required being reduced by orders of magnitude in comparison with conventional flat-plate

PV, there is a strong incentive to implement highly efficient PV cells in concentration systems which would normally be considered as far too expensive for conventional PV applications (such as multi-junction solar cells). Among the main limitations of CPV systems, one should mention 1) the inability of these systems to harvest diffuse light and 2) the risk of cell overheating associated with high illumination levels, requiring efficient cooling systems to be used. This technology will be further detailed in the following chapter.

5. Emerging PV

“Third generation solar cells” refer to recent PV cell technologies, mainly developed in the last two decades, and which currently instigate the most intensive research efforts among all PV cell technologies. These cells can be subdivided into two main groups: 1) solar cells aiming at overcoming the Shockley-Queisser limit for single-junction solar cells (~33%), such as multi-junction solar cells, intermediate band solar cells, quantum dots, hot carriers or up and down conversion (most of these technologies being in their research phase or early stages of development), and 2) cells with very low manufacturing cost such as dye sensitized cell, organic or perovskite cells.

a) Multi-junction solar cells

Multi-junction solar cells basically involve multiple *pn* junctions with different bandgaps stacked on top of each other, allowing a larger fraction of the solar spectrum to be harvested. III-V semiconductors are commonly used with multi-junction cells due to their high efficiency, as well as the flexibility they offer in terms of bandgap engineering and lattice matching. To date, solar to electricity record conversion efficiency is measured on a quadruple-junction cell (made of 4 different sub-cells) with an efficiency of 46%, under concentrated sunlight [14]. This technology will be further developed in the following chapter.

b) Intermediate band solar cells

The concept of intermediate band solar cells was first proposed by Luque and Marti in 1997 [41]. This emerging technology aims at increasing the conversion efficiency, by incorporating an intermediate band between the valence and conduction bands, creating three bandgap energies: E_g from the valence band to the conduction band, E_{g1} from the valence band to the intermediate band, and E_{g2} from the intermediate to the conduction band. This configuration allows the absorption of a broader range of photons, additional optical transitions between the intermediate, the valence and the conduction bands occurring in the cell [16, 42-45].

The theoretical efficiency of this technology can reach 46% under 1-sun illumination and 63% under maximum concentration, which is equivalent to the theoretical maximal efficiency of a triple-junction solar cell under the same illumination level [41, 44].

Intermediate bands can be created by introducing impurities into the materials, either by using materials which naturally possess multiple bands of narrow width, such as II-VI materials or semiconducting oxides [16, 46], or by using quantum dot technology.

c) **Quantum dots solar cells**

Quantum dots are tiny semiconductor particles, usually produced with II-IV, III-V or IV-VI materials, that can confine electrons when implemented in bulk semiconductor materials. Their nanometer size changes the particles' physical and optical properties (in comparison with "bulk" semiconductors). The optical properties of the quantum dot can be tuned by changing its size and shape, making this technology attractive for integration in multi-junction or intermediate band solar cells [34, 47]. Incorporation of quantum dots in bulk semiconductor materials gives rise to additional transitions (the bandgap of the dots being smaller than the "bulk" gap) and, in turn, broadens the absorption spectrum.

Quantum dot solar cells can theoretically reach up to 66% under full solar concentration [48]. However, their practical performances remain quite modest today, with a record of 13.4% obtained using cesium lead triiodide (CsPbI_3) as quantum dot materials.

d) **Hot carriers solar cells**

The concept of hot carrier was introduced by Ross and Nozik in 1982 [34]. In conventional cells, incident photons with energies greater or equal to the bandgap are absorbed with the excess energy (i.e. the difference between their initial energy and the bandgap) being lost as heat. "Hot carrier" refers to the energetic state of a charge carrier immediately after absorption of a high-energy photon, and before relaxation to the band edge: its temperature can reach up to $\sim 3000\text{K}$ [48].

"Hot carrier" solar cells are designed toward exploiting the energy of charge carriers while still hot, before their relaxation to the band edge [16, 18, 49]. The excess kinetic energy can be used to excite electrons via impact ionization, generating additional electron/hole pairs. Otherwise, the hot carriers can be extracted directly while still hot, and the excess kinetic energy is converted into electrical work. Electrons and holes should reach their respective contacts before losing their excess kinetic energy, a requirement which may be fulfilled with special energy-selective contacts preventing the contacts from cooling the carriers. Using quantum dots can retard the cooling down by slowing the energy relaxation from picoseconds to nanoseconds [18, 49-51].

The theoretical maximum efficiency under solar concentration is 86.7% [49, 50], but this technology is still in its research phase, and attempts to fabricate practical devices have led to significantly lower conversion efficiency.

e) **Up and down conversions**

Up and down spectral conversions are strategies used to better exploit the solar spectrum, by rearranging the photons' energy distribution to better match the cell bandgap.

Up-conversion consists in converting 2 or 3 low-energy photons into one high energy photon, usually greater than the bandgap energy, to ensure its absorption and conversion by the solar cell [18, 52, 53]. The up converter, which is placed below the cell, should be designed to reflect high energy photons stemming from the up-conversion process back to the cell, allowing generation of additional electron-hole pairs [53]. This strategy can be implemented in any technology of wide bandgap solar cell [53, 54]. Theoretically, it leads to

an efficiency of 47.6% under 1-sun illumination, and to a maximum efficiency of 63.2% under full concentration [52,53].

Down-conversion consists in the absorption of a very energetic photon, followed by re-emission of two photons with lower energies [18]. The down converter is placed in front of the cell, where it is exposed to ultraviolet photons, which are absorbed and converted into visible photons. This strategy can be implemented in any low-bandgap cell technology [54] and can reach a maximum efficiency of 39.6% under 1-sun illumination.

f) Dye sensitized solar cells

Dye sensitized solar cells are low-cost and easy to manufacture thin film cells, able to convert any visible light into electricity, using a conversion process similar to artificial photosynthesis. These cells were first developed in 1991 by M. Graetzel and B. O'Regan [33, 34, 44] and were only able to convert blue and ultraviolet light. Today, the absorbed light ranges from infrared to ultraviolet, with a cell record of 11.9% [14].

Dye sensitized solar cells use a dye, which is a photoactive material able to generate electricity when exposed to light [55].

The dye sensitizer absorbs the incident photons and excites electrons, making them free to move to the semiconductor materials (normally consisting in wide bandgaps semiconductors, to provide a better chemical stability, like TiO₂, ZnO or Nb₂O₅ [55]). The electrons then move toward an electrode that collects them to power a load, before travelling back to the dye molecules through a chemical electrolyte (usually an organic solvent with a redox system used to close the circuit) [33, 55, 56].

These cells can efficiently absorb diffuse light and operate in low-light intensity conditions, on cloudy days. The biggest issues related to the operation of dye sensitized cells concern the stability over time, and the degradation of the electrolyte in outdoor conditions, primarily because of its sensitivity to temperature. Many improvements are still required to better absorb solar photons, enhance carrier transportation, improve stability and replace the liquid electrolyte with a solid-state one after finding a way to introduce it inside the cell [18, 44].

g) Organic PV

Organic solar cells are manufactured from thin-film polymers or molecular semiconductors, and small molecules such as copper phthalocyanine, carbon fullerenes and their derivatives, mainly PCBM ([6,6]-phenyl C₆₁ butyric acid methyl ester). They require moderate manufacturing temperature and use green materials, but currently have low conversion efficiencies, with a cell record of 11.2% [14,18,33]. They are characterized by high absorption coefficients, and the amount of material required to absorb light is thus very small. These materials are also good candidates for flexible solar cells [44]. Because of the organic nature of these cells, it is common to refer to the lowest unoccupied molecular orbital (LUMO) and to the highest occupied molecular orbital (HOMO), rather than conduction band and valence band [57].

Absorbed photons do not directly generate electrons and holes, but *excitons* which are an electron and a hole bonded together with energy typically in the order of hundreds of meV. The separation between electrons and holes happens at the interface between two different materials, an electron donor and an electron acceptor, forming the active region of the cell. The electrons then migrate to the electron acceptor layer, from the HOMO of the donor to the HOMO of the acceptor [33,58]. Once the free charges are produced, they move through the materials, to be collected at their respective electrodes from where they move to the external circuit and generate a current flow [58].

A challenging issue with organic PV cells lies in the very small diffusion length of excitons, which may prevent them from crossing the absorber layer. As a solution, heterojunction semi-conductors consisting of two different organic materials forming the electron donor and acceptor were suggested. In this configuration, the different layers have reduced size, in the nanometer scale, which is closer to the exciton diffusion length [59].

Organic cells still face major issues preventing them from achieving high conversion efficiency. In fact, they present poor carrier transport properties, stability issues (since they degrade rapidly when exposed to sunlight, oxygen or water vapor), and a limited lifetime.

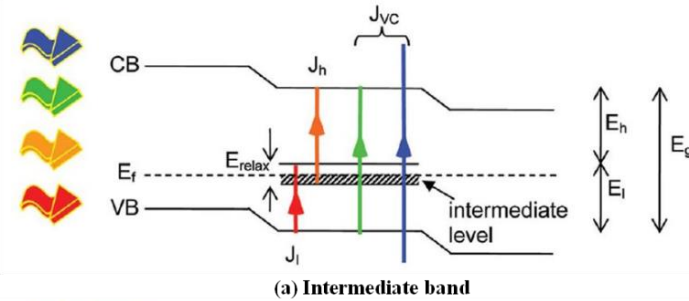
h) Perovskite solar cells

Perovskites cells are based on hybrid organic/inorganic light absorbing semiconductors and were first suggested in 2009 by Miyasaka as solid-state dye sensitizers because of their interesting properties as light harvesters [60]. The first research article describing perovskite as a semiconductor for solar cells, with very low efficiencies, was published in 2012. Within 6 years, the efficiency increased drastically and has reached today a value of 20.9% [14,34,60].

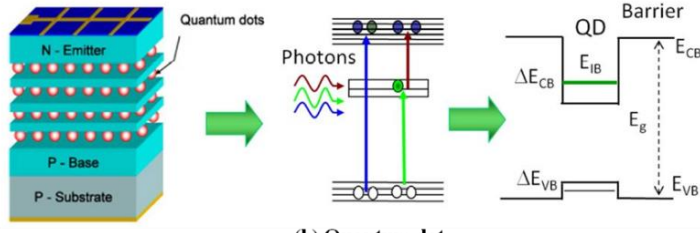
The absorber material is made of a mineral with a crystal structure in the form ABX_3 , with A being an organic cation, B an inorganic cation (usually Pb^{2+}) and X a halogen anion namely F^- , Cl^- , I^- or Br^- [61]. The absorber material is placed between an electron transporting layer, usually TiO_2 , and a hole transporting layer. The electron and hole extraction occurs at the interfaces between the electron transfer layer/perovskite and between perovskite/hole transfer layer respectively. The front of the cell consists of a transparent conductive oxide glass substrate while the back is made of an electrically conductive gold-coated electrode.

Perovskite cells are manufactured easily and at low-cost, without requiring high processing temperatures. They are lightweight and flexible [34]. A major concern with Perovskite cells is their stability, since the cells' performance decay rapidly in outdoor conditions when exposed to moist air, oxygen, water or UV light. In addition, these cells are much sensitive to temperature and their lifetime is still limited today [61-65].

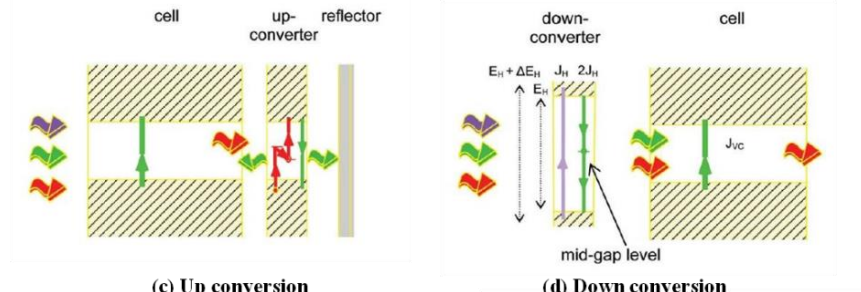
In summary, there are currently many PV technologies (Figure I-10) that can produce electrical energy efficiently, and at low costs. An inherent drawback of PV, however, lies in the complexity and the high cost of electricity storage. Alternatively, electrical energy can be produced thermodynamically via concentrated solar power systems, at a higher cost than PV, but with the option of storing excess energy easily and at low-cost.



(a) Intermediate band

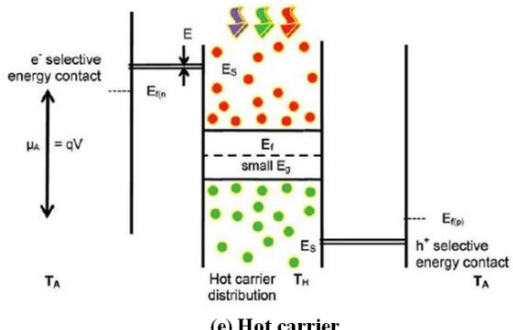


(b) Quantum dot

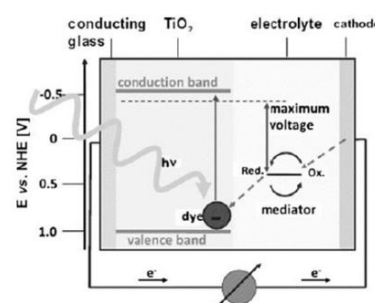


(c) Up conversion

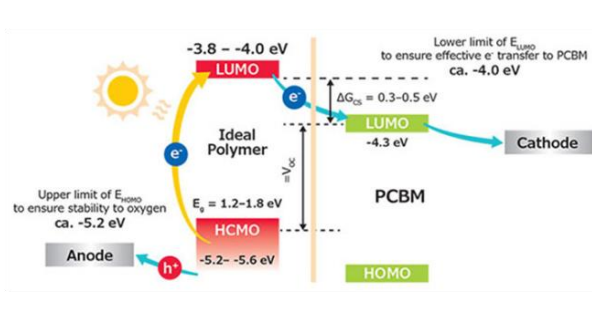
(d) Down conversion



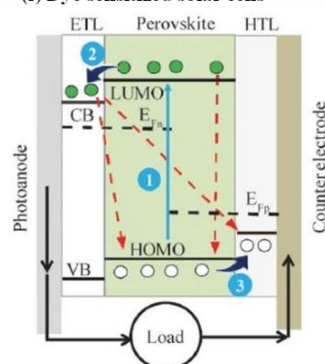
(e) Hot carrier



(f) Dye sensitized solar cells



(g) Organic solar cells



(h) Perovskite solar cells

FIGURE I-10 Summary of the third PV generation: (a) Intermediate band, (b) Quantum dot, (c) Up conversion, (d) Down conversion (e) Hot carrier, (f) Dye sensitized solar cells, (g) Organic solar cells, and (h) Perovskite solar cells [34, 66-68].

III. Solar thermal electricity

Solar energy can be converted to electrical energy using a heat engine. Solar energy is first converted to heat which is then used to produce electricity.

Typically, in concentrated solar power systems (CSP), an optical device concentrates solar radiation onto a thermal receiver, or collector, where solar photons are converted to heat, that increases the temperature of a heat transfer fluid circulating in the receiver. The generated heat can be used for electricity production: it is then transferred through the heat transfer fluid to water in order to produce steam that drives a turbine (heat-to-mechanical power conversion) coupled to a generator that produces electricity (mechanical-to-electrical power conversion). The excess energy can be stored thermally, allowing electricity production all day long, day and night, even on cloudy days [69]. The heat transfer fluid must be stable, even at high temperature, must withstand extreme weather conditions, must transfer the heat efficiently with no environmental impact and must not be expensive. Figure I-11 summarizes the operating principle of CSP systems.

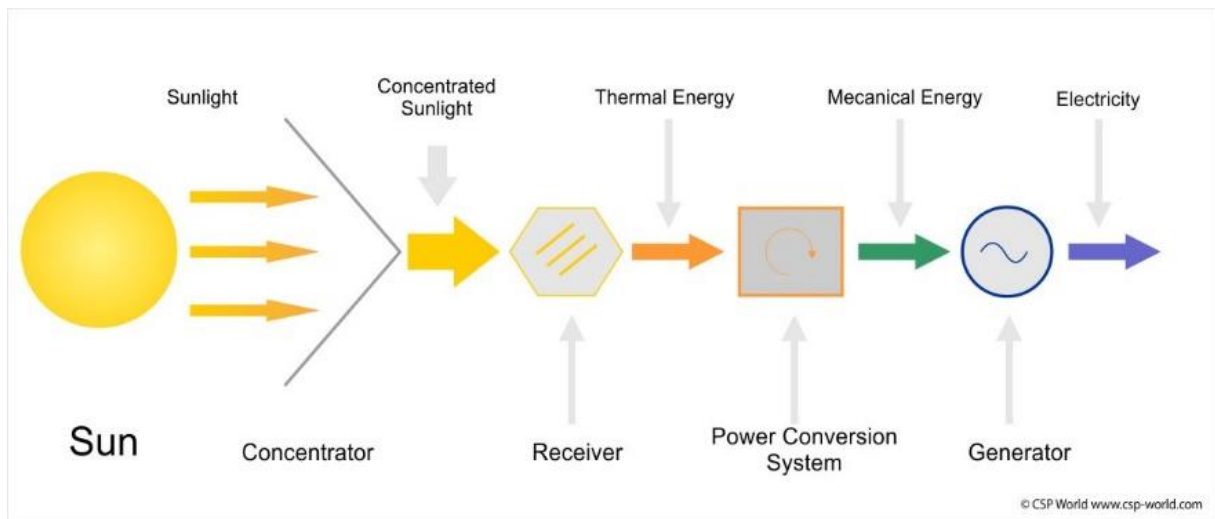


FIGURE I-11 Operating Principle of a Concentrated Solar Power System (CSP) [70].

Different CSP technologies can be distinguished: the parabolic trough collector, the linear Fresnel, the concentrated solar towers, and the parabolic dish. They are usually differentiated by the way they focus solar radiation (i.e. linear or point focus), the technology used to collect the solar energy, the receiver type (fixed or mobile), or the maximum temperature and concentration level attained [71].

A. CSP Technologies

1. Line focus collectors

a) Parabolic trough

Parabolic trough is the most mature CSP technology. It consists of U-shaped curved mirrors with single axis tracking that concentrate solar rays onto a receiver tube located along the focus line of the mirrors [69, 72]. The heat transfer fluid circulates in the tubes, absorbing heat and transporting it through the heat exchanger to a steam generator to produce high temperature steam. This steam may be used to drive a turbine to produce electricity or may be

stored for future use. Figure I-12 summarizes the operating principle of a parabolic trough power plant.

Parabolic trough power plants operate at concentration levels of less than 100 suns. The heat transfer fluids used for such technologies are usually synthetic oils which can be heated up to 390°C (a limiting temperature above which the oil degrades). The use of molten salt as heat transfer fluid to increase the operating temperature to 550°C is currently under investigation for such types of receivers [72].

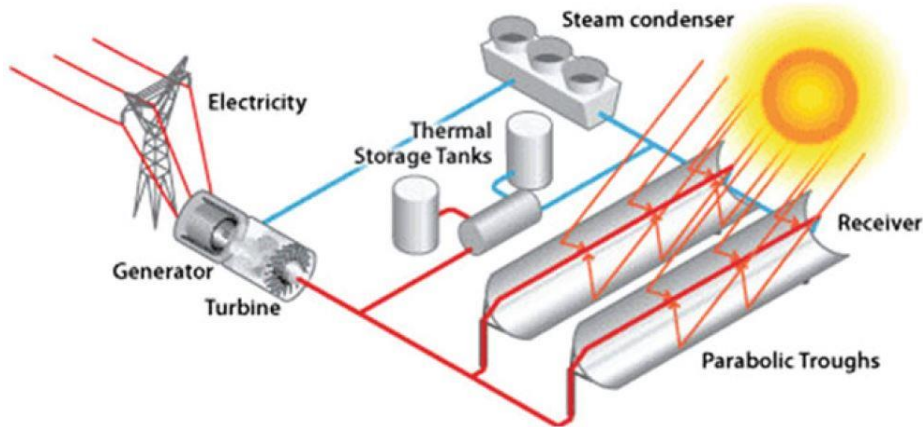


FIGURE I-12 Operating principle of a parabolic trough power plant. Source: EERE, Energy Efficiency and Renewable Energy, U.S. Department of Energy [73].



FIGURE I-13 Micro-Sol-R, PROMES-CNRS, Odeillo, France [74].

b) Linear Fresnel

The linear Fresnel technology takes its name from the French physicist Augustin-Jean Fresnel, who developed the Fresnel lens, where the surface of a standard lens is broken into many smaller surfaces with discontinuities between them. This same idea is applied to mirrors: different mirrors are used to form one concentrator, each positioned with a specific angle.

It uses ground-based flat or slightly curved mirrors, mounted on a single axis tracking system. Each mirror is autonomous and oriented to reflect and concentrate light to a fixed tube receiver, placed above the mirrors. The fluid circulating in the receiver absorbs the heat and transfers it through a heat exchanger to drive a steam generator. Water is the most used heat transfer fluid for low temperatures, synthetic oils are used for medium temperatures

steam while molten salts are preferred for higher temperatures [69,71,72]. A second reflector can be added on top of the receiver for an improved light focus: the mirrors concentrate light on the secondary optic which reflects the rays onto the receiver. Figure I-14 sums up the operating principle of linear Fresnel reflector solar plants.

Until today, Linear Fresnel reflectors have not been associated with thermal energy storage. They operate at concentration levels of 60-80 suns and can reach temperatures between 150 and 550°C, depending on the type of heat transfer fluid circulating in the system [72]. Their operating principle is comparable to parabolic trough technology but with lower manufacturing costs, lower thermodynamic efficiencies, and higher optical losses.

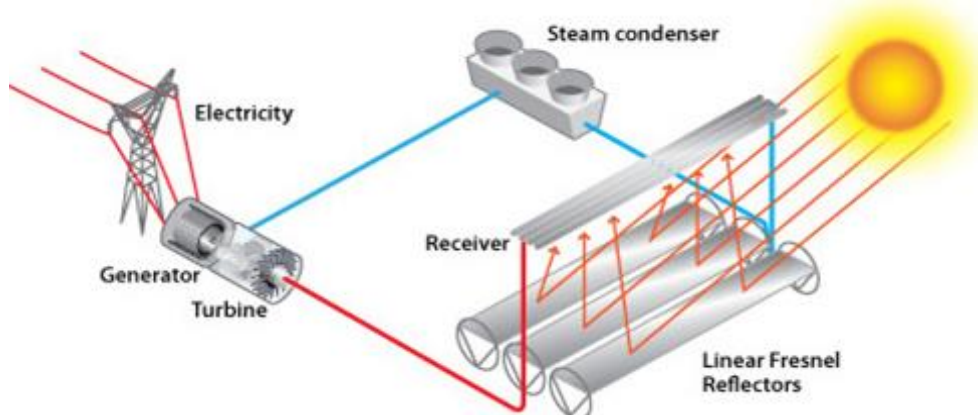


FIGURE I-14 Operating principle of a linear Fresnel reflector solar plant. Source: EERE, Energy Efficiency and Renewable Energy, U.S. Department of Energy [75].



FIGURE I-15 Areva Solar's Linear Fresnel Reflector, Bakersfield, CA, USA [76].

2. Point focus collectors

a) Solar tower

Solar towers are also known as central receivers since the system consists of a field of tracking mirrors (heliostats) concentrating solar radiation onto a receiver located at the top of a tower [71,72]. The cold heat transfer fluid is pumped to the top of the tower, where it absorbs solar photons which are converted into heat, and goes down to transfer the absorbed heat to the steam generator or to the thermal energy storage system. Figure I-16 illustrates the operating principle of central receiver solar plants.

Solar tower power plants operate at concentration levels of 300-1500 suns, leading to higher operating temperatures than the one typically achievable with parabolic trough

systems. The heat transfer fluid circulating in the tower can be water steam ($250\text{-}350^{\circ}\text{C}$), synthetic oil (390°C), or molten salt (550°C), the most used fluid with such types of reflectors. Consequently, depending on the type of the fluid, the maximal attained temperatures can vary between 250 and 550°C . Temperatures above 800°C can be reached with gases, such as atmospheric air, as heat transfer fluid [69, 72, 77].

Optical losses mirrors angular deviations and sun-tracking imperfections remain the main critical concerns with this technology.

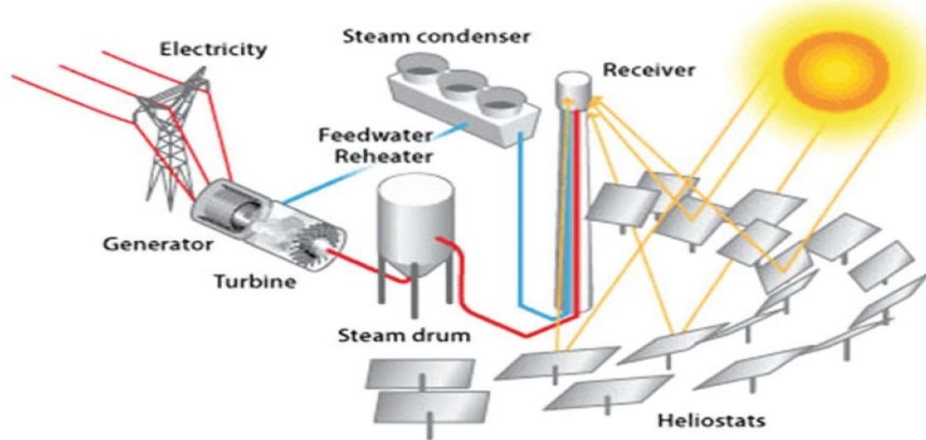


FIGURE I-16 Operating principle of a solar tower power plant. Source: EERE, Energy Efficiency and Renewable Energy, U.S. Department of Energy [78].



FIGURE I-17 THEMIS Solar Tower, PROMES-CNRS, Targassonne, France [79].

b) Parabolic dish

The parabolic dish system consists in a concave mirror dish used to concentrate solar light onto a receiver located at the focus point, the receiver being a Stirling engine (the most widely used), a micro-turbine or a solar cell array in the case of CPV technology. The system is equipped with a two-axis tracking system. Figure I-18 illustrates how such system operates.

The Stirling engine is a heated piston that absorbs the concentrated solar energy and increases the temperature of a heat transfer fluid, normally a gas (hydrogen or helium at high pressure). The gas goes through cycles of hot and cold temperatures, depending on whether the engine is storing or releasing energy. The heated gas expands inside the engine cylinders and, as a result, the pistons are driven followed by the electrical generator [69, 72, 77].

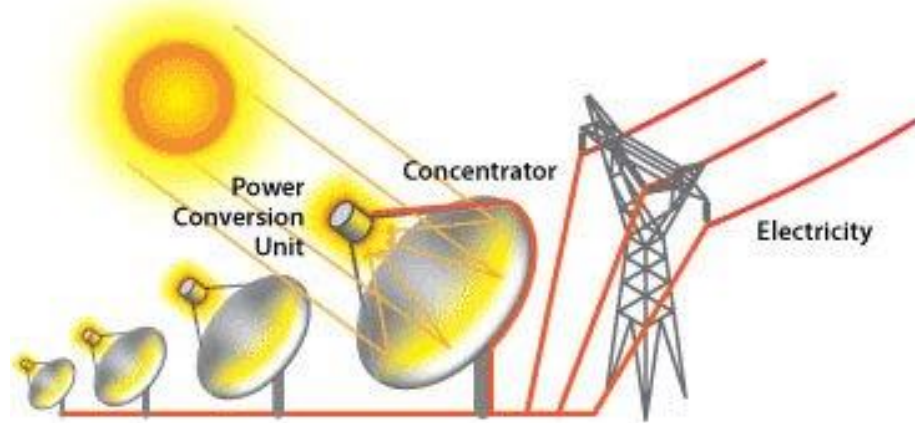


FIGURE I-18 Operating principle of parabolic dish power plants. Source: EERE, Energy Efficiency and Renewable Energy, U.S. Department of Energy [80].



FIGURE I-19 Stirling EuroDish, PROMES-CNRS, Odeillo, France [81].

Parabolic dishes operate at concentration levels of 600-2000 suns and can attain temperatures higher than all the previous CSP technologies, with a maximal temperature of 1500°C [69, 72] which leads to higher conversion efficiencies. They have minimal water requirement, the engine being air-cooled. Dish/stirling engines are not implemented nowadays due to their high initial cost, the Stirling engine being very expensive, and because of the lack of storage capabilities.

B. Thermal Energy Storage

Coupling CSP with thermal energy storage increases the usefulness of CSP power plants since they can store the excess energy as heat for future use [82].

Thermal energy storage uses specific materials that can maintain a certain temperature level for a long time when insulated. Different means exist to store heat, and the most important three include sensible, latent or chemical heat storage materials. Sensible heat storage materials accumulate heat when their temperature increases, using materials such as molten salts (for temperatures up to 550°C) and solid storage (ceramic, graphite and concrete) for higher temperatures. The latent heat storage materials, such as phase change materials, store energy as latent heat during a constant temperature phase transition, i.e. the heat of fusion (solid-liquid transition) and the heat of vaporization (liquid-vapor transition). They either absorb (storage) or release (retrieval) heat during the phase transition process. This technology represents a passive way of storing energy [82]. The thermo-chemical storage converts solar energy via reversible chemical reactions following the equation: AB + heat \leftrightarrow A + B, where heat breaks a compound into two different molecules; bringing them back releases energy [83-85].

The following part focuses only on the sensible heat storage materials, widely coupled to CSP [83]. This technology relies on a tank system, an active storage, which uses a heat transfer fluid as a medium to store the excess energy. It encloses the two-tank direct system, the two-tank indirect system and the single tank thermocline system.

In a two-tank direct system, the heat transfer fluid and the storage fluid are similar. Two different tanks, one at low temperature and the other at higher temperature, store the fluids. The cold fluid circulates to the receiver, absorbs heat, and moves to the hot tank for storage. When needed, the hot fluid flows to the steam generator through a heat exchanger, and cools down before returning back to the cold tank [83-85].

In a two-tank indirect system, the heat transfer and the storage fluids are different. The first collects and transports heat, while the second stores it. An intermediate heat exchanger facilitates the heat exchange between them. The storage operating principle remains similar to the direct system. Such system is used when the heat transfer fluid is expensive, or when it is not adapted as a storage fluid. An example of indirect system fluid is oil/salts systems where the heat transfer fluid is synthetic oil and the storage fluid is molten salts [83, 84].

In a single tank thermocline storage system, only one tank is installed, and high and low temperatures coexist. The hot and cold regions are separated by a medium with a thermal gradient known as *thermocline*. The hot fluid enters the thermocline from the top and exits from the bottom at a lower temperature, a process that moves the thermocline downward and adds thermal energy to the system. To decrease the temperature, the opposite process happens: energy is removed from the system which raises the thermocline to upper region. The heat transfer fluid can be used alone, or coupled with solid materials, such as silica sand [83, 85].

In passive systems, the storage medium remains stationary and the heat transfer fluid circulates in the storage only during charge or discharge. The heat transfer fluid transports heat to the storage medium to charge it, and receives energy from the system to discharge it. The solid materials are mainly concrete, sand, rocks or phase change materials [84, 85].

IV. References

- [1] J. Tsao, N. Lewis, and G. Crabtree, Solar FAQs, Sandia National Laboratories, US, 2006, www.sandia.gov.
- [2] G. M. Masters, The Solar Resource, in Renewable and Efficient Electric Power Systems, John Wiley & Sons, Inc., Hoboken, New Jersey, US, 2004.
- [3] C. Honsberg and S. Bowden, Air Mass, 2018. [Online]. Available: <https://pveducation.org/pvcdrom/properties-of-sunlight/air-mass>. [Accessed June 22, 2018].
- [4] A. Vossier, E. Al Alam, A. Dollet, and M. Amara, Assessing the efficiency of advanced multi-junctions solar cells in real working conditions, IEEE J. Photovolt., 5 (2015) 1805-1812.
- [5] P. Wurfel, Thermodynamic limitations to solar energy conversion. Physica E Low Dimens. Syst. Nanostruct., 14 (2002) 18-26.
- [6] C. H. Henry, Limiting efficiencies of ideal single and multiple energy gap terrestrial solar cells, J. Appl. Phys., 51 (1980) 4494-4500.
- [7] E. Becquerel, Mémoire sur les effets électriques produits sous l'influence des rayons solaires, Comptes Rendus de L'Académie des Sciences, 9 (1839) 561- 567.
- [8] W. Smith, Effect of Light on Selenium during the passage of an electric current, Nature, 7 (1873) 303.
- [9] G. M. Masters, Photovoltaic Materials and Electrical Characteristics, in Renewable and Efficient Electric Power Systems, John Wiley & Sons, Inc., Hoboken, New Jersey, US, 2004.
- [10] Adams, W. G. and R. Day, The Action of Light on Selenium, in Proceedings of the Royal Society of London, 25 (1877) 113-117.
- [11] C. E. Fritts, On a new form of selenium cell, and some electrical discoveries made by its use, Am. J. Sci., 26 (1883) 465-472.
- [12] A. Einstein, Über einen die Erzeugung und Verwandlung des Lichtes betreffenden heuristischen Gesichtspunkt. Ann. Phys., 322 (1905) 132-148.
- [13] H. J. Hovel and J. M. Woodall, Improved GaAs solar cells with very thin junctions. In Proc. of the IEEE 12th Photovoltaic Specialists Conference (PVSC-12), (1976) 945-947.
- [14] M. A. Green, Y. Hishikawa, E. D. Dunlop, D. H. Levi, J. Hohl-Ebinger and A. W.Y. Ho-Baillie, Solar cell efficiency tables (version 51), Prog. Photovolt. Res. Appl., 26 (2018) 3-12.
- [15] R. Fu, D. Feldman, R. Margolis, M. Woodhouse, and K. Ardani, U., S. Solar Photovoltaic System Cost Benchmark: Q1 2017, National Renewable Energy Laboratory, Denver, Golden, US, Tech. Rep. NREL/TP-6A20-68925, 2017.
- [16] J. Nelson, The physics of solar cells, Imperial College Press, London, 2004.
- [17] H. Tulsani, Electronic Devices, Jan. 17, 2017. [Online]. Available: <http://edetec106.blogspot.com/2016/01/differentiate-between-direct-and.html>. [Accessed June 22, 2018].

- [18] P. Wurfel, Physics of solar cells, 2nd edition, Wiley-VCH, Weinheim, 2009.
- [19] K. Mertens, Photovoltaics fundamentals, technology and practice, John Wiley & Sons, Munich, 2014.
- [20] L. S. Rohwer and J. E. Martins, Measuring the absolute quantum efficiency of luminescent materials, *J. lumin.*, 115 (2005) 77-90.
- [21] U. Rau, Reciprocity relation between photovoltaic quantum efficiency and electroluminescent emission of solar cells, *Phys. Rev. B*, 76 (2007) 085303.
- [22] M.A. Green, Green, M. A. (2012). Radiative efficiency of state-of-the-art photovoltaic cells, *Prog. Photovolt. Res. Appl.*, 20 (2012) 472-476.
- [23] A. Braun, E.A. Katz, D. Feuermann, B. M. Kayes, and J. M. Gordon, Photovoltaic performance enhancement by external recycling of photon emission, *Energ. Environ. Sci.*, 6 (2013) 1499-1503.
- [24] B.M. Kayes, H. Nie, R. Twist, S.G. Spruytte, F. Reinhardt, I.C. Kizilyalli, and G.S. Higashi, 27.6% conversion efficiency, a new record for single-junction solar cells under 1 sun illumination, In Proc. of the 37th IEEE Photovoltaic Specialist Conference (PVSC-37), (2011) 4-8.
- [25] X. Wang and M. S. Lundstrom, On the Use of Rau's Reciprocity to Deduce External Radiative Efficiency in Solar Cells, *IEEE J. Photovolt.*, 3 (2013) 1348-1353.
- [26] O.D. Miller, E. Yablonovitch, and S.R. Kurtz, Strong internal and external luminescence as solar cells approach the Shockley–Queisser limit, *IEEE J. Photovolt.*, 2 (2012) 303-311.
- [27] J.F. Geisz, M.A. Steiner, I. Garcia, S.R. Kurtz, and D.J. Friedman, Enhanced external radiative efficiency for 20.8% efficient single-junction GaInP solar cells, *Appl. Phys. Lett.* 103 (2013) 041118.
- [28] A. Luque and S. Hegedus, Handbook of photovoltaic science and engineering, John Wiley & Sons, West Sussex, England, 2003.
- [29] S. Bana and R. P. Saini, A mathematical modeling framework to evaluate the performance of single diode and double diode based SPV systems, *Energy Rep.*, 2 (2016) 171-187.
- [30] A. Cuevas, The recombination parameter J0, *Energy Procedia*, 55 (2014) 53-62.
- [31] Solmetric, [Online]. Available: http://solarprofessional.com/sites/default/files/articles/ajax/docs/2_SP4_5_pg76_Hernday-3_0.jpg. [Accessed July 24, 2018].
- [32] National Renewable Energy Laboratory – National Center for Photovoltaics, Research cell efficiency records, Sept. 2015. [Online]. Available: <https://www.energy.gov/eere/solar/downloads/research-cell-efficiency-records>. [Accessed June 22, 2018].
- [33] R. Swami, Solar cell, *Int. J. Sci. Res. Publ.*, 2 (2012), 1-5.
- [34] A.M. Bagher, M.M.A. Vahid, and M. Mohsen, Types of solar cells and application, *Amer. J. Opt. Photonics*, 3 (2015) 94-113.

- [35] K.L. Chopra, P.D. Paulson, V. Dutta, Thin-film solar cells: an overview, *Prog. Photovolt. Res. Appl.*, 12 (2004) 69-92.
- [36] M. A. Green, Thin-film solar cells: review of materials, technologies and commercial status, *J. Mater. Sci. Mater. Electron.*, 18 (2007) 15-19.
- [37] J. P. Connolly and D. Mencaraglia, III-V solar cells, in: *Materials Challenges: Inorganic Photovoltaic solar energy*, Editor: Stuart J. C. Irvine, 2014
- [38] K. T. Masloski, The GaAs solar cell research and development programs of the Air Force, 1980.
- [39] A. Willoughby and G. Conibeer, Solar cell materials: developing technologies, John Wiley & Sons, 2014.
- [40] F. Dimroth, High-efficiency solar cells from III-V compound semiconductors, *Phys. Stat. Sol. (c)*, 3 (2006) 373-379.
- [41] A. Marti and A. Luque, Intermediate Band Solar Cells, in: *Next Generation Photovoltaics: High Efficiency through Full Spectrum Utilization*, CRC Press, 2003.
- [42] T. S. Navruz and M. Saritas, Intermediate band solar cells, In Proc. of the 4th International Conference on Electrical and Electronics Engineering (ELECO), (2005) 7-11.
- [43] A. Luque, A. Marti, and C. Stanley, Understanding intermediate-band solar cells. *Nat. Photonics*, 6 (2012) 146-152.
- [44] A. Goetzberger, J. Luther, and G. Willeke, Solar cells: past, present, future, *Sol. Energy Mater. Sol. Cells*, 74 (2002) 1-11.
- [45] A. Luque, P.G. Linares, A. Mellor, V. Andreev, and A. Marti, Some advantages of intermediate band solar cells based on type II quantum dots, *Appl. Phys. Lett.*, 103 (2013) 123901.
- [46] A. Luque, and A. Martí, Increasing the efficiency of ideal solar cells by photon induced transitions at intermediate levels, *Phys. Rev. Lett.*, 78 (1997) 5014.
- [47] K. E. Jasim, Quantum dots solar cells, in *Solar Cells-New Approaches and Reviews*, Edited by L. A. Kosyachenko, InTechOpen, 2015.
- [48] A. J. Nozik, Quantum dot solar cells, *Physica E Low Dimens. Syst. Nanostruct.*, 14 (2002) 115-120.
- [49] M. A. Green, Third generation photovoltaics: solar cells for 2020 and beyond, *Physica E Low Dimens. Syst. Nanostruct.*, 14 (2002) 65-70.
- [50] J.F. Guillemoles, A. Le Bris, M. Paire, L. Lombez, S. Laribi, D. Lincot, C. Colin, S. Collin, J.L. Pelouard, M. Laroche, R. uben Esteban, J.J. Greffet, G. Boissier, and P. Christol, Hot-carrier solar cells, Institute of research and Development on Photovoltaic Energy, Chatou, France, Tech. Rep. 2011.
- [51] A. Le Bris and J-F. Guillemoles, Hot carrier solar cells: Achievable efficiency accounting for heat losses in the absorber and through contacts, *Appl. Phys. Lett.*, 97 (2010) 113506.
- [52] T. Trupke, A. Shalav, B.S. Richards, P. Würfel, and M.A. Green, Efficiency enhancement of solar cells by luminescent up-conversion of sunlight, *Sol. Energy Mater. Sol. Cells*, 90 (2006) 3327-3338.

- [53] A. Shalav, B.S. Richards, and M.A. Green, Luminescent layers for enhanced silicon solar cell performance: Up-conversion, *Sol. Energy Mater. Sol. Cells*, 91 (2007) 829-842.
- [54] D. Verma, T.O. Saetre, and O.M. Midtgård, Review on up/down conversion materials for solar cell application, In Proc. of the IEEE 38th Photovoltaic Specialists Conference (PVSC-38), (2012) 002608-002613.
- [55] M. Grätzel, Dye-sensitized solar cells, *J. Photochem. Photobiol. C*, 4 (2003) 145-153.
- [56] D. Wei, Dye sensitized solar cells, *Int. J. Mol. Sci.*, 11 (2010), 1103-1113.
- [57] P. Würfel, Photovoltaic principles and organic solar cells, *Chimia Int. J. Chem.*, 61 (2007) 770-774.
- [58] K. A. Vivek and G. D. Agrawal, Organic Solar Cells: Principles Mechanism and Recent Developments, *Int. J. Res. Eng. Technol.*, 3 (2014) 338-341.
- [59] M. Grätzel, Photoelectrochemical cells, *Nature*, 414 (2001) 338-344.
- [60] N. G. Park, Organometal perovskite light absorbers toward a 20% efficiency low-cost solid-state mesoscopic solar cell, *J. Phys. Chem. Lett.*, 4 (2013) 2423-2429.
- [61] M. A. Green, A. Ho-Baillie, and H.J. Snaith, The emergence of perovskite solar cells, *Nat. Photonics*, 8 (2014) 506-514.
- [62] N. Marinova, S. Valero, and J.L. Delgado, Organic and perovskite solar cells: Working principles, materials and interfaces, *J. Colloid Interface Sci.*, 488 (2017), 373-389.
- [63] I. Mesquita, L. Andrade, and A. Mendes, Perovskite solar cells: Materials, configurations and stability, *Renew. Sust. Energy Rev.*, 82 (2018) 2471-2489.
- [64] A.B. Djurišić, F.Z. Liu, H. W. Tam, M.K. Wong, A. Ng, C. Surya, W. Chen, Z.B. He, Perovskite solar cells-An overview of critical issues, *Prog. Quant. Electron.*, 53 (2017), 1-37.
- [65] H. S. Jung and N. G. Park, Perovskite solar cells: from materials to devices, *Small*, 11 (2015) 10-25.
- [66] V.V. Tyagi, N.A.A. Rahim, N.A. Rahim, and J.A.L. Selvaraj, Progress in solar PV technology: Research and achievement, *Renew. Sust. Energ. Rev.*, 20 (2013) 443–461.
- [67] G. Morse, R. Harding, N. Blouin, H. Buerckstrummer, A. Pron, S. Wieder, D. Mueller, and S. Berny, Organic Photovoltaic Applications for IoT, Architecture, and Wearables, *Mater. Matters*, 12 (2017) 101-117
- [68] T.A. Berhe, W.N. Su, C.H. Chen, C.J. Pan, J.H. Cheng, H.M. Chen, M.C. Tsai, L.Y. Chen, A.A. Dubale, and B. J. Hwang, Organometal halide perovskite solar cells: degradation and stability, *Energ. Environ. Sci.*, 9 (2016) 323-356.
- [69] S. A. Kalogirou, Solar thermal collectors and applications. *Prog. Energy Combust. Sci.*, 30 (2004) 231-295.
- [70] C. Gertig, CSP versus PV, drivers, challenges and perspectives, Power point Presentation. RINA Consulting. Available: <https://d2oc0ihd6a5bt.cloudfront.net/wp->

content/uploads/sites/837/2017/06/12_CSP-versus-PV-Drivers-Challenges-and-Perspectives.pdf.

- [71] D. Mills, Advances in solar thermal electricity technology, *Sol. Energy*, 76 (2004) 19-31.
- [72] R. Serrano, Concentrating Solar Thermal Technologies, in *Concentrating Solar Thermal Technologies*. Green Energy and Technology. Springer, Cham.
- [73] EERE, Office of Energy Efficiency and Renewable Energy, U.S. Department of Energy, Linear Concentrator Solar Power Plant Illustration. [Online]. Available: <https://www.energy.gov/eere/solar/downloads/linear-concentrator-solar-power-plant-illustration>. [Accessed June 22, 2018].
- [74] PROMES – CNRS, MicroSol-R : la nouvelle microcentrale solaire du four d’Odeillo, Sept. 26, 2016. [Online]. Available : <http://www.cnrs.fr/insis/recherche/actualites-institutionnelles/2016/09/microsol-r.htm>. [Accessed June 22, 2018].
- [75] EERE, Office of Energy Efficiency and Renewable Energy, U.S. Department of Energy, Linear Fresnel Power Plant Illustration. [Online]. Available: <https://www.energy.gov/eere/solar/downloads/linear-fresnel-power-plant-illustration>. [Accessed June 22, 2018].
- [76] Areva Solar, Bakersfield, CA, Areva Solar, 2018. [Online]. Available: <https://www.solec.org/solkote/solkote-featured-projects-and-images/ngallery/image/areva-solar-20/>. [Accessed June 22, 2018].
- [77] Y. Tian and C. Y. Zhao, A review of solar collectors and thermal energy storage in solar thermal applications, *Appl. Energy*, 104 (2013) 538-553.
- [78] EERE, Office of Energy Efficiency and Renewable Energy, U.S. Department of Energy, Concentrating Solar Power Tower Plant Illustration. [Online]. Available: <https://www.energy.gov/eere/solar/downloads/concentrating-solar-power-tower-plant-illustration>. [Accessed June 22, 2018].
- [79] Alastair Philip Wiper, Themis Experimental Solar Power Plant, France, Mar. 27, 2013. [Online]. Available: <http://alastairphilipwiper.com/blog/themis-experimental-solar-power-plant-france>. [Accessed June 22, 2018].
- [80] EERE, Office of Energy Efficiency and Renewable Energy, U.S. Department of Energy, Dish/Engine System Concentrating Solar Power Basics, Aug. 20, 2013. [Online]. Available: <https://www.energy.gov/eere/solar/articles/dishengine-system-concentrating-solar-power-basics>. [Accessed June 22, 2018].
- [81] Système Parabole-Stirling d’Odeillo, June 15, 2014. [Online]. Available: http://fr.solarpedia.net/wiki/index.php?title=Syst%C3%A8me_Parabole-Stirling_d%27Odeillo. [Accessed June 22, 2018].
- [82] H. Chen, T.N. Cong, W. Yang, C. Tan, Y. Li, and Y. Ding, Progress in electrical energy storage system: A critical review, *Prog. Nat. Sci.*, 19 (2009) 291-312.
- [83] G. Alva, Y. Lin, and G. Fang, An overview of thermal energy storage systems, *Energy*, 144 (2018) 341-378.

- [84] A. Gil, M. Medrano, I. Martorell, A. Lázaro, P. Dolado, B. Zalba, and L.F. Cabeza, State of the art on high temperature thermal energy storage for power generation. Part 1 - Concepts, materials and modellization. *Renew. Sust. Energy Rev.*, 14 (2010) 31-55.
- [85] S. Kuravi, J. Trahan, D.Y. Goswami, M.M. Rahman, and E.K Stefanakos, Thermal energy storage technologies and systems for concentrating solar power plants, *Prog. Energy Combust. Sci.*, 39 (2013) 285-319.

Chapter II: Literature review

Photovoltaic technology is based on the *direct* conversion of solar energy into electricity through photovoltaic effect. Nevertheless, its maximal theoretical limit remains much lower than the Carnot limit for solar energy conversion, due to several fundamental loss mechanisms precluding conventional single-junction PV cells to exceed conversion efficiencies of ~30%. This chapter describes the maximal PV theoretical limit, as well as the reasons explaining the large gap between these two efficiency limits. Finally, strategies aiming at overcoming this fundamental limit are detailed.

I. Photovoltaic technology

A. Shockley-Queisser formalism

In 1961, William Shockley and Hans J. Queisser proposed a detailed balanced formalism [1] to estimate the maximal theoretical efficiency of an ideal single-junction solar cell. Their model requires 4 parameters: the semiconductor bandgap value, the ambient temperature, the temperature of the sun, and the magnitude and spectral distribution of the solar irradiation. This efficiency limit, often referred to as the *radiative* limit, is based on a number of strong assumptions, namely [1,2]:

- 1) one absorbed photon can only generate a single electron-hole pair,
- 2) photons with energies lower than the bandgap energy cannot be converted,
- 3) under short-circuit current conditions, all the photo-generated carriers are collected and contribute to the photo-generated current,
- 4) no series resistances are assumed,
- 5) the recombination inside the cell are 100% radiative,
- 6) the ambient temperature (25°C) is the operating temperature.

It considers that the work extracted from a solar cell is simply the difference between the radiation absorbed and emitted by the cell, as illustrated by the following equation.

$$I/q = \dot{N}_S - \dot{N}_R = \alpha \dot{N}(E_g, \infty, T_s, 0, \Omega_{abs}) + \alpha \dot{N}(E_g, \infty, T_a, 0, 2\pi) - \varepsilon \dot{N}(E_g, \infty, T_c, qV, \Omega_{em}) \quad (\text{II-1})$$

with I the current, q the elementary charge, \dot{N}_S and \dot{N}_R the current contribution associated with the absorption and emission of photons respectively, α the absorptivity and ε the emissivity of the cell surface, E_g the bandgap, T_s , T_a and T_c the sun, ambient and cell temperatures respectively, Ω_{abs} and Ω_{em} the solid angles of absorption and emission and V the voltage. \dot{N} represents the photon flux emitted by a source over the energy ranging between E_i and E_j as shown in equation (II-2).

$$\dot{N}(E_i, E_j, T, \mu, \Omega) = \Omega \frac{2\pi}{h^3 c^2} \int_{E_i}^{E_j} \frac{E^2}{\exp\left(\frac{E-\mu}{kT}\right) - 1} dE \quad (\text{II-2})$$

with Ω the solid angle, h the Planck's constant, c the speed of light, k the Boltzmann constant, T the temperature and μ the chemical potential.

In these conditions, the maximal efficiency is computed as:

$$\eta = \frac{\{qV[\dot{N}_S(\mu = 0) - \dot{N}_R(\mu = qV)]\}_{max}}{P_{in}} \quad (II-3)$$

where P_{in} is the incident power. The efficiency can be computed as function of the bandgap, as illustrated in Fig.II-1 representing the radiative efficiency limit for a broad range of widely used semiconductors. The maximal attainable efficiency is approximately 33.5%, for bandgaps around 1.1-1.4eV, which coincides with Si (1.12eV) and GaAs (1.4eV). This limiting efficiency represents a reference value, based on which all the new emerging technologies are assessed [3]. For example, nowadays, GaAs solar cells reach 90% of the radiative limit with a record efficiency of 28.8% [4]: the gap in efficiency relative to the Shockley-Queisser limit stems from the presence of limiting mechanisms, such as series resistances or non-radiative recombination [2].

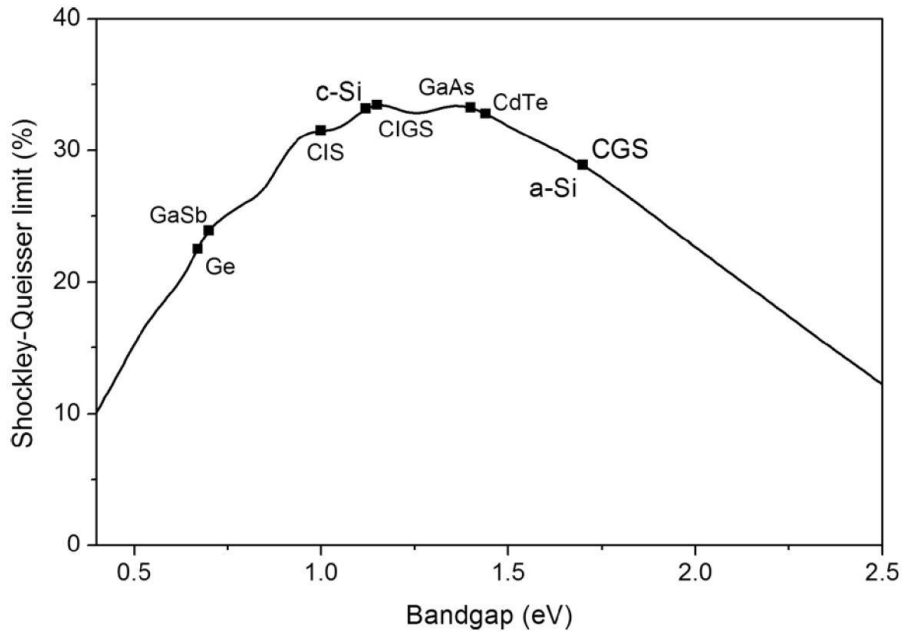


FIGURE II-1 Shockley-Queisser limit as a function of the bandgap [5].

While the Carnot limit for conversion of solar energy into electricity is ~93% [6,7], why is the solar cell efficiency limited to only ~33%? This is mainly due to fundamental losses inside the cells that do not allow an optimal conversion of the solar spectrum.

B. Fundamental losses in solar cells

Practically, solar cell performances are affected by different mechanisms that decrease their efficiency relative to the idealized radiative limit. *Extrinsic* losses such as resistive losses and non-radiative recombination are avoidable losses, which can theoretically be handled with an appropriate cell design, hence, they are not considered when computing the ultimate efficiency limit. However, *intrinsic* losses are unavoidable in conventional solar cells. The optical fundamental losses restrict the ultimate efficiency to 33.5%, mostly owing to the mismatch between the large spectral distribution of the solar spectrum and the inability of semiconductor materials to efficiently convert a broad range of photon energies.

Five fundamental losses, all dependent on the bandgap energy, can be identified, and are schematically illustrated in Fig.II-2. The dark blue curve shows the maximum electrical

work that can be extracted from a cell as a function of the semiconductor bandgap, with an optimal value around 1.4eV. *Thermalization* and *below- E_g* losses are shown in light blue and pink respectively, *Boltzmann* losses in green, *Carnot* losses in orange and *emission* losses in yellow.

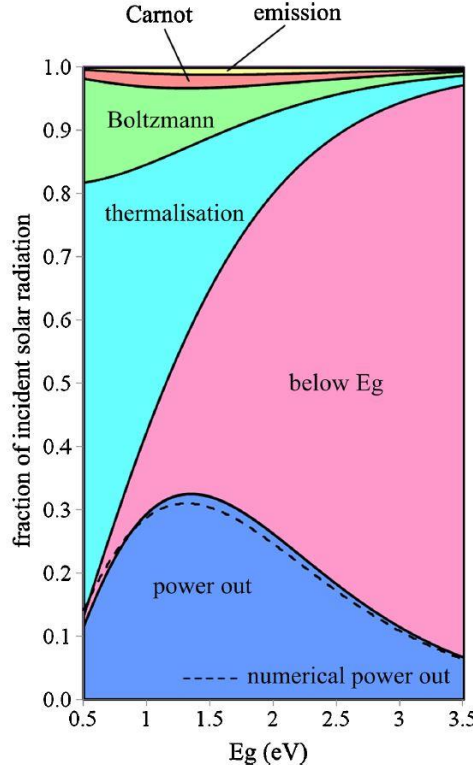


FIGURE II-2 Fundamental losses in single-junction solar cells [8].

Incident photons with energies higher or equal to the cell bandgap are absorbed and excite electrons, creating free carriers. Photons with energies close to the bandgap energy are efficiently converted into electricity while all the other photons generate losses inside the cell. In fact, very energetic photons propel electrons to high energy levels in the conduction band. These highly energetic carriers relax back to the conduction band edge, losing the excess energy (i.e. the difference between the absorbed photon energy and the bandgap) as heat, increasing the cell temperature by *thermalization*. These losses become more significant as the difference between the photon energy and the bandgap energy increases [8].

Electrons with energies lower than the bandgap pass through the cell without generating electron-hole pairs; hence they don't contribute to the photo-generated current. Such losses are known as *below- E_g* losses [8]. As the bandgap increases, *thermalization* losses decrease and *below- E_g* increase. The optimal bandgap for which the PV efficiency peaks corresponds to the value for which both losses are minimized.

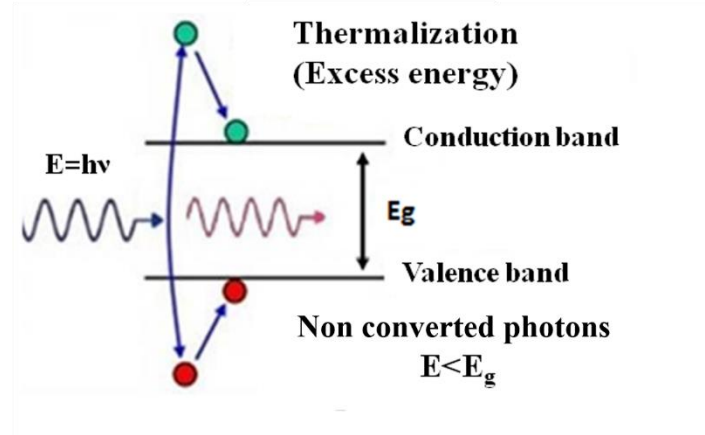


FIGURE II-3 Schematic illustration of the thermalization and below- E_g losses.

Boltzmann losses depend on the optical *étendue*: the sun appears to occupy a very small portion of the sky, due to its large distance from the Earth, leading to an apparent angle of the sun equal to 6.8×10^{-5} steradians (sr). On the other hand, photons emitted from the cell as a result of band-to-band recombination spread over a much larger angle, equal to 2π sr, covering the full hemisphere. The mismatch between the solid angles of absorption and emission generates *optical entropy*, S_{opt} , (eq. (II-4)) that reduces V_{oc} , by a factor of $((kT/q) \times \ln(\Omega_{em}/\Omega_{abs}))$, with T the cell's temperature, Ω_{em} the solid angle of emission and Ω_{abs} the solid angle of absorption [9]. Figure II-4 illustrates *Boltzmann* losses.

$$S_{opt} = k \times \ln\left(\frac{\Omega_{em}}{\Omega_{abs}}\right) \quad (\text{II-4})$$

Carnot losses stem from considering the solar cell as a heat engine transferring heat from the sun to the atmosphere. Absorbing energy from the sun and providing work induce unavoidable energy losses, known as *Carnot* losses, which are quantified as the ratio between the cell temperature and the apparent blackbody temperature of the sun. This loss reduces V_{oc} by a factor $E_g \times (T_c/T_s)$, T_c and T_s being the cell and the sun temperatures respectively [10]. It should be stressed that V_{oc} is fundamentally limited by the Carnot factor, the maximal V_{oc} being equal to the bandgap multiplied by this Carnot factor [11].

$$V_{oc_opt} = E_g \times \left(1 - \frac{T_c}{T_s}\right) \quad (\text{II-5})$$

Finally, the cell loses photons by emitting them radiatively after recombination, reducing the number of available free carriers and decreasing the photo-generated current. This loss mechanism is known as *emission* losses. The counterintuitive fact that significant emission losses is a *sine-qua-non* condition to be fulfilled toward ensuring high cell performance will be largely discussed in the following section.

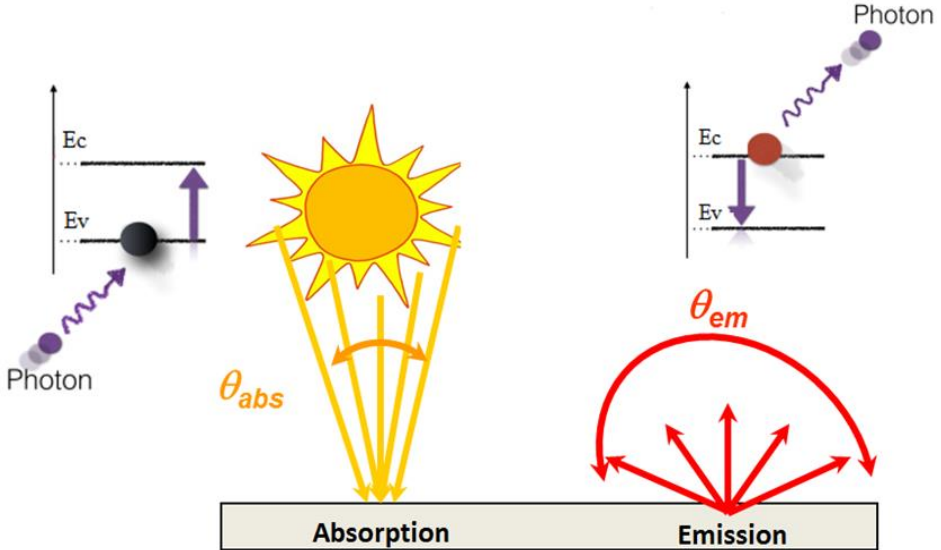


FIGURE II-4 Schematic showing the asymmetry between the angles of absorption and emission responsible for the Boltzmann losses.

To exceed the Shockley-Queisser limit and get closer to the Carnot limit, different strategies were proposed in the last decades aiming at lowering the amplitude of the fundamental losses described above. For instance, third generation solar cells including multi-junction solar cells, hot carriers, quantum dots, intermediate bands, instigated a significant research effort.

This thesis focuses on four concepts to reduce these fundamental losses: solar concentration and angular confinement to reduce the *Boltzmann* losses, multi-junction solar cells and hybrid PV/CSP systems, to reduce *thermalization* and *below-E_g* losses.

C. Multi-junction solar cells

To reduce *thermalization* and *below-E_g* losses, and to better exploit the energy of the solar spectrum, one of the most commonly used technologies is the so-called “multi-junction” solar cells. This cell technology consists in solar cells made using several *pn*-junctions, each capable of absorbing a specific range of photon energies so that in overall, the cell effectively absorbs and converts a larger fraction of the solar spectrum. Theoretically, the cell efficiency is boosted from 33% for a single-junction cell to 50% for triple-junction (composed of 3 different *pn*-junctions) solar cells [12] under a 1 sun illumination. Today, the record efficiency under one-sun illumination is 38.8% for a 5-junction cells [13] and 37.9% for a triple-junction cell [14], which both constitute significant improvements relative to the single-junction record efficiency value [4,15].

Figure II-5 compares the absorption of the solar spectrum by single and triple junction cells. Using only one semiconductor material (left) allows converting only a small part of the solar spectrum, as illustrated by the red-colored area, while the remaining fraction, in grey, represents the *thermalization* and *below-E_g* losses. Combining different materials (right), each capable of converting a reduced fraction of the solar spectrum, allows better conversion of this spectrum, together with a significant minimization of the losses associated with ineffective photons absorption. As can be seen in Fig.II-6, *thermalization* and *below-E_g*

losses decrease as the number of junctions increases in the stack, leading to higher generated power. Conversely, *Boltzmann*, *Carnot*, and *emission* losses intensify. This amplification stems from the thermodynamic equivalence between the increase in the number of junctions in a MJ solar cell, and the increase in the number of heat engines one can associate with each individual sub-cell [8]. These observations indicate that optical intrinsic losses strongly depend on the number of junctions in the stack.

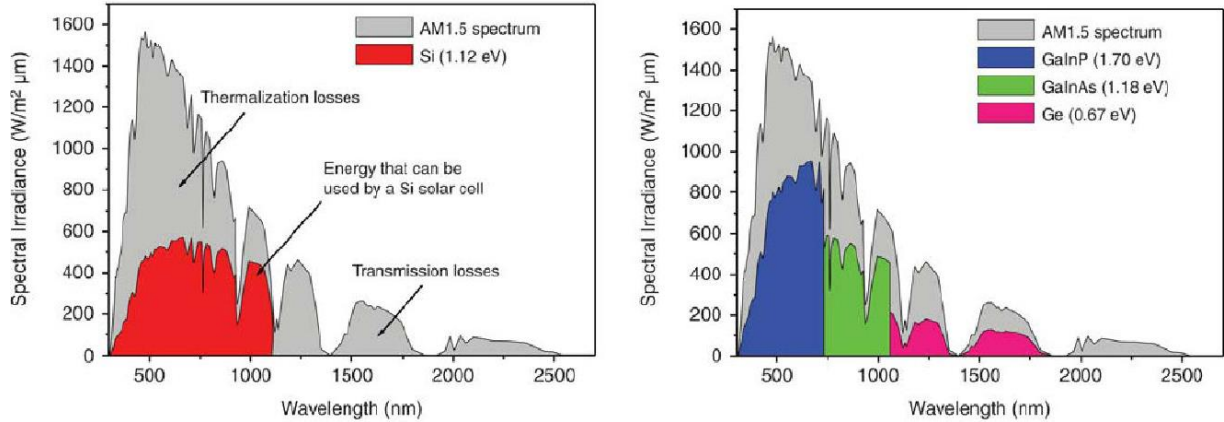


FIGURE II-5 Comparison of solar spectrum absorption for a single-junction cell and a triple-junction cell [16].

Multi-junction cells are fabricated by combining different semiconductors of increasing bandgap. The high-bandgap top cell absorbs the most energetic photons while the non-absorbed photons (*below-* E_g photons of the first material used) cross this junction without generating electron-hole pairs, and reach the following semiconductor having a slightly lower bandgap. This process is repeated until the remaining non-absorbed photons reach the bottom junction characterized by the smallest bandgap.

The implementation of such technology becomes more intricate as the number of sub-cells increases in the stack. In fact, beyond the necessary compatibility between two neighboring semi-conductors (in terms of lattice parameters for example), the optical properties of the materials should be tailored to allow the non-absorbed light to be transmitted to the adjacent sub-cells without any loss, which requires transparent interfaces at given wavelengths between two subsequent junctions. The photo-generated carriers should also be efficiently transmitted from one junction to the other in order to reach the external circuit.

In monolithic MJ cell architectures, where the different sub-cells are epitaxially grown on top of each other, the different junctions are connected in series via tunnel junctions. Tunnel junctions are very thin layer of heavily doped semiconductor materials, which allow the current flow through the different junctions by *tunneling effect*, a quantum property allowing the carriers to cross potential barriers usually forbidden by classical physics.

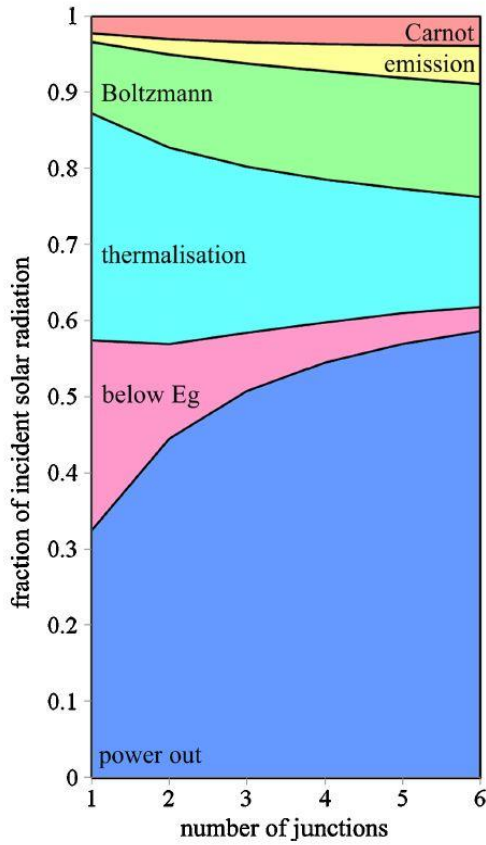


FIGURE II-6 Fundamental losses in multi-junction solar cells [8].

Since the different junctions are connected in series, the voltage extracted from the cell is the sum of the voltages of the different junctions. As a consequence of the series connection between the different sub-cells, the currents produced by each individual junction must be equal, with the output current supplied by the cell being limited by the sub-junction with the smallest current. To control the amount of generated current in each junction, the bandgap should be well tuned, and the thickness of each individual junction should be optimized [17,18].

Increasing the number of junctions in the stack increases the cell efficiency. In practice the gain in conversion efficiency becomes weaker as the number of sub-cells is increased in the stack [7,12,19]. Table II-1 [12], represents the optimal combination of bandgaps leading to the highest conversion efficiency, as well as the maximum theoretical efficiency for solar cells comprising between 1 and 10 junctions. It shows that the net gain in efficiency associated with the use of triple-junction solar cells is 17% (compared to single-junction solar cells), whereas the gain is only 11% between 3 and 10 junctions' solar cells. Henry et al. [7] first mentioned this effect, calculating an efficiency of 72% with 36 junctions, and they stressed the practical complexity of manufacturing multi-junction cells comprising more than 5 junctions. The theoretical limit can reach up to 86% while using an infinite number of junctions and maximum sunlight concentration.

TABLE II-1 Optimum electronic energy gaps for multi-junction cells with up to 10 junctions and their efficiencies at 1 sun illumination [12].

E _g \ N	E _{g1}	E _{g2}	E _{g3}	E _{g4}	E _{g5}	E _{g6}	E _{g7}	E _{g8}	E _{g9}	E _{g10}	η (%)
1	1.14										33.2
2	1.57	0.94									45.1
3	1.75	1.18	0.7								50.7
4	1.94	1.44	1.05	0.7							54.4
5	2.07	1.61	1.26	0.99	0.7						56.6
6	2.18	1.74	1.44	1.17	0.95	0.68					58.7
7	2.27	1.85	1.56	1.33	1.12	0.92	0.7				59.8
8	2.29	1.88	1.59	1.37	1.16	0.96	0.74	0.5			60.8
9	2.35	1.96	1.69	1.47	1.26	1.09	0.94	0.74	0.53		61.4
10	2.41	2.03	1.77	1.56	1.39	1.21	1.05	0.92	0.74	0.55	62

Nonetheless, this efficiency boost is achieved at the cost of higher complexity and manufacturing price. Increasing the number of junctions in the stack constitutes a technological challenge because of the increased manufacturing complexity, associated with the growth of multiple layers on top of the other. This manufacturing complexity probably explains why the vast majority of multi-junction cells manufactured to date only have 4 to 5 junctions [4]. Currently, cells with 6 junctions, having a theoretical efficiency of 58% [12], are under development [20].

III-V materials are commonly used in MJ cells due to the wide range of bandgaps they offer, the direct bandgap nature of most of them, and their high absorption coefficient. Because of their very high cost, MJ cells are restricted to niche markets, such as spatial applications (where the cost is a secondary issue) or concentrating photovoltaic applications (where the area of PV cell required is orders of magnitude lower than in conventional flat-plate PV for the same amount of power generated).

D. Concentrated Photovoltaics (CPV)

1. History

Solar concentration technology was first developed in the 7th century B.C. where it was intended to induce fire and kill insects. In the 2nd century B.C. Archimede used solar concentration to focus sunlight on a Roman ship; no proof existed on this incident, but it was proven to be possible in 1973. The petroleum crisis in 1973 instigated the development of solar energy as a substitute to oil and gas for energy production. But this crisis was rapidly solved, prematurely slowing down the development of the rising PV industry. In 1976, Sandia laboratories developed the first prototype of CPV system with a 1kW peak array, using Fresnel lenses, two axis tracking and silicon solar cells cooled by water circuit. The technology couldn't find any market because of serious concerns related to its viability (the solar resource exploited by CPV was thought to be too low to make this technology cost-effective): even though it was demonstrated that CPV mounted on a single axis tracking

converts annually more solar radiation than conventional PV, the technology couldn't emerge as its price was still expensive.

III-V solar technologies, especially multi-junction cells were developed in the early 2000, with promising efficiencies, but at very high costs. Combining them with concentrated solar power was suggested as a way to make concentrating PV cost-effective, instigating a significant research effort in this field [21, 22].

2. Concentration factor

The concentration factor, X , is computed as the ratio between the aperture area of the optical concentrator A_{conc} and the solar cell area A_{cell} . It is commonly measured in *suns* with 1 sun equivalent to 1000W/m^2 .

$$X = \frac{A_{conc}}{A_{cell}} \quad (\text{II-6})$$

It can also be computed as the ratio between the solid angle at the exit of the optical concentrator and the apparent solid angle of the sun, equal to 6.8×10^{-5} steradians (sr). The solid angle at the exit of the concentrator, Ω_{abs} , varies between 6.8×10^{-5} and π sr.

$$X = \frac{\Omega_{abs}}{\Omega_{sun}} = \frac{\Omega_{abs}}{6.8 \times 10^{-5}} \quad (\text{II-7})$$

From equation (II-7), the maximal attainable concentration factor is estimated to 46200 suns. This concentration can also be computed considering half-angles in radians (*rad*) (instead of sr), as shown in eq.(II-8), with θ_{abs} being the half-angle at the concentrator exit varying between 4.65×10^{-3} and $\pi/2$ rad, leading to a maximum concentration of 46250suns.

$$X = \frac{\sin^2(\theta_{abs})}{\sin^2(\theta_{sun})} = \frac{\sin^2(\theta_{abs})}{\sin^2(4.65 \times 10^{-3})} \quad (\text{II-8})$$

The maximal theoretical concentration is often referred to as “*thermodynamic*” limit of sunlight concentration since its value can be derived on some thermodynamic grounds: a blackbody exposed to concentrated solar radiation at an illumination level exceeding the maximum concentration would see its temperature exceeding that of the sun. This situation is not allowed by the second law of thermodynamics, which precludes that the temperature of an image exceeds the temperature of the object it is originating from. Heat would then be transferred from the low temperature engine to the high temperature receiver without using work [23].

Based on the concentration factor, three types of concentrating PV can be identified: low concentration PV (LCPV), medium concentration PV (MCPV) and high concentration PV (HCPV). The range of concentration enclosed in each type is not fixed and varies depending on the author, or even the publication dates. We consider that low concentration PV includes systems operating under 100 suns, while medium concentration PV is a nomination for concentration levels between 100 and 300, and all the concentrations higher than 300 suns are categorized into HCPV [24].

3. Interest

Concentrating PVs use optics to focus solar radiation onto a small cell area, reducing the amount of active material required to produce a given quantity of electricity and, in turn, the share of PV cell in the total cost of electricity. By increasing the angle of absorption, concentration reduces the asymmetry between the solid angles of emission and absorption, and consequently the optical entropy, leading to lower *Boltzmann* losses and enhanced conversion efficiencies.

4. Operating principle

Concentrated photovoltaic systems use an optical concentrator, usually parabolic mirrors (reflective system) or Fresnel lenses (refractive system), in combination with a solar cell placed at the focal point of the concentrator. The system is necessarily combined to a sun tracking system to ensure normal incidence of radiation on the surface of the optical concentrator, as shown in Fig.II-7.

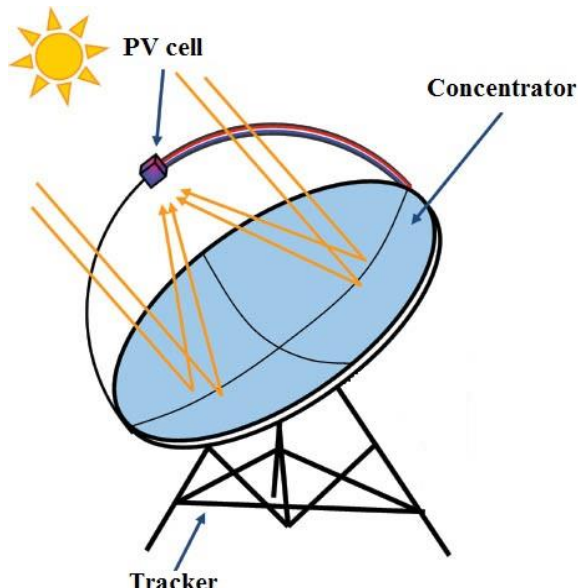


FIGURE II-7 Operating principle scheme of concentrated photovoltaic systems [25].

Some systems use secondary optics for a better light focus on the receiver, and a more homogenized concentrated beam, leading to a uniform energy distribution on the cell, and preventing localized illuminations and hot spots.

5. Optical concentrators

Solar concentrator technologies can be classified into two main categories based on the optical principle involved in the concentration of sunlight: reflective concentrators (such as parabolic dishes) or refractive concentrators (such as Fresnel lenses). They can also be differentiated based on the tracking strategy used (fixed, 1D, or 2D).

A suitable optical concentrator should be able to efficiently gather light onto a small receiver with a homogenous distribution to avoid hot spots. The acceptance angle of the concentrator, i.e. the maximum angle at which the radiation entering the concentrator can reach the cell, should also be as large as possible.

a) Parabolic mirrors

Parabolic mirrors have a single focal point where all the incident beams are concentrated. They can reach very high concentration levels, up to thousands of suns (> 10000 suns), with a theoretical maximum of 11500 suns occurring at a rim angle of 45° . Practically, optical errors such as misalignment with the sun, or imperfections in the concentrator surface, lower the maximum concentration attainable.

Secondary optics are commonly used, despite the reduction in the concentration factor, for a more homogeneous distribution of light. Kaleidoscopes, for example, involve multiple reflections onto the device internal walls, leading to a strong enhancement in the homogeneity of the light at the exit of the device [22].



FIGURE II-8 Parabolic mirror CPV [26].

b) Compound parabolic concentrator

The compound parabolic concentrator (CPC) is considered as an “ideal” optical concentrator, designed to efficiently collect and concentrate light, reaching maximum concentration levels at a minimum acceptance half-angle and maximal angular spread. To reach high concentrating factors, the CPC is required to be very tall and thin. As a consequence, it is mostly used for low concentration applications or as secondary optics combined to Fresnel lenses.

The concentrator sides consist in parabolas, with the focus point of one side being located on the lower side of the opposite parabola. Each parabola is tilted relative to the axis of the CPC. Light coming with an angle equal to the maximal acceptance half-angle is concentrated on the edges. As the ray angle becomes lower, the light is redirected downwards and undergoes successive reflections until it hits the receiver. If the angle is higher than the acceptance half angle, the beam is reflected back and escape from the CPC [22].

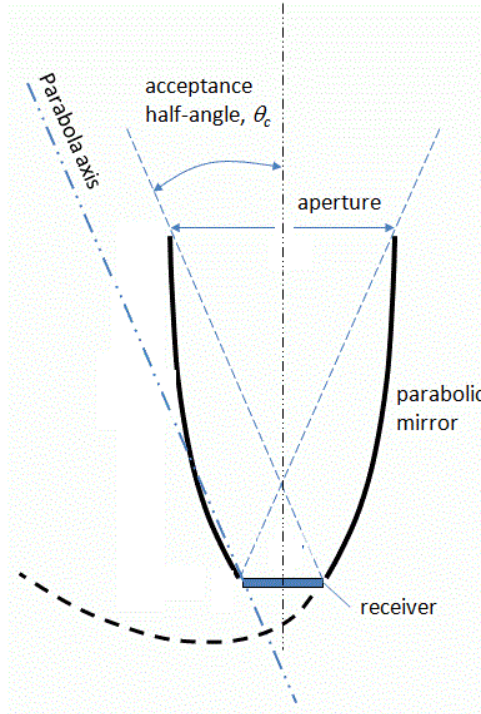


FIGURE II-9 Schematic of a CPC [27].

c) **Fresnel lenses**

Fresnel lenses are the most commonly used optical concentrators due to their low price, their compact size and their light weight. The Fresnel lens surface is subdivided into many sections of similar curvature but with discontinuities between them, with each section having its thickness reduced in comparison to a conventional lens, as sketched in Figure II-10. As can be seen, the different sections are oriented at a different angle to retain the ability of focusing light toward the center where the cell lies.

For years, the maximum concentration factor attainable with Fresnel lenses was assumed to be limited by *chromatic aberration*, the phenomenon by which the focal spot is spread due to the wavelength-dependence of light-refraction in the device (because of the wavelength dispersion in the refractive medium [28]). It was recently suggested that this limit may be dramatically increased (up to 8500 suns) by combining polycarbonate and PMMA lenses [28]. The main drawbacks of Fresnel lenses are principally associated with their imperfect transmissivity (in particular because of the presence of optical interfaces) and chromatic aberration [22,28-30].

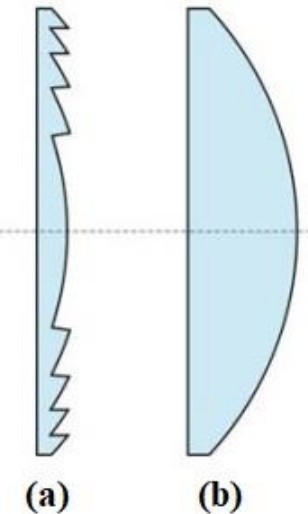


FIGURE II-10 (a) Scheme of a Fresnel lens, (b) scheme of a normal lens [31].

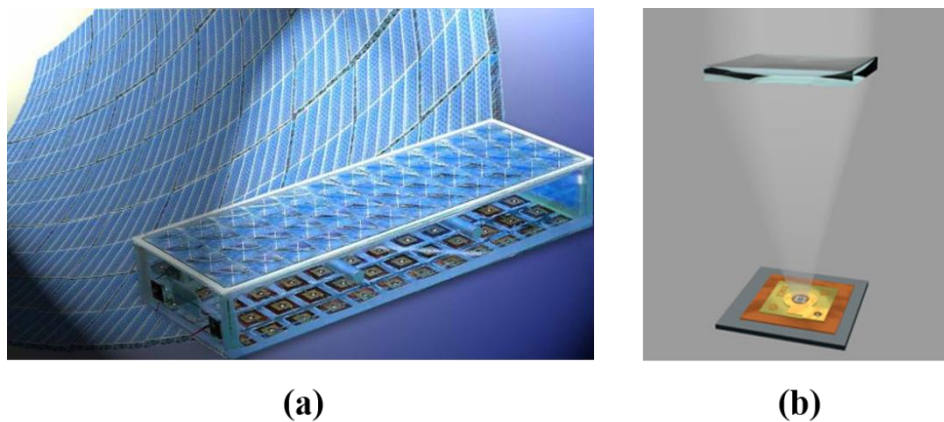


FIGURE II-11 (a) Fresnel module (b) Fresnel cell [25,32].

6. Tracking system

CPV systems can only convert normal direct radiation. Therefore, sunlight concentration requires the tracking system to guarantee a normal incidence of sunrays onto the concentrator surface.

CPV systems are subdivided into 3 main families: one axis tracking, two-axis tracking and static concentrators, based on their movement capability. In all cases, the tracking system must accurately point toward the sun to compensate for the change in the sun's position during the days (altitude angle) or the seasons (latitude) and in the azimuth angle, with a higher precision as the concentration factor increases.

The *apparent* size of the sun represents the fraction of the sky covered by the sun between two successive movements of the tracker: it is a strong function of both the tracking accuracy and the optical quality of the concentrator. The angle subtended by the sun is equal to 4.65 mrad for ideal tracking systems and increases as the time interval between two successive movements rises, as can be seen in Fig. II-12. This figure shows the angle subtended by the sun between two tracking movements, with θ_1 representing the angle at the

first position, and θ_2 the angle subtended by the sun after the tracker moved to the following position. The tracker must follow the sun precisely as it moves to ensure small apparent angles and high concentration levels.

Some of the tracking disadvantages include their cost, their maintenance, and the energy consumption [22, 33-35].

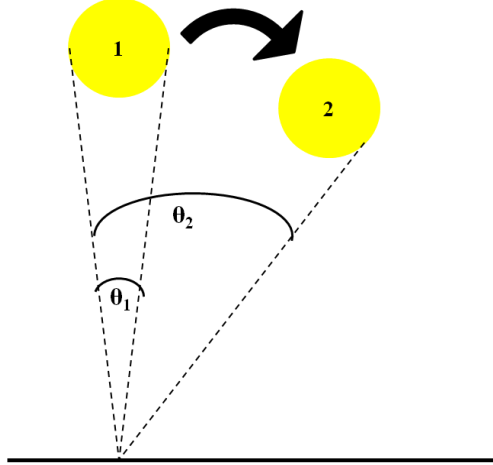


FIGURE II-12 Angle subtended by the sun between two tracking movements.

a) Single axis tracking

Single axis tracking can only evolve around one axis, with a single degree of flexibility, from east to west or from north to south. It costs less than dual axis and is more reliable, with a longer lifespan since fewer moving parts are involved, but it provides lower energy output. Such trackers are normally used with low concentrating systems [24].

b) Dual axis tracking

Dual axis tracking revolves around two directions, with 2 axis movement, allowing two degrees of freedom, both operating simultaneously. It points precisely toward the sun all day and year long. It usually tracks the sun along a vertical axis (azimuth rotation) and horizontal axis (elevation rotation) [22], aligned in the North-South and East-West positions, offering many possibilities to optimize the amount of collected energy. Two-axis tracking is more accurate than single-axis tracking systems, but since it requires more moving parts, this tracking strategy is more complex, more expensive, and requires additional maintenance. For conventional flat-plate PV modules, dual-axis tracking can boost the power output by 30-50% compared to static systems [22, 33-36]. Such tracking strategy is mainly implemented in high concentration systems where a tracking accuracy of $<0.1^\circ$ is required [21,24].

c) Static concentrator

Some optical concentrators concentrate solar radiation without any tracking system. They are known as *static* or *fixed* concentrators. As a consequence of the absence of sun tracking, the apparent size of the sun is very large, and the concentration level achievable is very low (recall from eq. II-7 and II-8 that the maximum illumination level achievable is inversely proportional to the apparent angle subtended by the sun). The use of static concentrator is usually not justified cost-effectively, since reducing the cell's manufacturing price does not compensate for the implementation of a static concentrator [21].

7. Concentrator cell designs and materials

Two technologies are mostly used in CPV applications, depending on the concentration ratio of the system: silicon solar cells (mainly for low to medium concentration applications) and III-V multi-junction cells (for high and ultra-high concentrations) [24]. Third generation cells (hot carriers, intermediate bands, quantum dots solar cells...) are also seen as promising candidates for CPV applications, instigating a broad range of research activities in this field.

8. Solar concentration and cell performances

Besides decreasing the cell's area required to produce a given amount of electricity and lowering the fraction of the cell cost among the total system cost, solar concentration enhances the conversion efficiency. Ideally, at the Shockley-Queisser limit, a single-junction solar cell submitted to 1 sun illumination reaches a maximum efficiency of 33% whereas under 46000 suns, this limit is increased to 40%. This upper bound is even boosted to 86.8% for multi-junction cells comprising an infinite number of sub-cells under maximum concentration, compared to 68.2% under 1 sun illumination. Infinite junction cells under 46000 suns allows the conversion of the whole solar spectrum, eliminating *below-E_g* and *thermalization* losses, along with *Boltzmann* losses since both angles of emission and absorption are equal [37, 38]. However, it should be noted that the Carnot limit is still not reached due to the increase in the Carnot and emission losses as the number of junctions increases in the stack [8].

a) Short-circuit current and solar concentration

The photo-generated and short-circuit currents increase linearly with solar illumination according to equation (II-9) representing I_{sc} at a given concentration X :

$$I_{sc}(X) = X \times I_{sc}(1) \quad (\text{II-9})$$

with $I_{sc}(1)$ the short-circuit current under 1 sun illumination level. The proportionality between these two values remains verified provided that 1) series resistance losses are not colossal and 2) the irradiance does not exceed a critical value above which optical absorption may be reduced.

b) Open-circuit voltage and solar concentration

V_{oc} increases logarithmically with concentration, or linearly with $\ln(X)$ since it depends on $\ln(I_{sc})$. The open-circuit voltage at a given concentration, $V_{oc}(X)$, can be expressed using eq. (II-10), with $V_{oc}(1)$ the open-circuit voltage under 1 sun illumination.

$$\begin{aligned} V_{oc}(X) &= \frac{nkT}{q} \ln\left(\frac{I_{sc}(X)}{I_0}\right) = \frac{nkT}{q} \ln\left(\frac{I_{sc}(1)}{I_0}\right) + \frac{nkT}{q} \ln(X) \\ &= V_{oc}(1) + \frac{nkT}{q} \ln(X) \end{aligned} \quad (\text{II-10})$$

As the voltage increases with concentration, V_{MPP} gets closer to V_{oc} increasing the fill factor to near unity (assuming no series resistance losses).

c) Conversion efficiency and solar concentration

In ideal solar cells, the conversion efficiency increases logarithmically with concentration, following the V_{oc} trend. The efficiency at a given concentration, $\eta(X)$ is computed using eq.(II-11).

$$\eta(X) = \frac{V_{oc}(X)I_{sc}(X)FF}{P_{in}(X)} \quad (\text{II-11})$$

Today's record efficiency is 46% for a 4 junction cells at a concentration of 508 suns [4] manufactured by Soitec.

Theoretically, the efficiency should increase indefinitely with increasing concentration, constituting a strong motivation for developing ultra-high concentration CPV systems. However, commercial cells nowadays operate at concentration levels of 500-1000 suns, which represents 1-2% of the maximal theoretical concentration [24]. Concentrations above 2000-3000 suns (commercial systems operating at 2000 suns being already developed) appear to be difficult to practically consider, due to several limiting mechanisms that may significantly affect the cell performance as the concentration increases.

9. Limiting mechanisms

Figure II-13 below shows the typical evolution of the conversion efficiency of a practical solar cell as function of the concentration factor. It is observed that the conversion efficiency increases, peaks at concentration level between 1000-3000 suns and starts to decrease as a result of several limiting mechanism such as series resistances, that strongly reduces the fill factor, and increasing operating cell temperature. It should be mentioned that even though the conversion efficiency shows a peak value, the power extracted from the cell continues to increase far above the optimal concentration [24,37,38].

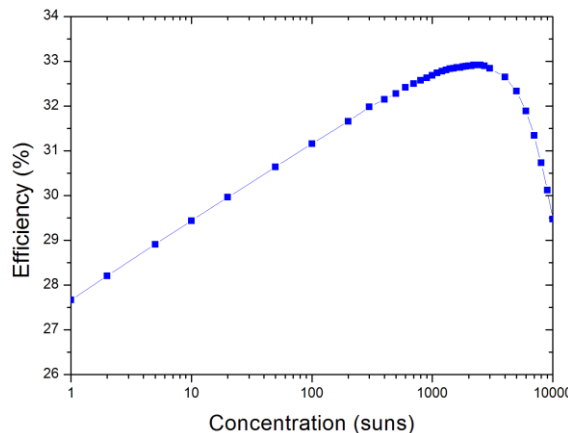


FIGURE II-13 Conversion efficiency as a function of the concentration ratio.

a) Series resistances

Resistive losses vary proportionally to the square of the current generated by the cell, which is a linear function of solar concentration. After combining eq.(I-10) and eq.(II-9), the losses at a given concentration $P_{loss}(X)$ are computed using eq.(II-12), with R_s the series resistance, assumed to be independent of the concentration.

$$P_{loss}(X) = R_s \times (I(X))^2 = R_s \times (I(1))^2 \times X^2 \quad (\text{II-12})$$

These losses are associated with the semiconductor layer resistances, the contact resistances at the semiconductor-metal interface, the grid resistances and the tunnel junction resistance. For the resistive losses to be minimal, the series resistance should be negligible. This can be achieved with a suitable cell design, optimal thicknesses for the emitter and window layers and by adjusting the doping level to reduce the semiconductor resistance [24,37,38].

b) Tunnel junctions (for multi-junction cells)

Tunnel junctions are important components to handle when designing solar cells intended to operate under high concentration levels. When the photo-generated current is smaller than the tunnel junction peak current, the junction acts as a resistance and the voltage decrease is proportional to the current density. When the photo-generated current is higher than this peak value, the tunnel junction enters a different operating regime, characterized by a strong voltage drop, and does not behave as a resistor any longer. So, to ensure effective tunneling effect, the peak current should be tailored to be high enough to accommodate for the increase of the photo-generated current under very high concentration levels [37,38].

c) High operating temperatures

Beside the heat generated by power losses, solar cells undergo inevitable heating when submitted to very high concentration factors. High operating temperatures lead to the decrease of the open-circuit voltage, mainly because of the strong temperature dependence of the dark current, lowering the conversion efficiency. To reduce the cell's temperature and avoid extra losses, an efficient cooling system is required for the cell [37,38].

d) Accuracy of tracking systems

As the concentration level increases, the accuracy of the tracking system required to follow the sun should necessarily be improved, making these systems more complex and expensive. Using secondary optics can compensate for the tracking errors at the expense of optical losses and higher system cost.

e) Diffuse light

Another issue limiting the performance of a CPV system is its inability to convert diffuse radiation, which constitutes an important fraction of the solar resource. As a consequence, CPV system installations are limited to regions with a high solar resource as well as an important fraction of direct sunlight.

10. Cooling Systems

To minimize the detrimental effects of temperature, and particularly when high concentration ratios are considered, concentrator cells need to be cooled down to keep their operating temperature near ambient. Different means can be used to extract the generated heat from the cell, passively or actively, and to dissipate it to the environment. Usually, the cell is bonded onto a heat receiver composed of a direct bonded copper (DBC) which facilitates heat extraction and temperature uniformity (to avoid hot spots) and ensures electrical insulation. As the concentration level increases, the DBC alone is not sufficient to dissipate the heat and the system is supplemented by a second heat spreader consisting in a high thermally conductive material allowing the extraction and evacuation of a greater

amount of heat. The receiver hence allows heat dissipation while ensuring electrical insulation. In all cases, there is a heat transfer between a heat exchanger (or a heat sink), a heat receiver on which the solar cells are mounted, and the cooling fluid, which can be a liquid (typically water) or a gas (typically air). The cooling system should be robust enough to withstand tracking anomalies or electrical faults. It should be reliable and should require minimal maintenance and power consumption not to increase too much the system cost [39,40].

Three different thermal resistance components can be identified:

- 1- the conduction resistances of the receiver (including the DBC and the heat spreader) and the heat exchanger,
- 2- the conduction resistance between the exchanger and the fluid (i.e. the convective resistance),
- 3- the resistance related to the fluid heat capacity C_p , associated with the fluid that is heating when crossing the heat exchanger.

a) **Passive cooling**

In passive cooling, heat is extracted from the cell where it is generated, to the ambient where it is dissipated, using a heat sink. The heat exchange is induced by the temperature difference between the cooling fluid and the exchanger. The most basic cooling systems include solids having high thermal conductivity such as copper and aluminum, in which fins have been extruded to increase the exchange surface with the ambient. More complex systems can be implemented using heat pipes, phase-change materials, or by improving naturally the fluid circulation in the cooler. It is suitable for isolated cells where 1) each cell is associated to an optical concentrator 2) the cell is located beneath the concentrator, avoiding any shadowing issue related to the blocking of light by the cooling device. In this case, each cell has an area equivalent to that of the concentrator available for heat sinking. The thermal contact resistance constitutes a major limiting factor for an efficient passive cooling and can be handled by reducing the thickness of the contact material between the receiver and the cooling material, or by increasing its thermal conductivity [39,40].

i. **Heat pipe cooling**

Heat pipe cooling basically consists in a sealed pipe or tube partially filled with a working fluid that is chosen according to the operating temperature range where both liquid and gaseous phase coexist: below the operating temperature the fluid cannot vaporize and above, it is transformed into gas. The liquid fluid absorbs heat from the cell and turns into vapor. The vapor travels along the heat pipe to a cold interface where it condensates back to liquid phase, releasing the latent heat. The liquid goes back to the hot interface through capillary action, gravity or centrifugal force and the process, driven by the temperature difference between the evaporator and the condenser, is repeated until all the excess heat is extracted. Such system is efficient for concentration levels up to 40 suns. It presents high thermal conductivity and heat transfer characteristics, and low thermal resistance. It is lightweight and doesn't contain any moving parts, thus requiring only little maintenance [39,40].

One particular type of heat pipe cooling is the thermosyphon or gravity dependent heat pipe, where the liquid returns to the evaporator by gravitational forces. The solar cell is located at the bottom of the heat pipe. The vapor rises up in the tube and gets condensed on the pipe walls by rejecting heat to the ambient.

ii. Phase change material

Phase change materials consist of materials having a high heat of fusion, that can store and release energy at a specific temperature by melting or solidifying. The material changes from solid to liquid when absorbing large amounts of heat from the cell, and solidifies when the energy is released to the ambient (with the option of being stored as latent heat for future use) [39,40].

b) Active cooling

Active cooling involves external mechanics such as pressurized air or liquid in forced motion, driven by a pump or a motor, to extract heat from the cell. It is used for systems operating under high concentrating factors or when the available area devoted for cooling is limited. It is more efficient than passive cooling but also more expensive, less reliable and requires a lot of maintenance. Different active cooling systems can be distinguished [39,40].

i. Forced air cooling

In forced air cooling system, the air is set in motion through a fan in the vicinity of the heat exchanger surface where the PV cells lie. It is less efficient than water cooling, requiring higher driving force to ensure the necessary movement of the air to cool the cell, but it can be used when water is a limited source. The extracted heat is lost to the ambient, and the system performances are mainly limited by the convective and conductive resistances.

ii. Water cooling

Water cooling is the most efficient cooling strategy and consists of a plate in which different channels carry the coolant to the heat exchanger, and flow behind the cell for cooling. It is mostly used for densely packed modules where the receiver, made of a large number of densely packed cells, is located slightly away from the focal spot, to improve illumination uniformity. Even though water cooling is an efficient approach, it is complex to build since it requires a closed loop system injecting water back to the system, unlike air [39,40].

iii. Micro-channel heat sink cooling

Micro-channel cooling consists of very small channels, as thin as human hairs in some cases, assembled on the back of the cell during the manufacturing process. The heat generated by the PV cell is transferred to the coolant by convective force. Such system can extract a very large amount of heat from a very small surface, due to the small size of the channels that decreases the thickness of the thermal boundary area and, in turn, the convective resistance. A drawback of these systems is that the temperature is not uniformly distributed [39,40].

Using a two-layered micro-channel heat sink with counter flow, known as manifold micro-channel heat sink, allows a better distribution of the temperature along the surface to

be cooled, because of the limited contact between the fluid and the base (since it circulates in the inlet and outlet manifolds).

iv. Jet impingement cooling

In the jet impingement cooling, a liquid is injected at a very high speed through a hole in the perpendicular direction of the surface to be cooled. Such technology is able to extract a large amount of heat due to the thin boundary surface between the jet and the PV cell. The efficiency of the cooling decreases as the distance to the jet axis increases. Multi-jet can be used to cool large surfaces, however raising additional concerns associated with the disturbances created by the interaction between two neighboring jets, decreasing the heat transfer coefficient. It is used for densely packed cells under high concentration ratios [39,40].

A cooling system combining micro-channels and jet impingement has already been proposed for HCPV applications [41].

v. Two-phase forced convection cooling

Forced convection under under-saturated boiling conditions is one of the most efficient heat transfer method. It is used to cool devices involving extremely large heat fluxes. The cooling system is designed to allow the coolant fluid to boil, extracting a large amount of heat from the hot surface and maintaining a constant temperature at the surface exchanger.

Concentrating sunlight onto solar cells allows reducing the *Boltzmann* losses by decreasing the angular asymmetry between the angles of absorption and emission. However, this technology is limited by resistive losses, as well as by the cell temperature that can dramatically alter the cell performance under high illumination levels. To overcome these limiting mechanisms, several authors proposed the use of angular confinement of the emitted light, which basically consists in reducing the solid angle of emission instead of modifying the angular properties of the absorbed light, to decrease *Boltzmann* losses. Theoretically this approach leads to the same limit as for solar concentration while benefitting from reduced resistive losses and lower operating temperatures [42].

E. Emission angular restriction

1. Interest

Angular restriction uses optics or angularly selective filters to reduce the photon emission solid angle. At a first sight, angular restriction appears as the exact counterpart of solar concentration, where the decrease in the *Boltzmann* losses is achieved by narrowing the emission angle rather than widening the absorption angle. Angular restriction basically consists in decreasing the amount of band-to-band photons (i.e. emitted via radiative recombination) that escape from the cell. In doing so, the photons are recycled and may contribute to the build-up of additional charge carriers in the cell, leading to increased open-circuit voltage.

Before explaining this strategy, one has to clarify several optical concepts related to light manipulation in solar cells.

2. Optical path length

The optical path length (OPL) is the product of the refractive index of a medium and the geometric length of the light path followed through the system where it propagates. It governs the light' phase, and controls light diffraction and interference in the medium.

When light travels through two different media with dissimilar refractive indices n_1 and n_2 , it refracts and changes direction according to Snell's law (eq.(II-13)), with i_1 and i_2 the angles of incidence and refraction respectively, measured relative to the normal at the boundary between both medium.

$$n_1 \sin i_1 = n_2 \sin i_2 \quad (\text{II-13})$$

If n_1 is greater than n_2 , and if the angle of incidence is greater than the *critical* angle, the beam is not refracted and total reflection occurs. The same principle applies to radiatively emitted photons in a PV cell. Radiative photons are emitted isotropically, in all directions. If they reach the boundary surface between the cell and the air with an angle lower than the critical angle, they escape from the cell. Otherwise they are reflected back to the cell and eventually reabsorbed in the semiconductor [43].

The incident light reaching a surface with irregularities in its shape scatters in all directions, with random angular distribution, independently of the incident beam direction. This is known as *diffuse* reflection. A Lambertian reflector, for which the incident light is reflected according to Lambert's cosine law (as explained in the following sections), provides an example of diffuse reflection. If the isotropic condition is fulfilled, the internal light distribution is identical in all directions. If it also happens to be ergodic (i.e. if the light distribution at a particular point is representative of the light distribution over the whole sample), the light path length enhancement can reach a maximum value of n_r^2 , with n_r the refractive index of the medium. This is known as the *Lambertian* limit, suggested by Yablonovitch in 1982 [44]. This limit can be enhanced by a factor of 2 if a back reflective surface is implemented: in this condition, photons can only escape the cell from the front side (photons reaching the rear of the cell being reflected back), thus dividing the escape probability by 2. Increasing the optical path length by $2n_r^2$ means that photons undergo $2n_r^2$ internal reflections on average before escaping from the cell [44-46].

3. Light extraction

The voltage at the operating point, V_{op} , can be expressed as function of V_{oc} as follow:

$$V_{op} = V_{oc} - \frac{kT}{q} \ln\left(1 + \frac{qV_{oc}}{kT}\right) \quad (\text{II-14})$$

The previous equation underlines the tight link between V_{oc} and the voltage at which the cell is operated, suggesting that reaching high *operating voltage* necessarily requires high *open-circuit voltage* to be achieved.

At open-circuit condition, no carrier can be extracted and all the electron-hole pairs must recombine, radiatively or not. The external photon emission rate is related to the internal recombination rate, so if all the recombination happens to be radiative the external photon emission and the internal recombination rates should ideally be equivalent. However, because of 1) the presence of non-ideal optical losses occurring in the cell, such as parasitic

absorption, or non-perfect mirror reflectivity and 2) the large difference in refractive index between the semiconductor material and the air, which tends to confine radiative photons in the cell, there is usually a wide discrepancy between the internal and the external photon emission rate [47]. Low external radiative efficiency negatively affects V_{oc} , as illustrated in eq. (II-15) below, with I_{0_rad} the dark current computed at the radiative limit [48,49].

$$V_{oc} = \frac{n k T}{q} \ln \frac{I_{sc}}{I_{0_rad}/ERE} \quad (\text{II-15})$$

Normally, solar cells should be designed to trap photons and keep them in the bulk material as long as possible for higher absorption and increased I_{sc} . However, as discussed above, keeping the photons in the cell rather than promoting their extraction increases the extent to which parasitic optical losses may lower the external photon emission rate (and in turn, the open-circuit voltage). Ideally, at open-circuit voltage, radiatively emitted photons should exactly counterbalance the incoming photons flux, a situation leading to the highest open-circuit voltage possible. Confining photons in the cell rather than facilitating their escape makes this idealized situation particularly difficult to reach (because of the parasitic optical losses occurring in the cell) leading to the following paradox: the solar cell should show enhanced light trapping and photon recycling to increase J_{sc} , but it should also improve light extraction to increase V_{oc} , since, as Yablonovitch formulated, “*a good solar cell should also be a good LED*” [48].

Non-radiative recombination, parasitic optical absorption and non-ideal back mirror reflectance make light extraction particularly difficult to achieve [43,47,48].

4. Photon recycling

Photon recycling is the repeated radiative emission and absorption of a photon with energy equal to the bandgap energy: this photon, to be recycled, should not be able to exit from the cell, a condition that is fulfilled if its angle is larger than the escape cone, leading to total internal reflection. It also requires the use of a back mirror to prevent photons escaping from the rear side. Photons that are reflected by the back mirror go upward and have higher probabilities to undergo successive total internal reflection since reflection does not change their incident angles [50].

The concept of photon recycling was first introduced in 1957 by Dumke, Moss, and Landsberg [51-53]. 10 years later this effect was observed experimentally, and it was shown that it affects the ERE and IRE of the semiconductor. As the photon recycling rate increases, the probability of non-radiative recombination increases, especially Auger recombination, which leads to a decrease in the radiative emission rate [54], and hence in V_{oc} . Using thinner cells is then necessary to reduce the amplitude of non-radiative recombination. In this case, light trapping should be particularly effective to guarantee a sufficiently high absorption in the cell, to compensate for the fundamentally low absorption of thin cells [43].

Photon recycling can increase V_{oc} (which increases due to the accumulation of charge carriers) along with boosting J_{sc} due to enhanced light trapping, leading to higher conversion efficiencies. In fact, at steady state, the carriers built-up in the n and p side controls the

differential potential. Increasing photon recycling rate increases the carrier density, which increases further the potential difference between the *p*-side and the *n*-side of the *pn*-junction.

5. Light trapping

Light trapping, or optical light enhancement, is a strategy used to increase the optical path length through surface texturization, angular restriction or a combination of both strategies, along with a highly reflective back mirror at the rear side of the cell. It enhances the conversion efficiency by improving light absorption.

For an optimal light trapping, different strategies may be combined together, namely surface texturization, adding a back mirror and filtering. Surface texturization randomizes the light scattering inside the cell, whereas the back mirror reflects the light hitting the back side of the cell, forcing it to exit only from the front side. And, finally, the filter, which is placed at the front of the cell, helps increasing re-absorption by reflecting back to the cell the radiatively emitted photons, depending on their emission angles, allowing only a fraction of light to escape. Usually, such cells are also mounted on a tracking system [47,48,55,56].

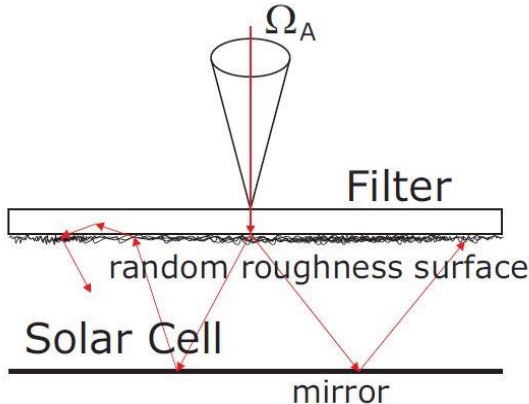


FIGURE II-14 Ultra-light trapping operating principle [55].

As stated earlier, adding an ideal back mirror increases the light path by a factor of 2 and enhances photon recycling [45,57-59]. Adding a light confinement option to the cell may improve the path length by a maximum factor of $4n_r^2$, meaning, that on average, light travels a path $4n_r^2$ times larger than the cell thickness [50]. This limit is valid for perfectly randomized surfaces and some strategies were suggested in order to exceed this limit, such as frequency shift [50,60-62].

Different approaches exist to enhance light trapping such as plasmonic, light interference, guided resonance, light scattering or recently angular restriction using angular selective filters or optical geometry devices. This chapter only focuses on surface texturization, the most commonly used method for light trapping, and angular confinement which is the object of this thesis.

a) Surface texturization

Surface texturization, or surface roughening, is the first implemented mean used to enhance the optical light path to improve light trapping and to reduce surface reflection losses [57]. It allows scattering and randomizing light inside the cell, with a better scattering as the

surface roughness increases. Due to surface irregularities stemming from texturization, the incident light is redirected in a different direction, and travels in the cell at wider angles relative to the surface normal. As a result, the probability of total internal reflection increases, since a larger fraction of the rays possess an angle larger than the critical angle, thus leading to increased optical path. Texturization is mainly used to increase the short-circuit current of semiconductors characterized by small absorption coefficient, or to compensate for the fundamentally low absorption properties of *thin* cells. Reducing the cell thickness decreases Auger recombination and hence, allows higher V_{oc} and conversion efficiency [45,54,55,60,63-67].

A *Lambertian* surface is a special type of texturization pattern allowing the highest degrees of directionality. It consists of a multi-facetted rough surface with varying roughness and angle orientation to distribute light isotropically inside the cell [58] independently of the incident angle. It scatters the light inside the cell with a cosine distribution: the intensity of the reflected light is described by a cosine distribution according to Lambert's cosine law (stating that the apparent intensity of light striking the surface changes with the slope of the surface and is proportional to the cosine of the angle formed between the incident light and the normal surface). For this type of surface, the light has the same radiance when viewed from any angle.

Other techniques are used for surface texturization, such as randomly arranged pyramidal structures or inverted pyramids where the light reflected from the surface has a chance to be reabsorbed due to the pyramids tilted surface, where light direction is oblique [57,61].

6. Emission angular confinement

Another strategy, recently suggested and already discussed above, is the use of emission angular restriction as a way to confine photons stemming from band-to band recombination in the cell. In doing so, one can modify the generation-recombination balance, leading to increased V_{oc} . Note that unlike competitor strategies aiming at improving the absorption of solar photons, angular confinement does not allow any significant improvement in the short-circuit current of the cell [49,66,68].

In the angular restriction strategy, optics are used on top of the cell to decrease the solid angles of emission [69]. The photons emitted radiatively cannot leave the cell unless they reach the cell/optic interface with an angle smaller than the escape cone defined by the added optics; otherwise, the photons are reflected back to the cell, reabsorbed and may create new electron-hole pairs.

a) Cell design and requirements

Angular restriction can theoretically be implemented in any cell technology. Since it is a recent strategy, it was only tested experimentally with GaAs and Si cells [66, 68].

A major requirement for this strategy to be effective lies in the external radiative efficiency (ERE) of the cell, which should be very high. Achieving high ERE requires two fundamental constraints to be fulfilled. First, the internal radiative efficiency of the cell should be as close as possible to 100% (meaning that most of the recombination occurring in

the cell are radiative). This constraint restricts the type of potential candidate materials to direct semiconductors, because of their fundamentally higher internal radiative efficiencies (than can approach 100% in the case of GaAs for example [70]). Second, the cell should be combined with very efficient angle-restricting optics, and the back mirror should be close to ideal with a reflectivity higher than 98% [48,49,71]. The thickness of the cell is also an important parameter to optimize, stemming from the necessary compromise between increased absorption (associated with high cell thickness) and decreased non-radiative recombination (which is usually achieved by decreasing the cell thickness) [43,54]. III-V semiconductors with high ERE, such as GaAs or GaInP thus constitute good candidates for the implementation of this strategy [68].

Angular restrictor optics used should ideally be lossless, with 100% reflection or transmission on a broad range of wavelengths. It should be closely coupled to the cell to further enhance V_{oc} [66,68].

b) Angular restriction and cell performances

The dual functions of angular restriction are light trapping and photon recycling. Angular restriction theoretically increases the cell efficiencies from 33% to 41% for single-junction solar cells operating at the radiative limit. It mostly affects V_{oc} , due to the decrease in the dark current by a factor s directly related to the narrowing in the emission angle, which can be expressed by eq. (II.16) with θ_{em} the half angle of emission of the photon emitted by radiative recombination [42,50]:

$$s = \frac{1}{(\sin(\theta_{em}))^2} \quad (\text{II-16})$$

leading to:

$$I_{0_s} = \frac{I_0}{s} \quad (\text{II-17})$$

The last two equations should only be considered when the ERE value is kept constant in the simulation. Otherwise, and as will be described later in this chapter, the effect of the emission angular restriction is considered directly in the computation of ERE.

Reducing the escape cone enhances photon recycling, which further increases the steady-state carrier density and, in turn, V_{oc} [43,49]. The maximum V_{oc} enhancement can reach 275 mV (raising the GaAs efficiency to 41%), if the solid angle of emission equals the solid angle of the sun. This voltage enhancement is strictly equivalent to the one achievable under maximal sunlight concentration (46250 suns): in both situations, the angular asymmetry between absorption and emission vanishes [49].

V_{oc} enhancement by angular restriction was experimentally proven by Braun et al. [49], and Kosten et al. [68]. Braun et al. demonstrated a 4 mV increase in V_{oc} while using a mirrored dome with an opening in the center. Kosten et al. experimentally showed the enhancement of photon recycling in angular restricted GaAs solar cells using a narrow band dielectric multilayer angular restrictor, together with a back mirror to reflect the photons and increase ERE. Despite its established theoretical validity, this concept couldn't be demonstrated experimentally until the recent Alta Device GaAs record cell was released: the

dramatic improvement in the ERE of this cell, in comparison with conventional GaAs cells, allowed this effect to be experimentally proven [47,68].

c) Optical devices for angular confinement

Confining the emission angle to trap photons inside the cell and enhance their recycling can be achieved via different optical means, such as compound parabolic concentrators (CPCs) or micro concentrators, domes for external confinement or even angularly selective filters.

i. Compound parabolic concentrators

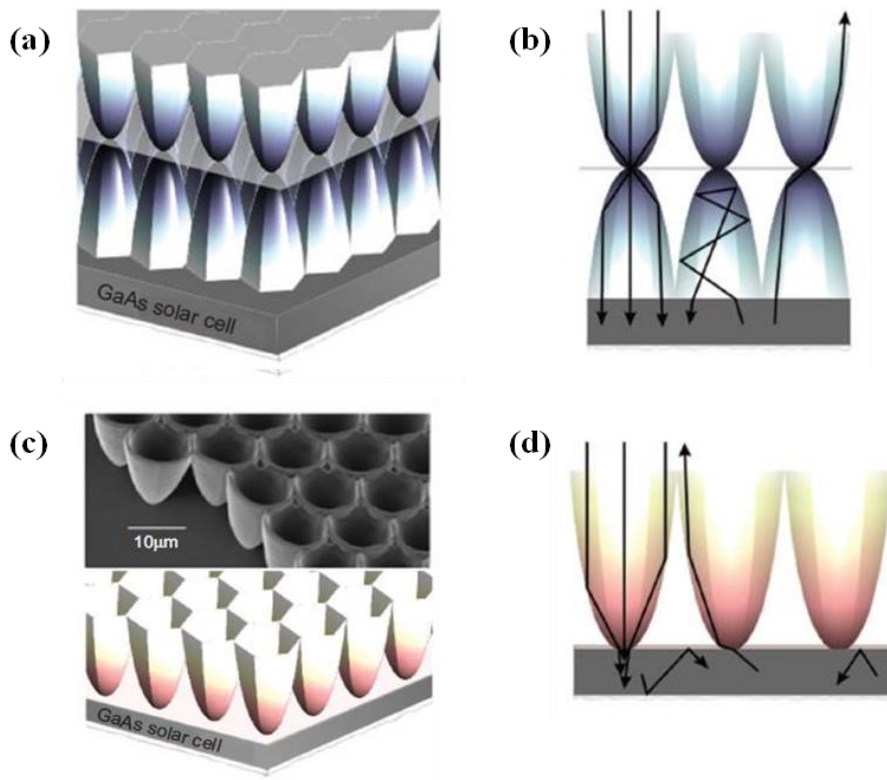


FIGURE II-15 Different CPCs designs suggested by Kosten et al. [54].

Micro-concentrators are formed by an array of compound parabolic concentrators (CPC) that are usually used for concentrating systems as primary or secondary optics, and hence can be used to confine the emission angle in solar cells (if designed and implemented in this goal). The rays entering the bottom entry of the CPC see their angle distribution narrowed around the optical axis of the CPC after multiple reflections on the internal walls of the device. CPCs must be very small and closely packed to allow a large number of photons to reach the cell, increasing the absorption rate. The micro-optical arrays should cover the total solar cell surface. The top of the cell is covered with metallic mirrors, except for the opening area of the CPCs bottom extremities. The amount of emitted radiation able to escape from the cell is basically governed by the ratio between the area of the cell surface covered with CPC, and the total area of the cell (i.e. CPC + mirror): the higher the mirrored area, the higher the restriction angle [54,58,66,71,72].

Gordon et al. [71] studied different designs to improve the devices in terms of compactness, amount of material used (to decrease the cost), as well as the ease of manufacturing. They compared a conventional CPC with a hexagonal structure and suggested the use of truncated CPC where the bottom is replaced by a thin dielectric slab or a simple paraboloid dielectric to improve the compactness of the device.

Kosten et al. [54] also presented two different designs with CPCs both having the top of the CPC in hexagonal shape and the bottom with circular opening. The first includes double array of CPCs separated by a perfect broadband reflector, as illustrated in Fig.II-15 (a) and (b). The reflections allow the incident light to reach the cell and the broadband reflector is used to restrict the emitted light from escaping the cell. Using double arrays of CPCs homogenizes light near its normal incidence, minimizing undesirable reflection losses and enhancing the device performances. They also confirmed the use of truncated CPCs to improve angular confinement. The second design, represented in Fig.II-15 (c) and (d), shows a single array of metal coated CPCs allowing an easier manufacturing process. The bottom of the cups is separated by an optimal distance equal or smaller than the carrier diffusion length which implies CPCs with very small diameters and a very high metal reflectivity [54,66].

ii. Domes for external confinement

A second method to restrict the solid angle of emission is to place the cell inside a cavity, a mirrored dome, with an ideal mirror reflectance, having a central opening allowing the light to enter and exit the system. If the radiatively emitted photons reach the exit hole, with an angle less than the opening angle, they can escape from the system. Otherwise the mirrored walls reflect the photons back to the cell. The solar cell should have an ideal back mirror for this strategy to be efficient. To achieve the best performances, the cell should ideally be textured as well. This system was described by Luque [58] and tested by Braun et al. [49] (Fig.II-16) with no intention of industrial or any other applications. Such system can be used with or without concentration, depending on the optics used [49,58].

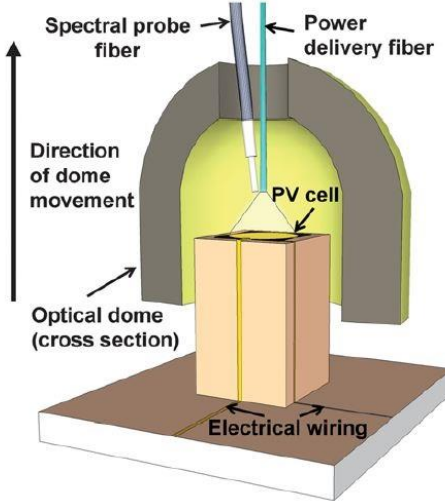


FIGURE II-16 Schematic of a mirrored dome for angular confinement [49].

iii. Angular selective filters

Angular selective filters are used for two purposes: restrict the emission angle to increase V_{oc} and enhance photon absorption to raise J_{sc} . They are usually combined with textured surfaces [69]. They are practically characterized by a critical angle banning the escape of photons reaching the device with an angle exceeding this limiting value [55,65]. The filters should ideally have a transmittance as close as possible to 100% between the critical angle and normal incidence, and a reflectivity of 1 for all the other angles, to avoid the escape of non-absorbed light. Ideally the filter should only affect the angular properties of the beam; however practical angular selective filters show wavelength dependence that induces different behavior as a function of the wavelength of the incident photon. Unlike optical devices based on light reflection (CPCs, dome), angular selective filters allow diffuse light to be absorbed, thus leading to increased generated current [68].

Two types of filters can be implemented: 1) narrowband filters, reflecting photons with energies close to the bandgap and with high emission angles back to the cell 2) broadband filters, reflecting any photon with an angle higher than the escape cone. Narrowband angular restrictor allows capturing diffuse light and increasing the generated current, unlike broadband angle restrictor [68,69]. Höhn et al. [69] showed that the narrowband filters globally offer improved performance. The different filters can be differentiated into Rugate, Bragg, or 3D photonic structures.

a. Rugate filters

Rugate filters, also known as gradient index filters [68], are the most commonly used filters for angular restriction. They are narrowband angular restrictor made of very thin optical films characterized by a continuously varying refractive index [73,74]. The smooth and periodic variation of the refractive index minimizes undesired reflection losses [56,60,66,73,75].

The Rugate structure presents a sharp transition in reflectivity, limiting the light escape cone in the range 1050-1200 nm. Since it restricts angle for a wavelength range and is

transparent outside this range, it enhances the absorption of diffuse light. It should have perfect transmission for a broad range of wavelength and ideal reflection over a narrow wavelength range close to the bandgap (corresponding to the energy of the emitted photons), giving rise to an optimal reflection around the designed wavelength [57].

b. Bragg filters

Bragg filters basically consist in associating two materials with different refractive indices, ordered periodically. Conventional Bragg filters are unsuitable for PV applications since they present undesirable reflection losses. Designing a filter involving a continuous refractive index profile, instead of a stack of different materials showing abrupt changes in their refractive index, can compensate for this inconvenience [65,76]. As for Rugate filters, Bragg filters operate both as a transmitter and a reflector. They transmit light for a broad range of wavelengths and reflects photons whose energy is close to the bandgap back to the cell.

c. 3D photonic structure

Photonic crystals are dielectric materials in which holes are drilled at regular intervals. This creates a photonic gap that can be tuned by varying the filling fraction of the material, by filling the holes with matters (solids (Si, polymers, etc.), liquids or gases) having a refractive index greater than 1 (the refractive index of air), or by introducing defects (by eliminating or adding dielectric materials). The largest photonic gaps are observed for the smallest fill fraction, where a large fraction of the materials is surrounded by air. The gaps characterize a frequency range for which light propagation is not allowed, the remaining frequencies being unaffected and absorbed: it reflects a frequency range and allows the remaining part to pass through. Photonic crystals are made from semiconductor materials such as Si, Ge, GaAs or InP and can be distinguished into 1D (like Rugate and Bragg filters), 2D and 3D.

3D photonic filters are directional selective filters used to control light. Their periodical variation is obtained through dielectrics or the combination of dielectric and metallic materials, whose stacking sequence is repeated. The filters should efficiently transmit light over a large spectral range, for a crystal direction pointing the sun, allowing the incident photons to reach the cell. The non-absorbed light trying to escape the cell through the filter with an angle greater than the critical angle is reflected back to the cell. For all the other directions, the filter is opaque, avoiding the escape of photons. These filters can be differentiated into different types, the Opal and inverted Opal filters being the most used for angular restriction. The Opal filters are based on the opal natural structure, where different spheres are periodically spaced. The light exiting from the perforated material is refracted or reflected at the glass/air interface based on its incident angle. For the inverted opal, the gaps between the spheres are filled to vary the difference in the refractive index, and the spheres are then dissolved through chemical means [55,57,77-81].

d) Limitations

Even though a V_{oc} improvement of 275 mV can theoretically be expected in the limiting case where the emitted radiation is sent back to the sun (and assuming 100% external

radiative efficiency), experimental evidence of angular restriction only showed very limited improvement in the cell V_{oc} [49]. In fact, angular restriction may be dramatically penalized by several limiting mechanisms, such as non-radiative recombination (or low ERE), non-ideal back mirror, or absorbing contacts. So, careful cell design is a necessary condition to be fulfilled for angular restriction to be effective [43].

i. Low ERE

The presence of non-radiative recombination (SRH, Auger) inside the cell is the most limiting mechanism for angular restriction strategies, leading to a decrease in both IRE and ERE, and hence, to lower solar cell performances. In fact, increasing non-radiative recombination reduces the number of available free carriers, which degrades the photon-recycling and amplifies the dark current affecting V_{oc} . From eq. (II-15) it can be seen that decreasing ERE due to the presence of non-radiative recombination increases the dark saturation current (I_0 being equal to I_{0_rad}/ERE) which decreases V_{oc} .

Höhn, et al. showed that taking into consideration non-radiative recombination in solar cells leads to different maximum limits for solar concentration and angular restriction, both being equivalent at the radiative limit only [82]. While accounting for radiative and Auger recombination only, the relative gain in efficiency between a system with no angular restriction ($\theta_{em}=90^\circ$) and a system characterized by an angle of emission of 15° is 2.23% under 1 sun illumination and 1.90% for a concentration of 500 suns. The opposite trend is observed if only radiative and SRH recombinations are taken into account: there is no relative gain in efficiency under 1 sun illumination, and this gain increases to 0.67% at 500 suns. While accounting for the three recombination mechanisms, the relative gain is about 1.96% at 500 suns, and increases to 2.91% when both angles equal 15° (which is equivalent to a concentration of 3080 suns).

Braun et al. demonstrated experimentally the effect of photon recycling on decreasing the dark current and increasing V_{oc} . The large gap between the enhancement they found experimentally and the theoretical maximum is attributed to the ERE of the cell, which appears to be not high enough to provide a significant boost in V_{oc} (despite the record ERE value of the tested cell, with a value of 24.5%) [49]. These results stress the importance of very high ERE toward increasing the cell performance through angular restriction of the emitted light.

ii. Non-ideal back mirror

Another important limiting mechanism is associated with the reflectivity of the back mirror used to guarantee that photons only exit the cell from the front surface [48]: to ensure efficient reflection of the photons hitting the back of the cell, the reflectivity should be higher than 98%. In reality, mirrors are not perfectly reflective, causing internal photons parasitic absorption and thus lower ERE [43,47,48,54,83].

iii. Cell thickness

Because of the thickness dependence of the non-radiative recombination rate (which tends to increase with increasing thickness), the cell is required to be thin to ensure high ERE. In fact a compromise in the thickness should be found between two opposite trends: the cells

should be thick enough to enhance absorption but they also should be thin to reduce the amplitude of non-radiative recombination, and to ensure that the minority carrier diffusion length is greater than the material cell thickness [43,84,85].

Kosten et al. discussed the optimization of the cell thickness for different degrees of angular restriction, and for ideal and more realistic cells accounting for non-radiative recombination [42]. They showed that, for ideal solar cells and maximal angular confinement degrees, the conversion efficiency is independent of the cell thickness. As the emission angle increases, the cells performances are reduced and the optimal thickness increases as a consequence of the weaker photon recycling occurring in the cell. For non-ideal solar cells including non-radiative recombination, the performances are lower relative to the ideal case, and the cells behave differently while varying the thickness and the emission angle. As for the ideal case, low angles of emission are most beneficial with thin solar cells. On the other hand, the performances decrease for thicker cells since the non-radiative recombination rate, mainly Auger, is greater. This observation is even more pronounced for the highest degrees of angular restriction. As the angle of emission increases, thicker cells are favored to enhance photons absorption in the absence of light trapping. These results reveal the importance of using thin cells with maximal angular restriction. These conclusions were also discussed by Kosten et al. [54,66].

Other losses include the non-absorption of diffuse light that increases proportionally to angular restriction [66]. Absorptive contacts are also an issue since they may absorb photons propagating in the cell, thus decreasing the ERE.

F. Combining CPV and angular restriction

Concentrating photovoltaics and angular restriction are two complementary strategies, both methods being thermodynamically equivalent at the radiative limit. In fact, practical concentrating photovoltaic systems typically involve sunlight concentration levels of ~500-1000 suns, which fundamentally represent relatively small angles of absorption. In CPV systems, the increase in the carrier concentration is achieved by increasing the number of absorbed photons through sunlight concentration. There is no specific need for photon recycling or light trapping, but this strategy is highly limited by resistive losses and potentially high operating temperatures. On the other hand, angular restriction reduces the optical *étendue* by decreasing the solid angle of emission using optical devices and filters: the increase in the charge carrier build up is achieved through enhanced light trapping and photon recycling, and is mostly restricted by low ERE values [43,66,74,82,86].

Hence, combining these 2 strategies could allow benefitting from the advantages of both approaches, by reducing the optical entropy loss by simultaneously decreasing the emission angle and increasing the absorption angles. Combining both strategies offers an extra-degree of freedom in the quest of high conversion efficiencies, by partially relaxing the constraints and mitigating the amplitude of the main limiting mechanism associated with each approach (by tuning the optimal absorption and emission angles) [82].

The combination of concentrated photovoltaic and angular restriction gained interest recently, especially with the release of the record GaAs solar cell with a high ERE of 24.5%

[74,82,86,87]. Schilling et al. experimentally proved the V_{oc} enhancement with the combination of a dielectric back mirror, angular restriction and concentration [87].

Hohn et al. [82] clarified the effect of non-radiative recombination on this strategy, showing that Auger recombination decreases the open-circuit voltage and the efficiency especially at high concentrations, whereas SRH recombination doesn't prevent the improvement in both V_{oc} and efficiency. The recombination currents generated by the different recombination mechanisms show distinct voltage dependencies. When only Auger and radiative recombination are assumed, Auger recombination increases at a faster rate with increasing applied voltage compared to radiative recombination. The increase in the Auger recombination rate results in decreasing the V_{oc} gain stemming from angular restriction. Accounting only for SRH and radiative recombination does not affect the V_{oc} boost since radiative recombination increases at a faster rate with increasing voltage, compared to SRH. Considering the three recombination types simultaneously requires optimizing the concentration ratio depending on the limiting recombination mechanism: high concentrations if SRH dominates, low concentrations in the case of Auger-dominated recombination, to increase the benefits of angular confinement and maximize V_{oc} enhancement. When radiative recombination dominates, the optimal gain occurs at medium concentration to avoid reaching regions with non-radiative recombination dominance. So accounting for both Auger and SRH leads to an angular restriction gain that drops with increasing concentration levels [82]. These authors predicted a gain of 3.14% relative in efficiency for realistic solar cells with a solar illumination of 500 suns and an emission angle of 15° [82].

II. Hybrid PV-CSP Systems

A. Interest

As seen in the previous chapters, PV cells directly produce electrical energy from the sun, but their efficiency is fundamentally limited by 1) their inability to convert photons whose energy is lower than the bandgap 2) *thermalization* losses, associated with the cooling of high-energy photons. Add to this, the expensive and complex electrochemical energy storage, which currently precludes a wider deployment of PV technology. On the other hand, CSP produces thermal electricity using the entire solar spectrum at higher cost than PV but allows simple and affordable storage of heat.

To benefit from the strengths of these two complementary strategies, an emerging concept consists in merging both systems into hybrid PV/CSP systems: such systems allow to produce electricity in an affordable way using PV cells, and to benefit from the heat storage capabilities of CSP, offering uninterrupted solar electricity production at a competitive cost. Overall, the electricity is generated at lower cost than CSP alone, as illustrated in Fig.II-17, and with higher output powers, compared to PV or CSP used alone [88].

Figure II-17 shows the cost and dispatchability of a PV system used alone or with electrochemical storage, CSP with thermal storage, and a hybrid PV/CSP system with thermal storage. PV systems supply low-cost electricity only during sunny hours, and cannot provide electricity during the peak demand. Adding electrochemical storage raises the electricity cost without significantly increasing its dispatchability. CSP systems provide a

dispatchable electricity production, but at the expense of the electricity cost. Combining PV and CSP systems with heat storage thus allows affordable and dispatchable electricity production throughout the day.

Such systems may decrease the *below- E_g* and *thermalization* PV losses since the non-converted photons and the heat generated by PV (all losses in PV, except optical losses and radiative recombination, generate heat) can be used by the CSP system. *Boltzmann* losses in PV may also be reduced if CPV technology is considered. In all cases, hybrid systems increase the overall efficiency and better exploit the solar spectrum [88,89].

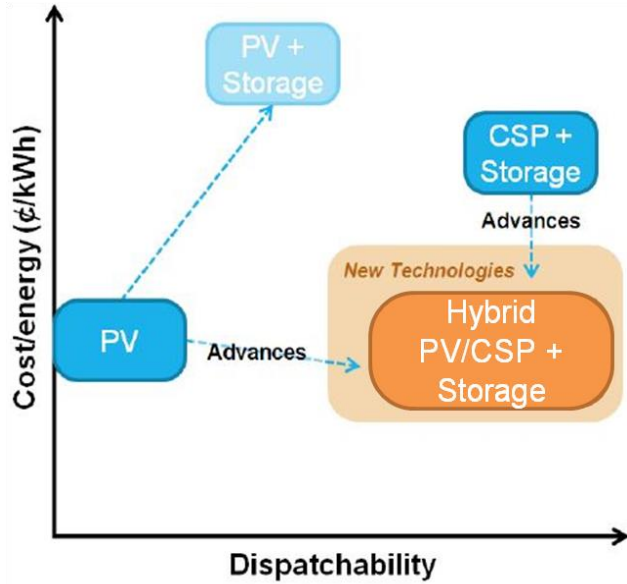


FIGURE II-17 Comparison of cost and dispatchability for PV or CSP used alone or combined as a hybrid system [88].

Different hybrid approaches were suggested in the past years, which mainly belongs to 3 main families, “one sun PV”, “spectrum splitting” and “high-temperature PV” approaches.

B. Hybrid PV/CSP approaches

Hybrid PV/CSP systems involve two separated or connected sub-systems to produce electricity. A fraction of the incident photons is absorbed by the PV (or CPV) sub-system and the remaining photons are used by the CSP sub-system (either converted directly, or stored as heat for subsequent use).

1. “One-sun PV” Approach

The “one-sun PV” approach consists in covering the surface of an optical concentrator with PV cells, behaving both as a PV converter for high-energy photons, and as a reflector for below-bandgap photons. These cells, operating under one-sun illumination, offer the advantage of converting diffuse and direct radiation, and should incorporate an optical layer, aiming at directing the beam onto PV or CSP, depending on the photons energy [90-92]. A two cut-off energies optical element can also be implemented, allowing high energy photons to be redirected onto the thermal system rather than on the PV cells, thus mitigating

thermalization losses. Since PV and CSP sub-systems are not directly connected, they operate at significantly different temperatures and illumination levels. However, heat losses generated by *thermalization* are lost to the environment, and only *below- E_g* losses are reduced (unless the filter has two cut-off energies).

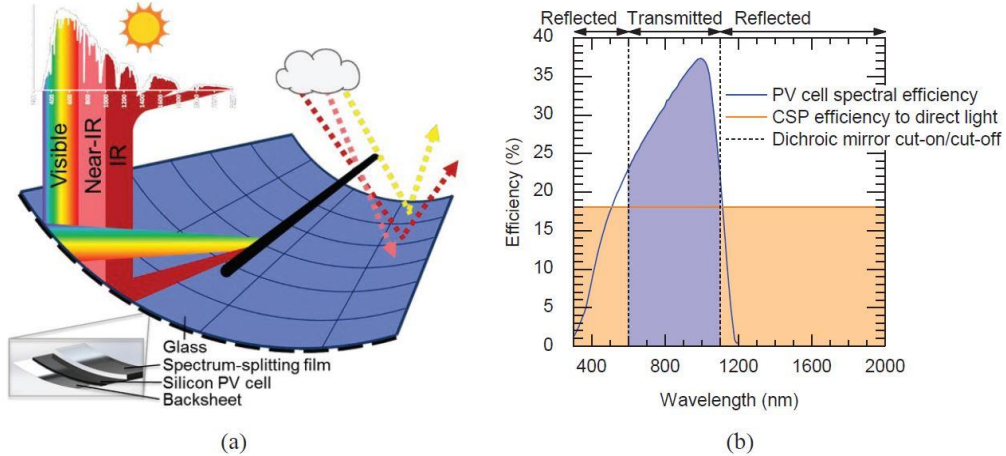


FIGURE II-18 Schematic of the one-sun PV developed at Arizona state university (a) and diagram of the spectrum splitting showing the fraction of light transmitted to the cells and the one concentrated onto the thermal receiver (b). Courtesy of Dr. Zachary Holman [93].

Holman et al. [93-95], from Arizona State University studied this strategy in details. They developed a dichroic PV mirror, using Silicon solar cells coated with an optical layer allowing near-infrared light to be redirected to the cell, while visible and infra-red light is sent onto the thermal system. The schematic of this technology, named *PVMirror*, is represented in Fig.II-18. This system was experimentally shown to increase the power output by 15% relative to PV alone [93-95].

Some of the challenges include the manufacturing of low-cost and efficient dichroic mirrors with reduced parasitic absorption.

2. “Spectrum Splitting” Approach

The “spectrum splitting” strategy uses separated CPV and CSP subsystems along with a spectrum splitting device or a selective filter, with one or two cut-off energies, to split the solar spectrum toward the PV cell or the thermal receiver based on the photons energy. Such system leads to reduced *Boltzmann* losses (because of the use of concentrated sunlight), as well as lower *below- E_g* and *thermalization* losses (if filters with two cut-off energies are used). Both sub-systems being separated, the operating temperature and concentration levels can be controlled independently. However, similarly to the “one-sun” approach described above, the heat generated by the PV is also lost to the environment [89,96-99]. Figure II-19 illustrates the operating principle of this approach, assuming two cut-off energies (E_L and E_H being the low and high cut-off energies respectively). PV cells being only effective for a narrow wavelength range, near bandgap photons are directed toward the cell while the remaining part is transmitted to the thermal receiver to increase its temperature. The benefit

of adding a second cut-off energy decreases for high bandgaps, with a relative improvement of less than 5% for E_g values greater or equal to 1.5eV.

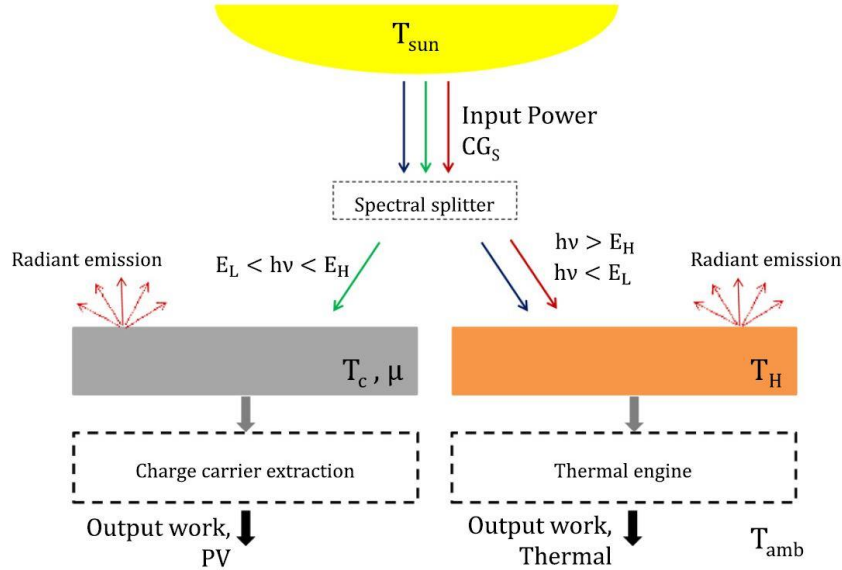


FIGURE II-19 Schematic of a spectrum splitting strategy assuming a spectral splitting device with 2 cut-off energies, with E_L and E_H the low and high cut-off energies respectively [99].

Since the spectrum is split, there are less losses due to the spectral mismatch between the incident light and the absorption properties of each converter, so the overall conversion efficiency increases, increasing the power generated by conventional parabolic troughs by ~10% [98].

The spectrum splitting device can be obtained using different means. Optical band pass filters are used to transmit a portion of the incident light to the PV while reflecting the remaining part and can be based on Rugate or Bragg filter types. They are efficient, affordable, easy to manufacture, and are suitable for such hybrid applications. Dichroic interference mirrors provide a sharp cut-off for splitting the incident beam. Secondary non-imaging optics such as CPCs can also act as optical spectrum splitting device [100,101]. Liquid absorption filters (liquids with nanoparticles, heat transfer fluids, etc.), may be used to absorb a fraction of the incident solar radiation, thus acting as band pass filters. The heat transfer fluids may behave as both transfer fluids and filters when combined with semiconductor doped glass, chosen based on their optical properties and the range of wavelength they can transmit or reflect [102,103]. Using liquids for spectrum splitting presents many drawbacks since they are degradable, especially at high temperatures or under high UV light, and they also show stability and lifetime issues [97]. The solar cell itself can act as a solid absorption filter as well, due to its ability to only convert photons with energy exceeding the bandgap. GaAs, GaInP as well as tandem III-V GaAs/GaInP are used as spectrum splitting solar cell mirrors due to their high efficiencies and narrow band response, GaAs having a sharp cut-off at a wavelength of 870nm [89,96,104-106].

The main challenges associated with this strategy include the manufacturing of highly efficient optical filters that can withstand high illumination levels.

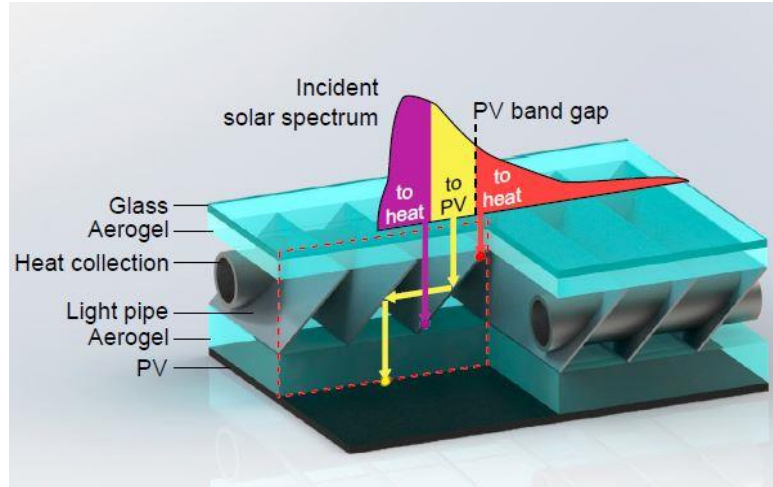


FIGURE II-20 Schematic of the “HEATS” receiver, based on spectrum splitting hybrid strategy [107].

Recently a new type of “spectral splitting” hybrid system, known as “HEATS” receiver, was suggested by Weinstein et al. [107] and involves light pipes as optical splitters, as illustrated in Fig.II-20. The light pipe is a thin film coated on a thermally conductive substrate, absorbing the low and high energies photons as thermal energy, and redirecting the near bandgap photons to the solar cell. They are formed with parallel fins covered with a selective coating, and connected to the pipe carrying a heat transfer fluid. The light pipe and the solar cells being physically separated by an aerogel, the cell can still operate at ambient temperature [107].

3. “High temperature PV” approach

a) Operating Principle

The third hybrid approach is referred to as “high Temperature PV”, also known as “PV topping”. This strategy involves an integrated solar receiver where the PV cell also behaves as a thermal absorber, implying very-high temperature operation of the PV converter. Photons with energies higher than the bandgap are absorbed by the solar cells that transmit the $below-E_g$ photons to the thermal receiver. Unlike the other competing strategies, the residual heat generated by CPV, mainly through *thermalization*, is used by CSP, since both systems are connected to each other. Because they are in direct contact, both subsystems should operate at the same illumination level and temperature, which should be tuned to ensure maximum efficiency of the system [88,89,96,108]. This concept, illustrated in Fig.II-21, was already suggested in the beginning of the 90’s by Luque and Marti [109], who mentioned that such strategies could theoretically reach performances up to 86% (equivalent to the maximum efficiency achievable under maximum sunlight concentration and using MJ cells comprising an infinite number of junctions) [91]. More recently, Branz et al. [96] showed that this strategy increases the solar to electricity conversion efficiency, in comparison with PV or CSP used alone.

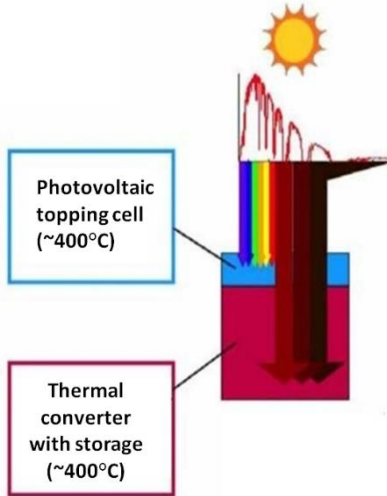


FIGURE II-21 Schematic of the high temperature PV approach [110].

One of the major limitations of this approach is associated with the very high-temperature operation of PV cells, which may dramatically alter their performance, and which remains largely unknown today. The detrimental effects of temperature on the PV cell performance is known for decades [109,111,112], and the implementation of this strategy was originally thought to be non-viable due to the dramatic effect of high-temperature operation on the cell efficiency. However, recent results stressing the benefits of sunlight concentration in mitigating the detrimental effects of temperature instigated a renewed interest for this strategy: achieving high solar to electricity conversion efficiency is indeed possible with this approach, provided that PV cells are under highly concentrated sunlight [113,114], and their bandgap are tailored to these extreme conditions [88]. An optimal operating temperature should be found as a compromise between: PV decreasing with increasing T , and thermal receiver performances being enhanced as the temperature increases.

Making PV cells operate at very high temperature and developing solar cells that efficiently perform over a lifetime of 20-30 years are critical challenges that recently interested many scientists. Novel studies show encouraging results of PV operating at high temperatures, up to 600°C, under 1000-1500 suns with limited degradation using III-V materials [108,113-118]. The development of high-temperature cells also instigated a significant research work in the last years, resulting in performances reaching 42% of the SQ limit recently [115].

b) Effect of high temperatures on solar cells

High operating temperature affects the different electrical parameters of solar cells. It degrades the semiconductor materials, as well as the metallization, and reduces the long-term stability. It is thus of prime importance to understand these effects toward adapting the cell architecture for extreme temperatures [108]. The temperature dependence of solar cells have been widely investigated, mostly for temperatures limited to 120°C, since no applications required PV cell operation at temperatures significantly higher than this value until recently. Cotal [119] studied multi-junction cells up to 950 suns and 85°C, Kinsey et al. up to 1000 suns and 120°C [120] Siefer et al. [121] up to 1100 suns and 65°C and Braun et al. [114] up

to 8600 suns and 75°C. With the development of hybrid systems, the need for high temperature PV encourages scientists to extend investigations on the temperature behavior of PV cells up to 600°C [108,115,117,118].

The Bandgap of a solar cell is known to decrease with temperature, as detailed in chapter V, and the dark current to increase proportionally to the cube of the temperature [113,122]. These two phenomena affect the various cell electrical parameters in different ways.

i. Short-circuit current

As the bandgap decreases with increasing temperature, more photons are absorbed in the cell, which leads to increased short-circuit current. The temperature-dependence of I_{sc} for a single junction solar cell, assuming a linear variation of the current with solar concentration, can be expressed as [113]:

$$\frac{dI_{sc}}{dT} = -q \times f(E_g) \frac{dE_g}{dT} \quad (\text{II-18})$$

with $f(E_g)$ the spectral photon density flux and dE_g/dT the bandgap temperature coefficient.

This equation does not usually hold for multi-junction solar cells where the junctions are connected in series, due to the current constraint condition between the different sub-cells. The general equation describing the short-circuit current variation with temperature is then expressed as [113]:

$$\frac{dI_{sc}^{MJ}}{dT} = q \left[f(E_g^{i-1}) \frac{dE_g^{i-1}}{dT} - f(E_g^i) \frac{dE_g^i}{dT} \right] \quad (\text{II-19})$$

with I_{sc}^{MJ} the short-circuit current of the multi-junction solar cell, i the index of the limiting sub-cell and $i-1$ the index of the sub-cell on top of it.

ii. Open-circuit voltage

The dark-current equation represented in eq.I-12 can be expressed as [122,123]:

$$I_0 = CT^3 \exp\left(\frac{-E_g}{kT}\right) \quad (\text{II-20})$$

As a result:

$$\frac{1}{I_0} \frac{dI_0}{dT} = \frac{3}{T} - \frac{1}{kT} \left(-\frac{E_g}{T} + \frac{dE_g}{dT} \right) \quad (\text{II-21})$$

and the variation of V_{oc} with temperature can be written as:

$$\frac{dV_{oc}}{T} = \frac{nKT}{q} \left(\frac{1}{I_{sc}} \frac{dI_{sc}}{dT} - \frac{1}{I_0} \frac{dI_0}{dT} \right) \quad (\text{II-22})$$

V_{oc} depends on the temperature and the concentration ratio, due to its dependency on I_0 and I_{sc} respectively, and increases with increasing concentration levels. Its variation with temperature can also be expressed as follow [113]:

$$\frac{dV_{oc}(T, X)}{dT} = \frac{dV_{oc}(T)}{dT} \Big|_{1\text{sun}} + \frac{nk}{q} \ln(X) \quad (\text{II-23})$$

dV_{oc}/dT being the voltage temperature coefficient, which is negative, leading to a decrease in V_{oc} with increasing temperature, since the variation of I_0 with the temperature is stronger than the variation of I_{sc} .

This decrease in V_{oc} with increasing temperature was shown experimentally by many authors, such as Braun et al. [113], who studied the effect of temperature up to illumination levels of ~9000 suns. They also showed that this drop shrinks with increasing concentration level, as $|dV_{oc}/dT|$ decreases with increasing X .

iii. Conversion efficiency

The relative temperature coefficient of the conversion efficiency decreases with increasing T [115] since its variation depends upon the variations of I_{sc} , V_{oc} and FF , which show different temperature dependence behaviors. Based on the efficiency equation mentioned in chapter I, the variation in efficiency with temperature can be expressed as [123]:

$$\frac{1}{\eta} \frac{d\eta}{dT} = \frac{1}{V_{oc}} \frac{dV_{oc}}{dT} + \frac{1}{I_{sc}} \frac{dI_{sc}}{dT} + \frac{1}{FF} \frac{dFF}{dT} \quad (\text{II-24})$$

The variation of the fill factor with temperature depends strongly on the resistive losses. These variations are not considered in this section since ideal solar cells with no series resistances are investigated.

iv. EQE

As the temperature increases, the EQE shifts toward higher wavelength values, which results from decreasing bandgap with temperature [115,117,118]. The EQE at the short wavelengths region is impacted: it decreases as a result of the increased absorption of the short wavelength photons in the Anti-Reflective Coating at high temperatures [115].

In the case of multi-junction solar cells, the electrical parameters are more sensitive to temperature variations, due to the series connection between sub-cells, and to the current-matching constraints.

Perl et al. [108,115] experimentally studied the effects of temperature and concentration on the different electrical parameters of AlGaInP and GaAs solar cells as well as of the tandem (Al)GaInP/GaAs cell up to 400°C and 1500 suns. They showed that the extent to which high-illumination conditions reduce the detrimental effect of temperature is a function of the cell temperature, the effect being stronger for high temperature values. The efficiency at ambient temperature was shown to increase by less than 5% in absolute gain between 1 and 1500 suns, but this increase is slightly higher than 10% at 400°C. They also revealed little degradation of the cells after exposure to 400°C for hundreds of hours, with a degradation of only 1% in the efficiency and no noticeable V_{oc} drop after 200h at 400°C [108,115]. Contrary to expectations, larger bandgap semiconductors don't necessarily lead to higher V_{oc} at high temperatures, due to the bandgap dependence of the dark-current. As the temperature increases, and as a consequence of this bandgap dependence, the dark current of high bandgap materials increases at a faster rate with temperature, compared to low bandgap semiconductors. As a result, the decrease in the V_{oc} of wide bandgap solar cells with high operating temperature is more pronounced. Consequently, this affects the way high-

temperature MJ cells should be designed, the use of high bandgap materials being not necessarily associated with higher V_{oc} .

Sun et al. also studied GaAs solar cells after 200 hours exposure at 400-450 °C. They found that the EQE remains unchanged, the V_{oc} decreases by ~0.03mV and the FF by 1% [116].

Maros et al. [118] studied the characteristics of GaAs solar cells up to 450°C. The EQE was shown to be almost stable up to 300°C, and to degrade rapidly as the temperature increases above this value. After cooling down, this effect seems to be reversible since EQE recovered to its initial values. Conversely, the degradation in V_{oc} appeared to be irreversible. These results were confirmed by Williams et al. for operating temperature up to 600°C [117].

Friedman et al. [124] highlighted the lower sensitivity of high-temperature tandem (Al)GaInP/GaAs cells performances to current mismatch condition at high temperatures, due to the high increase in the dark current which raises the difference between J_{sc} and J_{MPP} . This leads to a decrease in the sensitivity to the spectral content of the light.

Data regarding solar cell operation at high temperatures and concentration levels remain scarce, and a deeper understanding of the semiconductor physics at high temperature is still needed.

C. Energy Analysis

1. Absorber heat loss

The hybrid PV/CSP system loses heat to the environment via convective and radiative transfers. The radiative power density P_{rad} is estimated using equation (II-25) below:

$$P_{rad} = \varepsilon\sigma \times (T^4 - T_a^4) \quad (\text{II-25})$$

with T the operating temperature, T_a the ambient temperature, ε the emissivity and σ the Stefan-Boltzmann constant.

The convective power density P_{conv} can be expressed using equation (II-26):

$$P_{conv} = h_c \times (T - T_a) \quad (\text{II-26})$$

h_c being the convective heat transfer coefficient that depends on the wind speed and the absorber orientation, and that can be approximated as 10 W m⁻² K⁻¹ [125-127].

2. Thermal converter efficiency

The thermal receiver operates under high sunlight concentration, and high temperature. It is well known that its efficiency increases with increasing temperature, with an upper efficiency limit equal to the Carnot limit:

$$\eta_{carnot} = 1 - \frac{T_a}{T} \quad (\text{II-27})$$

where T_a represents the ambient temperature and T the operating temperature [105]. This limit increases as the temperature difference increases which justifies the need for very high thermal receiver temperature. Practically, most of the thermal receivers reach about 2/3 of this limit, a value we will consider in our calculations [96].

In the absence of any loss mechanism, the efficiency of the thermal converter is assumed to be [96]:

$$\eta_{CSP} = (1 - \eta_{PV}) \times \frac{2}{3} (1 - \frac{T_a}{T}) \quad (\text{II-28})$$

In more realistic systems, the heat used by the CSP is the fraction of the incident power which has not been converted by the PV cell or wasted as radiative or convective losses, and can be estimated as:

$$P_{CSP} = (P_{in} - P_{PV} - P_{rad} - P_{conv}) \frac{2}{3} \times (1 - \frac{T_a}{T}) \quad (\text{II-29})$$

The turbine efficiency is then:

$$\eta_{CSP} = \frac{P_{CSP}}{P_{in}} \quad (\text{II-30})$$

The remainder of the incident power represents the heat rejection from the turbine.

3. Hybrid efficiency

The hybrid efficiency is the sum of the photovoltaic and thermal efficiencies and can be computed as follow:

$$\eta_{hybrid} = \eta_{PV} + \eta_{CSP} \quad (\text{II-31})$$

D. Economical review

Economical assessments of hybrid PV/CSP systems are currently scarce. In 2015, Branz et al. [96] provided a first estimation of the financial benefit associated with the use of hybrid PV/CSP systems, in comparison with conventional CSP or PV with or without storage. They showed that hybrid systems can be built at lower cost than CSP or PV with storage. This price is decreasing with decreasing CSP and PV expenses, especially with the PV cost expected to drop by 71% by 2050 [128].

To compare the cost of these different strategies, namely PV or CSP, and hybrid PV/CSP systems, one should start by computing the levelized cost of electricity (LCOE) of each system. LCOE helps comparing the cost of electricity from different strategies and sources since it provides a common basis for comparison. It represents the cost of electricity produced by the system over its lifetime and is calculated as the ratio between the initial cost of the system taking into account operational and maintenance cost, and the amount of electricity generated during its lifetime. Any system improvement leading to a decrease in the initial cost, the operational or the maintenance cost, or alternatively, in an increase in the electricity production, decreases the LCOE and hence is better to consider for implementation.

Based on this parameter, it is shown that the CSP LCOE is 2-3 times higher than that of the PV [93], which is currently below 0.05\$/kWh in some regions of the US [93]. Including an electrochemical storage almost triples the price of PV, since no suitable storage was developed to satisfy low capital cost, long lifetime and cycling durability [88,93,96]. Storing electrical energy with batteries adds an extra 0.1\$/kWh, which is much greater than storing energy with CSP systems, that only adds 0.03\$/kWh to the LCOE if stored at 580°C,

or nearly 0.06\$/kWh if stored at lower temperatures. The one sun approach, for example, leads to a reduction of 15-20% in the LCOE compared to conventional CSP systems [93].

The LCOE of CSP is significantly higher than the one of PV, but in the meantime, thermal storage is significantly cheaper: one could thus benefit from adding a thermal storage to the PV system to lower the LCOE compared to CSP, and increase the ability of the system to provide uninterrupted electricity production.

III. References

- [1] W. Shockley and H. J. Queisser, Detailed balance limit of efficiency of pn junction solar cells, *J. Appl. Phys.*, 32 (1961) 510-519.
- [2] A. Vossier, F. Gualdi, A. Dollet, R. Ares, and V. Aimez, Approaching the Shockley-Queisser limit: General assessment of the main limiting mechanisms in photovoltaic cells, *J. Appl. Phys.*, 117 (2015) 015102.
- [3] Y. Xu, T. Gong, and J. N. Munday, The Shockley-Queisser limit for nanostructured solar cells, *Sci. Rep.*, 5 (2015) 13536.
- [4] M. A. Green, Y. Hishikawa, E. D. Dunlop, D. H. Levi, J. Hohl-Ebinger and A. W.Y. Ho-Baillie, Solar cell efficiency tables (version 51), *Prog. Photovolt. Res. Appl.*, 26 (2018) 3-12.
- [5] O. M. Ten Kate, M. De Jong, H. T. Hintzen, and E. Van der Kolk, Efficiency enhancement calculations of state-of-the-art solar cells by luminescent layers with spectral shifting, quantum cutting, and quantum tripling function, *J. Appl. Phys.*, 114 (2013) 084502.
- [6] P. Wurfel, Thermodynamic limitations to solar energy conversion. *Physica E Low Dimens. Syst. Nanostruct.*, 14 (2002) 18-26.
- [7] C. H. Henry, Limiting efficiencies of ideal single and multiple energy gap terrestrial solar cells, *J. Appl. Phys.*, 51 (1980) 4494-4500.
- [8] L. C. Hirst and N. J. Ekins-Daukes, Fundamental losses in solar cells, *Prog. Photovolt: Res. Appl.*, 19 (2011) 286–293.
- [9] T. Markvart, Solar cell as a heat engine: energy–entropy analysis of photovoltaic conversion, *phys. stat. sol. (a)*, 205 (2008) 2752–2756.
- [10] P.T. Landsberg and V. Badescu, Carnot factor in solar cell efficiencies, *J. Phys. D: Appl. Phys.* 33 (2000) 3004–3008.
- [11] T. Markvart, Thermodynamics of losses in photovoltaic conversion, *Appl. Phys. Lett.*, 91 (2007) 064102.
- [12] A. Vossier, E. Al Alam, A. Dollet, and M. Amara, Assessing the efficiency of advanced multi-junctions solar cells in real working conditions, *IEEE J. Photovolt.*, 5 (2015) 1805-1812.
- [13] P.T. Chiu, D.L. Law, R.L. Woo, S. Singer, D. Bhusari , W.D. Hong, A. Zakaria, J.C. Boisvert, S. Mesropian, R.R. King, and N.H. Karam, 35.8% space and 38.8% terrestrial 5J direct bonded cells, In Proc. of the 40th IEEE Photovoltaic Specialist Conference (PVSC-40), (2014) 11-13.

- [14] K. Sasaki, T. Agui, K. Nakaido, N. Takahashi, R. Onitsuka, and T. Takamoto, Proceedings, Development of InGaP/GaAs/InGaAs inverted triple junction concentrator solar cells, In. AIP Conference Proceedings, 1556 (2013) 22-25.
- [15] B.M. Kayes, H. Nie, R. Twist, S.G. Spruytte, F. Reinhardt, I.C. Kizilyalli, and G.S. Higashi, 27.6% conversion efficiency, a new record for single-junction solar cells under 1 sun illumination, In Proc. of the 37th IEEE Photovoltaic Specialist Conference (PVSC-37), (2011) 4-8.
- [16] Dirk, File:SpectrumAbsorption1.JPG, May 11, 2010. [Online]. Available: <http://www.appropedia.org/File:SpectrumAbsorption1.JPG>. [Accessed August 27, 2018].
- [17] N.V. Yastrebova, High-efficiency multi-junction solar cells: Current status and future potential, Centre for Research in Photonics, University of Ottawa, Canada, Tech. Rep., April 2007.
- [18] M. Yamaguchi, T. Takamoto, K. Araki, and N. Ekins-Daukes, Multi-junction III-V solar cells: current status and future potential, Sol. Energ., 79 (2005) 78-85.
- [19] A.S. Brown and M.A. Green, Limiting efficiency for current-constrained two-terminal tandem cell stacks, Prog. Photovolt.: Res. Appl. 10 (2002) 299-307.
- [20] National Renewable Energy Laboratory (NREL), U.S. Department of Energy, High-Concentration III-V Multijunction solar cells. [Online]. Available: <https://www.nrel.gov/pv/high-concentration-iii-v-multijunction-solar-cells.html>. [Accessed September 19, 2018].
- [21] K. Lovegrove and W. Stein, Concentrating solar power technology: Principles, developments and applications, Woodhead Publishing Series in Energy: Number 21, Sawston, Cambridge, US, 2012.
- [22] A. Luque and S. Hegedus, Handbook of photovoltaic science and engineering, John Wiley & Sons, West Sussex, England, 2003.
- [23] Z. R. Abrams and X. Zhang, The concentration limit for solar cells based on entropy production, arXiv preprint arXiv:1207.3893 (2012).
- [24] S.P. Philips, A.W. Bett, K. Horowitz and S. Kurtz, Current status of concentrator photovoltaic (CPV) technology, Fraunhofer Institute for Solar Energy Systems ISE, Freiburg, Germany and National Renewable Energy Lab. (NREL), Golden, Colorado, US, Tech. Rep. NREL/TP-5J00-65130, December 2015.
- [25] S.P. Philipps and A.W. Bett, III-V Multi-junction solar cells and concentrating photovoltaic (CPV) Systems, Adv. Opt. Techn., 3 (2014) 469-478.
- [26] Le solaire photovoltaïque à concentration, June 21, 2008. [Online]. Available: http://energieverte.canalblog.com/archives/energies_renouvelables/index.html. [Accessed August 6, 2018].
- [27] PennState, John and Willie Leone Family, Department of Energy and Mineral Engineering, CPC Collectors - Concentration of Diffuse Radiation, 2018. [Online]. Available: <https://www.e-education.psu.edu/eme812/node/558>. [Accessed August 7, 2018].
- [28] K. Shanks, S. Senthilarasu, and T. K. Mallick, Optics for concentrating photovoltaics: Trends, limits and opportunities for materials and design, Renew. Sust. Energ. Rev., 60 (2016) 394-407.

- [29] W.T. Xie, Y.J. Dai, R.Z. Wang, and K. Sumathy, Concentrated solar energy applications using Fresnel lenses: A review, *Renew. Sust. Energ. Rev.*, 15 (2011) 2588-2606.
- [30] K. Ryu, J.G. Rhee, K.M. Park, and J. Kim, Concept and design of modular Fresnel lenses for concentration solar PV system, *Sol. Energ.*, 80 (2006) 1580-1587.
- [31] Jamer Gamboa, Augustin Fresnel. [Online]. Available: <http://proyectoidis.org/agustin-fresnel/>. [Accessed August 7, 2018].
- [32] James Fraser, The Energy Blog, Concentrix Concentrating Photovoltaic Technology, Mar. 05, 2006. [Online]. Available: http://thefraserdomain.typepad.com/energy/2006/03/concentrix_conc.html. [Accessed August 7, 2018].
- [33] R. Eke, A. Senturk, Performance comparison of a double-axis sun tracking versus fixed PV system, *Sol. Energ.*, 86 (2012) 2665-2672.
- [34] H. Mousazadeh, A. Keyhani, A. Javadi, H. Mobli, K. Abrinia, and A. Sharifi, A review of principle and sun-tracking methods for maximizing solar systems output, *Renew. Sust. Energ. Rev.*, 13 (2009) 1800-1818.
- [35] S. A. Kalogirou, Solar thermal collectors and applications, *Prog. Energ. Comb. Sci.*, 30 (2004) 231-295.
- [36] F. J. Gomez-Gila, X. Wang, and A. Barnett, Energy production of photovoltaic systems: Fixed, tracking, and concentrating, *Renew. Sust. Energ. Rev.*, 16 (2012) 306-313.
- [37] A. Vossier, D. Chemisana, G. Flamant, and A. Dollet, Very high fluxes for concentrating photovoltaics: Considerations from simple experiments and modeling, *Renew. Energy.*, 38 (2012) 31-39.
- [38] H. Cotal, C. Fetzer, J. Boisvert, G. Kinsey, R. King, P. Hebert, H. Yoon and N. Karam, III-V multijunction solar cells for concentrating photovoltaics, *Energ. Environ. Sci.*, 2 (2009) 174-192.
- [39] S. Jakhar, M.S. Soni, and N. Gakkhar, Historical and recent development of concentrating photovoltaic cooling technologies, *Renew. Sust. Energ. Rev.*, 60 (2016), 41-59.
- [40] A. Royne, C. J. Dey, and D. R. Mills, Cooling of photovoltaic cells under concentrated illumination: a critical review, *Sol. Energ. Mater. Sol. Cell.*, 86 (2005) 451-483.
- [41] J. Barrau, A. Perona, A. Dollet, and J. Rosell, Outdoor test of a hybrid jet impingement/micro-channel cooling device for densely packed concentrated photovoltaic cells, *Sol. Energ.*, 107 (2014) 113-121.
- [42] E.D. Kosten and H.A. Atwater, Limiting acceptance angle to maximize efficiency in solar cells, In Proc. Of SPIE, Nonimaging optics: Efficient design for Illumination and Solar Concentration VIII, 8124 (2011) 81240F.
- [43] M. R. Khan, X. Wang, and M. A. Alam, Nonideal effects limit the efficiency gain for angle-restricted solar cells, *IEEE J. Photovolt.*, 6 (2016) 172-178.
- [44] E. Yablonovitch, Statistical ray optics, *JOSA*, 72 (1982) 899-907.
- [45] E. Yablonovitch and G. D. Cody, Intensity Enhancement in Textured Optical Sheets for Solar Cells, *IEEE Trans. Electron Devices*, 29 (1982) 300-305.

- [46] E. Garnett and P. Yang, Light Trapping in Silicon Nanowire Solar Cells, *Nano Lett.*, 10 (2010) 1082-1087.
- [47] O.D. Miller and E. Yablonovitch, Photon extraction: the key physics for approaching solar cell efficiency limits, In Proc. of SPIE, Active Photonic Materials V, 8808 (2013) 880807.
- [48] O.D. Miller, E. Yablonovitch, and S.R. Kurtz, Strong internal and external luminescence as solar cells approach the Shockley–Queisser limit, *IEEE J. Photovolt.*, 2 (2012) 303-311.
- [49] A. Braun, E.A. Katz, D. Feuermann, B. M. Kayes, and J. M. Gordon, Photovoltaic performance enhancement by external recycling of photon emission, *Energ. Environ. Sci.*, 6 (2013) 1499-1503.
- [50] U. Rau, U. W. Paetzold, and T. Kirchartz, Thermodynamics of light management in photovoltaic devices, *Phys. Rev. B*, 90 (2014) 035211.
- [51] W. P. Dumke, Spontaneous radiative recombination in semiconductors, *Phys. Rev.* 105 (1957) 139.
- [52] T. S. Moss, MOSS, T. S. Theory of the spectral distribution of recombination radiation from InSb, In. Proc. of the Physical Society Section B, 70 (1957) 247.
- [53] P. T. Landsberg, Lifetimes of excess carriers in InSb, In. Proc. of the Physical Society Section B, 70 (1957) 1175.
- [54] E.D. Kosten, J.H. Atwater, J. Parsons, A. Polman, and H.A. Atwater, Highly efficient GaAs solar cells by limiting light emission angle, *Light: Sci. App.*, 2 (2013) e45.
- [55] J. Üpping, C. Ulbrich, C. Helgert, M. Peters, L. Steidl, R. Zentel, T. Pertsch, U. Rau, and R. B. Wehrspohn, Inverted-opal photonic crystals for ultra light trapping in solar cells, In Proc. of SPIE, Photonics for Solar Energy Systems III, 7725 (2010) 772519.
- [56] S. Fahr, C. Ulbrich, T. Kirchartz, U. Rau, C. Rockstuhl, and F. Lederer, Rugate filter for light-trapping in solar cells, *Opt. Express*, 16 (2008) 9332-9343.
- [57] R.B. Wehrspohn, U. Rau, and A. Gombert, *Photon Management in solar cells*, Wiley-VCH, Weinheim, Germany, 2015.
- [58] A. Luque, The confinement of light in solar cells, *Sol. Energ. Mat.*, 23 (1991) 152-163.
- [59] N. Vandamme, H.L. Chen, A. Gaucher, B. Behaghel, A. Lemaître, A. Cattoni, C. Dupuis, N. Bardou, J.F. Guillemoles, and S. Collin, Ultrathin GaAs Solar Cells With a Silver Back Mirror, *IEEE J. Photovolt.*, 5 (2015) 565-570.
- [60] C. Ulbrich, S. Fahr, J. Üpping, M. Peters, T. Kirchartz, C. Rockstuhl, R. Wehrspohn, A. Gombert, F. Lederer, and U. Rau, Directional selectivity and ultra-light trapping in solar cells, *Phys. Status Solidi A*, 205 (2008) 2831-2843.
- [61] I.M. Peters, Phase space considerations for light path lengths in planar, isotropic absorbers, *Opt. Express*, 22 (2014) A908-A920.
- [62] T. Markvart, Beyond the Yablonovitch limit: Trapping light by frequency shift, *Appl. Phys. Lett.*, 98 (2011) 071107.
- [63] J. Nelson, *The physics of solar cells*, Imperial College Press, London, 2004.

- [64] P. Verlinden, O. Evrard, E. Mazy and A. Crahay, The surface texturization of solar cells: A new method using V-grooves with controllable sidewall angles, *Sol. Energ. Mat. Sol. cell.*, 26 (1992) 71-78.
- [65] M. Peters, J.C. Goldschmidt, T. Kirchartz and B. Bläsi, The photonic light trap – Improved light trapping in solar cells by angularly selective filters, *Sol. Energ. Mater. Sol. Cell.*, 93 (2009) 1721-1727.
- [66] E. D. Kosten, B. K. Newman, J. V. Lloyd, A. Polman, and H. A. Atwater, Limiting light escape angle in silicon photovoltaics: Ideal and realistic cells, *IEEE J. Photovolt.*, 5 (2015) 61-69.
- [67] P. Wurfel, Physics of solar cells, 2nd edition, Wiley-VCH, Weinheim, 2009.
- [68] E.D. Kosten, B.M. Kayes, and H.A. Atwater, Experimental demonstration of enhanced photon recycling in angle-restricted GaAs solar cells, *Energ. Environ. Sci.*, 7 (2014) 1907-1912.
- [69] O. Höhn, T. Kraus, G. Bauhuis, U. T. Schwarz, and B. Bläsi, Maximal power output by solar cells with angular confinement, *Opt. Express*, 22 (2014) A715-A722.
- [70] I. Schnitzer, E. Yablonovitch, C. Caneau, and T. J. Gmitter, Ultrahigh spontaneous emission quantum efficiency, 99.7% internally and 72% externally, from AlGaAs/GaAs/AlGaAs double heterostructures, *Appl. Phys. Lett.*, 62 (1993) 131-133.
- [71] J.M. Gordon, D. Feuermann, and H. Mashaal, Angular confinement in solar cells: viable micro-optical designs, In Proc. of SPIE, Nonimaging Optics: Efficient design for illumination and solar concentration XI, 9191 (2014) 91910F.
- [72] L.V. Dijk, U.W. Paetzold, G.A. Blab, R.E.I. Schropp, and M. Di Vece, 3D-printed external light trap for solar cells, *Prog. Photovolt. Res. Appl.*, 24 (2016) 623-633.
- [73] S. Shu, and Y.Y. Li, Metallic rugate structures for perfect absorbers in visible and near-infrared regions, *Opt. Lett.*, 37 (2012) 3495-3497.
- [74] O. Höhn, M. Peters, M. Zilk, C. Ulbrich, A. Hoffmann, U.T. Schwartz, and B. Bläsi, Combination of angular selective photonic structure and concentrating solar cell system, In Proc. of the 27th EUPVSEC, (2012) 353-357.
- [75] B. G. Bovard, Rugate filter theory: an overview, *Appl. Opt.*, 32 (1993) 5427-5442.
- [76] X. Wang, Z. Gong, K. Dong, S. Lou, J. Slack, A. Anders, and J. Yao, Tunable Bragg filters with a phase transition material defect layer, *Opt. Express*, 24 (2016) 20365-20372.
- [77] R.B. Wehrspohn and J. Üpping, 3D photonic crystals for photon management in solar cells, *J. Opt.*, 14 (2012) 024003.
- [78] J. Üpping, A. Bielawny, C. Ulbrich, M. Peters, J. C. Goldschmidt, L. Steidl, R. Zentel, T. Beckers, A. Lambertz, R. Cariub, U. Rau and R. B. Wehrspohn, 3D photonic crystals for photon management in solar cells, In Proc. of SPIE, Active Photonic Materials III, 7756 (2010) 77560A.
- [79] H.B. Sun, S. Matsuo, and H. Misawa, Three-dimensional photonic crystal structures achieved with two-photon-absorption photopolymerization of resin, *Appl. Phys. Lett.*, 74 (1999) 786-788.
- [80] M.N. Armenise, C.E. Campanella, C. Ciminelli, F. Dell'Olio, and V.M.N. Passaro, Phononic and photonic band gap structures: modelling and applications, *Phys. Proc.*, 3 (2010) 357–364.

- [81] S. Y. Lin, J. G. Fleming, D. L. Hetherington, B. K. Smith, R. Biswas, K. M. Ho, M. M. Sigalas, W. Zubrzycki, S. R. Kurtz, and Jim Bur, A three-dimensional photonic crystal operating at infrared wavelengths, *Nature*, 394 (1998) 251-253.
- [82] O. Höhn, T. Kraus, U. T. Schwartz, B. Bläsi, Effects of angular confinement and concentration to realistic solar cells, *J. Appl. Phys.*, 117 (2015) 034503.
- [83] X. Wang, M. R. Khan, J. L. Gray, M. Alam, and M. S. Lundstrom, Design of GaAs solar cells operating close to the Shockley–Queisser limit, *IEEE J. Photovolt.*, 3 (2013) 737-744.
- [84] A.W. Walker, O. Höhn, D.N. Micha, B. Bläsi, A.W. Bett, and F. Dimroth, Impact of photon recycling on GaAs solar cell designs, *IEEE J. Photovolt.*, 5 (2015) 1636-1645.
- [85] H.A. Atwater and A. Polman, Plasmonics for improved photovoltaic devices, *Nat. Mater.*, 9 (2015), 205-213.
- [86] M. Peters, J.C. Goldschmidt, and B. Bläsi, Angular confinement and concentration in photovoltaic converters, *Sol. Energ. Mater. Sol. Cell.*, 94 (2010) 1393-1398.
- [87] C.L. Schilling, O. Höhn, D.N. Micha, S. Heckelmann, V. Klinger, E. Oliva, S.W. Glunz, and F. Dimroth, Combining Photon Recycling and Concentrated Illumination in a GaAs Heterojunction Solar Cell, *IEEE J. Photovolt.*, 8 (2018) 348-354.
- [88] ARPA-E , Full-Spectrum Optimized Conversion and Utilization of Sunlight (FOCUS), FOCUS Program Overview, United States Department of Energy, Funding Opportunity Announcement, 2013.
- [89] X. Ju, C. Xu, Y. Hu, X. Han, G. Wei, and X. Du, A review on the development of photovoltaic/concentrated solar power (PVCSP) hybrid systems, *Sol. Energ. Mater. Sol. Cell.*, 161 (2017) 305-327.
- [90] T.P. Otanicar, S. Theisen, T. Norman, H. Tyagi, and R. A. Taylor, Envisioning advanced solar electricity generation: Parametric studies of CPV/T systems with spectral filtering and high temperature PV, *Appl. Energ.*, 140 (2015) 224-233.
- [91] Y.V. Vorobiev, J. Gonzalez-Hernandez, and A. Kribus, Analysis of potential conversion efficiency of a solar hybrid system with high-temperature stage, *J. Sol. Energ. Eng.*, 128 (2006) 258-260.
- [92] Y. Vorobiev, J. Gonzalez-Hernandez, P. Vorobiev, and L. Bulat, Thermal-photovoltaic solar hybrid system for efficient solar energy conversion, *Sol. Energ.*, 80 (2006) 170-176.
- [93] K. Fisher, Z. Yu, R. Striling, and Z. Holman, PVMirrors: Hybrid PV/CSP collectors that enable lower LCOEs, In AIP Conference Proceedings, 1850 (2017) 020004.
- [94] Z.J. Yu, K.C. Fisher, B.M. Wheelwright, R.P. Angel, and Z.C. Holman, PVMirror: A New Concept for Tandem Solar Cells and Hybrid Solar Converters, *IEEE J. Photovolt.*, 5 (2015) 1791-1799.
- [95] J.Y. Zhengshan, K.C. Fisher, and Z.C. Holman, Evaluation of Spectrum-Splitting Dichroic Mirrors for PVMirror Tandem Solar Cells, In Proc. of the 42nd IEEE Photovoltaic Specialist Conference (PVSC-42), (2015).
- [96] H.M. Branz, W. Regan, K.J. Gerst, J.B. Borak, and E.A. Santori, Hybrid solar converters for maximum exergy and inexpensive dispatchable electricity, *Energy Environ. Sci.*, 8 (2015) 3083-3091.

- [97] Y. Ji, A. Ollanik, N. Farrar-Foley, Q. Xu, L. Madrone, P. Lynn, V. Romanin, D. Codd, and M. Escarra, Transmissive Spectrum Splitting Multi-junction Solar Module for Hybrid CPV/CSP System, In Proc. of the 42nd IEEE Photovoltaic Specialist Conference (PVSC-42), (2015).
- [98] M. Orosz, N. Zweibaum, T. Lance, M. Ruiz, and R. Morad, Spectrum-splitting hybrid CSP-CPV solar energy system with standalone and parabolic trough plant retrofit applications, In AIP Conference Proceedings, 1734 (2016) 070023.
- [99] D.M. Bierman, A. Lenert, and E.N. Wang, Spectral splitting optimization for high-efficiency solar photovoltaic and thermal power generation, *Appl. Phys. Lett.*, 109 (2016) 243904.
- [100] B.K. Widyolar, M. Abdelhamid, L. Jiang, R. Winston, E. Yablonovitch, G. Scranton, D. Cygan, H. Abbasi, and A. Kozlov, Design, simulation and experimental characterization of a novel parabolic trough hybrid solar photovoltaic/thermal (PV/T) collector, *Renew. Energ.*, 101 (2017) 1379-1389.
- [101] D. Cygan, H. Abbasi, A. Kozlov, J. Pondo, R. Winston, B. Widyolar, L. Jiang, M. Abdelhamid, A.P. Kirk, M. Drees, H. Miyamoto, V.C. Elarde, and M.L. Osowski, Full Spectrum Solar System: Hybrid Concentrated Photovoltaic/Concentrated Solar Power (CPV-CSP), *MRS Adv.*, 1 (2016) 2941-2946.
- [102] A. Mojiri, C. Stanley, D. Rodriguez-Sanchez, V. Everett, A. Blakers, and G. Rosengarten, A spectral-splitting PV–thermal volumetric solar receiver. *Appl. Energ.*, 169 (2016) 63-71.
- [103] C. Stanley, A. Mojiri, M. Rahat, A. Blakers, and G. Rosengarten, Performance testing of a spectral beam splitting hybrid PVT solar receiver for linear concentrators, *Appl. Energ.*, 168 (2016) 303-313.
- [104] M. Abdelhamid, B. K. Widyolar, L. Jiang, R. Winston, E., Yablonovitch, G. Scranton, D. Cygan, H. Abbasi, and A. Kozlov, Novel double-stage high-concentrated solar hybrid photovoltaic/thermal (PV/T) collector with nonimaging optics and GaAs solar cells reflector, *Appl. Energ.*, 182 (2016) 68-79.
- [105] B. Widyolar, L. Jiang, M. Abdelhamid, and R. Winston, Design and modeling of a spectrum-splitting hybrid CSP-CPV parabolic trough using two-stage high concentration optics and dual junction InGaP/ GaAs solar cells, *Sol. Energ.*, 165 (2018) 75-84.
- [106] B. Widyolar, L. Jiang, and R. Winston, Spectral beam splitting in hybrid PV/T parabolic trough systems for power generation, *Appl. Energ.*, 209 (2018) 236-250.
- [107] L.A. Weinstein, K. McEnaney, E. Strobach, S. Yang, B. Bhatia, L. Zhao, Y. Huang, J. Loomis, F. Cao, S.V. Boriskina, Z. Ren, E. N. Wang, and G. Chen, A Hybrid Electric and Thermal Solar Receiver, *Joule*, 2 (2018) 962-975.
- [108] E. E. Perl, J. Simon, J. F. Geisz, M. L. Lee, D. J. Friedman, and M. A. Steiner, Measurements and Modeling of III–V Solar Cells at High Temperatures up to 400 °C, *IEEE J. Photovolt.*, 6 (2016) 1345-1352.
- [109] A. Luque and A. Marti, Limiting efficiency of coupled thermal and photovoltaic converters, *Sol. Energ. Mater. Sol. Cell.*, 58 (1999) 147-165.

- [110] R. France, Multijunction solar cells for high-temperature operation in hybrid CPV-CSP systems, Invited Oral Presentation at the 12th International Conference on Concentrator Photovoltaic Systems (CPV-12), Freiburg, Germany, 25–27 April 2016.
- [111] J.J. Wysocki and P. Rappaport, Effect of temperature on photovoltaic solar energy conversion, *J. Appl. Phys.*, 31 (1960) 571-578.
- [112] A. Agarwala, V.K. Tewary, S.K. Agarwal, and S.C. Jain, Temperature effects in silicon solar cells, *Solid State Electron.*, 23 (1980) 1021-1028.
- [113] A. Braun, E. A. Katz and J. M. Gordon, Basic aspects of the temperature coefficients of concentrator solar cell performance parameters, *Prog. Photovolt. Res. Appl.*, 21 (2013) 1087-1094.
- [114] A. Braun, B. Hirsch, A. Vossier, E.A. Katz, and J.M. Gordon, Temperature dynamics of multijunction concentrator solar cells up to ultra-high irradiance, *Prog. Photovolt. Res. Appl.*, 21 (2013) 202-208.
- [115] E.E. Perl, J. Simon, D.J. Friedman, N. Jain, P. Sharps, C. McPheevers, Y. Sun, Minjoo L. Lee, and M.A. Steiner, (Al)GaInP/GaAs Tandem Solar Cells for Power Conversion at Elevated Temperature and High Concentration, *IEEE J. Photovolt.*, 8 (2018) 640-645.
- [116] Y. Sun, J. Faucher, D. Jung, M. Vaisman, C. McPheevers, P. Sharps, E. Perl, J. Simon, M. Steiner, D. Friedman, and M. L. Lee, Thermal Stability of GaAs Solar cells for high temperature applications, In Proc. of the IEEE 43rd Photovoltaic Specialists Conf. (PVSC-43), (2016).
- [117] J. J. Williams, H. McFavilen, A.M. Fischer, D. Ding, S. Young, E. Vadiee, F.A. Ponce, C. Arena, C.B. Honsberg and S.M. Goodnick, Refractory $In_xGa_{1-x}N$ solar cells for high-temperature applications, *IEEE J. Photovolt.*, 7 (2017) 1646-1652.
- [118] A. Maros, S. Gangam, Y. Fang, J. Smith, D. Vasileska, S. Goodnick, M. I. Bertoni and C. B. Honsberg, High temperature characterization of GaAs single junction solar cells, In Proc. of the IEEE 42nd Photovoltaic Specialist Conference (PVSC-42), (2015).
- [119] H. Cotal and R. Sherif, Temperature Dependence of the IV Parameters from Triple Junction GaInP/InGaAs/Ge Concentrator Solar Cells, in Proc. of the IEEE 4th World Conference on Photovoltaic Energy Conversion, (2006), 845 –848.
- [120] G. S. Kinsey, P. Hebert, K. E. Barbour, D. D. Krut, H. L. Cotal, and R. A. Sherif, Concentrator multijunction solar cell characteristics under variable intensity and temperature, *Prog. Photovolt. Res. Appl.*, 16 (2008) 503-508.
- [121] G. Siefer and A. W. Bett, Analysis of temperature coefficients for III-V multijunction concentrator cells, *Prog. Photovolt: Res. Appl.*, 22 (2014) 515-524.
- [122] P. Singh, N.M. Ravindra, Temperature dependence of solar cell performance – an analysis, *Sol. Energ. Mater. Sol. Cell.*, 101 (2015) 36-45.
- [123] J.C.C. Fan, Theoretical temperature dependence of solar cell parameters, *Sol. Cell.*, 17 (1986) 309-315.
- [124] D.J. Friedman, M.A. Steiner, E.E. Perl, and J. Simon, Spectral and Concentration Sensitivity of Multijunction Solar Cells at High Temperature, National Renewable Energy Lab. (NREL), Golden, Colorado, US, Tech. Rep. NREL/CP-5J00-67787), June 2017.

- [125] X. Han, C. Xu, X. Ju, X. Du, and Y. Yang, Energy analysis of a hybrid solar concentrating photovoltaic/concentrating solar power (CPV/CSP) system, *Sci. Bull.*, 60 (2015) 460–469.
- [126] X. Han, G. Zhao, C. Xu, X. Ju, X. Du, and Y. Yang, Parametric analysis of a hybrid solar concentrating photovoltaic/concentrating solar power (CPV/CSP) system, *Appl. Energ.*, 189 (2017) 520–533.
- [127] C.K. Ho and B.D. Iverson, Review of high-temperature central receiver designs for concentrating solar power, *Renew. Sust. Energ. Rev.*, 29 (2014) 835-846.
- [128] Bloomberg NEF, New Energy Outlook 2018, 2018. [Online]. Available: <https://about.bnef.com/new-energy-outlook/>. [Accessed August 23, 2018].

Chapter III: Concentrated multi-junction solar cells

High PV performances can be achieved using solar concentration together with multi-junction solar cells, allowing an efficient conversion of the broad solar spectrum. To date, the solar-to-PV electricity efficiency record is achieved with a four-junction solar cell at a concentration of 508 suns [1], with an impressive value of 46%. To reach greater performances, higher concentration factors are required along with more mature cell architectures and better optimization of the semiconductor materials exploited. However, under high illumination levels, the cell is mostly limited by resistive losses arising from the finite electrical conductivity of the semiconductor materials and the electrical contacts. It was recently demonstrated that the extent to which the performances are affected by series resistances strongly depends on the semiconductor bandgap. As a consequence, and seeking highly efficient CPV systems, this chapter investigates, theoretically, how series resistances affect the performances of the concentrator solar cells and how this parameter alters the optimal bandgap combination for the different junctions in the stack.

I. Methodology and Assumptions

A. Objectives

As mentioned previously, resistive losses constitute a major limiting mechanism affecting the efficient operation of concentrator solar cells, in particular under high illumination levels. Resistive losses lead to a drop in the fill factor and, consequently, to the degradation of the conversion efficiency. The amplitude of resistive losses effect strongly depends on the semiconductor bandgap considered, the extent of these losses being stronger for low material bandgaps. As a consequence, accounting for series resistances in solar cells modifies the optimal bandgap combination leading to the highest achievable performances, especially at high concentration factors or for high values of the series resistance. Therefore these losses should be properly considered when designing concentrated single or multi-junction solar cells intended to operate under very high solar fluxes.

This chapter tries to answer whether it is possible to enhance the cell performances, under very high illumination levels and accounting for resistive losses, by carefully optimizing the bandgap combination of the different sub-cells of a multi-junction cell, to minimize the series resistance effect. To answer this question, we first study, by numerical modeling, how the series resistances affect the performances and the bandgap combination of multi-junction solar cells, considering concentration dependent and independent series resistances. Then, we evaluate how bandgap optimization mitigates the negative effect of the resistive losses on the cell electrical performances.

B. Methodology

1. Series Resistances

a) General considerations

The series resistance of a single-junction solar cell includes different components, as illustrated in Fig.III-1 below. Basically, the most important contributions for the series resistance of a PV cell include the front contact and grid resistances, the window, emitter, base and substrate resistances, and the back contact resistance. Tunnel junction resistances

are added in the case of multi-junction solar cells. The substrate resistances are usually small relative to the resistance of the other components [2].

The metal grid role is to collect electrons from the semiconductor and transfer them to the external circuit [3]. Its optimal design is found as a compromise between decreasing the losses associated with this grid, including the shadowing losses resulting from the portion of the cell area covered by metal and preventing light from reaching the cell, and the emitter and front contact resistances [4]. Its design is also based on the minimization of busbar and finger resistances. The emitter resistance is a function of the finger spacing in the front contact grid: its optimization implies decreasing the spacing between the fingers at the expense of the shadowing losses (due to the increase in the fingers number) [2]. On the other hand, the window layer allows an efficient collection of the photo-generated carriers while preventing their recombination. Finally the back contact closes the circuit and needs a suitable design only in the case of thin solar cells [5]. It should also be mentioned that the different components can be separated into vertical or lateral resistances depending on the current flow direction [6].

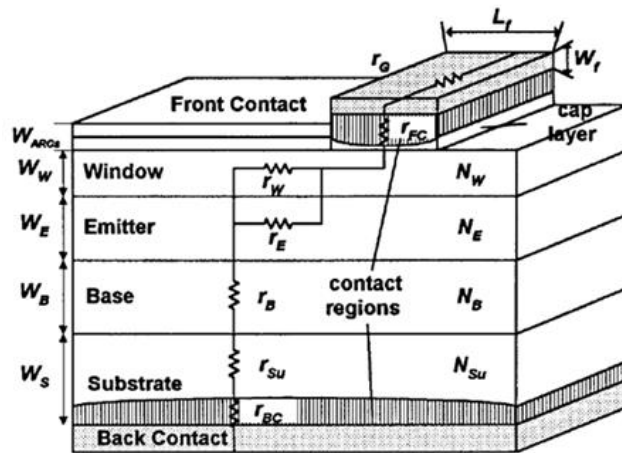


FIGURE III-1 The different components of the series resistance in a single-junction solar cell [6].

Series resistances engender resistive losses in concentrated solar cells that grow proportionally to the square of the generated current (which is a linear function of concentration). As a result, these limiting losses are colossal under high and ultra-high concentration factors, potentially leading to a dramatic decrease in the fill factor and the cell conversion efficiency. For instance, at an illumination level of 1000 suns, the current increases by a factor of 10^3 whereas the resistive losses intensifies by a factor of 10^6 [2,6-8].

To better understand the impact of this parameter on the cell's electrical performances, Vossier et al. [9] suggested an index, the SQ index, which is the ratio between the efficiency of a *real* solar cell (i.e. affected by non-ideal limiting mechanisms, such as series resistance losses, non-radiative recombination) and the SQ limit for that cell, providing an indication on how close these solar cells may approach their theoretical limit. For the low series resistance scenario ($R_s=0.001 \Omega \cdot \text{cm}^2$) and under 1 sun illumination, the SQ index is close to ideal, with a value approaching 1. This index decreases as the concentration factor

increases, at a much faster rate for lower bandgap than for higher bandgap semiconductors. As the series resistance increases, this index degrades very quickly with rising concentration in the case of low-bandgap materials, but remains closer to ideal over a broad range of illumination levels with high bandgap materials.

Series resistances are normally considered as independent of the illumination level to which the cells are submitted. However, a different scenario was considered by Algora et al. [6] or Paire et al. [10]: they observed that the overall series resistance decreases with increasing photo-generated current at high concentration levels. Algora et al. [6] investigated the dependence of the different series resistance components on the concentration ratio, up to 10000 suns, for GaAs solar cells. They explicitly studied the series resistance value as a function of different parameters such as the concentration ratio, the cell area, the thickness, etc... The optimal area leading to the highest cell performance was shown to stem from a compromise between resistive losses (which are a decreasing function of the cell area) and perimeter recombination, which tends to increase with decreasing cell dimensions. There is an overall strong incentive toward reducing the cell area, the effect of series resistance being more important than the effect of perimeter recombination (which may become critical for cell dimensions below $\sim 1\text{mm}^2$) [4,6]. In fact, decreasing the cell area reduces the series resistance up to a limiting value beyond which the area-independent component of the series resistance becomes dominant, suppressing the benefit of reducing the dimensions even more. This component varies from one cell technology to another [10-12]. The reduction in size also simplifies the cooling of the cell at high concentration levels [13]. The balance between the different series resistance contributions was also shown to vary depending on the illumination level to which the cell is exposed: in particular, one should differentiate a fixed resistance contribution including the back contact and the vertical component (base and substrate), and a concentration dependent part consisting of the emitter resistance, the front contact, and grid resistance. The concentration-dependent resistance decreases with increasing illumination levels, leading to a decrease in the overall series resistance value, up to a concentration level beyond which the illumination-independent resistance becomes dominant [6].

Operating at high illumination levels requires minimizing the resistive losses in concentrated solar cells in order to improve the cell electrical performances. A significant amount of research work aiming at handling these losses has been pursued in the last 15 years, toward ensuring efficient solar cell operation up to 1000 suns, with minimal losses and degradations [2,14].

Designing the front contact grid requires a compromise to be found between the emitter resistance decrease, the metal/semiconductor contact, the losses in the grid metallization itself and the shading losses linked to the front grid [5,10,15].

To lessen the semiconductor resistance, the emitter and window layers thicknesses are tailored [3].

The described strategies allow significant improvements in the ability of the cell to efficiently convert concentrated sunlight, with peak efficiency values currently occurring at several hundred or even one thousand of suns [15-17].

It was pointed out that series resistances affect the cells differently depending on the semiconductor bandgap, their effect being particularly strong for low bandgap materials as a result of the high photo-generated current. The optimal bandgap, or combination of bandgaps (in the case of MJ cell architecture), is commonly derived assuming that the cell operates in the radiative limit, and in the absence of any series resistance losses. One may question how accounting for series resistance effects would 1) affect the optimal combination of bandgaps leading to the highest solar to electricity conversion efficiency 2) improve the cell performance relative to conventionally designed solar cells. Here, we aim to explore the extent to which a series-resistance dependent bandgap optimization may affect the cell performances, up to illumination levels as high as 10000 suns.

b) Series Resistance Scenario

As mentioned before, it is usually assumed in the literature that the total series resistance is concentration independent [4]; however, some authors showed a strong dependency of the series resistance on the illumination level, the total series resistance value decreasing noticeably with increasing concentration factors [6]. This decrease is attributed to the enhanced conductivity in the cell with growing illumination levels, because of the increase in the excess carrier concentration.

In this chapter, both scenarios are considered and compared. We first assumed a lumped concentration-independent series resistance (assuming only the total series resistance value, which is the sum of its different components), with typical values of $0.01 \Omega \text{ cm}^2$. This value represents typical series resistance found for state-of-the-art concentrator triple and quadruple junction solar cells [18] (values ranging between 0.01 and $0.025 \Omega \text{ cm}^2$ are mentioned in the literature, depending on the cell design parameters [2]).

Then, a concentration-dependent resistance is considered based on the work described in [6]. It assumes that the lumped parameter is the sum of two resistance components at any concentration value: 1) the concentration-dependent component, a variable term including the emitter, the front contact, and the grid resistances, that changes as the concentration factor is varied, and 2) a fixed concentration-independent term consisting of the vertical resistances, the back contact, the tunnel diodes, etc... Usually, for III-V semiconductors used in concentrator solar cells, the fixed resistance component associated with the vertical flow of current is negligible compared to the variable contribution, up to almost 3000 suns. The values used for the concentration-dependent components are taken from [6] assuming a total resistance varying logarithmically between $0.46 \Omega \text{ cm}^2$ at one sun illumination and $0.15 \text{ m}\Omega \text{ cm}^2$ at 10000 suns. Additional $0.14 \text{ m}\Omega \text{ cm}^2$ tunnel junction resistances were added per junction to the concentration-independent term, when multi-junction cells are considered, to account for the presence of tunnel diodes between each sub-cell [19].

2. Description of the Algorithm

To study the effect of series resistances on the cell architecture, and to seek the optimal bandgap combination, an algorithm is elaborated using Matlab R2012a environment (Mathworks Inc, Natick, MA, USA). It is based on the resolution of the general *I-V* characteristic equation, accounting for series resistances (equation (I-9)), for a broad range of cell architectures, series resistance values and solar concentrations, assuming a diode ideality factor equal to 1.

TABLE III-1 Summary of the equations used in the program

$$I = I_{ph} - I_0 \left(e^{\frac{qV+IR_s}{nkT}} - 1 \right) \quad (\text{I-32})$$

$$I_0 = \frac{q}{k} \times \frac{15\sigma}{\pi^4} \times T^3 \times \int_u^{\infty} \frac{x^2}{e^x - 1} dx \quad (\text{I-12})$$

$$x = \frac{E}{kT}$$

$$u = \frac{E_g}{kT}$$

$$I_{ph} = X \times q \int_{E_g}^{\infty} EQE(E) \times f(E) dE \quad (\text{I-13})$$

$$f(E) = \frac{2\pi}{h^3 c^2} \frac{E^2}{\exp\left(\frac{E-\mu}{kT}\right) - 1} \quad (\text{I-14})$$

Iso-efficiency curves, which represent the efficiency with which solar energy is converted as a function of the bandgap of the different sub-cells constituting the stack, are then generated. They allow assessing the amplitude of the resistive losses, and determining the maximum theoretical conversion efficiency achievable, as well as the optimal bandgap combination used to achieve it, for every resistance/concentration considered. The red color represents high conversion efficiencies while bluish colors denote low performances values.

The two series resistance scenarios described earlier were considered. For the concentration-independent scenario, the series resistance value is varied between $0.01 \Omega \text{ cm}^2$, a state-of-the-art value, and $0.1 \Omega \text{ cm}^2$, a worst-case scenario value considered to better grasp the extent to which very-high resistive losses may affect the optimal cell architecture.

A second set of calculations considers distributed series resistances. A lumped parameter assumes a single series resistance value evenly distributed between the different junctions in the stack. On the other hand, a distributed resistance is computed for each individual junction, considering the different components of the series resistance present in

each junction separately, as well as the tunnel resistances to account for the electrical and optical interconnection between each junction.

The EQE is taken as a step function with an ideal absorption of 1 for photons having energies higher or equal to the bandgap, and no absorption for low energy photons. The calculations were realized assuming AM1.5D spectrum.

In the case of multi-junction solar cells, the *I-V* equation is computed for each individual sub-cell. Due to the current constraint condition between the different junctions in the stack, the current generated by the cell is governed by the lowest current density provided by each individual sub-cell. The limiting current is then applied to the other junctions, and the voltages associated are computed accordingly. The total voltage of the solar cell is then simply calculated as the sum of the voltages of each sub-cell.

The bandgap optimization was first realized using iso-efficiency curves plotted as a function of the bandgap of two of the junctions, while fixing the others to values found in the literature.

For a triple-junction cell, iso-efficiency curves are plotted as a function of the top and middle junctions, while fixing the bottom junction to 0.7eV (a typical value for conventional triple-junction solar cells involving a Ge low-bandgap junction). As the number of junctions increases, iso-efficiency curves do not allow to properly determine the optimal combination of electronic energy gaps, since the number of *fixed* bandgap junctions values must increase too: iso-efficiency curves only allow exploring the optimal combination of two electronic energy gaps, the other being constrained. To deal with cells comprising three or more junctions, the bandgap combination is derived using a genetic algorithm, a built-in Matlab program used for optimization. It directly provides the best combination of electronic energy gaps leading to the highest efficiency, within minutes or a couple of hours (compared to weeks for our basic algorithm). The genetic algorithm is implemented in Matlab R2016b environment (Mathworks Inc, Natick, MA, USA).

3. Genetic Algorithm

Genetic algorithm is an optimization method inspired by Darwin's evolution theory, or natural selection, which was proposed in the 1970s by Holland [20]. It is a powerful optimization tool capable of searching through large sets of data and is based on the idea that a character allowing an individual to survive long enough to reproduce may be easily passed on to the next generation [21,22].

It relies on a set of initial solutions, in our case the electronic energy gaps of the cell (with a number of gaps depending on the cell architecture investigated), as an initial population [23], usually randomly selected. Each solution is evaluated based on a criterion, which in our case is the objective function $1 - \eta$, where η is the photovoltaic conversion efficiency, which should be minimized. A *fitness* score is then attributed to each individual, based on its ability to efficiently solve the objective function, to evaluate how well it can handle that particular problem [24].

From this initial set of individuals, a new population is formed based on various genetic operations, repeated until the required number of individuals in the new population is reached:

- 1) *Selection*: this operation selects the best individuals based on their score, to be part of the new population. The selected data are called “*parents*”. It is a way to select the individuals that can survive and transmit their traits to the next generation, again, based on their fitness value. It allows more copies of the best individuals with higher scores, hence giving a higher probability of survival for those individuals. If only selection is used, the new generation is an exact copy of the best parents.
- 2) *Cross-over*: this operation combines traits from the two selected parents to form a new solution. The traits are randomly exchanged between the parents, generating new individuals that are completely different from the previous ones. It mixes the parents traits in favor of traits with higher scores, to make the population evolve toward the best possible solution.
- 3) *Mutation*: this operation applies random changes to the parent’s solution to create new sets of individuals, to maintain diversity among the population.

In most cases, the best two individuals are selected from a population. Various operations are done on these two selected individuals, many repeated random mutations or cross-over, or even exact replicate, to complete the new generated set, keeping the best individuals and removing the others. Sometimes the new population is a complete replacement of the previous generation, with all the members created by recombination (mutation and cross-over) and some other solutions only have 1 new individual in the set at each generation, the least fit member being replaced. The generated population replaces the previous one and, for every new population, the fitness is evaluated for each individual.

The genetic algorithm goes through different generations until one of the stop criteria is met. The stop criterion can be: 1) the maximal number of iterations being reached, 2) a generation of solutions that fully satisfies a set of constraints, the fitness having reached a predefined value, or 3) a convergence of the best-fitness solution with no more improvement, the solution converging when the new population does not differ anymore from the previous ones [25].

In our case, the optimal set of bandgap is defined as the outcome of successive generations selected for their ability to minimize the objective function, hence maximizing the cell conversion efficiency for any particular set of series resistance and concentration factor.

II. Results

A. Effect of concentration on real solar cells

Figure III-2 represents iso-efficiency curves for triple-junction solar cells characterized by a series resistance of $0.01 \Omega \text{ cm}^2$, evenly distributed between the junctions, as a function of the bandgaps of the top and middle junctions. It assumes a 0.7eV gap for the bottom sub-cell, corresponding to a Ge sub-cell, and different concentration factors, namely

(a) 1, (b) 1000, (c) 5000 and (d) 10000 suns. Figure III-3 represents the iso-efficiency curves for the same concentration factors, but with a series resistance of $0.05 \Omega \text{ cm}^2$.

For both series resistance values, increasing the concentration level leads to increased conversion efficiency, up to an illumination level beyond which the performances are degraded due to resistive losses. The illumination level also affects the optimal bandgap combination: up to 1000 suns, the variations are relatively modest with no or little modification of the bandgap optimal combination. As the intensities increase, one can notice significant modifications in the optimal bandgap combination, which tends to move toward higher values. The amplitude of the shift is more pronounced as the series resistance value increases. These results confirm the need to tailor the different bandgaps in the stack to ensure reduced resistive losses.

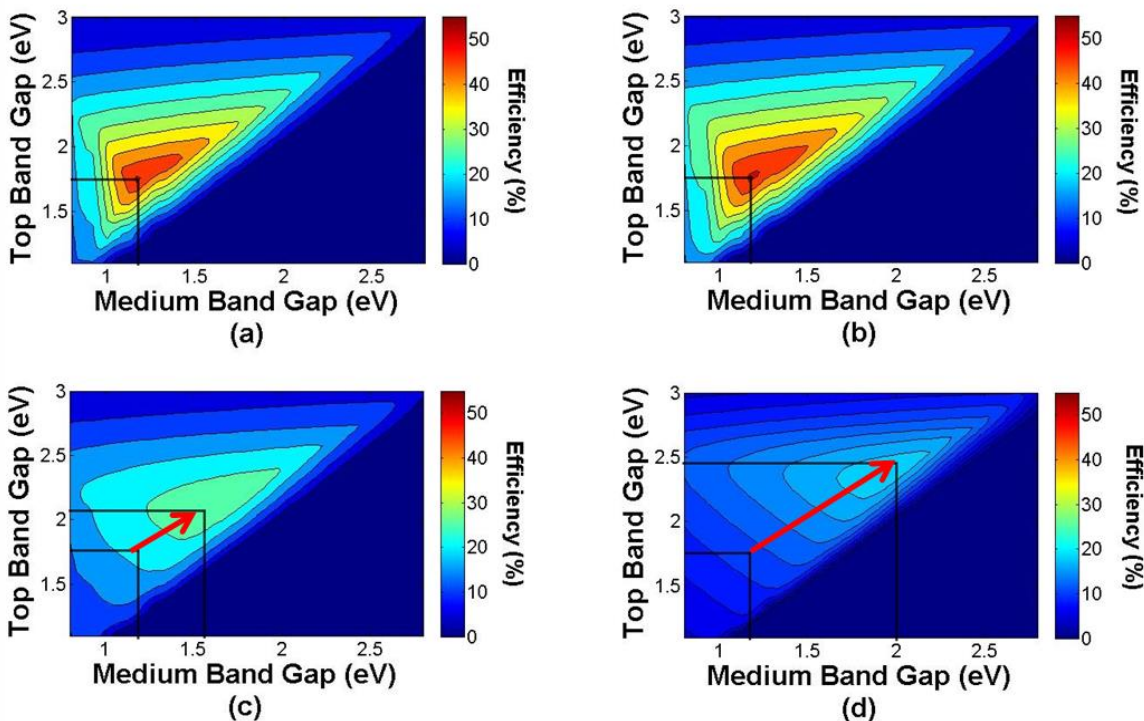


FIGURE III-2 Iso-efficiency curves for a triple-junction solar cell with a total series resistance of $0.01 \Omega \text{ cm}^2$, assuming a 0.7eV bottom cell bandgap under concentration levels of (a) 1 sun, (b) 1000suns, (c) 5000 suns and (d) 10000 suns.

In the concentration-dependent series resistance scenario, the trends are quite different. In fact, as the series resistance decreases with increasing concentration, the resistive losses remain negligible so the advantages of bandgap tailoring remain insignificant.

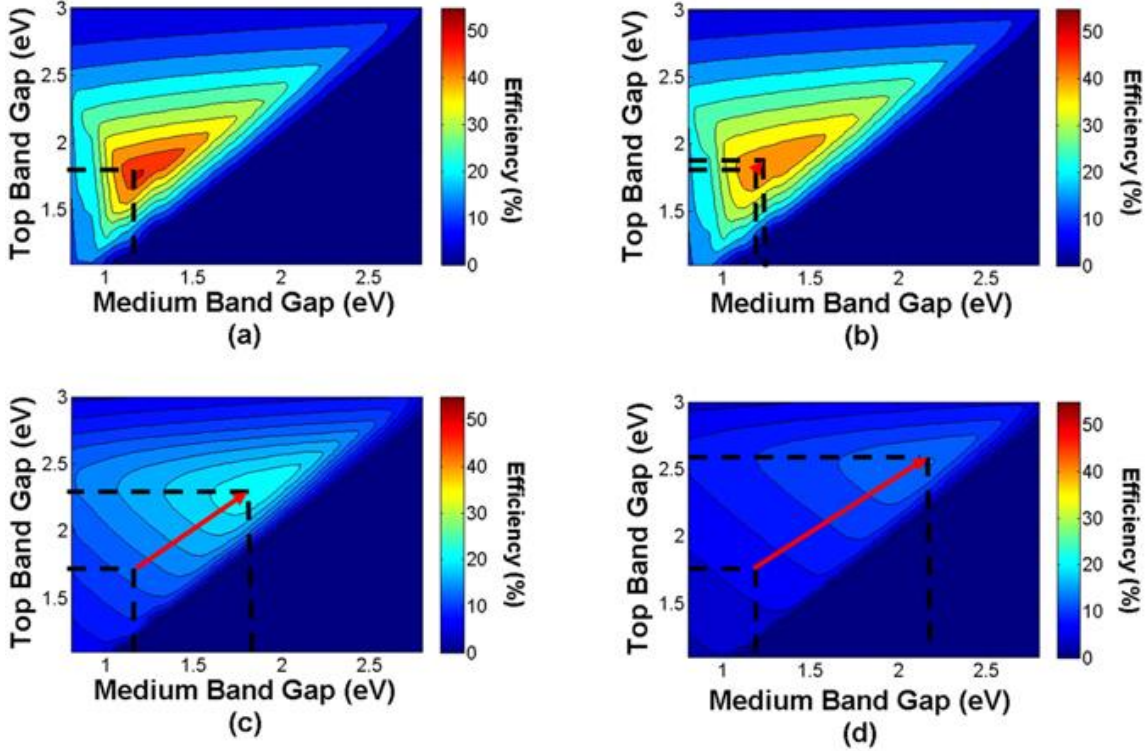


FIGURE III-3 Iso-efficiency curves for a triple-junction solar cell with a total series resistance of $0.05 \Omega \text{ cm}^2$, assuming a 0.7 eV bottom cell bandgap under concentration levels of (a) 1 sun, (b) 1000 suns, (c) 5000 suns and (d) 10000 suns.

B. Effect of series resistances

Under 1-sun illumination, series resistances do not affect the conversion efficiencies nor the optimal combination of bandgaps, even for high series resistance values, due to the modest current flowing through the cell. The observations change as sunlight concentration increases.

Figure III-4 represents iso efficiency curves for triple-junction solar cells, assuming a concentration factor of 1000 suns, as a function of the bandgaps of the top and middle junctions, while fixing the bottom junction to 0.7 eV. It considers different series resistance values, evenly distributed between the junctions, i.e., a) ideal cell, $R_s=0 \Omega \text{ cm}^2$, (b) $R_s= 0.01 \Omega \text{ cm}^2$, (c) $R_s= 0.05 \Omega \text{ cm}^2$, and (d) $R_s= 0.1 \Omega \text{ cm}^2$. Figure III-5 illustrates iso-efficiency curves for a concentration ratio of 2500 suns and series resistances values of (a) $0.01 \Omega \text{ cm}^2$ and (b) $0.05 \Omega \text{ cm}^2$. In these cases, the series resistances considered are concentration-independent.

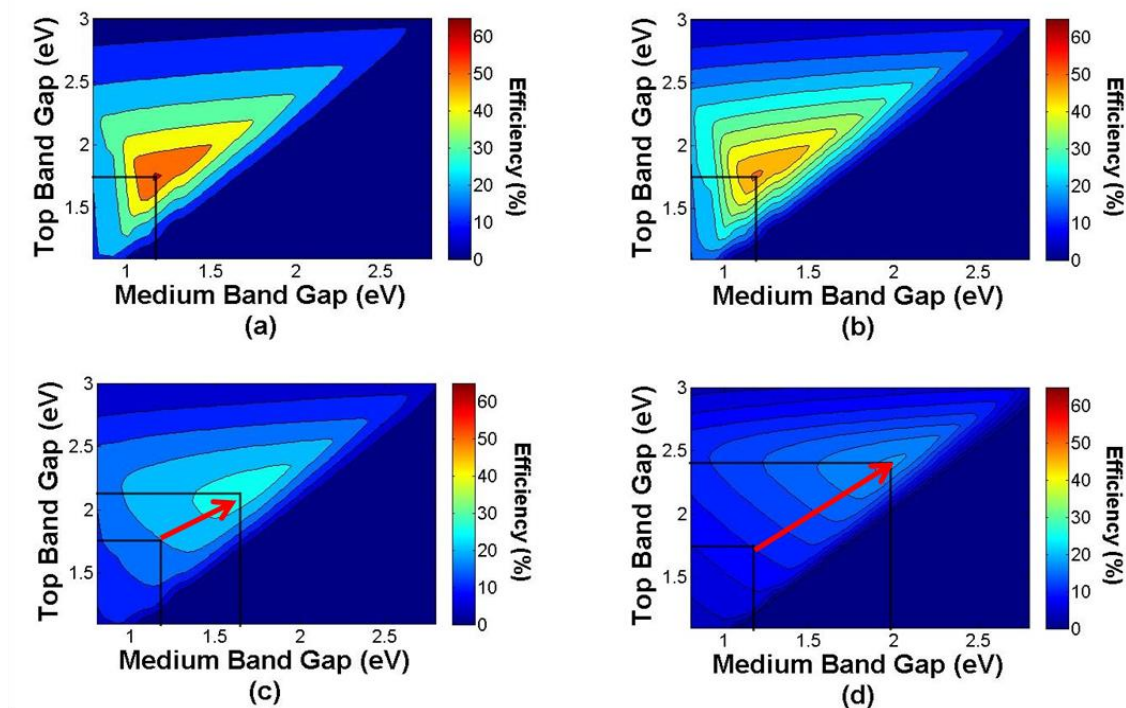


FIGURE III-4 Iso-efficiency curves for a triple-junction solar cell under a concentration of 1000 suns, with different values of the total series resistance (a) $0 \Omega \text{ cm}^2$, (b) $0.01 \Omega \text{ cm}^2$, (c) $0.05 \Omega \text{ cm}^2$ and (d) $0.1 \Omega \text{ cm}^2$.

Comparing the 4 different graphs illustrated in Fig.III-4 allows concluding that increasing the series resistance value decreases the conversion efficiency, compared to the ideal case, and this decrease is more pronounced as the series resistance value increases. It also shows that accounting for the resistive losses causes a shift toward higher bandgap values for the different sub-cells of the multi-junction stack. This shift is more pronounced as the series resistance value increases.

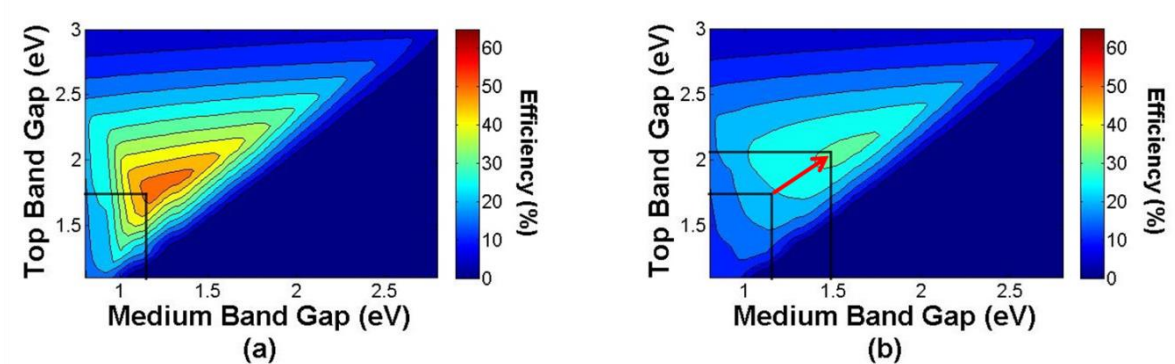


FIGURE III-5 Iso-efficiency curves for a triple-junction solar cell under a concentration of 2500 suns, with different values of the total series resistance (a) $0.01 \Omega \text{ cm}^2$ and (b) $0.05 \Omega \text{ cm}^2$.

Increasing the concentration ratio enhances the cell performances for relatively low series resistance, but degrades the efficiency as the resistive losses become important, as can be noted from Fig.III-5. It also shifts the optimal bandgap combination toward higher values

with increasing resistances. For example, the optimal bandgap combination of a cell having a $0.01 \Omega \text{ cm}^2$ lumped resistance assuming a sunlight illumination of 2500 suns is found to be 1.75/1.18/0.7 eV. In the meantime, a cell characterized by a $0.05 \Omega \text{ cm}^2$ series resistance value shows a strong displacement in its optimal bandgap combination, toward a combination of 2.07/1.58/0.7eV (the bottom junction being fixed).

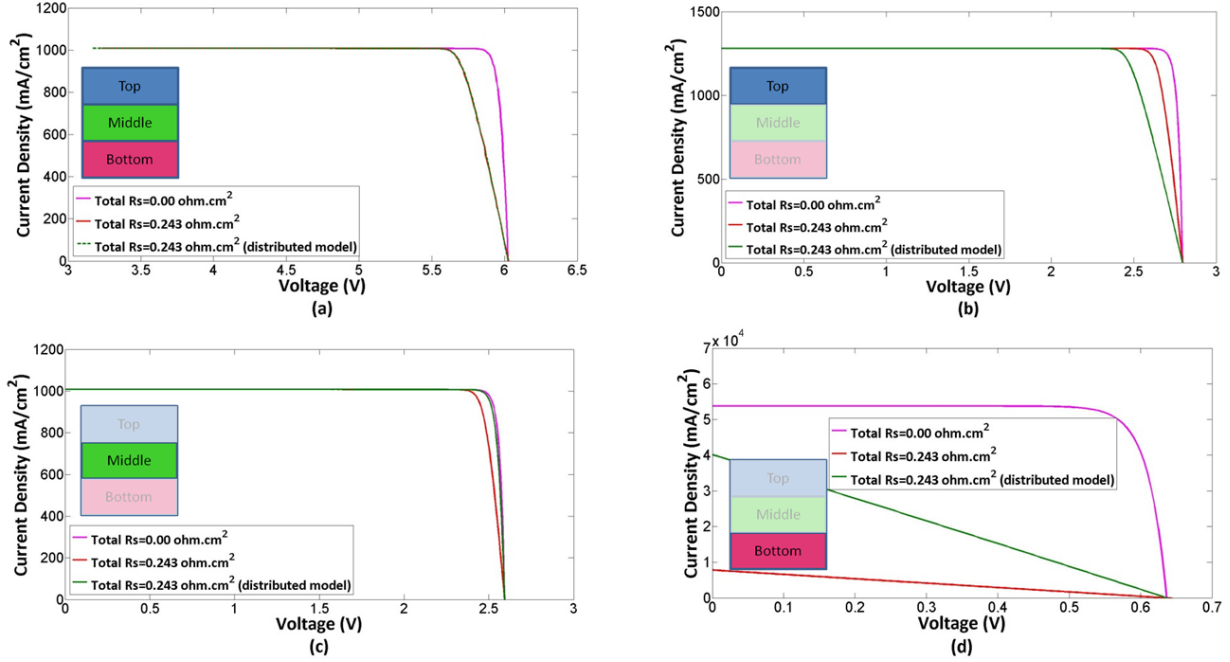


FIGURE III-6 I - V curves for triple-junction cells (a) as well as for each junction alone: top junction (b), middle junction (c) and bottom junction (d), for ideal cases, evenly distributed resistance and non-evenly distributed resistance assuming a concentration factor of 1000 suns.

The conclusions are different in the case of the illumination-dependent series resistances. The observations mentioned earlier still hold: the increasing current resulting from higher concentration ratios does not lead to colossal resistive losses due to the decrease in the series resistance, which reduces the penalties of operating under high concentration factors. As a consequence, the decrease in the maximal conversion efficiency and the variation in the optimal bandgap combination seem to be negligible.

The nature of the series resistance scenario (lumped or distributed) does not alter the overall conclusions since the global series resistance (as well as the resistive losses) is identical in both cases. However, noticeable differences are observed while considering each junction alone. Figure III-6 illustrates the I - V curves of a triple-junction solar cell (Fig.III-6(a)) as well as of the individual top, middle and bottom junctions (Fig.III-6(b), (c) and (d) respectively). It assumes a concentrating ratio of 1000 suns, and different series resistance scenarios. The pink curve represents an ideal solar cell with no series resistance, the red curve a lumped series resistance with a total value of $0.243 \Omega \text{ cm}^2$ and the green curve a distributed resistance computed for each junction based on the distributed model, with a same global value of $0.243 \Omega \text{ cm}^2$. The cell I - V curves are identical for lumped and distributed series resistance, and show a lower fill factor compared to the ideal case due to resistive losses.

Thus, the global conversion efficiency is independent of the method used to estimate the series resistance value. This result is not surprising due to the series connections between the different sub-cells leading to a total resistance equivalent to the sum of the resistances in each individual junction.

TABLE III-2 Optimal bandgap combination for a 3J solar cell using genetic algorithm, for illumination levels ranging between 1 and 10000 suns and for two series resistance values 0.01 and 0.05 $\Omega \text{ cm}^2$.

Rs ($\Omega \text{ cm}^2$)	Concentration (suns)	Optimal Bandgap $E_{g1}/E_{g2}/E_{g3}$ (eV)
0 (Ref)	1	1.75/1.18/0.7
0.01	1	1.75/1.18/0.7
	1000	1.75/1.18/0.7
	2500	1.75/1.18/0.7
	5000	1.88/1.37/0.95
	10000	2.06/1.55/1.17
0.05	1	1.75/1.18/0.7
	1000	1.94/1.39/0.95
	2500	2.18/1.69/1.34
	5000	2.31/1.9/1.59
	10000	2.50/2.12/1.85

On the other hand, the individual *I-V* characteristics of each sub-cell vary based on the method used to estimate the series resistance in each junction. The resistance of the top junction accounts for the front contact resistance, the fingers, or the bus bar, which are usually significant. So, while comparing the *I-V* curves of cells with resistances being evenly distributed or not, one can notice that the second case leads to a higher resistance in the top junction which degrades the *I-V* curve, and gives rise to lower fill factors. The two lower junctions present the opposite behavior: the resistance of the lower junctions being lower in the case of the non-evenly distributed resistances, the corresponding *I-V* curves show higher fill factors, and therefore better conversion efficiencies, compared to the evenly distributed case. The use of the distributed model is thus necessary to understand precisely the *individual* characteristics of each junction constituting the stack.

Table III-2 lists the optimal bandgap combination for different triple-junction solar cells having series resistance values of $0.01 \Omega \text{ cm}^2$ (low-case scenario, based on the state-of-the-art solar cell) and $0.05 \Omega \text{ cm}^2$ (high-case scenario considered for comparison, to better grasp the effect of the resistive losses), and for concentration factors varying between 1 and 10000 suns.

The series resistances considered are illumination-independent. The zero series resistance represents the ideal cell and is mentioned here as a reference case with the optimal bandgap combination being equal to 1.75/1.18/0.7 for an ideal triple-junction cell under 1 sun illumination [26].

For the low series resistance scenario, the optimal combination remains unchanged up to 2500 suns while it is constant up to 1000 suns for the high-resistance scenario. Beyond these concentrations, the optimal bandgap combination appears to change noticeably and the alteration is even stronger as the illumination intensities become higher. The extent to which the bandgap is modified depends on the value of both the series resistance and the concentration level to which the cell is submitted. In the most extreme concentrations, especially for significant series resistance values, the bandgap combination does not include any low bandgap material due to the high resistive losses associated with low E_g semiconductors. The optimization in this case leads to a combination of medium to large bandgap to compensate for the resistive losses, stemming in cells showing larger voltages, at the expense of the current (which is indeed minimized toward lowering the amplitude of series resistance losses).

C. Discussion

Ideally, sunlight illumination enhances the cell performances. Practically, when accounting for series resistance, the PV conversion efficiency is improved with increasing illumination levels up to a limiting value beyond which the overall performance degrades, depending on the value of the series resistance. In fact, the open-circuit voltage increase with rising concentration is mainly responsible for increasing the conversion efficiency, but the detrimental effect of the resistive losses tends to amplify as the illumination level to which the cell is exposed increases, progressively counterbalancing the benefits of sunlight concentration. Besides decreasing the conversion efficiency, high series resistance values lead to a shift in the optimal bandgap combination toward higher values, mainly under high solar illuminations. These two conclusions are justified in this section.

The main electrical parameters, i.e. FF , V_{oc} , J_{sc} , and η , are compared for various series resistances and concentration factors, for both *non-optimized* and *optimized* bandgap combination. *Non-optimized* cells refer to cells whose bandgaps have been designed assuming no resistance losses and 1 sun illumination: 1.75/1.18/0.7eV. Table III-3 lists the main electrical parameters of the non-optimized cells, together with the cells optimized assuming series resistance of 0.01 and 0.05 $\Omega \text{ cm}^2$ and for illumination levels of 1000, 2500, 5000 and 10000 suns. The ideal cell with no series resistance is indicated as a reference case.

From table III-3, one can observe a significant enhancement in the optimized cell performances compared to the non-optimized one, due to the increase in V_{oc} and FF as the bandgaps shift toward higher values. The gain in FF , V_{oc} and η is even more obvious as the concentration increases or as the series resistance value becomes higher.

TABLE III-3 Main electrical parameters of a triple-junction solar cell with non-optimized and optimized bandgap combination.

Rs ($\Omega \text{ cm}^2$)	X (suns)	Non-optimized cell				Optimized cell			
		FF	V_{oc} (V)	J_{sc} (mA/cm 2)	η (%)	FF	V_{oc} (V)	J_{sc} (mA/cm 2)	η^* (%)
0 (Ref)	1	-	-	-	-	0.89	2.84	18.18	51.07
0.01	1000	0.86	3.37	18.18×10^3	58.18	0.86	3.37	18.18×10^3	58.18 (+0%)
	2500	0.78	3.44	4.54×10^4	54.21	0.78	3.44	4.54×10^4	54.21 (+0%)
	5000	0.66	3.49	9.09×10^4	46.54	0.74	4.03	7.5×10^4	49.6 (+3.06%)
	10000	0.45	3.55	18.18×10^4	32.04	0.71	4.63	1.12×10^5	40.54 (+8.5%)
0.05	1000	0.65	3.37	18.18×10^3	44.15	0.77	3.98	1.36×10^4	46.31 (+2.16%)
	2500	0.36	3.44	4.54×10^4	24.87	0.72	4.91	2.28×10^4	35.91 (+11.04%)
	5000	0.25	3.49	6.79×10^4	13.29	0.63	5.52	3.59×10^4	27.54 (+14.25%)
	10000	0.25	3.55	7.03×10^4	6.91	0.57	6.2	4.90×10^4	19.10 (+12.19%)

*In parentheses: the relative efficiency gain compared to the non-optimized case.

Hence, proper bandgap tailoring is crucial as the concentration increases and especially for cells with high series resistance values.

Figure III-7 portrays the ratio between the optimized and non-optimized bandgap values for each sub-cell in a triple-junction solar cell, as well as the corresponding optimized and non-optimized efficiencies as a function of the series resistance, assuming a concentration factor of 5000 suns. The red line corresponds to the top bandgap ratio, the green and blue lines to the middle and bottom ones respectively, while the black curve denotes the optimized efficiency and the pink the non-optimized one. The shift in the optimal bandgap, as well as the increase in the optimized conversion efficiency, compared to the non-optimized situation, grow progressively as the series resistance value intensifies. For low series resistance scenarios, up to $0.01 \Omega \text{ cm}^2$, the benefit for bandgap optimization remains modest with a relative efficiency gain of almost 3% whereas beyond this resistance value, the relative gain strongly rises to reach almost 15% for cells having a series resistance value of $0.05 \Omega \text{ cm}^2$.

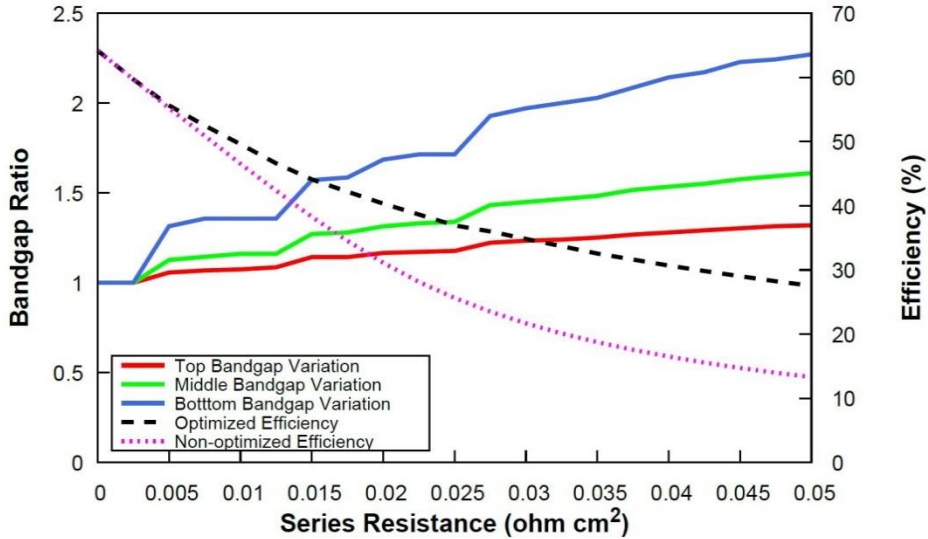


FIGURE III-7 Ratio between the optimized and non-optimized bandgaps of each sub-cell for a triple-junction cell, and their corresponding efficiencies, as a function of the series resistance value, assuming a concentration ratio of 5000 suns.

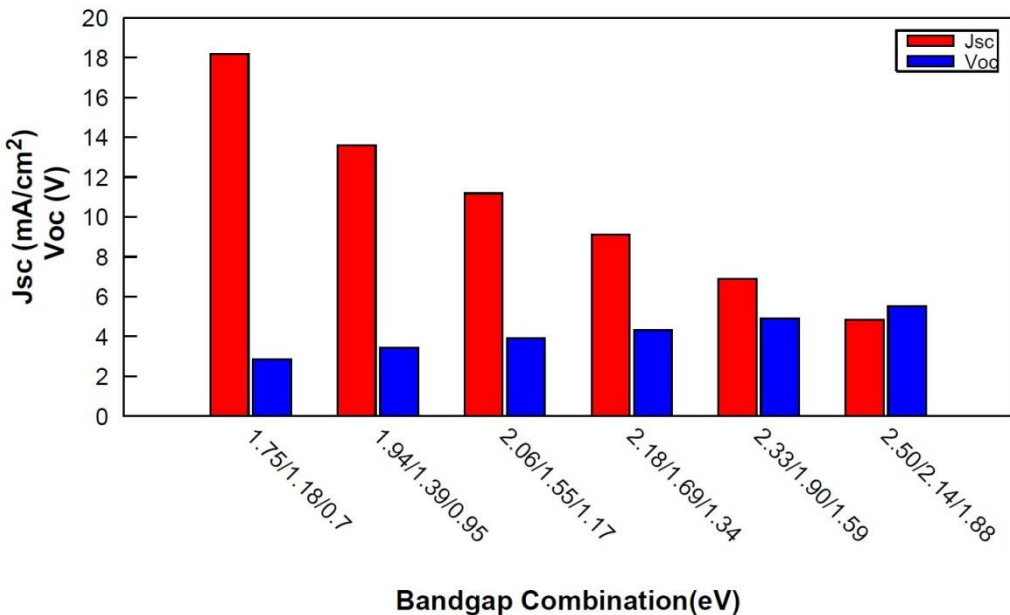


FIGURE III-8 J_{sc} and V_{oc} computed assuming 1 sun illumination for triple-junction solar cells for different combinations of bandgaps taken from Table III-2.

Figure III-8 represents the short-circuit current density as well as the open circuit voltage computed under 1 sun illumination, for different bandgap combination of triple-junction solar cells taken from Table III-2. As the values of the different bandgaps in the stack increase toward higher electronic energy gaps, one can notice a considerable drop in the short-circuit current (since the number of absorbed photons decreases) along with an increase in the open-circuit voltage. Under high concentration levels, the balance between both parameters is drastically altered compared to the reference case (with no series resistance) leading to a less negative effect of the resistive losses.

Figure III-9 illustrates the I - V curve of a triple-junction solar cell having a fixed total series resistance of $0.05 \Omega \text{ cm}^2$ assuming a sunlight illumination of 5000 suns, both for a non-optimized cell, having a bandgap combination of $1.75/1.18/0.7\text{eV}$ (a) and for an optimized cell with the bandgap combination taken from Table III-2 (b). Each graph includes several curves exhibiting the global electrical performance of the multi-junction solar cell (red curve) and the electrical performance of each individual sub-cell in the stack (green, blue and black for the top, middle and bottom junctions respectively). From this figure we can clearly see how tailoring the bandgap combination increases the fill factor (which rises from 0.25 to 0.64) and the maximum output power (which grows from 60 to 123 W/mm^2) engendering a significant increase in conversion efficiency. One can notice that the lowest current doesn't drive the current of the multi-junction cell in figure III-9 (a). A similar case was described by Braun et.al [27], and the origin of this counterintuitive behavior was attributed to the reverse bias operation of one of the subcell in the stack: in this particular case, the overall short-circuit current of the MJ cell is not limited by the sub-cell generating the smallest current.

Optimizing the bandgap combination can thus alleviate the effect of resistive losses on the cell performances at high illumination levels. To better understand the advantages of this strategy, the efficiency is plotted as a function of the concentration (varying between 1 and 10000 suns) for a set of triple-junction solar cells having series resistance values of $0.01 \Omega \text{ cm}^2$ (Fig III-10 (a)) and $0.05 \Omega \text{ cm}^2$ (Fig.III-11 (a)), with optimized bandgap combination.

To better grasp the benefit of bandgap optimization, the relative efficiency variation is also illustrated for both resistance scenarios. This variation is computed as the difference between the conversion efficiencies of the optimized cell and the ideal cell at 1 sun illumination, relative to the ideal cell efficiency (Fig.III-10 (b) and Fig.III-11(b)).

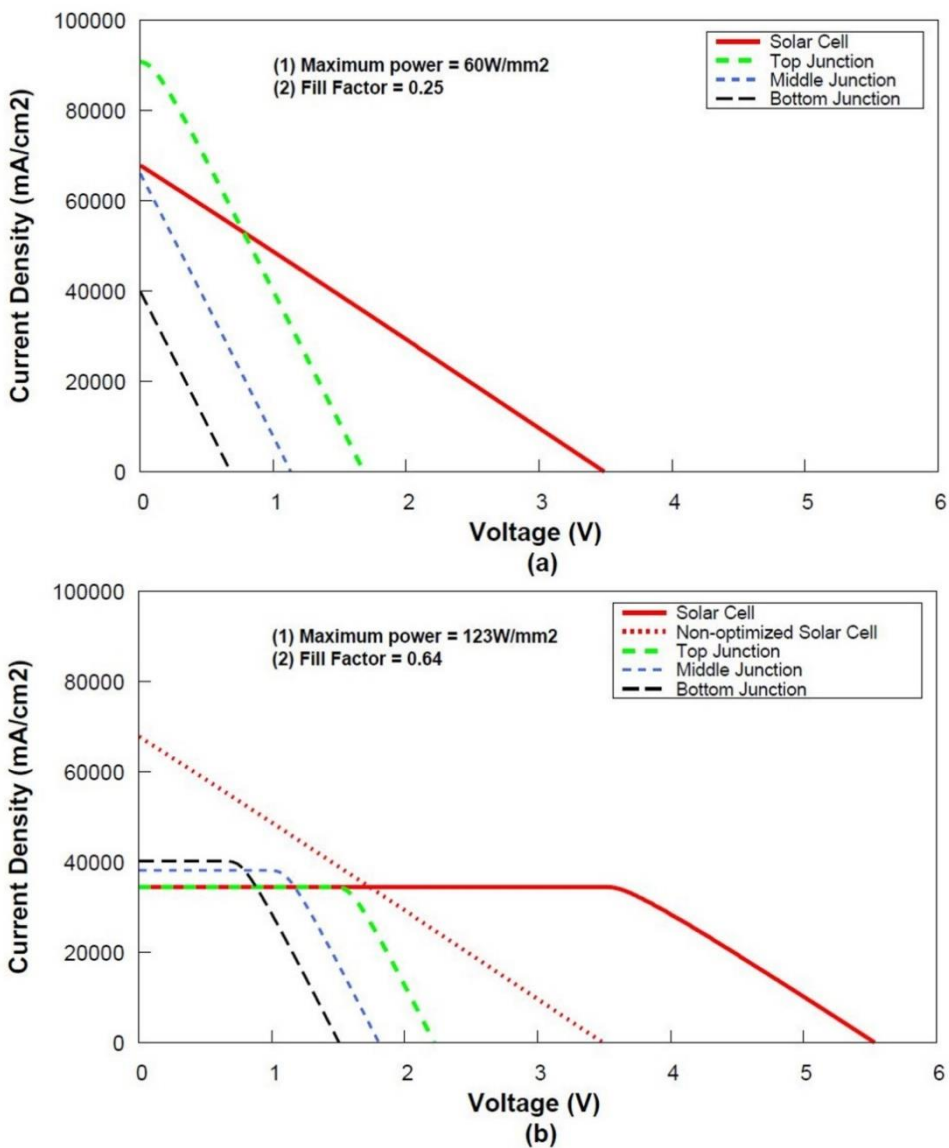
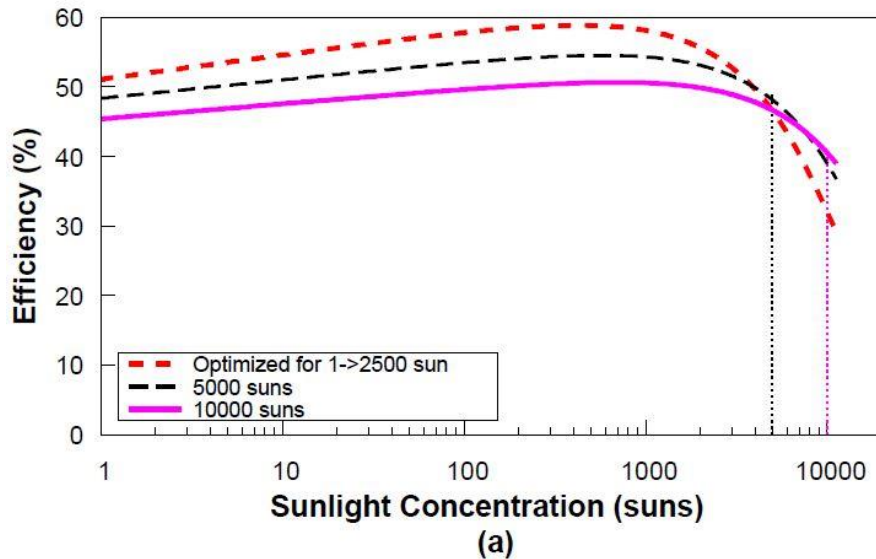


FIGURE III-9 I-V curve of a triple-junction solar cells having a total series resistance of $0.05 \Omega \text{ cm}^2$ assuming an illumination level of 5000 suns for non-optimized (a) and optimized bandgap combination (b).

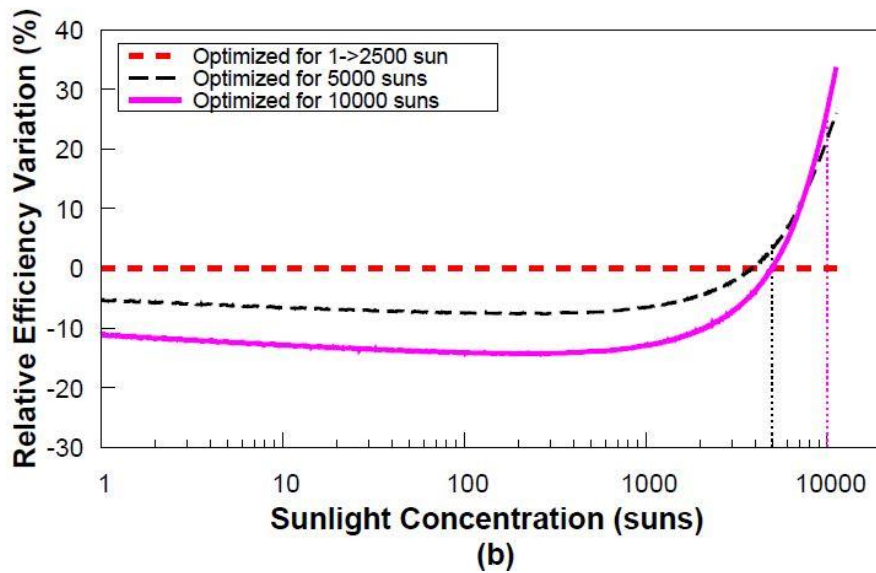
One can distinguish two separate zones in the relative efficiency variations:

- 1) A negative region, corresponding to the zone where bandgap tailoring does not lead to any efficiency enhancement.
- 2) A positive region, characterizing the range of illumination levels for which bandgap optimization triggers conversion efficiency improvements.

In all cases, the red curve represents the “non-optimized” curve (for a concentration of 1 sun and a bandgap combination of 1.75/1.18/0.7eV) whereas the other curves denote optimized solar cells for different sets of concentrations and series resistance values.



(a)



(b)

FIGURE III-10 Conversion efficiency (a) and relative efficiency variation (b) as a function of the concentration factors for a triple-junction solar cell having a fixed series resistance value of $0.01 \Omega \text{ cm}^2$.

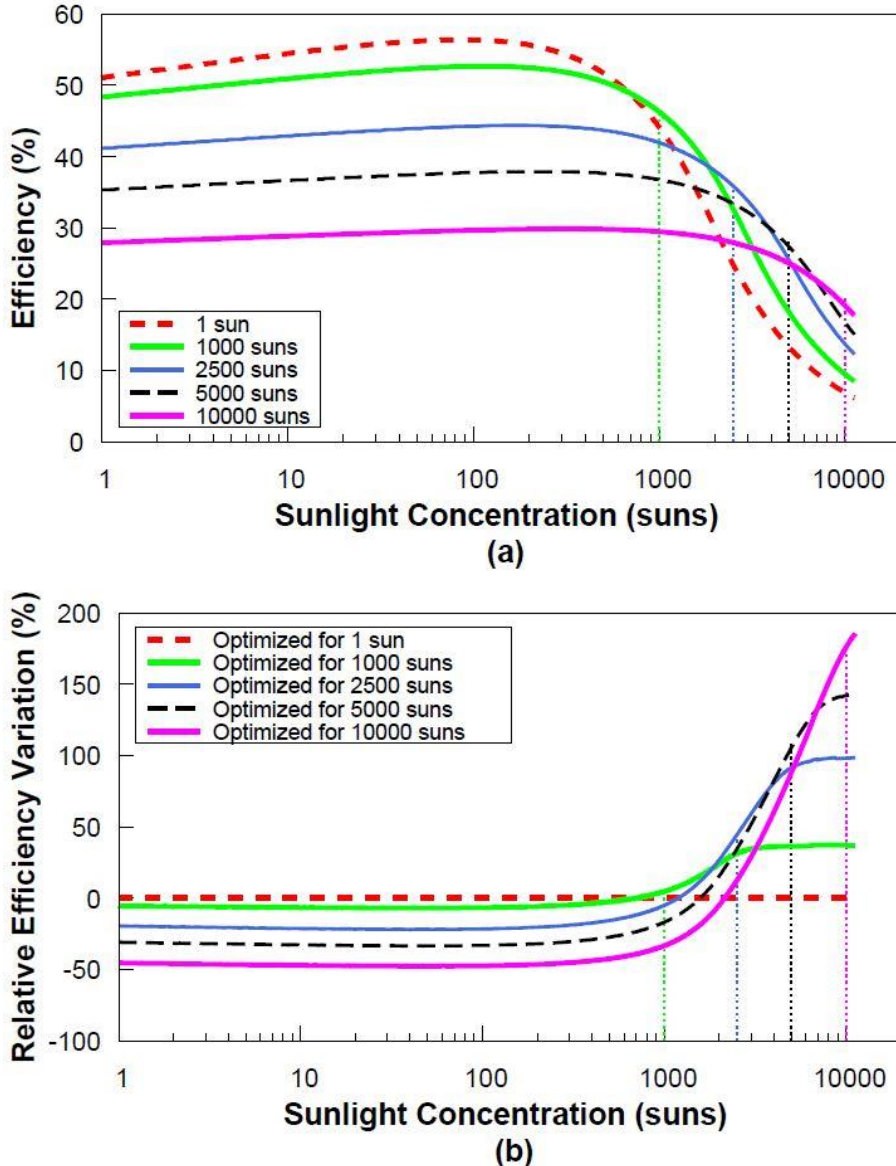


FIGURE III-11 Conversion efficiency (a) and relative efficiency variation (b) as a function of the concentration factors for a triple-junction solar cell having a fixed series resistance value of $0.05 \Omega \text{ cm}^2$.

For the low series resistance scenario (Fig.III-10(a)), the curves plotted for solar cells assuming a concentration level between 1 and 2500 suns are identical, as a consequence of the insignificant resistive losses that do not affect the cell efficiency nor the optimal bandgap combination. Optimizing the cells at higher concentration levels leads to the emergence of a range of illumination levels where the solar cells outperform conventionally designed solar cells: the optimized-cell typically shows lower efficiency (relative to conventionally designed cells) under illumination levels smaller than the optimization concentration. However, there is a noticeable benefit associated with optimization if the cell is exposed to illumination levels approaching or exceeding the target illumination level relative to which the cell is designed. The efficiency gap between optimized and non-optimized cells appears to increase significantly as the illumination level to which the cell is exposed rises, constituting a strong incentive toward bandgap optimization of PV cells for ultra-high sunlight concentrations.

Fig.III-10 (b) illustrates the relative efficiency variation as a function of the illumination level. For a low series resistance value, the gain in efficiency due to bandgap fine tuning is relatively modest. For a cell optimized to operate at 5000 suns, for example, the performance enhancement starts to be observed at an illumination level of 3700 suns, relative to the reference case at a concentration of 1 sun, with a gain reaching ~4% at 5000 suns. For cells optimized at an illumination level of 10000 suns, the efficiency improvement start to be noticed at around 5000 suns, with higher relative gain in efficiency reaching around ~27% relative to the reference case.

For the high resistance scenario, assuming a value of $0.05 \Omega \text{ cm}^2$, (Fig.III-11) the gain in efficiency is higher: the benefit for a good cell architecture design is modest for an illumination level of 1000 suns (with an enhancement of almost 5% at the optimized concentration level) even if the relative gains appear as soon as 700 suns. The efficiency improvement seems to be much more significant as the concentration level increases. For instance, the efficiency gain for a cell optimized at 2500 suns appears at an illumination level of 1200 suns and reaches an intensification of almost ~45% at 2500 suns. For the 5000 suns-optimized cells, the enhancement appears around 1500 suns with a boost of ~105% at the optimized illumination, whereas for the 10000 suns-optimized cells, the gain appears at around 2000 suns, reaching ~175% relative amplification at 10000 suns. In this case also, the maximum peak concentration is shifted toward higher value and the improvement in the efficiency, compared to the one-sun case, occurs after the peak illumination.

The results were mostly presented for triple-junction cells, even if cells involving a higher number of sub-cells in the stack were studied (up to 6 junctions). For a larger number of junctions, the conclusions remain unchanged. Increasing the number of sub-cells in a MJ stack may lead to increased series resistance (principally because of the presence of additional tunnel junction between each sub-cell), however because of the reduced current associated with cell architectures involving a high number of sub-cells, there is an overall benefit in terms of series resistance losses, and thus a lower incentive for bandgap optimization.

III. Conclusion

Series resistances are undoubtedly major limiting factors currently preventing solar cells from performing efficiently at illumination levels typically exceeding 1000 suns. In this chapter, we investigated how tailoring the optimal bandgap combination toward minimizing the detrimental effect of series resistance losses can improve the conversion efficiency even at ultra-high concentration factors.

The series resistance effects appear to be stronger for low bandgap semiconductors. In fact, for a given illumination level, lower bandgaps lead to higher photo-generated current due to the increased number of absorbed photons, resulting in higher resistive losses and stronger efficiency degradation.

Our results demonstrate that:

- 1) For concentration levels lower than 1000 suns, tailoring the bandgap combination to account for series resistance losses provides insignificant improvements in the cell efficiency, a consequence of the relatively low series resistance value characterizing today's state-of-the-art concentrator solar cell.
- 2) At very high illumination level (typically above 1000 suns) and/or high series resistance value, there is a strong incentive toward tailoring the cell architecture to minimize the effects of series resistance losses. The gap between optimized and non-optimized cells was shown to be very significant as the illumination level to which the cell is exposed reaches values of several thousand of suns.

Higher bandgap values imply higher open-circuit voltages and lower short-circuit currents, due to the decrease in the number of absorbed photons, contributing to a drop in the resistive losses. As a consequence, a higher bandgap reduces the series resistance detrimental effect, especially at high concentration levels, and improves the conversion efficiency. The benefit for bandgap tuning is more pronounced as the concentration level increases, but also for higher series resistance values. Thus, the conversion efficiency can be boosted under ultra-high illumination through a suitable bandgap tuning to reduce resistive losses while enhancing the open-circuit voltage.

The optimal bandgap combination may give a hint to the cell manufacturers on the choice of the semiconductor materials to be used. Additional technological constraints related to the compatibility between the different materials used in the stack are to be accounted for, which constrain the number of possibilities regarding the choice of materials. It is important to stress that, despite the significant benefits associated with bandgap optimization, the dramatic effects of series resistance currently preclude solar cells achieving very high efficiencies under illumination levels of several thousand suns: careful cell design aiming at decreasing the series resistance value well below its current value remains a major requirement toward ensuring high conversion efficiency under ultra-high solar concentrations.

In the case of concentration-dependent series resistance, where the resistive losses are assumed to vary as a function of the illumination level to which the cell is exposed, we showed that these conclusions do not hold any longer, since the series resistance value (and thus the associated resistive losses) decreases with increasing illumination level. As a consequence, the conversion efficiency is not as much altered and there is no real need for bandgap optimization.

These results provide insights extending beyond the sole effects of series resistance losses: there is a strong incentive toward adapting the cell architecture, in terms of electronic properties of the materials used, to the conditions to which the cells are exposed. This is particularly relevant for applications involving extreme operating conditions (such as ultra-high flux CPV, or hybrid PV/CSP systems involving high solar concentrations and high operating temperatures) [28-30].

IV. References

- [1] M. A. Green, Y. Hishikawa, E. D. Dunlop, D. H. Levi, J. Hohl-Ebinger and A. W.Y. Ho-Baillie, Solar cell efficiency tables (version 51), *Prog. Photovolt. Res. Appl.*, 26 (2018) 3-12.
- [2] K. Nishioka, T. Takamoto, T. Agui, M. Kaneiwa, Y. Uraoka, and T. Fuyuki, Evaluation of InGaP/InGaAs/Ge triple-junction solar cell and optimization of solar cell's structure focusing on series resistance for high-efficiency concentrator photovoltaic systems, *Sol. Energ. Mater. Sol. Cell.*, 90 (2006) 1308-1321.
- [3] H. Cotal, C. Fetzer, J. Boisvert, G. Kinsey, R. King, P. Hebert, H. Yoon, and N. Karam, III-V multijunction solar cells for concentrating photovoltaics, *Energ. Environ. Sci.*, 2 (2009) 174-192.
- [4] A. Vossier, B. Hirsch, E. A. Katz, and J. M. Gordon, On the ultra-miniaturization of concentrator solar cells, *Sol. Energ. Mater. Sol. Cell.*, 95 (2011) 1188-1192.
- [5] A. Cheknane, B. Benyoucef, J.P. Charles, R. Zerdoum, and M. Trari, Minimization of the effect of the collecting grid in a solar cell based silicon, *Sol. Energ. Mater. Sol. Cell.* 87 (2005) 557-565.
- [6] C. Algara and V. Díaz, Influence of series resistance on guidelines for manufacture of concentrator p-on-n GaAs solar cells, *Prog. Photovolt.: Res. Appl.*, 8 (2000) 211-225.
- [7] M. Yamaguchi, T. Takamoto, K. Araki, and N. Ekins-Daukes, Multi-junction III-V solar cells: current status and future potential, *Sol. Energ.*, 79 (2005) 78-85.
- [8] A. Vossier, D. Chemisana, G. Flamant, and A. Dollet, Very high fluxes for concentrating photovoltaics: Considerations from simple experiments and modeling, *Renew. Energ.*, 38 (2012) 31-39.
- [9] A. Vossier, F. Gualdi, A. Dollet, R. Ares, and V. Aimez, Approaching the Shockley-Queisser limit: General assessment of the main limiting mechanisms in photovoltaic cells. *J. Appl. Phys.*, 117 (2015) 015102.
- [10] M. Paire, L. Lombez, N. Péré-Laperne, S. Collin, J.-L. Pelouard, D. Lincot, and J.-F. Guillemoles, Microscale solar cells for high concentration on polycrystalline Cu(In,Ga)Se₂ thin films, *Appl. Phys. Lett.*, 98 (2011) 264102.
- [11] M. Paire, A. Shams, L. Lombez, N. Péré-Laperne, S. Collin, J.-L. Pelouard, J.-F. Guillemoles, and D. Lincot, Resistive and thermal scale effects for Cu(In, Ga)Se₂ polycrystalline thin film microcells under concentration, *Energ. Environ. Sci.*, 4 (2011) 4972-4977.
- [12] M. Paire, L. Lombez, J.-F. Guillemoles, and D. Lincot, Toward microscale Cu(In,Ga)Se₂ solar cells for efficient conversion and optimized material usage: Theoretical evaluation, *J. Appl. Phys.*, 108 (2010) 034907.
- [13] C. Algara, E. Ortiz, I. Rey-Stolle, V. Diaz, R. Pena, V.M. Andreev, V.P. Khvostikov, and V.D. Rumyantsev, A GaAs solar cell with an efficiency of 26.2% at 1000 suns and 25.0% at 2000 suns, *IEEE Trans. Electron Devices*, 48 (2001) 840-844.
- [14] R. Stevenson, Powerful PVs approach 50 percent efficiency, *IEEE Spectrum*, 49 (2012) 14-16.

- [15] I. Garcia, I Rey-Stolle, B. Galiana, and C. Algara, A 32.6% efficient lattice-matched dual junction solar cell working at 1000 suns, *Appl. Phys. Lett.* 94 (2009) 053509.
- [16] F. Dimroth, M. Grave, P. Beutel, U. Fiedeler, C. Karcher, T.N.D. Tibbits, E. Oliva, G. Siefer, M. Schachtner, A. Wekkeli, A.W. Bett, R. Krause, M. Piccin, N. Blanc, C. Drazek, E. Guiot, B. Ghyselen, T. Salvetat, A. Tauzin, T. Signamarcheix, A. Dobrich, T. Hannappel, and L. Schwarzburg, Wafer bonded four-junction GaInP/GaAs//GaInAsP/GaInAs concentrator solar cells with 44.7% efficiency, *Prog. Photovolt: Res. Appl.* 22 (2014) 277–282.
- [17] A. Luque, Will we exceed 50% efficiency in photovoltaics?, *J. Appl. Phys.*, 110 (2011) 031301.
- [18] J.F. Geisz, M.A. Steiner, I. Garcia, R.M. France, W.E. McMahon, C.R. Osterwald, and D.J. Friedman, Generalized Optoelectronic Model of Series-Connected Multijunction Solar Cells, *IEEE J. Photovolt.* 5 (2015) 1827–1839.
- [19] E. Barrigón, I. Garcia, L. Barrutia, I. Rey-Stolle, and C. Algara, Highly conductive p⁺⁺-AlGaAs/n⁺⁺-GaInP tunnel junctions for ultra-high concentrator solar cells. *Prog. Photovolt: Res. Appl.*, 22 (2014) 399-404.
- [20] J.H. Holland, *Adaptation in Natural and Artificial Systems*, University of Michigan press, Cambridge, MA, US, Second Edition, 1992 (First Edition, 1975).
- [21] P. Xu, S. Sui, and Z. Du, Application of Hybrid Genetic Algorithm Based on Simulated Annealing in Function Optimization, *Int. J. Math. Comp. Phys. Elec. Comp. Eng.*, 9 (2015) 677-680.
- [22] A. J. Chipperfield and P. J. Fleming, The MATLAB Genetic Algorithm Toolbox, In Proc. of the IEE Colloquium on applied control techniques using MATLAB, 1995.
- [23] S.N. Sivanandam, S.N. Deepa, *Introduction to Genetic Algorithms*, Springer, Berlin, Heidelberg, Germany, 2008.
- [24] J. McCall, Genetic algorithms for modelling and optimization, *J. Comput. Appl. Math.*, 184 (2005) 205-222.
- [25] A. Chipperfield, P. Fleming, H. Pohlheim, and C. Fonseca, *Genetic Algorithm Toolbox User's Guide – Matlab*, Version 1.2, Automatic control and systems engineering, University of Sheffield.
- [26] A. Vossier, E. Al Alam, A. Dollet, and M. Amara, Assessing the Efficiency of Advanced Multijunction Solar Cells in Real Working Conditions: A Theoretical Analysis. *IEEE J. Photovolt.*, 5 (2015) 1805-1812.
- [27] A. Braun, N. Szabó, K. Schwarzburg, T. Hannappel, E. A. Katz, and J. M. Gordon, Current-limiting behavior in multijunction solar cells, *App. Phys. Let.*, 98 (2011) 223506.
- [28] A. Braun, B. Hirsch, A. Vossier, E.A. Katz, and J.M. Gordon, Temperature dynamics of multijunction concentrator solar cells up to ultra-high irradiance, *Prog. Photovolt: Res. Appl.*, 21 (2013) 202-208.
- [29] A. Braun, E.A. Katz, and J.M. Gordon, Basic aspects of the temperature coefficients of concentrator solar cell performance parameters, *Prog. Photovolt: Res. Appl.*, 21 (2013) 1087-1094.

- [30] F. Paredes, F.M. Montagnino, P. Salinari, G. Bonsignore, S. Milone, S. Agnello, M. Barbera, F.M. Gelardi, L. Sciortino, A. Collura, U. Lo Cicero, and M. Cannas, Combined heat and power generation with a HCPV system at 2000 suns. In AIP Conference Proceedings, 1679 (2015) 100003.

Chapter IV: Combining CPV and angular restriction

One of the main reasons preventing PV cells from getting close to the Carnot limit is the asymmetry between the solid angles of absorption and emission. In conventional flat-plate PV, the absorption angle is equal to the apparent angle of the sun, $\sim 6.8 \times 10^{-5}$ sr while the emission angle covers the whole hemisphere (Fig.IV-1(a)) [1]. Two strategies may be considered to reduce this angular discrepancy. The first one consists in concentrating solar radiation (Fig.IV-1(b)) to increase the angle of absorption. This approach allows increasing conversion efficiencies while reducing the cell area and consequently the system cost. However, it is limited by high resistive losses and increasing operating temperatures, especially under high concentration levels [2].

A second strategy consists in limiting the solid angle of emission (photons stemming from band-to-band recombination and escaping the cell) through optical means such as optical filters or compound parabolic concentrators (CPCs) (Fig.IV-1(c)) [3,4]. This approach seems promising insofar as it improves the conversion efficiency, while allowing a significant reduction in both the resistive losses and the cell heating, in comparison with concentrating systems, without requiring cumbersome optical concentrating systems. Even in this case, achieving maximum conversion efficiencies is particularly challenging, since the cells are typically limited by their inability to emit light efficiently. The system also requires large cell area to compensate for the low electrical power extracted due to its operation at 1 sun illumination.

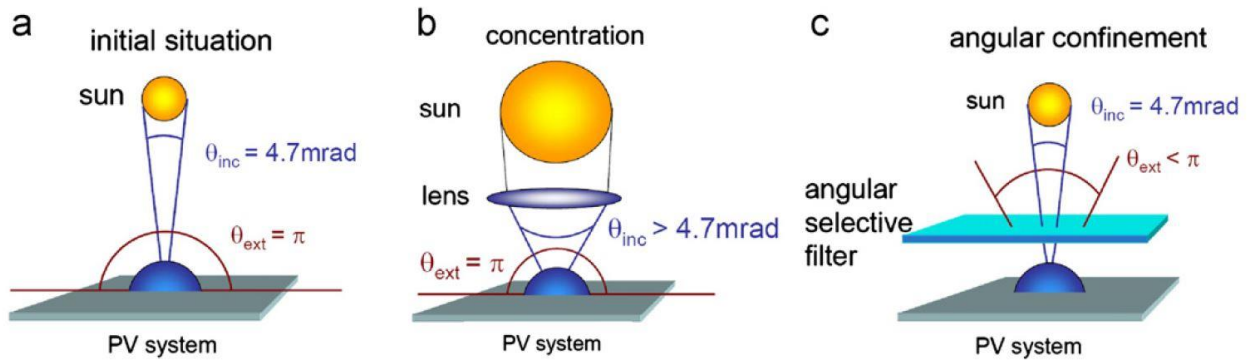


FIGURE IV-1 Sketch illustrating the broad discrepancies between the angles of emission and absorption (a) and the solutions used to decrease this asymmetry: solar concentration (b) and angular restriction (c) [5].

The original strategy considered in this chapter lies in the combination of both approaches, in order to increase the solar cell performances as well as the maximum output power per unit area, while reducing the impact of series resistances and non-radiative recombination [6]. Three main questions are investigated here, namely: 1) how this strategy permits increasing the conversion efficiencies, 2) what the optimal combination of solid angles of absorption and emission is and 3) how the main limiting mechanisms affect the cell performances, depending on the angular properties of the absorbed and emitted fluxes.

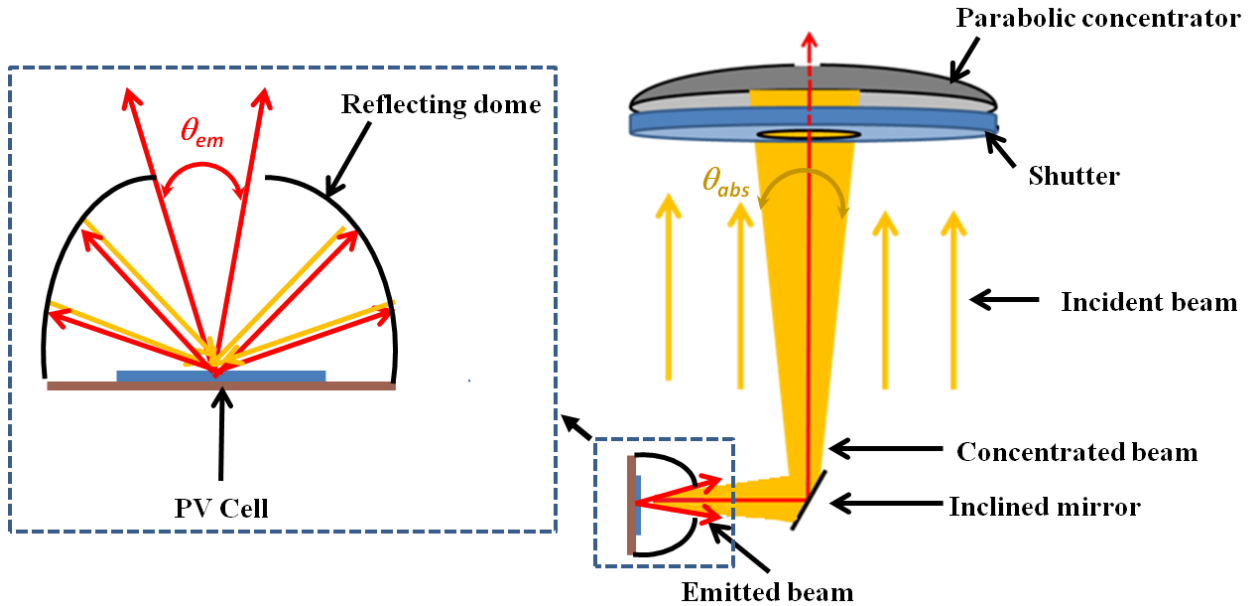


FIGURE IV-2 Schematic of the combination of solar concentration with angular restriction.

I. Methodology and Assumptions

A. Objectives

Angular restriction and sunlight concentration have similar maximal theoretical efficiencies. They both suffer from several limiting mechanisms, that may drastically alter the benefits of implementing them, particularly 1) resistive losses (a major loss mechanism severely decreasing the fill factor of concentrator solar cells) and 2) low external radiative efficiencies (limiting the V_{oc} enhancement in the angular restriction strategy). Combining both approaches offers an extra degree of freedom in the quest of high PV efficiencies, and can be a suitable solution allowing operation at relatively low concentrations and low degrees of angular restriction.

To validate the benefits of this strategy, we evaluate the conversion efficiency enhancement as a function of the angular properties of the solid angles of absorption and emission. In the light of these results, we aim to better understand the extent of the negative effect of series resistances and non-radiative recombination on the cells electrical performances, when simultaneously operated under solar illumination and angular restriction. We also seek to find the optimal combination of the solid angles of absorption and emission (a compromise between the concentration ratio and the degree of angular restriction) leading to the highest performances for a broad range of series resistances and *ERE* values.

B. Methodology

To study the effects of series resistances and non-radiative recombination, the algorithm described in the previous chapter, considering the detailed balance formalism, still holds (with some modifications). It is based on the resolution of the general *I-V* characteristic equation for ideal solar cells operating in the radiative limit, as well as for *real* cells considering series resistance, non-radiative recombination or both, using Matlab. The electrical behavior of the *ideal* and *real* cell (i.e. penalized by non-ideal limiting mechanisms)

is respectively described by eq. (I-7) and (I-9). Non-radiative recombination are taken into account in the *ERE* factor, affecting the ideal *I-V* characteristic equation by modifying the dark current calculated in the radiative limit (J_{0_rad}) by eq. (I-12), as illustrated in eq. (IV-1) [7]. In the first calculations, the *ERE* is assumed fixed and varies between 1% (a typical value for efficient solar cells nowadays [8]) and 100% (ideal solar cells).

$$J = J_{ph} - \frac{J_{0_rad}}{ERE} \left(e^{\frac{qV}{nkT}} - 1 \right) \quad (\text{IV-1})$$

And then both losses are taken into account as illustrated in eq. (IV-2):

$$J = J_{ph} - \frac{J_{0_rad}}{ERE} \left(e^{\frac{q(V+JR_s)}{nkT}} - 1 \right) \quad (\text{IV-2})$$

The angles of absorption are correlated to the concentration factors using eq.(II-8), while the dark current dependence on the emission angle is described by eq.(II-16) and (II-17). Table IV-1 lists the different equations implemented in the program, assuming that the ideality factor n is equal to 1.

TABLE IV-1 List of the different equations used in the algorithm

$I = I_{ph} - I_0 \left(e^{\frac{qV}{nkT}} - 1 \right)$ (I-3)
--

$I = I_{ph} - I_0 \left(e^{\frac{qV+IR_s}{nkT}} - 1 \right)$ (I-4)

$J = J_{ph} - \frac{J_{0_rad}}{ERE} \left(e^{\frac{qV}{nkT}} - 1 \right)$ (IV-1)
--

$J = J_{ph} - \frac{J_{0_rad}}{ERE} \left(e^{\frac{qV+JR_s}{nkT}} - 1 \right)$ (IV-2)

$J_{0_rad} = \frac{q}{k} \times \frac{15\sigma}{\pi^4} \times T^3 \times \int_u^{\infty} \frac{x^2}{e^x - 1} dx$ (I-12)
--

$x = \frac{E}{kT}$

$u = \frac{E_g}{kT}$

$X = \frac{\sin^2(\theta_{abs})}{\sin^2(\theta_{sun})} = \frac{\sin^2(\theta_{abs})}{\sin^2(4.65 \times 10^{-3})}$ (II-2)

$s = \frac{1}{(\sin(\theta_{em}))^2}$ (II-3)
--

$I_{0_s} = \frac{I_0}{s}$ (II-4)

The cells electrical parameters are studied over a broad range of absorption and emission angles. Iso-efficiency curves, which represent the efficiency with which solar energy is converted as a function of the solid angles of absorption and emission, are then generated for ideal cells and for different cases of *real* cells. They allow determining the best angular combination based on the maximum efficiency while accounting for the main limiting mechanisms. The red color represents high conversion efficiencies while bluish colors denote low performances values. For every iso-efficiency curves, the area below the $x=y$ line (black area) represents a forbidden angular region, since the angles of absorption should necessarily be equal or smaller than the angles of emission, otherwise a negative entropy term would be generated, which would violate the second law of thermodynamics.

II. Results

A. Ideal Solar Cells

Ideally, at the radiative limit, the best cells performances occur when both angles of absorption and emission are equal (independently of the angular values), hence eliminating *Boltzmann* losses.

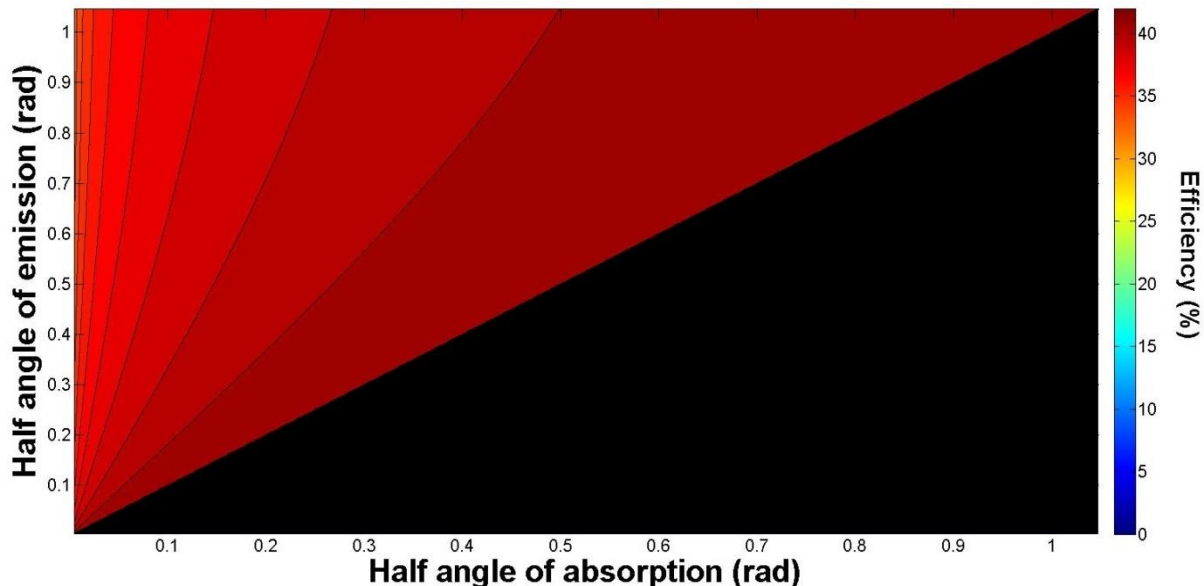


FIGURE IV-3 Iso-efficiency curves for an ideal single-junction solar cell characterized by a bandgap of 1.4eV, as a function of the solar angles of emission and absorption, assuming no series resistances and an ERE of 100%.

Figure IV-3 represents iso-efficiency curves for ideal single-junction solar cells, assuming a bandgap of 1.4 eV, no series resistances and an external radiative efficiency of 100%, as a function of the half-angles of absorption and emission. The angles vary between 4.65 mrad (equivalent to an illumination of 1 sun) and $\pi/3$ rad (corresponding to ~ 35000 suns). The maximal efficiency reaches almost 42% with an open-circuit voltage of 1.4V and a fill factor of 0.918. These performances are observed for all equal angles of absorption and emission. For the remaining angular combinations, one can clearly see that increasing the angle of absorption (moving from left to right) or decreasing the angle of emission (from top to bottom) leads to higher efficiencies.

B. Effect of series resistances

Series resistances are major limiting mechanisms in concentrated solar cells, as seen and detailed in the previous chapter. Their drastic effect is mainly noticeable at very high concentration levels, for large angles of absorption, where the generated current is important. When combining solar concentration with angular restriction, one can hence expect to detect maximal efficiencies whenever the solid angles of absorption and emission are equal and small (corresponding to modest concentration factors and high degrees of angular restriction), preventing colossal resistive losses.

Figure IV-4 illustrates iso-efficiency curves for single-junction solar cells assuming a bandgap of 1.4 eV, an external radiative efficiency of 100% and series resistance values of $0.001 \Omega \text{ cm}^2$ (a) and $0.01 \Omega \text{ cm}^2$ (b) as a function of the half-angles of emission and absorption. High series resistance values limit the maximal attainable concentration because of the huge resistive losses at high sunlight illuminations, which explains why the range of absorption angles does not extend to $\pi/2$ rad (which is equivalent to the thermodynamic limit of sunlight concentration, 46250 suns) in the iso-efficiency curves.

Comparing both graphs confirms the results mentioned in the previous chapter. One can clearly see the enhancement of the cell performances as the concentration increases, up to a peak concentration value above which the resistive losses become significant, thus leading to a decrease in the conversion efficiency. Series resistance losses are important at high solar illumination and their effects are greater as the values of the series resistance increase. As a result, the performance degradation is much more noticeable for cells having a series resistance of $0.01 \Omega \text{ cm}^2$ (Fig. IV-4(b)) compared to cells with $R_s=0.001 \Omega \text{ cm}^2$ (Fig IV-4(a)). On the other hand, the maximal efficiency reached remains identical (close to 40%) in both scenarios, since it occurs for small angles of absorption and emission, in a region where the resistive losses remain negligible. As the series resistance value increases, the angular extent for which the performances are optimal shrinks, without affecting the peak efficiency value.

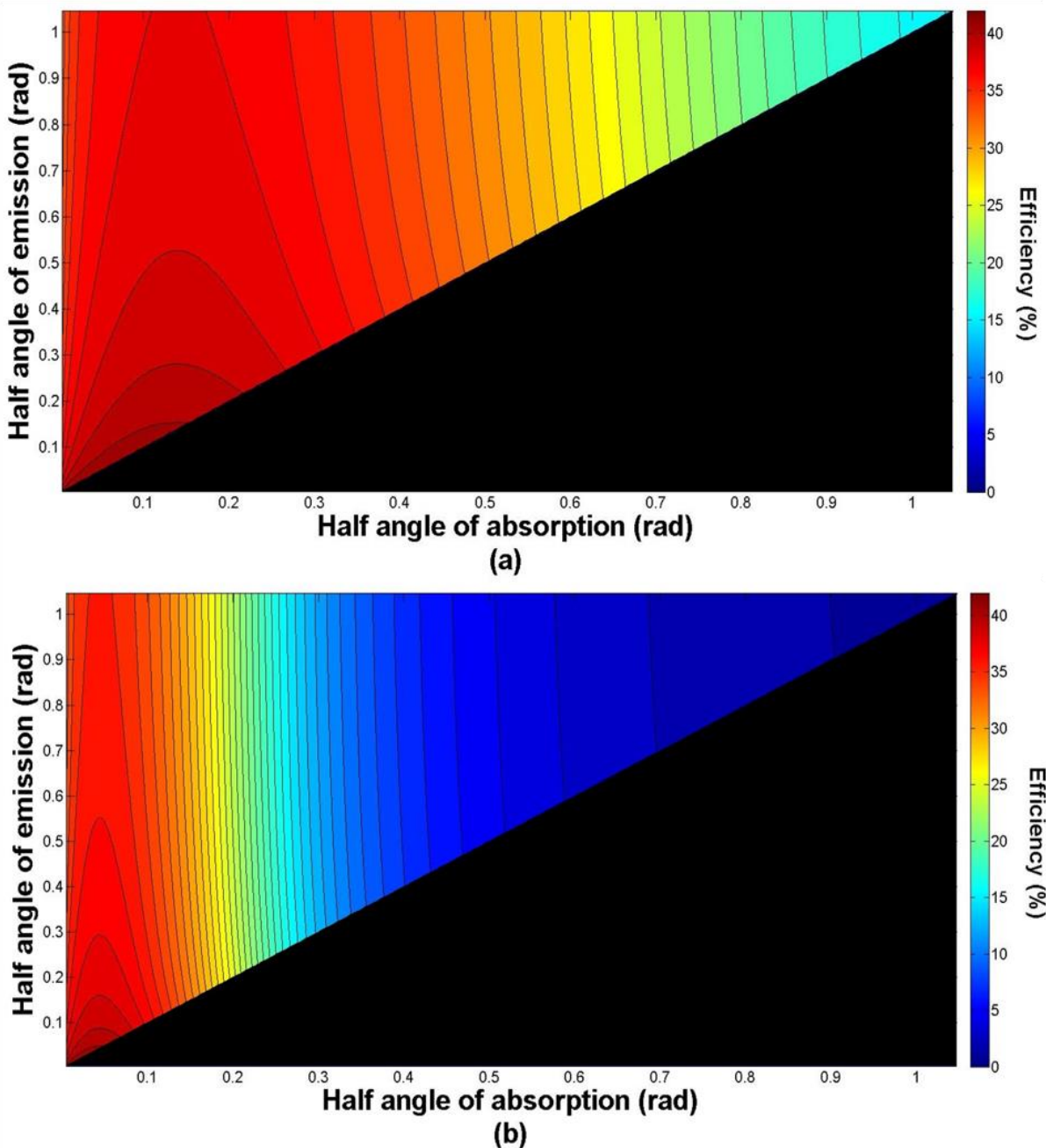


FIGURE IV-4 Iso-efficiency curves for single-junction solar cells characterized by a bandgap of 1.4 eV, as a function of the solar angles of emission and absorption, assuming an ERE of 100% and series resistances of $0.001 \Omega \text{ cm}^2$ (a) and $0.01 \Omega \text{ cm}^2$ (b).

C. Effect of non-radiative recombination

Non-radiative recombination is a major limiting mechanism strongly affecting solar cells with angular confinement. In fact, high non-radiative recombination rates increase the dark current which, in turn, deteriorates the open-circuit voltage and the conversion efficiency.

Figures IV-5 represents iso- V_{oc} curves as a function of the half-angles of absorption and emission for ideal single-junction solar cells, assuming no series resistances (the V_{oc} being independent of this parameter), a bandgap of 1.4 eV and different ERE values, namely

100% (a), 24.5% (b) and 1% (c). It is obvious that V_{oc} increases with increasing angle of absorption (i.e. higher concentration factor), decreasing angle of emission (higher degree of angular restriction) as well as with higher *ERE* value.

Figure IV-6 illustrates the V_{oc} variation as a function of the emission angle for different *ERE* values (a) as well as the relative variation in V_{oc} , relative to the *ideal* case (i.e. no series resistances, 100% radiative recombination, 1 sun illumination and no angular restriction). In both cases, the angle of emission is set to 4.65 mrad, which is equivalent to a 1 sun illumination. These graphs show that the decrease rate of V_{oc} becomes faster as *ERE* decreases, higher *ERE* leading to higher V_{oc} . The maximal gain compared to the ideal case also depends on the non-radiative recombination fraction. It reaches $\sim 25\%$ for cells having an *ERE* of 100% with maximal degree of angular confinement ($\theta_{em}=4.65\text{mrad}$) and falls to 14% for an *ERE* equal to 1%.

One would expect that the dramatic effect of non-radiative recombination is mainly noticeable at very high degree of angular restriction. In fact, higher degree of angular confinement leads to an increase in the non-radiative recombination rate, which decreases the *ERE* and consequently, V_{oc} . When combining solar concentration with angular restriction, optimal efficiencies are expected to be found for large and equal solid angles of absorption and emission (when no series resistances are considered). Such combination ensures high concentration and low degree of angular restriction, hence eliminating the negative impact of non-radiative recombination.

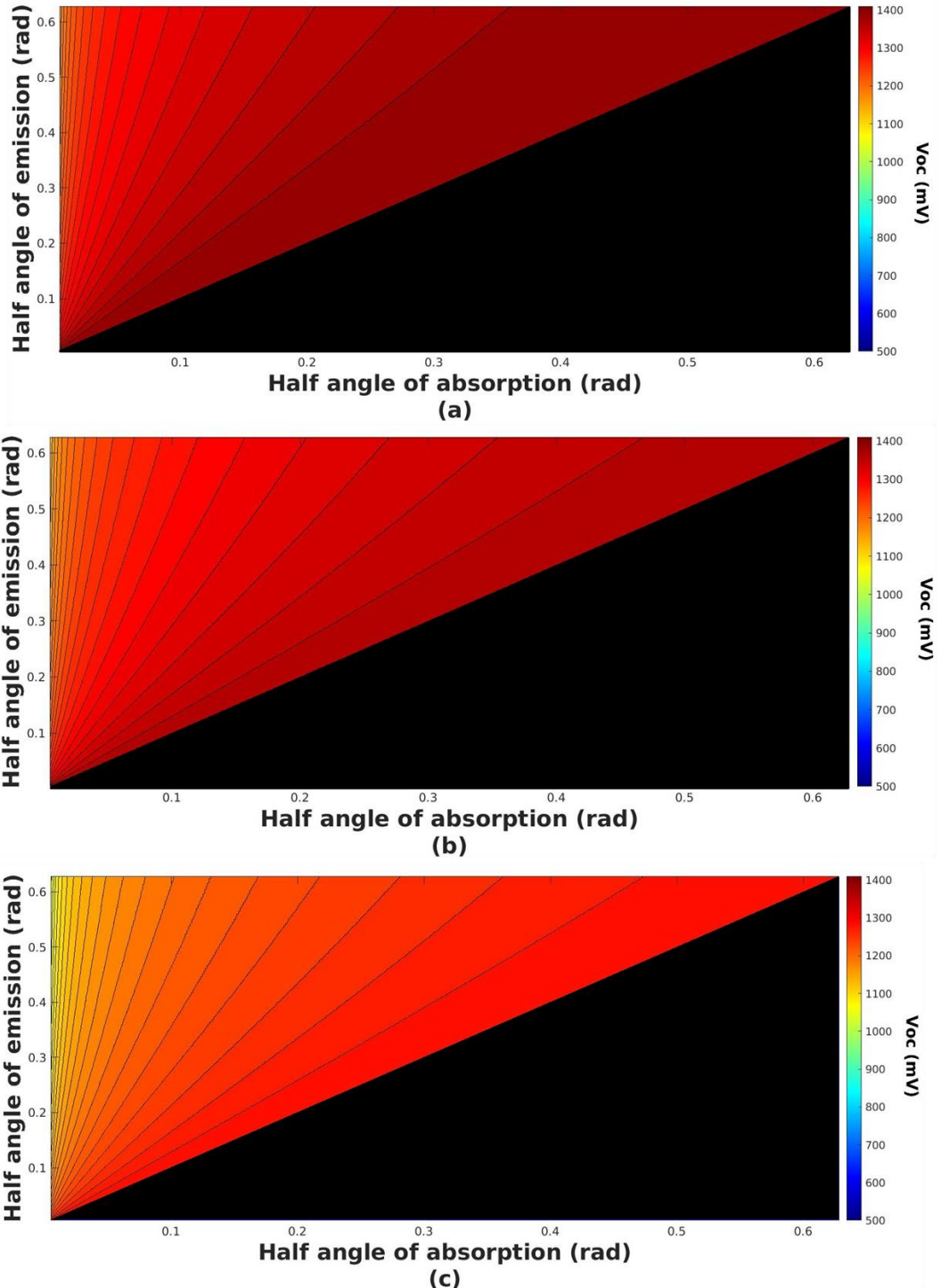


FIGURE IV-5 Iso- V_{oc} curves for ideal single-junction solar cells assuming a bandgap of 1.4eV, no series resistances and ERE values of 100% (a), 24.5% (b) and 1% (c).

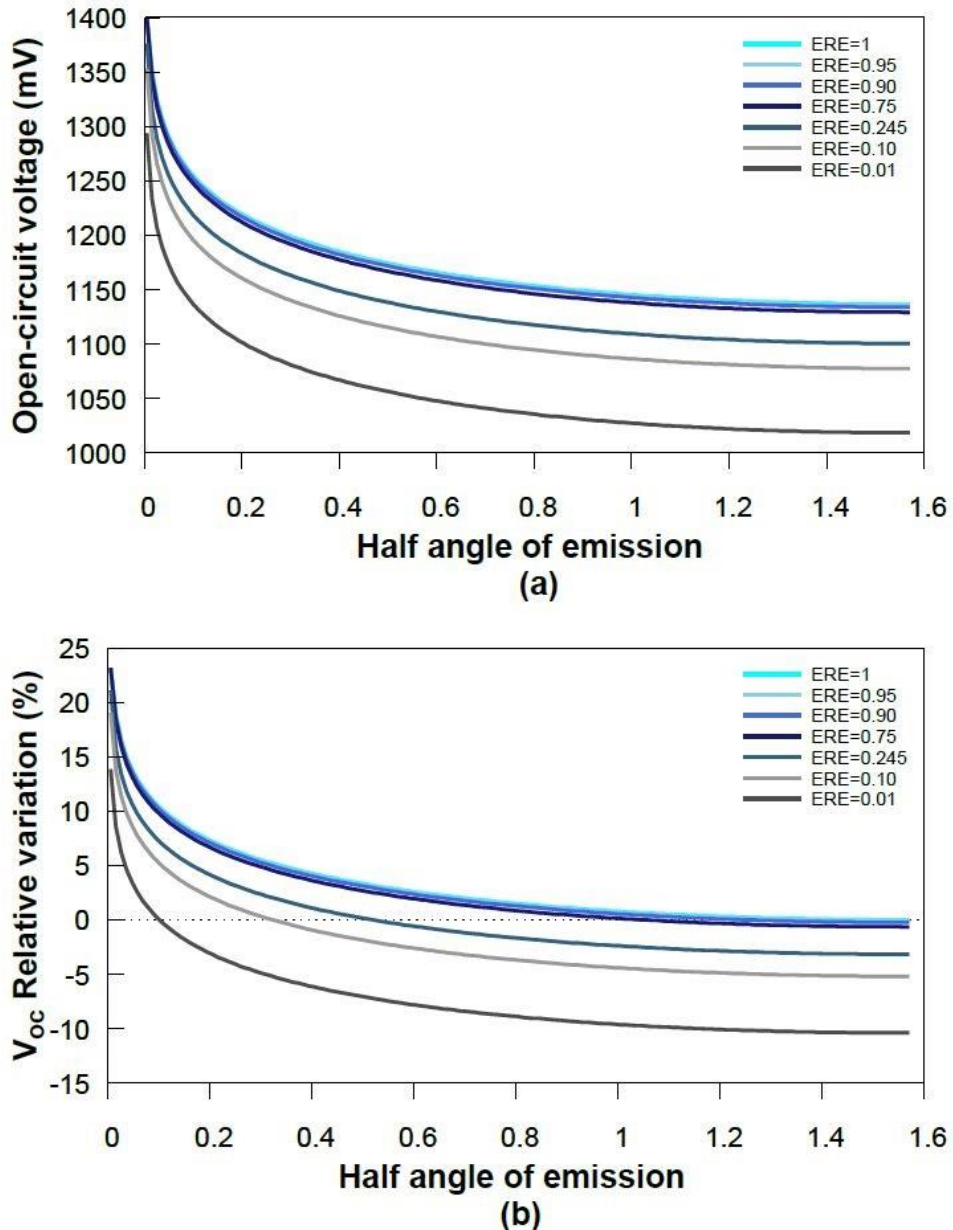


FIGURE IV-6 V_{oc} and V_{oc} relative variation with respect to ideal conventional cells as a function of the angles of emission and for different ERE values, assuming an angle of absorption equal to 4.65 mrad (equivalent to 1 sun illumination) and a bandgap of 1.4 eV.

Figure IV-7 illustrates iso-efficiency curves for single-junction solar cells assuming a bandgap of 1.4 eV, no series resistances and external radiative efficiencies of 1% (a) and 30% (b) as a function of the half-angles of emission and absorption. These two graphs show that smaller ERE leads to lower cells efficiencies. The solar cell characterized by an ERE of 1% (Fig. IV-7 (a)) presents a maximal V_{oc} of 1.29V and an optimal efficiency of ~38% whereas a cell having an ERE of 30% (Fig. IV-7 (b)) exhibits a V_{oc} of 1.38V and a maximal efficiency of ~41%. In both cases, the optimal efficiency is found for equal angles of absorption and emission, independently of the angular values. Contrary to our expectations, these observations do not demonstrate any strong negative effect of non-radiative recombination, as previously mentioned in the literature. To better describe their effect on the cell electrical behavior, an extended model is required.

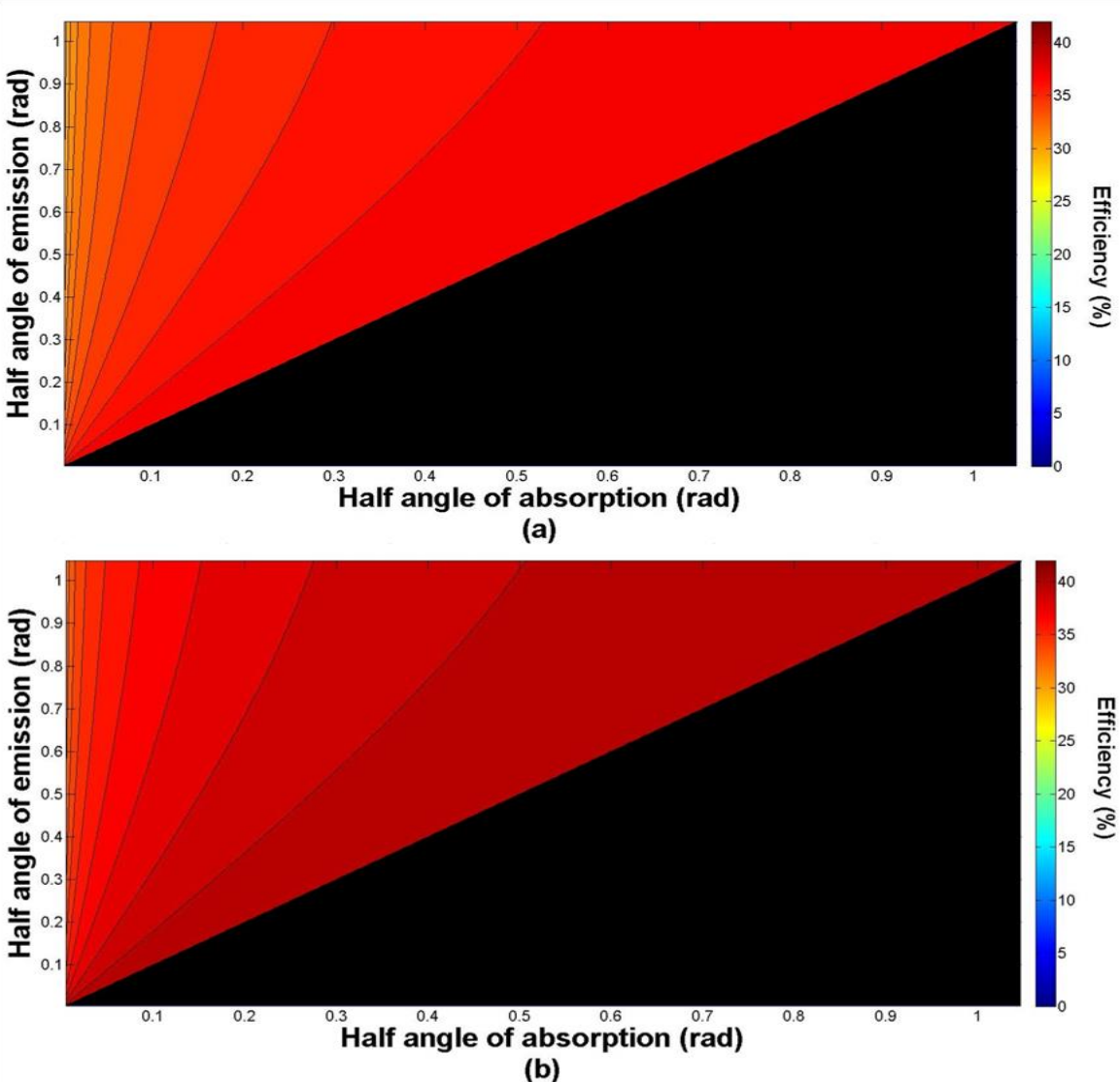


FIGURE IV-7 Iso-efficiency curves for single-junction solar cells, characterized by a bandgap of 1.4eV as a function of the solar angles of emission and absorption, assuming no series resistances and an ERE of 1% (a) and 30% (b).

It should be stressed that increasing the concentration ratio enhances the performances of cells submitted to angular restriction. Thus, combining both strategies allows alleviating the detrimental effect of non-radiative recombination. As an example, when assuming a cell with an ERE of 1%, under 1 sun illumination ($\theta_{abs} = 4.65\text{mrad}$) and a θ_{em} of $\pi/5$, V_{oc} is found to be equal to 1.05V and the efficiency reaches $\sim 30\%$. The same cell submitted to a concentration level of ~ 16000 suns (corresponding to an angle of absorption equal to the angle of emission of $\pi/5$ rad) reveals a V_{oc} of 1.3V and an efficiency of $\sim 38\%$. Combining both enhances the V_{oc} by 25mV and boosts the efficiency by $\sim 8\%$ absolute gain. Thus, increasing the concentration for a given degree of angular confinement enhances the performances.

D. Effect of series resistances and non-radiative recombination

When accounting for both series resistances and non-radiative recombination, one would expect that the effect of each limiting mechanism is discernible on the iso-efficiency

curves. The optimal combination of absorption and emission angles should thus be achieved if both angles are equal, and for intermediate angular values, to ensure low concentration factors together with low degrees of angular restriction, and to limit the effects of both limiting mechanisms.

Figure IV-8 represents iso-efficiency curves for single-junction solar cells assuming a bandgap of 1.4 eV, as a function of the half-angles of emission and absorption, for different values of the series resistances and *ERE*. It considers an *ERE* of 1% and a series resistance of $0.001 \Omega \text{ cm}^2$ (a), an *ERE* of 30% and a R_s value of $0.001 \Omega \text{ cm}^2$ (b) and an *ERE* of 30% and a R_s value of $0.01 \Omega \text{ cm}^2$ (c). These graphs summarize what was already seen:

- 1) Increasing the *ERE* enhances the cell performances.
- 2) Increasing the series resistance leads to a strong degradation in the cell performances, beyond a limiting absorption angle value, due to colossal resistive losses.

The different cases shown in Fig.IV-8 demonstrate that the optimal angular combination occurs for limited and equal angles of absorption and emission (i.e. for low illumination levels but with maximum degrees of angular restriction). The detrimental effect of series resistance appears to be the main factor of efficiency degradation, causing a dramatic drop in the maximum conversion efficiency achievable with increasing illumination level (with an amplitude function of the series resistance value). There is also, to a lesser extent, a negative effect of non-radiative recombination which translates into progressively lower conversion efficiency as the *ERE* values are decreased. Overall, these results prove that the impact of resistive losses on the combination of angular restriction and solar concentration is more significant than the effect of low *ERE*.

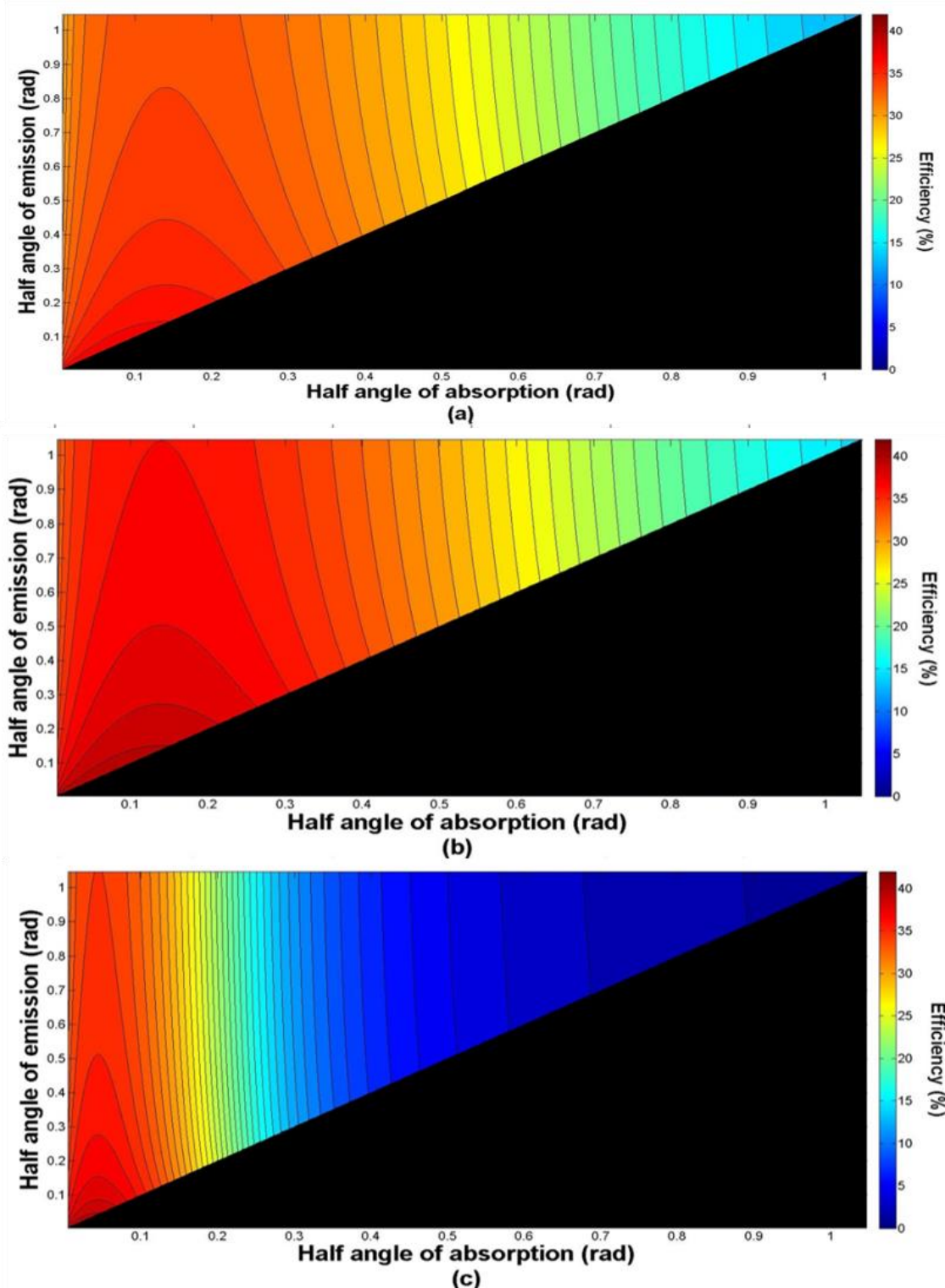


FIGURE IV-8 Iso-efficiency curves for a single-junction solar cell characterized by a bandgap of 1.4eV, as a function of the solar angles of emission and absorption, assuming an ERE of 1% and a R_s of $0.001\Omega \text{ cm}^2$ (a) an ERE of 30% and a R_s of $0.001\Omega \text{ cm}^2$ (b) and an ERE of 30% and a R_s of $0.01\Omega \text{ cm}^2$ (c).

TABLE IV-2 Comparison of open-circuit voltage, fill factor and conversion efficiency for five different cases of series resistances and radiative efficiencies, for equal solid angles of absorption and emission (4.65mrad for the maximum scenario, and $\pi/10$ for the minimum scenario).

Case	V_{oc} (V)	FF	η (%)
$Rs = 0.0 \Omega \text{ cm}^2$ $ERE=100\%$	1.4	0.92 (Max)	41.59 (Max)
		0.92 (Min)	41.59 (Min)
$Rs = 0.001 \Omega \text{ cm}^2$ $ERE=30\%$	1.38	0.91 (Max)	40.61 (Max)
		0.82 (Min)	36.63 (Min)
$Rs = 0.01 \Omega \text{ cm}^2$ $ERE=30\%$	1.38	0.91 (Max)	40.61 (Max)
		0.26 (Min)	11.67 (Min)
$Rs = 0.001 \Omega \text{ cm}^2$ $ERE=1\%$	1.29	0.90 (Max)	37.84 (Max)
		0.81 (Min)	33.88 (Min)
$Rs = 0.01 \Omega \text{ cm}^2$ $ERE=1\%$	1.29	0.90 (Max)	37.84 (Max)
		0.26 (Min)	10.25 (Min)

Table IV-2 summarizes the electrical parameters that are affected by the limiting mechanisms considered, namely V_{oc} , FF and η , computed for equal angles of absorption and emission. We restrict our analysis to extreme restriction or concentrations cases, referred as *Max* for the maximum restriction case (corresponding to absorption and emission angles of 4.65 mrad (equivalent to 1 sun illumination and maximum angular confinement)) and *Min* for the minimum angular restriction case considered in this table (with absorption and emission angles of $\pi/10$ (corresponding to ~ 4400 suns)). It is worth noticing that the maximum efficiencies achievable are comparable to the case where only series resistances losses are considered, stressing the major influence of this loss mechanism on the efficiency one can expect from this strategy.

Table IV-3 illustrates the impact of each limiting mechanism on the optimal efficiency. Only one cell configuration is considered: a single-junction solar cell characterized by a bandgap of 1.4 eV, a series resistance value of $0.01 \Omega \text{ cm}^2$ and an ERE of 1%, which are typical values for high-efficiency GaAs cells. Four different scenarios are considered, where the solid angles of absorption and emission are identical: 1) both angles equal to the apparent angle of the sun, 2) angles of 0.01 rad (equivalent to sunlight concentration of ~ 5 suns), 3) angles of 0.11 rad (analogous to concentrations of ~ 560 suns, for which the fill factor loss offsets the V_{oc} gain) and 4) angles of $\pi/20$ rad (corresponding to ~ 1130 suns, typical concentration levels used in CPV nowadays). The reference case (no sunlight concentration, no angular restriction) is also mentioned, assuming an ideal cell without any series resistance, and 100% radiative recombination. The values mentioned in parentheses represent the relative variation for each scenario investigated, compared to the reference case. Under non-concentrated sunlight and maximal angular restriction, the overall

efficiency is improved by 15% relative, due to the boost in V_{oc} , even though the ERE value is low. For very low concentrating factors, namely 5-10 suns, the V_{oc} enhancement persists due to the parity between both solid angles leading to relative efficiency enhancement of 15%. As the concentration increases, resistive losses become important and worsen the fill factor. Up to a concentration of ~ 560 suns, the improvement in V_{oc} still counterbalances the reduction in the fill factor when compared to the reference case. Above this limit, the V_{oc} enhancement cannot compensate for the resistive losses anymore, leading to lower overall performances.

TABLE IV-3 Comparison of open-circuit voltage, fill factor and conversion efficiency for four different cases of series resistances, radiative efficiencies and solid angles of absorption and emission.

Case	V_{oc} (V)	FF	η (%)
$Rs = 0.0 \Omega \text{ cm}^2$			
$ERE=100\%$			
$\Theta_{abs} = 4.65 \times 10^{-3}$ (X= 1 sun)	1.137	0.89	32.86
$\Theta_{em} = \pi/2$			
$Rs = 0.01 \Omega \text{ cm}^2$			
$ERE=1\%$			
$\Theta_{abs} = 4.65 \times 10^{-3}$ (X=1 sun)	1.29 (+13%)	0.9 (+1%)	37.84 (+15%)
$\Theta_{em} = 4.65 \times 10^{-3}$			
$Rs = 0.01 \Omega \text{ cm}^2$			
$ERE=1\%$			
$\Theta_{abs} = 0.01$ (X = 5 suns)	1.29 (+13%)	0.9 (+1%)	37.8 (+15%)
$\Theta_{em} = 0.01$			
$Rs = 0.01 \Omega \text{ cm}^2$			
$ERE=1\%$			
$\Theta_{abs} = 0.11$ (X = ~ 560 suns)	1.29 (+13%)	0.78 (-14%)	32.84 (+0%)
$\Theta_{em} = 0.11$			
$Rs = 0.01 \Omega \text{ cm}^2$			
$ERE=1\%$			
$\Theta_{abs} = \pi/20$ (X=1130 suns)	1.29 (+13%)	0.66 (-26%)	27.8 (-15%)
$\Theta_{em} = \pi/20$			

E. Extended model

The above results show unconformities with one's expectation whenever low ERE values are considered, their impact being smaller than the series resistance effect. Resistive losses depend on two parameters: the fixed series resistance value and the generated current which varies linearly with sunlight concentration, resulting in losses varying with the square of the concentration factor. Resistive losses are thus dependent upon the concentration ratio, and are modified depending on the absorption angle value, which explains why they constitute the dominant limiting mechanisms especially at very high concentrating factors.

Conversely, assuming a fixed non-radiative recombination fraction (i.e. ERE is fixed) leads to a similar increase in the dark current for every iteration of the calculation, since non-radiative recombination losses are independent from any other parameter. This assumption may be inaccurate because one can expect that the angular confinement alters the fraction of non-radiative recombination. So, it is important to find a model capable of accounting for the variations in the non-radiative recombination fraction with angular restriction.

To do so, we start by computing the external radiative efficiency for each point of the *I-V* characteristic general equation using the equation described by Geiss et al. [9] and Steiner et al. [10], and illustrated by eq.(I-5), linking the external radiative efficiency to the internal radiative efficiency through the probability densities of escaped or reabsorbed photons.

The internal radiative efficiency is computed as:

$$IRE = \frac{R_{rad}}{R_{rad} + R_{Auger} + R_{SRH}} \quad (\text{IV-5})$$

with R_{rad} , R_{Auger} and R_{SRH} the radiative, Auger and Shockley-Read Hall recombination rates respectively. These different recombination rates are implemented as follow [11-13]. For the radiative recombination rate,

$$R_{rad} = B_r (n_e n_h - n_i^2)$$

with B_r the radiative coefficient, n_e and n_h the electron and hole concentrations respectively, and n_i the intrinsic concentration of electrons and holes. The variables n_e , n_h and n_i can be expressed as:

$$n_e = n_{e0} + n_{ex} \quad (\text{IV-6})$$

$$n_h = n_{h0} + n_{ex} \quad (\text{IV-7})$$

$$n_i^2 = n_{e0} n_{h0} \quad (\text{IV-8})$$

n_{e0} represents the concentration of electrons at equilibrium, n_{ex} the excess carrier concentration (which is identical for electrons and holes in the low injection regime in order to satisfy the condition of charge neutrality) and n_{h0} the concentration of holes at equilibrium. After replacing equations (IV-4) to (IV-6) in equation (IV-3), developing and reducing the new expression, the radiative recombination rate is expressed as (eq. (IV-7)):

$$\begin{aligned} R_{rad} &= B_r ((n_{e0} + n_{ex}) \times (n_{h0} + n_{ex}) - n_{e0} n_{h0}) \\ R_{rad} &= B_r n_{ex} (n_{e0} + n_{h0} + n_{ex}) \end{aligned} \quad (\text{IV-9})$$

Auger recombination rate is described by equation (IV-8), with C_n and C_p the capture probability coefficients depending on the nature of the third carrier (electron or hole).

$$\begin{aligned} R_{Auger} &= C_n (n_e^2 n_h - n_{e0}^2 n_{h0}) + C_p (n_h^2 n_e - n_{h0}^2 n_{e0}) \\ R_{Auger} &= C_n ((n_{e0} + n_{ex})^2 (n_{h0} + n_{ex}) - n_{e0}^2 n_{h0}) \\ &\quad + C_p ((n_{h0} + n_{ex})^2 (n_{e0} + n_{ex}) - n_{h0}^2 n_{e0}) \end{aligned} \quad (\text{IV-10})$$

Finally, the SRH recombination rate is described by equation (IV-9), with τ_{n0} and τ_{p0} the lifetime of electrons and holes, n_t the concentration of electrons in the impurities, and p_t the concentration of holes in the impurities.

$$R_{SRH} = \frac{n_e n_h - n_i^2}{\tau_{p0}(n_e + n_t) + \tau_{n0}(n_h + p_t)}$$

$$R_{SRH} = \frac{n_{ex}(n_{e0} + n_{h0} + n_{ex})}{\tau_{p0}(n_{e0} + n_{ex} + n_t) + \tau_{n0}(n_{h0} + n_{ex} + p_t)} \quad (\text{IV-11})$$

The applied voltage is related to the excess carrier concentration using eq.(IV-10) below [14].

$$n_h n_e = n_i^2 e^{\frac{qV}{kT}}$$

$$(n_{e0} + n_{ex}) \times (n_{h0} + n_{ex}) = n_{e0} n_{h0} e^{\frac{qV}{kT}}$$

$$n_{ex}(n_{e0} + n_{h0} + n_{ex}) = n_{e0} n_{h0} (e^{\frac{qV}{kT}} - 1) \quad (\text{IV-12})$$

Taking into account these recombination mechanisms requires the use of a material-specific model instead of the general ones considered above, since the lifetime and the carrier concentration parameters depend on the semiconductor used. Three semiconductor materials were studied in our case: Ge, Si and GaAs.

The variations in the internal radiative efficiency are illustrated as a function of the applied voltage in Fig.IV-9 for different semiconductors materials, namely Ge (a), Si (b) and GaAs (c). The values of the different semiconductor parameters are summarized in Table IV-4. Distinct regions can be observed in each graph. For low applied voltages, IRE is controlled by Shockley-Read-Hall recombination. Then, the internal radiative efficiencies increase with increasing applied voltages, implying a rise in the radiative recombination rate. For GaAs, the IRE reaches almost 100% around 1.4V, a voltage equivalent to the bandgap of this semiconductor material (confirming the extremely high radiative efficiency value one can expect with this material, as already stressed by Schnitzer et al. [15]). For Ge and Si, Auger recombination takes over due its cubic proportionality to carrier concentration, leading to a noticeable IRE decrease in the high voltage range. This third region is not yet reached in the case of GaAs for the voltage range studied.

TABLE IV-4 Main optical and electrical parameters of GaAs, Si and Ge

Parameters	GaAs	Si	Ge
E_g	1.42	1.12	0.66
n_i	2.1×10^6	1.1×10^{10}	2×10^{13}
N_a	1×10^{16}	1×10^{16}	1×10^{16}
N_d	1×10^{18}	1×10^{18}	1×10^{18}

n_{h0} (assuming p-doping)	Na	Na	Na
n_{e0} (assuming p-doping)	$\frac{n_i^2}{n_{h0}}$	$\frac{n_i^2}{n_{h0}}$	$\frac{n_i^2}{n_{h0}}$
B_r	7.2×10^{-10}	1.1×10^{-14}	6.41×10^{-14}
C_n	5×10^{-30}	1.1×10^{-30}	2.2×10^{-30}
C_p	6×10^{-31}	0.3×10^{-30}	5.4×10^{-31}
N_t	1×10^{14}	1×10^{11}	5×10^{12}
σ_n	1×10^{-15}	5×10^{-14}	1×10^{-14}
σ_p	1×10^{-15}	7×10^{-17}	4×10^{-16}
v_n	4.4×10^7	2.3×10^7	3.1×10^7
v_p	1.8×10^7	1.6×10^7	1.9×10^7
τ_{n0}	$\frac{1}{N_t \times v_n \times \sigma_n}$	$\frac{1}{N_t \times v_n \times \sigma_n}$	$\frac{1}{N_t \times v_n \times \sigma_n}$
τ_{p0}	$\frac{1}{N_t \times v_p \times \sigma_p}$	$\frac{1}{N_t \times v_p \times \sigma_p}$	$\frac{1}{N_t \times v_p \times \sigma_p}$

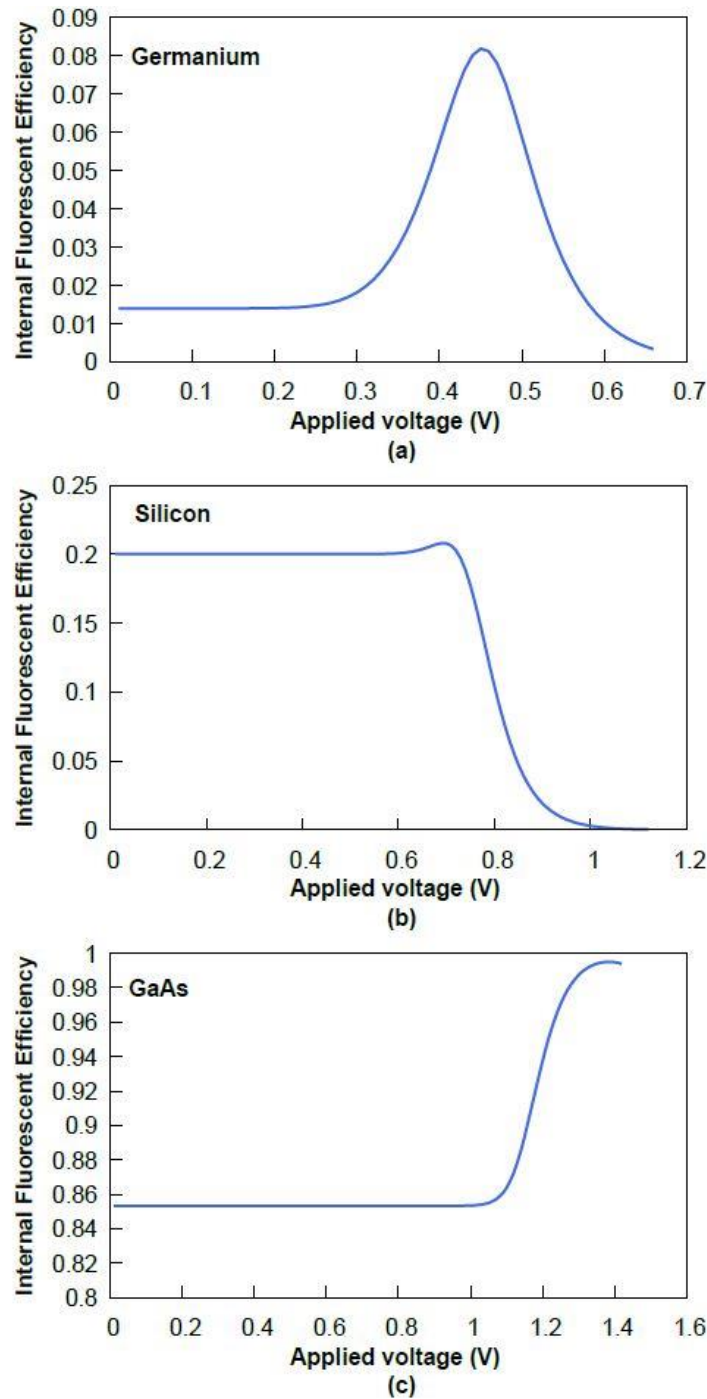


FIGURE IV-9 Variation of the IRE (equivalent to the internal fluorescent efficiency) as a function of the applied voltage for Ge, Si and GaAs semiconductors.

The ratio between radiative and non-radiative recombination is found to be a function of the applied voltage. However, it is of paramount importance to grasp how this ratio varies with the degree of angular restriction, to precisely assess the effects of non-radiative losses on both the iso-efficiency and the iso- V_{oc} curves.

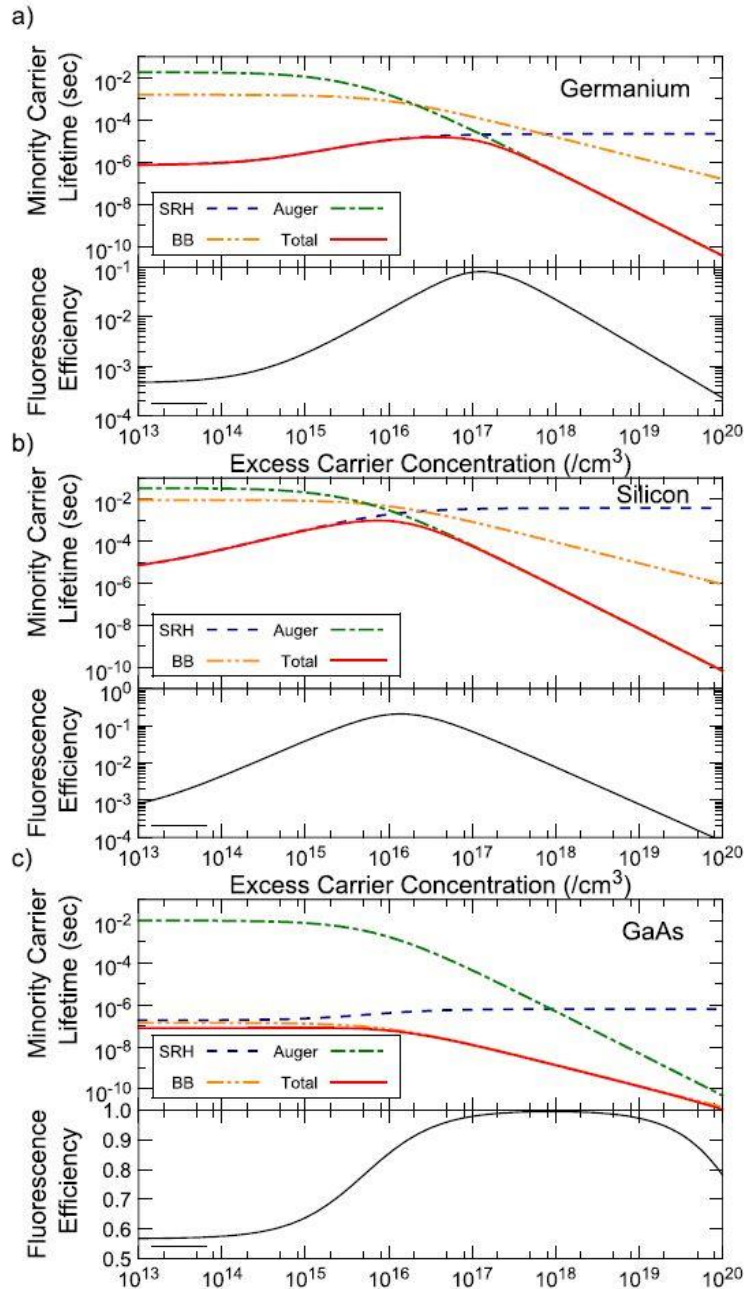


FIGURE IV-10 Minority carrier lifetime and internal fluorescence efficiency as a function of the excess carrier concentration for three semiconductor materials: Ge (a), Si (b) and GaAs (c) [7].

Thus, the second part of this study consists in finding how varying the angles of emission affects the *ERE* value. To solve this issue, the problem was divided into three parts:

- 1- Finding a relation between angular restriction and minority carrier lifetime.
- 2- Understanding how the minority carrier lifetime affects the internal radiative efficiency.
- 3- Finding an equation linking *ERE* to *IRE*.

The minority carrier lifetime and the *IRE* are plotted as a function of the excess carrier concentration in Fig.IV-10 [7], for three semiconductor materials Ge (a), Si (b) and

GaAs (c). The calculations are performed using equations (IV-3), (IV-7)-(IV-9) knowing that the carrier lifetime can simply be expressed as:

$$\tau_i = \frac{n_{ex}}{R_i} \quad (\text{IV-13})$$

with R_i the recombination rate and τ_i its respective lifetime. For Ge and Si semiconductors, characterized by strong SRH and Auger recombination rates, the IRE remains very low over a broad range of n_{ex} , despite the noticeable increase in the radiative recombination one can observe for intermediate values of the excess carrier concentration. Conversely, in the case of GaAs, radiative recombination dominate over a large range of excess carrier concentration, leading to IRE approaching 100% for excess carrier concentrations typically comprised between 10^{17} and $10^{19} / \text{cm}^3$.

After addressing the first two points (parts 2- and 3-) mentioned earlier, in order to understand the emission angle effect on the ERE, one has to clarify how the *external* radiative efficiency is correlated to both the different recombination rates and the angular properties of the emitted beam.

A direct link between the different recombination currents and the ERE value can be derived using the approach suggested by Höhn et al. [14] and Rau et al. [16]. In this approach the ERE is computed as:

$$ERE = \frac{J_{rad}}{J_{rad} + J_{Auger} + J_{SRH}} \quad (\text{IV-14})$$

with J_{rad} , J_{Auger} and J_{SRH} the radiative, Auger and SRH recombination currents respectively, where:

$$J_{rad}(V, \theta_{ext}) = q \int_0^\varphi \int_0^{\theta_{em}} \int_0^\infty \alpha(\lambda, W) \frac{2hc^2}{\lambda^5} \times \left(\frac{1}{\exp\left(-\frac{hc}{\lambda kT}\right) - 1} - \frac{1}{\exp\left(-\frac{hc}{\lambda kT} - q \cdot 0\right) - 1} \right) \times \frac{\lambda}{hc} \cos\theta d\lambda d\Omega$$

$$J_{rad}(V, \theta_{ext}) = q \int_0^\varphi \int_0^{\theta_{em}} \int_0^\infty \alpha(\lambda, W) \frac{2hc^2}{\lambda^5} \times \left(\frac{1}{\exp\left(-\frac{hc}{\lambda kT}\right) - 1} \right) \times \frac{\lambda}{hc} \cos\theta d\lambda d\Omega \times \left(\exp\left(\frac{qV}{kT}\right) - 1 \right) \quad (\text{IV-15})$$

$$J_{Auger}(V) = qC_{Auger} W n_i^3 \exp\frac{3qV}{2kT} \quad (\text{IV-16})$$

$$J_{SRH}(V) = q \frac{n_i}{\tau_{n0} + \tau_{p0}} W \exp\left(\frac{qV}{2kT}\right) \quad (\text{IV-17})$$

with α the absorptivity, λ the wavelength, W the cell thickness, θ_{em} the angle of emission (which depends on the angular confinement) and C_{Auger} the Auger coefficient.

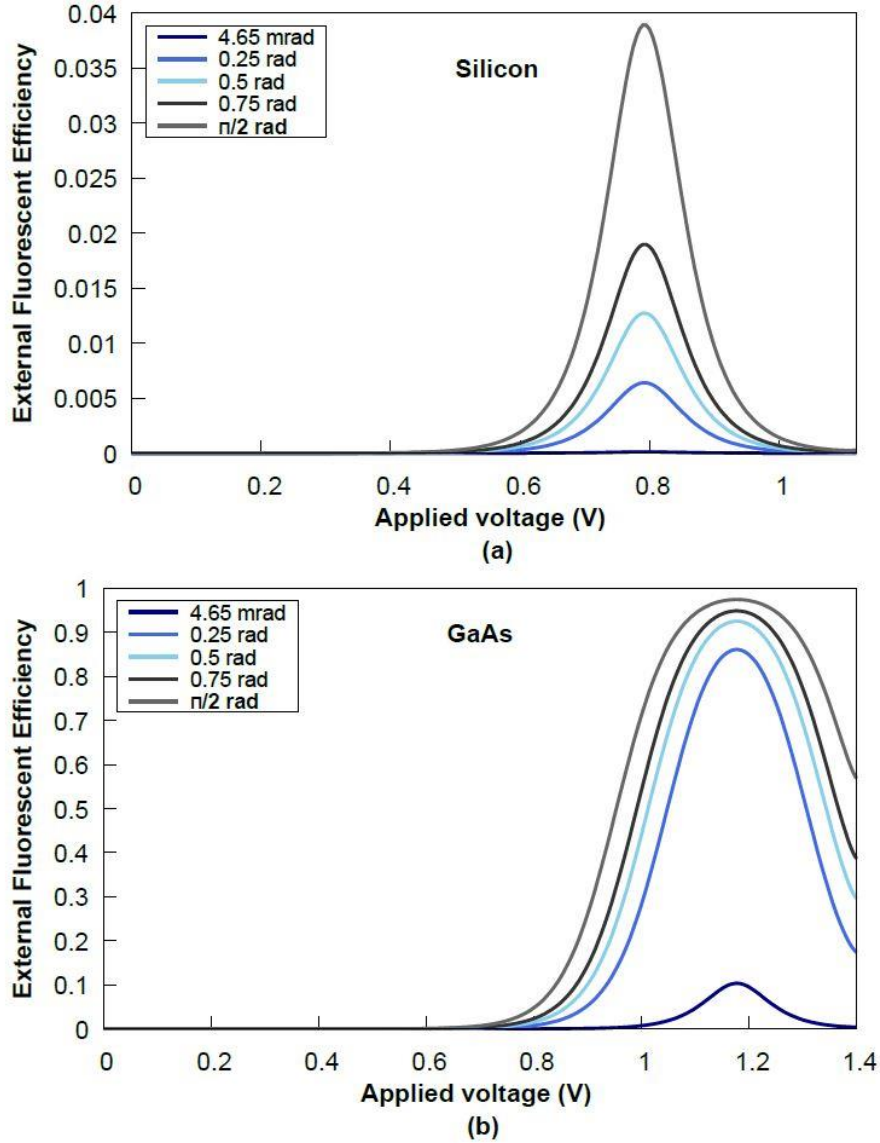


FIGURE IV-11 Variation of the ERE as a function of the applied voltage for Si (a) and GaAs (b) semiconductors assuming thicknesses of 100μm for Si and of 1μm for GaAs.

Using equations (IV-12) to (IV-15) and the appropriate semiconductor parameters, the external radiative efficiency is computed for Silicon and GaAs solar cells. Figure IV-11 represents the variation in the external radiative efficiency as a function of the applied voltage for these two materials (upper graph for Si assuming a thickness of 100μm (a), lower graph for GaAs with a thickness of 1μm (b)). Different emission angles are considered, varying between the maximum restriction angle (4.65 mrad) and $\pi/2$ (no angular restriction). As expected, the ERE decreases with increasing angular restriction for both cases, with a greater relative decrease rate at very high degrees of angular confinement for GaAs (and a lower decrease rate for low to medium/high angular confinement). Similarly to what was already

observed for the IRE, one can still identify three different regions in the graph, denoting voltage ranges where SRH, Radiative and Auger recombination respectively dominates. However some inconsistencies in the SRH-dominated voltage range can be noticed (the ERE being almost zero). Nonetheless, the model can be implemented to compute the cells performances accounting for the ERE variation with angular restriction (since the ERE at the operating point falls in the radiative region, thus minimizing the error committed).

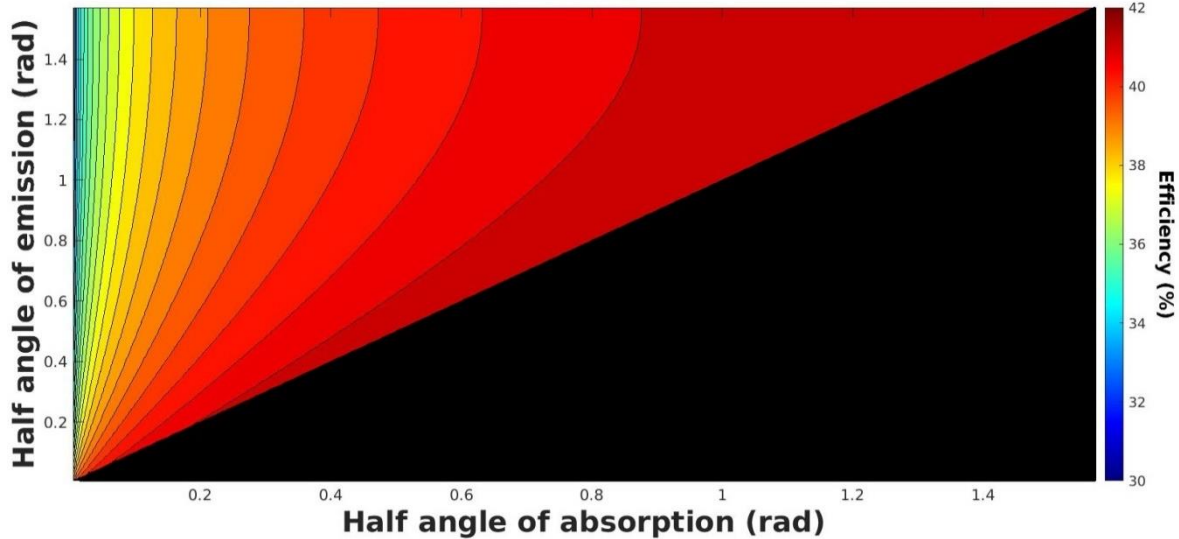


FIGURE IV-12 Iso-efficiency curve for a single-junction solar cell, characterized by a bandgap of 1.4eV as a function of the solar angles of emission and absorption, assuming no series resistances and an ERE varying with the degree of angular restriction.

Figure IV-12 represents iso-efficiency curves for single-junction solar cells, assuming a bandgap of 1.4 eV (which is equivalent to the bandgap of GaAs), no series resistances and an external radiative efficiency varying with the degree of angular restriction. The maximal efficiency reaches almost 41.5% with a V_{oc} of 1.4V and a fill factor of ~0.9. These performances are noticed for equal and large angles of emission and absorption. One should note the modest effect of these losses on the maximum conversion efficiency attainable, which remains close to 39% under maximum angular restriction.

Figure IV-13 represents iso-efficiency curves for single-junction solar cells, assuming a bandgap of 1.4 eV, a series resistance value of $0.001 \Omega \text{ cm}^2$ and an external radiative efficiency varying with the degree of angular restriction. The maximal efficiency is ~41% with a V_{oc} of 1.4V and a fill factor of ~0.9. These performances are noticed for relatively small angles of emission and absorption (typically between 0.046 and 0.11 rad), as one would expect when accounting for the combined effect of series resistance and ERE. Resistive losses remain the dominant limiting mechanisms, especially with increasing concentration, restricting the range of maximum efficiency attainable to a narrow angular extent in the low absorption/emission angle regions.

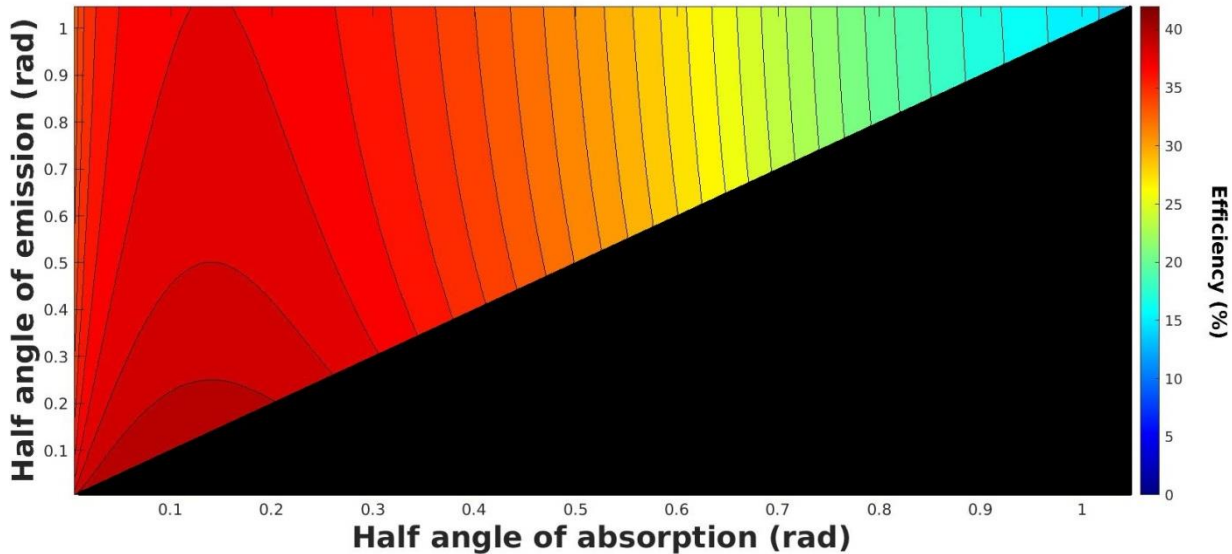


FIGURE IV-13 Iso-efficiency curve for a single-junction solar cell, characterized by a bandgap of 1.4eV as a function of the angles of absorption and emission, assuming a series resistance of $0.001 \Omega \text{ cm}^2$ and an ERE varying with the degree of angular restriction.

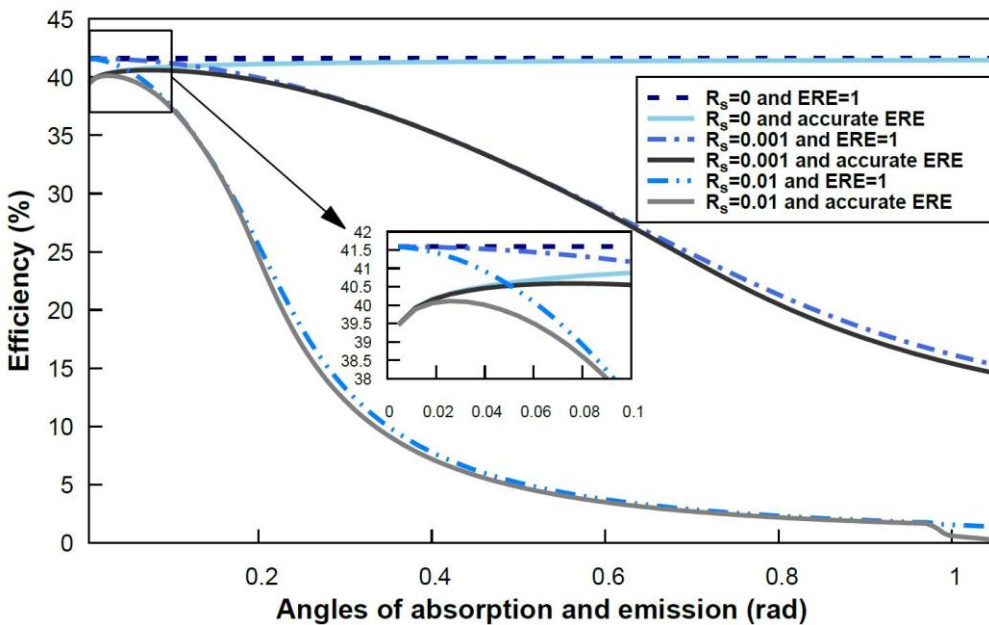


FIGURE IV-14 Efficiency as a function of the angles of absorption and emission (assumed to be equal) for different combinations of ERE and series resistance values.

Figure IV-14 illustrates the efficiency computed as a function of the solid angles of absorption and emission (assumed to be equal) for different combinations of series resistances and external radiative efficiencies, namely: ERE = 1 and $R_s=0 \Omega \text{ cm}^2$, accurate ERE (computed as function of the solid angle of emission) and $R_s=0 \Omega \text{ cm}^2$, ERE = 1 and $R_s=0.001 \Omega \text{ cm}^2$, accurate ERE and $R_s=0.001 \Omega \text{ cm}^2$, ERE = 1 and $R_s=0.01 \Omega \text{ cm}^2$, and accurate ERE and $R_s=0.01 \Omega \text{ cm}^2$. This plot illustrates the predominant effect of series resistance losses on the angular dependence of the maximum efficiency achievable: despite the minor effect of non-ideal ERE (which translates into a slight deviation of the curves precisely describing the angular dependence of ERE relative to the curves assuming 100%

ERE , in particular in the low angular range), there is a considerable effect of series resistance losses for a broad angular extent, which largely controls the maximum efficiency one can expect with this strategy.

These results were generated accounting twice for the effect of the emission angular restriction: in the computations of J_0 and of ERE . This inaccuracy will be corrected in a future work.

III. Conclusions

Combining solar concentration and angular restriction is a strategy developed to reduce the *Boltzmann* losses, thus aiming at achieving higher photovoltaic conversion efficiencies while lessening the effect of the limiting mechanisms corresponding to each strategy used alone. This chapter tried to evaluate how this approach enhances the cell's conversion efficiency, and to quantify the load of the different major limiting mechanisms which are resistive losses and low ERE values, as a function of the angular properties of the light absorbed and emitted.

The results obtained indicates that series resistances constitute the dominant limiting mechanisms in this strategy due to the dependence of resistive losses on the angles of absorption (i.e the concentration factors). On the other hand, low ERE levels decrease V_{oc} and the cell performances but their impact remains modest and is attenuated with increasing concentration ratio. The optimal performances are obtained for equal solid angles of absorption and emission, where the *Boltzmann* loss factor vanishes, with an angular range value depending on the limiting mechanisms considered.

Since angular restriction modifies the ERE value, a relationship should be found between ERE and the degree of angular confinement, to see the effect of the non-radiative losses as the solid angle of emission changes. Two models were described to tackle this issue, both of them being partially implemented and requiring further studies.

IV. References

- [1] L. C. Hirst and N. J. Ekins-Daukes, Fundamental losses in solar cells, *Prog. Photovolt: Res. Appl.*, 19 (2011) 286–293.
- [2] A. Vossier, D. Chemisana, G. Flamant, and A. Dollet, Very high fluxes for concentrating photovoltaics: Considerations from simple experiments and modeling, *Renew. Energ.*, 38 (2012) 31-39.
- [3] E.D. Kosten, J.H. Atwater, J. Parsons, A. Polman, and H.A. Atwater, Highly efficient GaAs solar cells by limiting light emission angle, *Light: Sci. App.*, 2 (2013) e45.
- [4] J.N. Munday, The effect of photonic bandgap materials on the Shockley-Queisser limit, *J. Appl. Phys.* 112 (2012) 064501.
- [5] M. Peters, J.C. Goldschmidt, and B. Bläsi, Angular confinement and concentration in photovoltaic converters, *Sol. Energ. Mater. Sol. Cell.*, 94 (2010) 1393-1398.
- [6] C.L. Schilling, O. Höhn, D.N. Micha, S. Heckelmann, V. Klinger, E. Oliva, S.W. Glunz, and F. Dimroth, Combining Photon Recycling and Concentrated Illumination in a GaAs Heterojunction Solar Cell, *IEEE J. Photovolt.*, 8 (2018) 348-354.

- [7] A. Vossier, F. Gualdi, A. Dollet, R. Ares, and V. Aimez, Approaching the Shockley-Queisser limit: General assessment of the main limiting mechanisms in photovoltaic cells, *J. Appl. Phys.*, 117 (2015) 015102.
- [8] M.A. Green, Green, M. A. (2012). Radiative efficiency of state-of-the-art photovoltaic cells, *Prog. Photovolt. Res. Appl.*, 20 (2012) 472-476
- [9] J.F. Geisz, M.A. Steiner, I. Garcia, S.R. Kurtz, and D.J. Friedman, Enhanced external radiative efficiency for 20.8% efficient single-junction GaInP solar cells, *Appl. Phys. Lett.* 103 (2013) 041118.
- [10] M. A. Steiner, J.F. Geisz, I. García, D.J. Friedman, A. Duda, and S.R. Kurtz, Optical enhancement of the open-circuit voltage in high quality GaAs solar cells, *J. Appl. Phys.* 113 (2013), 123109.
- [11] P. Wurfel, Physics of solar cells, 2nd edition, Wiley-VCH, Weinheim, 2009.
- [12] J. Nelson, The physics of solar cells, Imperial College Press, London, 2004.
- [13] S.S. Li, Semiconductor Physical Electronics, 2nd edition, Springer Science+Business Media, LLC, New York, USA, 2006.
- [14] O. Höhn, T. Kraus, U. T. Schwartz, B. Bläsi, Effects of angular confinement and concentration to realistic solar cells, *J. Appl. Phys.*, 117 (2015) 034503.
- [15] I. Schnitzer, E. Yablonovitch, C. Caneau, and T. J. Gmitter, Ultrahigh spontaneous emission quantum efficiency, 99.7% internally and 72% externally, from AlGaAs/GaAs/AlGaAs double heterostructures, *Appl. Phys. Lett.*, 62 (1993) 131-133.
- [16] U. Rau, U. W. Paetzold, and T. Kirchartz, Thermodynamics of light management in photovoltaic devices, *Phys. Rev. B*, 90 (2014) 035211.

Chapter V: Hybrid PV/CSP Systems

Hybrid PV/CSP systems appear as a promising technology toward effectively converting sunlight into electricity in an efficient, affordable, and dispatchable manner. They may simultaneously benefit from the high conversion efficiency and the low-cost of PV technology, together with the heat-storage capabilities of CSP systems. 3 main strategies are currently under investigation (see chapter II for a deeper description) and are schematically depicted in Figure V-1.

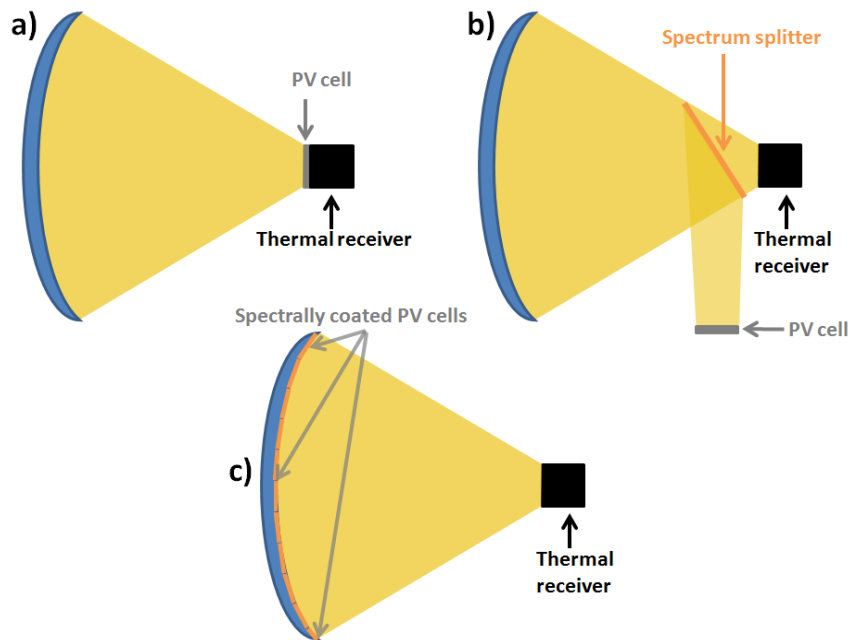


FIGURE V-1 Schematic of the 3 PV/CSP hybrid strategies investigated: (a) “high temperature PV”, (b) “spectrum splitting” and (c) “one-sun PV” approaches.

This chapter addresses 2 scientific issues of paramount importance in the quest of highly efficient hybrid systems: 1) The existence of different hybrid strategies raises the need for a rigorous comparison between them, based upon key indicators such as a) the solar to electricity conversion efficiency b) the dispatchability of the electricity generated (which translates the balance between the electricity generated by PV and CSP). 2) The “high temperature” approach involves PV cells operating under extreme conditions of temperature and illumination. Achieving the highest solar to electricity conversion using this approach requires the cell architecture to be optimized to such extreme conditions and the temperature and illumination dependence of the PV cells to be perfectly known. These 2 crucial points will be addressed in the second part of this chapter.

I. Comparison of the performances of the hybrid approaches

A. Methodology and assumptions

1. Objectives

As exposed previously, a suitable hybrid system should simultaneously fulfill 2 key criteria: 1) it should have a high solar to electricity conversion efficiency, 2) it should show a balanced share between PV and CSP electricity production to ensure both affordable and dispatchable electricity production (otherwise, the system has a PV or a thermal

predominance), leading to a) non-sufficient energy storage (if the system is predominantly PV) or b) expensive electricity production (if the system is mostly thermal).

These 2 criteria are evaluated as a function of the semiconductor bandgap energy, first in the radiative limit for PV operation (assuming no resistive losses, no non-radiative recombination, one electron-hole pair engendered per absorbed photon and no absorbed photon with energy lower than the bandgap energy), and then for more realistic solar cells with non-radiative recombination or resistive losses. The assessment is then broadened to evaluate the benefit for an additional spectrum-splitting degree of freedom in the case of the “spectrum-splitting” and the “one-sun” approach.

In order to answer these questions, a number of assumptions are formulated, both for the PV cell and the thermal receiver operation.

2. Assumptions

a) One-sun PV approach

The one sun PV approach, which relies on solar cells covering the surface of an optical concentrator, operates at ambient temperature and under 1 sun illumination. Because these cells are not submitted to concentrated sunlight, the amount of solar radiation available exceeds that of the 2 other approaches, since they are also exposed to diffuse sunlight (unlike PV cells at the focus of a solar concentrator). This strategy implies a splitting of the spectral distribution of the incoming photons into 2, or more, distinct ranges of energy. With one cut-off energy ($E_{cutoff1} = E_g$), photons with energies equal or higher than the bandgap of the PV cell are transmitted to the solar cells, while the less energetic photons are diverted to the thermal receiver. By adding a second cut-off energy, with $E_{cutoff2} > E_g$, highly energetic photons, which are inefficiently converted by the PV cells, are redirected to the thermal receiver.

b) Spectrum Splitting Approach

The spectrum splitting strategy consists in using a spectrum splitting device that redirects the photons of the concentrated solar radiation, depending on their energy, toward the PV cells or the thermal absorber. As PV cells are supposed to operate under concentrated sunlight, only the direct normal solar radiation can be converted by the cells. Since both subsystems are apart from each other, this system offers an increased versatility in the sense that the operating conditions (illumination level and operating temperature) of each subsystem can be controlled independently. In this case also, a spectrum splitting device with two cut-off energies can be integrated in the system to improve the conversion of the solar spectrum.

c) High-temperature PV approach

This approach is based on the use of an integrated receiver, the top of which comprises PV cells that are thermally bonded to a thermal receiver below them, capable of absorbing both the heat resulting from non-ideal PV conversion (carrier recombination), the heat generated by *thermalization*, as well as the non-converted photons. Optical concentration values of hundreds to thousands of suns are envisioned. This amalgamated absorber would operate at the temperatures required for efficient turbine conversion but engenders the intrinsic reduction of PV efficiency with temperature. Unlike the two previous approaches,

the use of an integrated receiver avoids any additional degree of freedom in the control of the spectral distribution of the light impinging the converter: each photon should ideally be absorbed, independently of its wavelength.

d) Thermal receiver

The heat transfer fluid and the turbine properties limit the operating temperature of the thermal receiver. Most of the line-focus CSP power plants operate around 666K since synthetic oil, which decomposes at almost 673K, is commonly used in such systems. Replacing synthetic oil with molten salts increases the operating temperature to ~823K [1-4]. We thus considered these two receiver temperatures, 666 and 823K, even if higher temperatures can be reached with point focus systems. We explored a broad range of illumination levels, corresponding to different families of optical concentrators, namely 25 and 50 suns (corresponding to the illumination levels achievable with line focus concentrating systems), and 1000 and 2000 suns (typical values for point focus systems).

In all cases the thermal receiver is assumed to operate at 2/3 of the Carnot limit, a practical bound representative of realistic operation for a broad range of CSP systems covering a large range of operating temperatures and sunlight concentrations [5].

e) General hypotheses

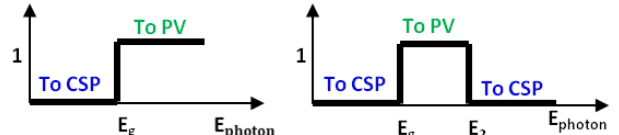
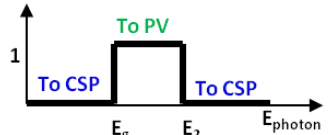
Each sub-system (i.e. the PV or CSP part of the hybrid system) of each hybrid approach investigated is assumed to operate under concentrated sunlight, with the notable exception of the PV cells in the one-sun approach. These cells being exposed to global (rather than direct) solar radiation, the conversion efficiency of each system is estimated based on global solar radiation, to ensure the consistency of our comparison. A global/direct ratio of 1.3 is assumed, based on data collected from 5 different highly insolated locations in the US: Albuquerque, Las Vegas, Phoenix, Redding and Reno.

Another practical consequence stemming from the use of non-concentrated light in the “one-sun” approach, is associated with the nature of the PV cells considered. For economic reasons, using non-concentrated light precludes the integration of advanced MJ solar cells in the “one-sun PV” approach system even if using this technology improves photovoltaic and overall hybrid efficiencies. Again, for the consistency of the comparison, single-junction solar cells-based systems are considered for all the calculations.

Add to this that, since the aim of the study is to find general comparison trends for the different hybrid approaches, no optical losses were assumed, as they depend strongly on the type of the solar concentrator, on the quality of the mirrors or the lenses used, and on the location of the installation.

Table V-1 summarizes the different PV cells operating conditions for the three hybrid systems studied.

TABLE V-1 PV operating conditions for the 3 hybrid approaches considered in this study.

	High temperature PV	Spectrum Splitting	One-sun cell
PV temperature	T_{CSP}	T_a (298K)	T_a (298K)
PV concentration	1000 suns	1000 suns	1 sun
Absorbed solar radiation	Direct	Direct	Direct + diffuse
Cut-off energy	-----	 1 or 2 cut-off energies	

3. Description of the Algorithm

TABLE V- 2 Summary of the equations used in this chapter

$$J = J_{ph} - J_0 \left(e^{\frac{qV}{nkT}} - 1 \right) \quad (\text{I-18})$$

$$J = J_{ph} - J_0 \left(e^{\frac{qV+IR_s}{nkT}} - 1 \right) \quad (\text{I-19})$$

$$J = J_{ph} - \frac{J_{0_rad}}{ERE} \left(e^{\frac{qV}{nkT}} - 1 \right) \quad (\text{IV-1})$$

$$E_g(T) = -0.5 \times 10^{-3} \times (T - T_{opt}) + E_{g_opt} \quad (\text{V-3})$$

$$P_{\text{rad}} = \varepsilon \sigma \times (T^4 - T_a^4) \quad (\text{II-25})$$

$$P_{\text{conv}} = h_c \times (T - T_a) \quad (\text{II-26})$$

$$P_{CSP} = (P_{in} - P_{PV} - P_{rad} - P_{conv}) \frac{2}{3} \times (1 - \frac{T_a}{T}) \quad (\text{II-29})$$

$$\eta_{hybrid} = \eta_{PV} + \eta_{CSP} \quad (\text{II-31})$$

The comparison of the different hybrid systems is done using Matlab. The algorithm, which is similar to the one described in chapter III, solves the general *I-V* characteristic equation for ideal solar cells (eq. (I-7)), and accounting for series resistances (eq. (I-9)) and non-radiative recombination (eq. (IV-1)), for a broad range of temperatures and concentrations. After computing the PV efficiency, the overall hybrid efficiency is found using eq. (II-25), (II-26), (II-29) and (II-31) detailed in chapter II, assuming a heat transfer coefficient of $20 \text{ W m}^{-2} \text{ K}^{-1}$ to compute the convective losses. The second cut-off energy is optimized using genetic algorithm, aiming to maximize the peak overall efficiency. For a better clarity, Table V-2 recalls the equations used in this chapter, with the diode ideality factor n and the emissivity ε both equal to 1.

B. Results

1. Ideal solar cells

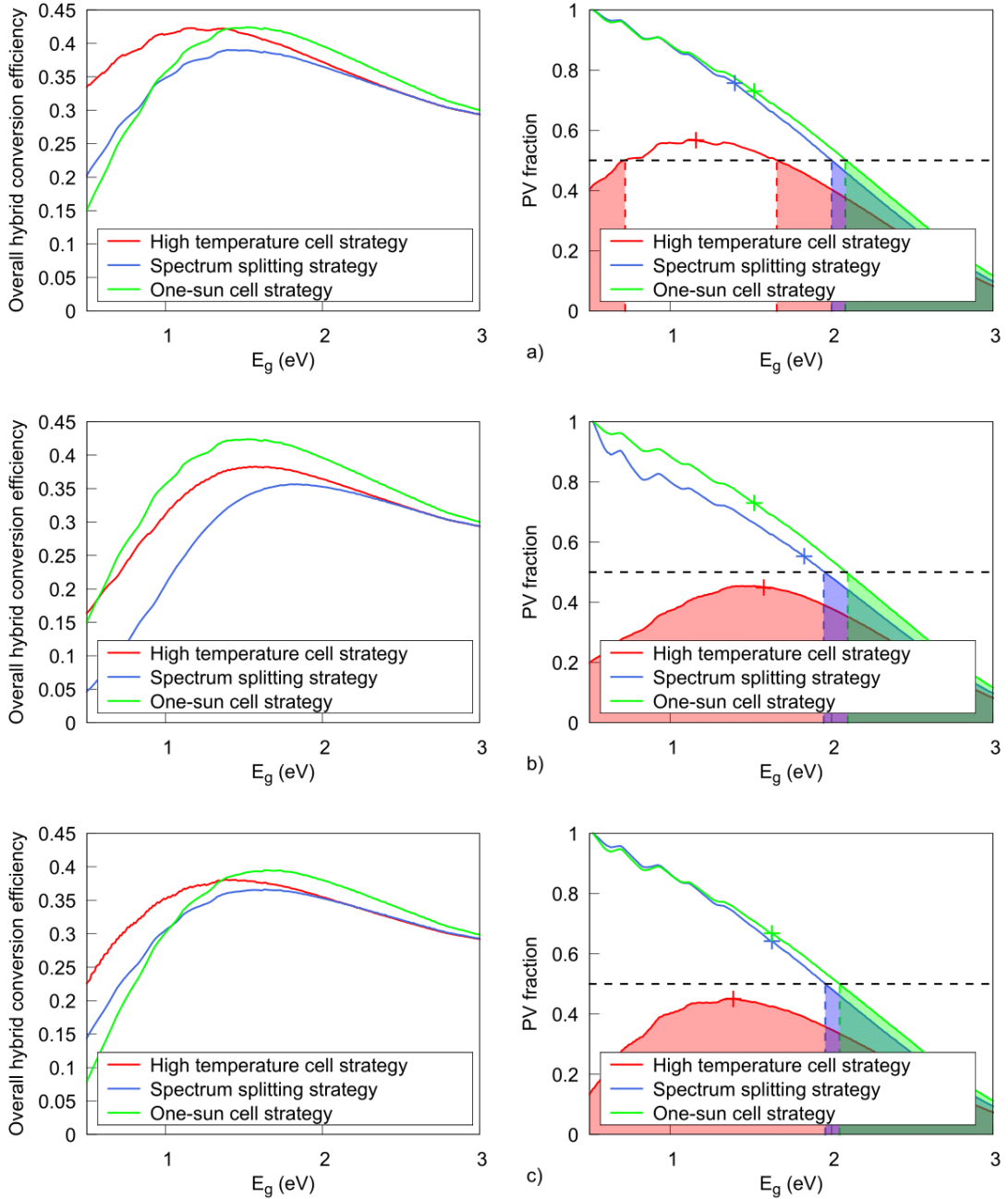


FIGURE V-2 Overall hybrid conversion efficiency (left) and PV contribution to total electricity generated (right) as function of the electronic energy gap for the three hybrid systems with ideal solar cell at a concentration level of 1000 suns operating at the radiative limit (a), solar cells with $R_s = 0.01 \Omega\text{-cm}^2$ (b) and solar cells with ERE = 1% (c).

The left-hand side graphs of figure V-2 represent the maximum achievable efficiency for the three described types of hybrid PV/CSP systems as a function of E_g , while the right-hand side graphs illustrate the PV fraction of the generated electricity. The crosses indicate the PV fraction corresponding to the point of maximum system efficiency, and the colored parts represent PV fractions less or equal to 0.5. The thermal receiver operates at

a temperature of 666K and a sunlight illumination of 1000 suns. The PV operating conditions are listed in Table V-1.

In the case of an ideal single-junction solar cell (no series resistances and ERE=100%), as observed in fig. V-2(a), the different strategies considered show similar trends for the bandgap dependence of the conversion efficiency, with peak efficiencies occurring in the range 1.1-1.5 eV. Both, the “high-temperature PV” and the “one-sun PV” approaches demonstrate the highest performance, with a maximum efficiency of 42%, against 39% for the spectrum-splitting approach. Some differences can be observed in the contribution of each sub-systems: for the “one-sun PV” and the “spectrum-splitting” strategies the PV fraction decreases as the bandgap increases. At the bandgap value corresponding to the highest efficiency, the system is mostly photovoltaic with a fraction of 0.757 and 0.731 for the “spectrum splitting” and the “one-sun PV” respectively. On the other hand, we find a more balanced share between the electricity generated by PV and CSP for the high-temperature approach for a wide range of bandgaps, with a fraction of 0.567 at the point of maximal efficiency.

2. Realistic solar cells

Graphs 2(b) and 2(c) consider more realistic cells with non-negligible series resistance ($R_s = 0.01 \Omega\text{-cm}^2$) and non-radiative recombination (with an external radiative efficiency ERE = 1%) respectively. The values of series resistance and external luminescence efficiency are chosen based on state-of-the-art single-junction concentrated PV at ambient temperature [6, 7].

Taking into account non-negligible series resistances does not affect the “one-sun PV” approach since solar cells are not submitted to concentrated sunlight. As a result, resistive losses remain negligible and both the system efficiency and the PV fraction variations remain similar to the ideal case. For the two other strategies, and as described earlier, considering important series resistance values generates high resistive losses (these losses being proportional to the square of the current, which increases linearly with concentration). Hence, the conversion efficiency is reduced, and the optimal bandgaps shift toward higher values (from 1.16 to 1.58 for the “high-temperature” cell, and from 1.4 to 1.83 for the “spectrum splitting”), as a result of the lower penalty associated with series resistance losses for high bandgap materials. We clearly see a decrease in the PV fraction, the best-balanced share remaining associated with the “high temperature PV” approach.

Taking into account low external radiative efficiency modestly reduces the maximal overall hybrid conversion efficiency, since this limiting mechanism mostly affects low-bandgap solar cells. Optimal bandgaps being relatively high, the lessening of the maximal overall efficiency remains acceptable. In this case also, the “one-sun PV” approach presents the highest conversion efficiency, followed by the “high temperature cell” then by the “spectrum splitting” strategies. The lowest efficiencies occur for both approaches involving concentrated sunlight, even though concentration reduces the cell sensitivity to non-radiative recombination.

One would presume that hybrid approaches involving sunlight concentration onto the PV cells outperform the “one sun approach”. However, these expectations are not observed because of 1) the fundamental inability of strategies involving concentrated sunlight to convert diffuse radiation 2) the significant negative effect of temperature in the “high-temperature” approach and 3) the incapability of the “spectrum-splitting” system to convert heat generated by *thermalization*, and by non-radiative recombination and resistive losses when relevant.

Table V-3 summarizes the maximal efficiency as well as the PV fraction of the generated electricity for the three different approaches, in the idealized case and considering non-negligible series resistance and non-radiative losses. The values in brackets represent the variation in efficiency relative to the ideal case.

TABLE V-3 Maximum efficiency (η) and PV fraction (PV_f) at the point of optimal efficiency computed for each hybrid strategy.

PV cell model	High temperature cell	Spectrum splitting	1-sun cell
Radiative limit	$\eta=42.3\%$ $PV_f=56.7\%$	$\eta=39.0\%$ $PV_f=75.7\%$	$\eta=42.4\%$ $PV_f=73.1\%$
$R_s = 0.01 \Omega \text{ cm}^2$	$\eta=38.3\% (-10\%)$ $PV_f=44.9\%$	$\eta=35.7\% (-9\%)$ $PV_f=55.3\%$	$\eta=42.4\% (0\%)$ $PV_f=73.1\%$
ERE = 1 %	$\eta=38.1\% (-10\%)$ $PV_f=45\%$	$\eta=36.7\% (-6\%)$ $PV_f=64.2\%$	$\eta=39.5\% (-7\%)$ $PV_f=66.9\%$

Table V-4 summarizes the results for ideal solar cells-based hybrid approaches at different temperatures and concentration levels.

TABLE V-4 Maximum system efficiency for the 3 hybrid strategies, based on ideal solar cells, for different concentration levels and two receiver temperatures, 666 and 823K, as well as the PV fraction.

Approach	Concentration (suns)	Hybrid efficiency (%)		PV fraction	
		666K	823K	666K	823K
High-temperature PV	25	0.350	0.286	0.525	0.508
	50	0.378	0.351	0.512	0.449
	1,000	0.423	0.430	0.567	0.485
	2,000	0.433	0.441	0.584	0.502
Spectrum-splitting strategy	25	0.332	0.279	0.722	0.801
	50	0.356	0.340	0.682	0.714
	1,000	0.390	0.403	0.757	0.637

	2,000	0.396	0.411	0.756	0.680
1-sun cell strategy	25	0.386	0.331	0.804	0.882
	50	0.407	0.389	0.762	0.750
	1,000	0.424	0.438	0.731	0.667
	2,000	0.426	0.443	0.728	0.660

3. Two-cut-off energies

Figure V-3 represents the maximum hybrid efficiency (left) and the PV fraction (right) as a function of the electronic energy gap, while implementing a high cut-off energy to the spectrum splitting device, to further improve the solar energy absorption. Graphs (3a) consider ideal solar cells operating in the radiative limit, while Fig.V-3 (b) and Fig.V-3 (c) consider more realistic cells with non-negligible series resistance ($R_s = 0.01 \Omega\text{-cm}^2$) and low external radiative efficiency ($ERE = 1\%$) respectively. For clarity, the results obtained with only one cut-off energy are included as dashed colored curves. Since the cut-off energies are irrelevant to the high temperature PV approach, the respective results are omitted except for the overall efficiency represented in the left-hand side, for comparison purpose.

The graphs in the inset of the figures in the right-hand side illustrate the optimal second cut-off energies for both the spectrum splitting and the one-sun PV strategies as a function of the electronic energy gap. The black line indicates the points where $E_{cutoff} = E_g$. For a better equilibrium between PV and CSP, the second cut-off energy should be sufficiently far away from the bandgap energy, to allow a significant fraction of the solar energy to be converted by the PV, and to avoid having a predominantly thermal system.

For both the “one-sun” and the “spectrum-splitting” strategy, adding a high energy cut-off increases strongly the overall hybrid efficiencies and improves significantly the balance between PV and CSP, but only for low bandgap energies. Conversely, higher gaps are associated with lower *thermalization* losses which mean less improvement due to the high-energy cut-off.

To sum up, in all cases, adding a second cut-off energy to the spectrum splitting device does not increase the overall hybrid efficiency maximal value. In the radiative limit as well as for more realistic solar cells, it allows a more balanced share between the electricity produced by each sub-system only for $E_g < 1\text{eV}$, a region that does not correspond to the peak efficiency. For the spectrum splitting approach, and assuming the system is penalized by non-negligible series resistance losses, the implementation of an additional cut-off energy leads to an increased number of photons redirected onto the thermal converter, which results in predominantly thermal system in the region of low to medium bandgaps.

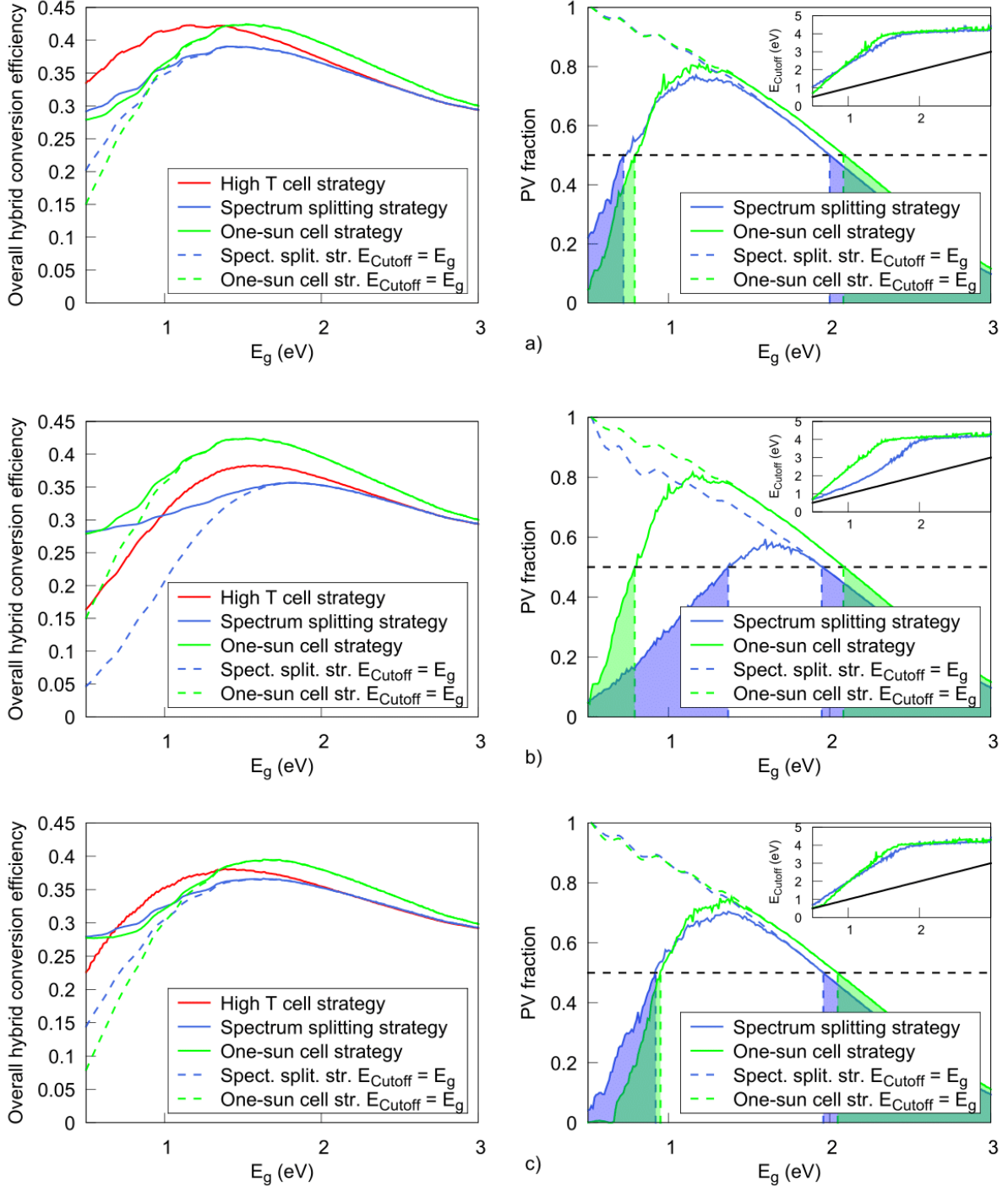


FIGURE V-3 Overall hybrid conversion efficiency (left) and PV contribution to total electricity generated (right) as function of the electronic energy gap, with two cut-off energies in the spectrum splitting device, for the three hybrid systems with ideal solar cell at a concentration level of 1000 suns operating at the radiative limit (a), solar cells with $R_s = 0.01 \Omega \cdot \text{cm}^2$ (b) and solar cells with ERE = 1% (c).

C. Conclusion

As a conclusion, based on the different cases studied and on the two criteria considered, the high temperature PV approach shows the best performance among the different strategies considered, with a peak conversion efficiency of ~42% (comparable with the one-sun strategy), and a relatively balanced share between PV and CSP in the power

output of the system. In addition, the implementation of multi-junction solar cells in the high temperature approach may boost the overall system efficiency, potentially allowing this strategy to outperform significantly the one-sun strategy (that operates only with single-junction cells). Such systems require extreme conditions of temperature and illumination, a range of operating conditions which has not been well investigated yet. Consequently, in the following section, solar cell performances are studied at very high temperatures and illumination levels, and the hybrid systems are assessed.

We also showed that adding a high-cut-off energy to the spectrum splitting device used for the one-sun PV and the spectrum splitting strategies does not improve the overall peak efficiency since it affects mostly low bandgap regions, where the PV *thermalization* losses are important.

II. High Temperature PV approach

A. Methodology and assumptions

1. Objectives

The high temperature PV approach requires operating solar cells at very high temperatures. Most of the cells nowadays are designed, tested and certified at ambient temperature (298K) with limited temperature range validity (typically up to 120°C). Such temperature range is not sufficiently large for the selected approach, as this parameter may vary between ambient and ~1000K. In the absence of a detailed theory describing solar cells operation at high temperatures, many issues should be tackled to evaluate the performances of such hybrid systems.

Major challenges are 1) to understand how to make PV cells efficiently operate at very high temperatures while maintaining negligible losses, and 2) to find the best cell architecture leading to the highest performance. The main objective here is to assess the ability of PV cells to operate at high temperatures, with the aim of reaching high overall hybrid efficiencies while assuring a balanced share between the energy produced by PV and CSP.

To tackle these issues, the electronic energy gaps of single and multi-junction solar cells are first optimized in order to maximize the photovoltaic conversion efficiency. The maximum performances of solar cells are then evaluated, assuming that they operate in the radiative limit, for a wide range of temperatures and sunlight illuminations. For this purpose, the principal electrical parameters, namely V_{oc} , J_{sc} , FF and η are computed and plotted as a function of the temperature for different cell architectures and concentration levels.

Once the upper limits on photovoltaic performances are established, we analyze the hybrid PV/CSP system power generation, where the performances are also optimized for a wide range of temperatures and solar illuminations.

2. Assumptions

a) Solar cells

Single and multi-junction solar cells were examined for the “high temperature PV” approach, in the radiative limit. The electronic energy gaps of the different cell architectures

considered should be tailored toward ensuring the highest solar to electricity conversion efficiency. Thus, an accurate knowledge of the bandgap temperature dependence is required, and a precise analytical model is needed to perform numerical analysis aiming to predict the bandgap variation with temperature. It is known that bandgap decreases with increasing temperature due to electron-phonon interaction, the phonon distribution as well as the lattice dilatation with temperature [8, 9]. These causes are complex to quantify, preventing the implementation of any general model accurately describing the variation of bandgap with temperature.

In the past decades, researchers used to derive bandgap values at high temperature experimentally [9]. Many models were proposed to quantify such dependence. Varshni was the first to suggest a semi-empirical model to estimate the temperature dependence of the bandgap, as represented in equation (V-1) [8],

$$E_g(T) = E_g(0) - \frac{\alpha T^2}{T + \beta} \quad (\text{V-1})$$

To compute the bandgap at a specific temperature, $E_g(T)$, the model necessitates three parameters, i.e. $E_g(0)$, the value of the bandgap at 0K, and α and β , material constants, with β being related to the Debye temperature (an upper bound for the temperature below which quantum effects can be seen). This model evaluates the temperature dependence of the electronic energy gap with reasonable accuracy, but it cannot be applied to a broad range of temperature, nor for wide bandgaps, and it doesn't consider any phonon effects [10]. Despite its major drawbacks, this model remains the most widely used today.

Viña, et al. [11] proposed a model handling the electron-photon interaction, which is also limited since it cannot be used for a wide range of temperature and still cannot treat the phonon dispersion issue at high temperature. Many other models were proposed to correct Varshni's model [12, 13] and the best model known is described by Pässler [10, 14] and accounts for the phonon effects. However, the analytical function considered for the phonon effect estimation strongly depends on the coupling coefficients whose values are sparsely documented [15].

In the absence of any general theory able to precisely describe the temperature dependence of the bandgap, for a broad range of materials and temperature, and since most of the models are not valid at very high temperature, we opt for the most widely used model, the Varshni's equation to estimate a bandgap temperature coefficient that can be used in our simulations.

The bandgaps of a wide range of semi-conductors described in [16] are plotted as a function of temperature, using equation (V-1), as shown in Figure V-4, with an average value of -0.472meV/K. Table V-5 compares measured bandgaps temperature coefficients for GaAs [16,17] and a number of III-V semiconductors that are also candidates for efficient concentrator cells. Based on these data, we assume a bandgap temperature coefficient of -0.5 meV/K leading to the following relation:

$$E_g(T) = E_g(0) - 0.5 \times 10^{-3} \times T \quad (\text{V-2})$$

with T in K, E_g in eV, and $E_g(0)$ denoting the bandgap at $T = 0$ K.

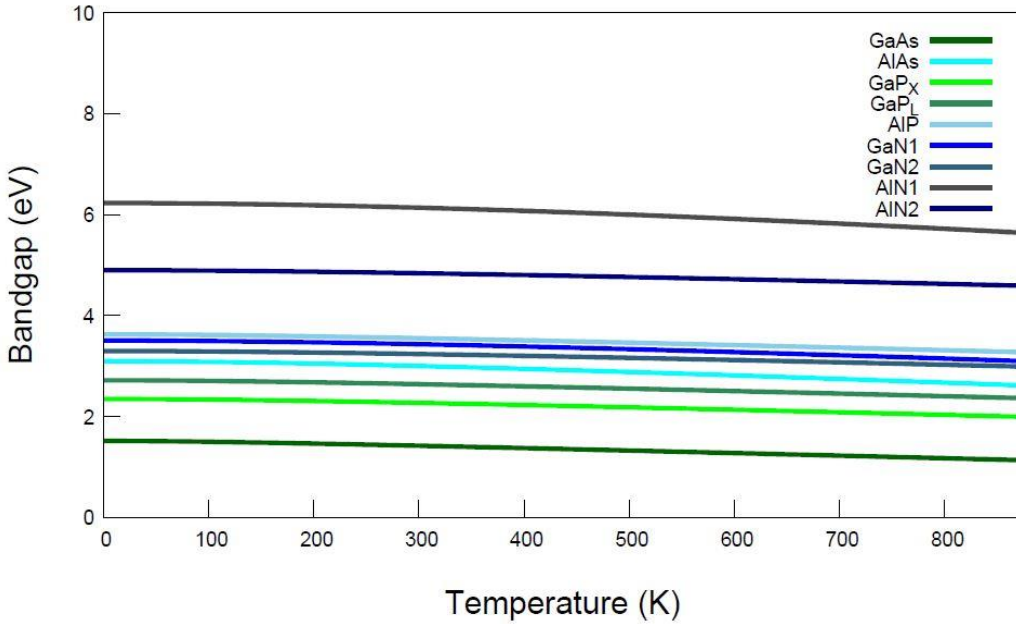


FIGURE V-4 Material specific temperature dependent bandgaps as a function of temperature.

TABLE V-5 Bandgap temperature coefficient for III-V semiconductors.

Material	Temperature range (K)	Bandgap temperature coefficient (meV/K)	References
GaP	300-1273	[-0.45 -0.54]	[18-20]
GaAs	21-973	[-0.45 -0.5]	[17, 20-22]
InGaP	523	-0.51	[22]
AlGaInP	298-673	-0.48	[23]
AlN	150-350	-0.55	[24]

After finding the relation describing the bandgap variation with temperature, the gaps are optimized for operating temperatures of 523K, 773K and 973K. The bandgap values for temperatures diverging from the temperature at which the optimization is done are calculated on the range 298-1050K, using equation (V-3) that stems from equation (V-2).

$$E_g(T) = -0.5 \times 10^{-3} \times (T - T_{opt}) + E_{g,opt} \quad (\text{V-3})$$

with T_{opt} the temperature of optimization and $E_{g,opt}$ the bandgap optimized at T_{opt} .

We evaluate and plot the main electrical parameters, namely V_{oc} , J_{sc} variation, FF and η_{PV} , for ideal solar cells in the radiative limit, under the AM1.5D spectrum, and for different operating temperatures and sunlight illuminations. We consider single, double and triple junction cells to understand the extent to which high temperatures may alter the performance of different cell architectures, for three optimization temperatures.

b) Hybrid system

In a second phase, the hybrid system performances are investigated for different temperatures and concentration levels. The systems are based on tandem cells with their bandgap optimized for each temperature and concentration, maximizing the photovoltaic

conversion efficiency. We start by exploring PV cells operating in the radiative limit, then we account for more realistic cells operating at 2/3 of the ideal limit, a practical bound representative of real operation for a broad range of commercial cells [25, 26]. In all cases, thermal receivers are assumed to operate at 2/3 of the Carnot limit [5]. Radiative and convective losses are computed based on equations (II-24) and (II-25).

3. Description of the algorithm

The program used to study the effects of temperature on the main electrical parameters, (i.e. V_{oc} , J_{sc} , FF and η), and to search for the optimal bandgaps (or combination of bandgaps in the case of MJ cells) is similar to the one described in chapter III, solving for the general I - V characteristic equation for ideal solar cells (eq. (I-7)), at the radiative limit (check Table V-7 for the list of equations). A broad range of temperatures and concentration factors are evaluated, for single and multi-junction solar cells. The overall system efficiency is assessed using the same algorithm described earlier in this chapter. It should be noted that the optimal bandgaps are optimized using genetic algorithm for different cell architectures and several pairs of temperatures and solar concentration factors.

B. Results

1. Single junction solar cells

a) *SO limit at high temperatures*

Shockley-Queisser efficiency limits are usually represented as a function of the cell electronic energy gap at ambient temperature. Figure V-5 represents these performances at 298K for 1-sun illumination as well as for higher temperatures and concentrations. It illustrates the efficiency of a single junction solar cell as a function of the electronic energy gap for a broad range of temperatures and concentrations, assuming an AM1.5D spectrum. In this case, there is no need to assume any bandgap coefficient, since the gap is being varied over a broad range in order to find its optimal value for each temperature and concentration, rather than being derived from a bandgap value at a specific temperature.

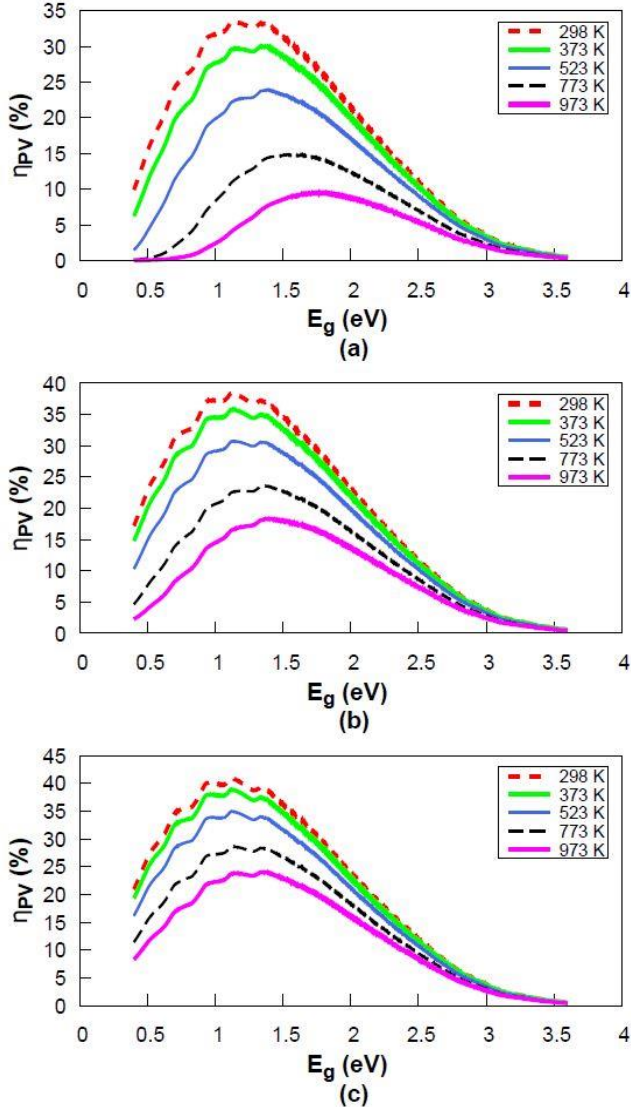


FIGURE V-5 Maximal theoretical achievable PV efficiency for a single-junction cell as a function of the gap for temperatures between 298 and 973K and for concentration level of 1 (a), 100(b) and 1000 (c) suns.

Even though the effect of high temperatures on PV is investigated here, we represent the trends for low temperatures and 1 sun illumination level as a reference basis (note that 1 sun illumination precludes attaining high receiver temperature, unless electrical or fluid heating is used).

Concentrations of 1, 100 and 1000 suns are chosen, and are respectively representative of the illumination level achievable without any optical concentrator, with a line focus system (parabolic trough) [27], and with a point focus (solar tower) [28]. Even if the maximum theoretical concentration can reach 46000 suns [29], we don't consider illumination levels exceeding 1000 suns, a practical limit observed for many commercial CPV systems nowadays.

For single-junction solar cells, the conversion efficiency decreases with increasing temperature. Figure V-5 shows that at very low concentration, the optimal bandgap shifts toward higher electronic energy gaps as the temperature increases. As the concentration rises,

the temperature effect is lessened: the difference between the curves corresponding to various temperatures becomes smaller, and the shift toward higher bandgaps almost disappears at very high concentration. Using solar concentration can thus improve solar cell operation at high temperatures by increasing its conversion efficiency, and by reducing the penalty associated with increasing temperature (the improvements being mostly observed for low to intermediate bandgaps). The benefit of sunlight concentration on the ability of PV cells to accommodate high operating temperature have been demonstrated for temperatures up to tens of degrees above the ambient [30-32], but not for such high temperatures.

b) Electrical parameters variations

Figure V-6 represents the temperature dependence of η_{PV} , V_{oc} , J_{sc} variation relative to the J_{sc} value at the optimization temperature, 523K, and FF for a single-junction cell. The PV cells are tailored for an optimal operation at 523K, and concentrations of 1, 100 and 1,000 suns are investigated. The optimized bandgap values used are listed in Table V-6.

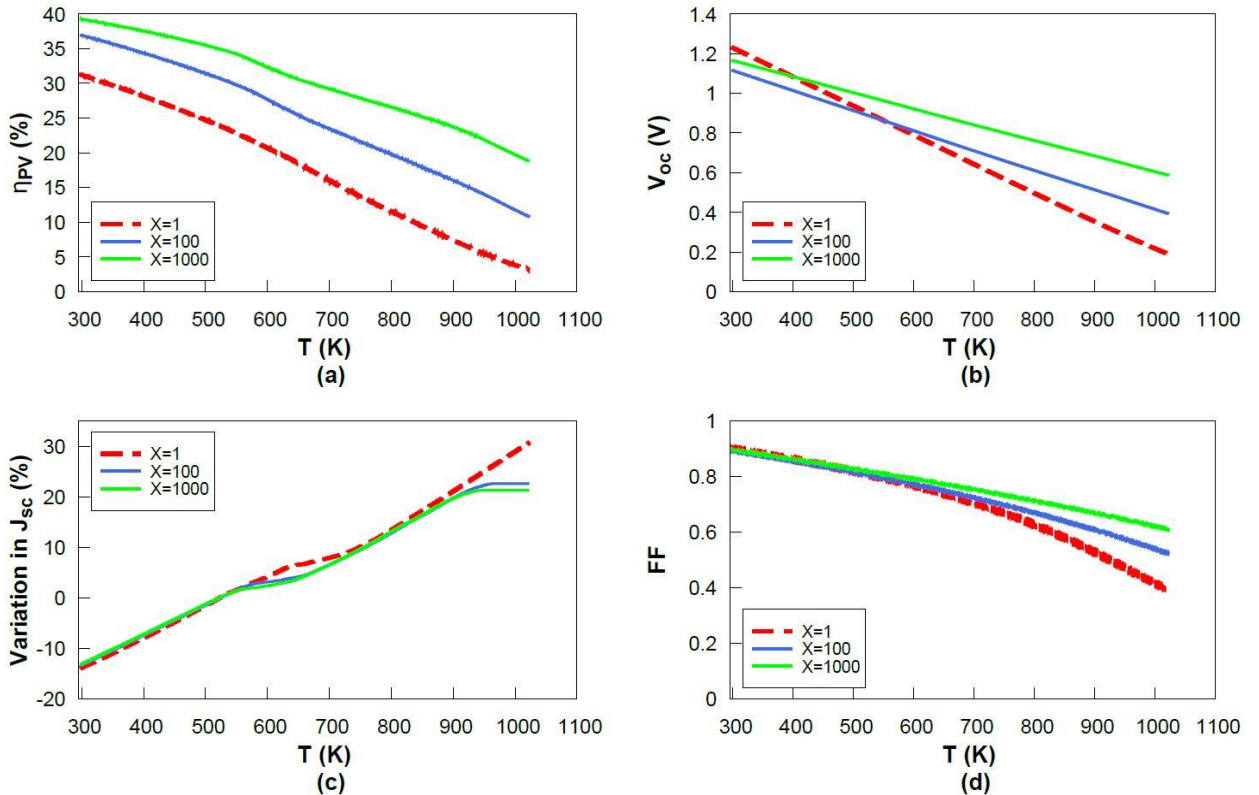


FIGURE V-6 (a) η_{PV} , (b) V_{oc} , (c) variation of J_{sc} and (d) FF, as a function of T for a single-junction cell optimized at $T = 523\text{ K}$ (see Table V-6), for $X = 1, 100$ and $1,000$ suns.

Figure V-7 represents the temperature dependence of η_{PV} , V_{oc} , FF, as well as the J_{sc} variation relative to the 773K-optimized cell value, for a single-junction cell optimized at 773K, and for concentrations of 1, 100 and 1,000 suns.

Figures V-6(c) and V-7(c) illustrate the temperature behavior of the short-circuit current density, which increases with temperature, unlike the other electrical parameters. Photons from a larger spectral range are absorbed as E_g decreases due to increasing temperature, which raises the photo-generated current. The short-circuit current density

intensifies with temperature at various rates due to the discontinuous nature of the AM1.5D spectrum (characterized by large absorption bands in the mid infra-red region). Hence, the gain in J_{sc} associated with increasing temperature, or more specifically with the changes in E_g , is variable as well. The extent to which this effect may alter the temperature dependence of J_{sc} is highly dependent on the bandgap value and hence on the converted fraction of the solar spectrum. In fact, since the optimal bandgap combination differs from one illumination level to the other, an additional discrepancy is appended to the temperature behavior (which translates into different temperature behaviors for $T > 900\text{K}$ for the 523K-optimized cell, or $T > 850\text{K}$ for the 773K optimized cell).

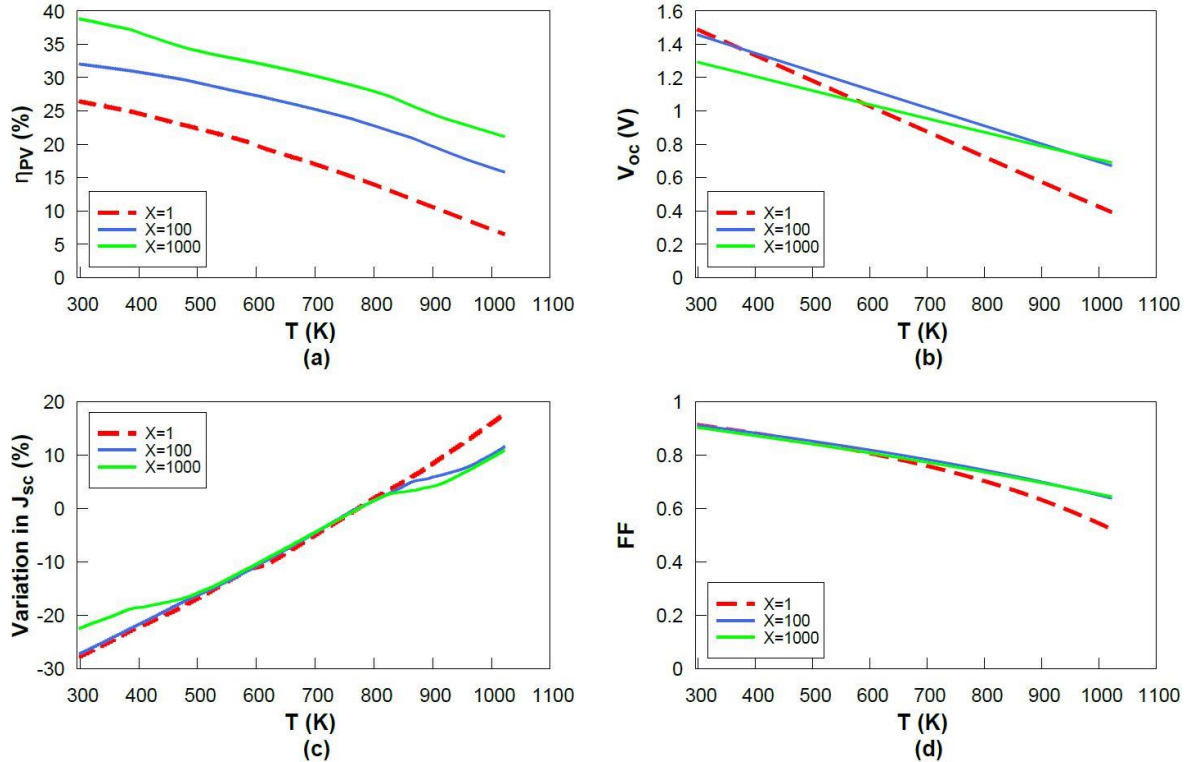


FIGURE V-7 (a) η_{PV} , (b) V_{oc} , (c) variation of J_{sc} and (d) FF, as a function of T for a single-junction cell optimized at $T = 773\text{ K}$ (see Table V-6), for $X = 1, 100$ and $1,000$ suns.

Unlike J_{sc} , V_{oc} is a decreasing function of the temperature, as shown in figures V-6(b) and V-7(b). The behavior of V_{oc} stems from two competing factors: the bandgap and temperature dependence of J_0 (which is proportional to the cube of the temperature) and the reliance of J_{ph} on E_g and on the concentration level (J_{ph} increases linearly with increasing sunlight illumination). As a result, and for a given concentration, V_{oc} decreases linearly with increasing temperature due to the exponential increase of J_0 with decreasing E_g . The detrimental effect of temperature on V_{oc} is significantly mitigated with increasing concentration.

The same trends hold for the fill factor (figures V-6(d) and V-7(d)), with solar illumination reducing the negative effect of temperature on this parameter. Up to 600K , the fill factor is not significantly affected by concentration and its lessening with temperature is still acceptable. Above this temperature, the strong decrease in V_{oc} causes a noticeable decrease in FF. We should note that the behavior described applies only for ideal solar cells,

assuming no resistive losses. Otherwise, the decrease is more pronounced at high temperature (due to reduced carrier mobility [33]) and high concentration (due to increased current).

The conversion efficiency decreases with increasing temperature, as a result of the negative temperature effect on V_{oc} and FF, which is not counterbalanced by the slightly positive effect of temperature on J_{sc} (as can be seen in fig.V-6(a) and fig.V-7(a)). These two graphs also point out the ability of solar concentration to decrease temperature sensitivity.

In the following section, we investigate how multi-junction solar cells are affected by high-temperature operation.

2. Multi-junction solar cells

a) Bandgap optimization

Prior to evaluating the temperature dependence of the main electrical parameters of the cell, we first investigate the maximum efficiency achievable with tandem and triple junction solar cells as a function of the electronic energy gaps of the materials involved in the stack.

Iso-efficiency curves are plotted as a function of the bandgaps of the top and bottom junctions for tandem cells, and for different temperatures and sunlight illuminations, in order to optimize the electronic energy gap. A genetic algorithm is also used for this purpose, mainly for triple-junction solar cells (as explained in chapter III).

Figure V-8 represents iso-efficiency curves for tandem cells, and for temperatures of 298 (a), 523 (b), 773 (c) and 973K (d), assuming an illumination level of 100 suns. Figure V-9 depicts the trends for similar operating temperatures, but assuming an illumination level of 1000 suns. Table V-6 summarizes the optimal bandgaps for single, double and triple junction solar cells, computed at temperatures of 298, 523, 773 and 973K and for solar illuminations of 1, 100 and 1000 suns. The values in brackets displayed for the temperatures 523, 773 and 973K indicate the corresponding bandgap value at 298K, computed using equation (V-2) (which differs from the values indicated in the first lines of Table V-6 showing the optimal electronic energy gaps for an optimization temperature of 298K).

The conclusions described for the single-junction cells can be extended for double and triple junction PV: as the temperature increases, the efficiency decreases and the optimal combination of E_g shifts toward higher values. Concentrating solar illumination increases the efficiency and reduces the bandgap shift relative to the optimal bandgap combination at 298K (the optimal gaps remain close to the ones at one-sun illumination).

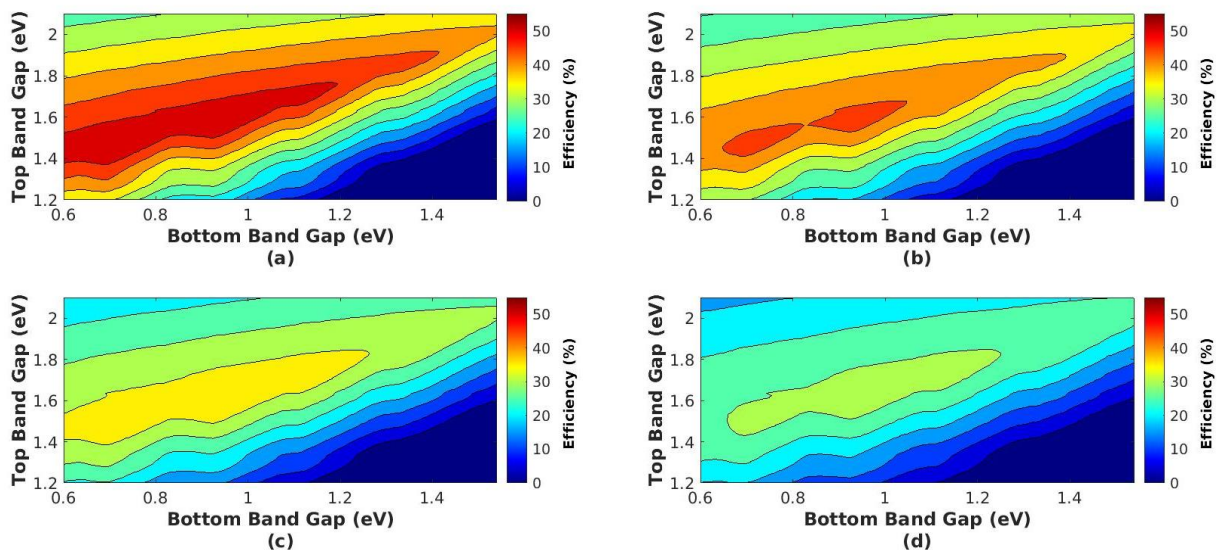
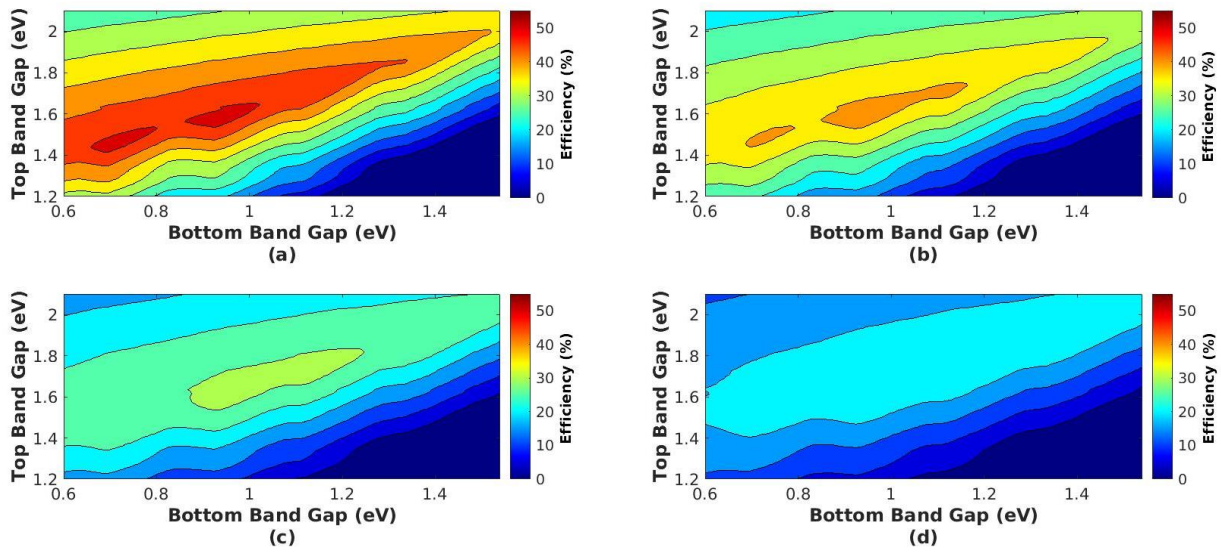


TABLE V-6 Optimal bandgap for single, double and triple junction cells, optimized at 298, 523, 773 and 973K at 1, 100 and 1000 suns solar illuminations.

T (K)	Cell architecture	Concentration (suns)	E_{g1} (eV)	E_{g2} (eV)	E_{g3} (eV)
298 K	1 junction	1	1.14	-	-
		100	1.12	-	-
		1,000	1.12	-	-
	2 junctions	1	1.57	0.93	-
		100	1.57	0.93	-
		1,000	1.45	0.71	-
	3 junctions	1	1.75	1.18	0.7
		100	1.75	1.18	0.7
		1,000	1.75	1.18	0.7
523 K	1 junction	1	1.39 (1.50)	-	-
		100	1.14 (1.25)	-	-
		1,000	1.13 (1.24)	-	-
	2 junctions	1	1.73 (1.84)	1.12 (1.23)	-
		100	1.58 (1.69)	0.94 (1.05)	-
		1,000	1.58 (1.69)	0.93 (1.04)	-
	3 junctions	1	1.88 (1.99)	1.37 (1.48)	0.94 (1.05)
		100	1.88 (1.99)	1.36 (1.47)	0.94 (1.05)
		1,000	1.75 (1.86)	1.18 (1.29)	0.70 (0.81)
773 K	1 junction	1	1.54 (1.78)	-	-
		100	1.38 (1.62)	-	-
		1,000	1.14 (1.38)	-	-
	2 junctions	1	1.90 (2.14)	1.37 (1.61)	-
		100	1.72 (1.96)	1.12 (1.36)	-
		1,000	1.58 (1.82)	0.93 (1.17)	-
	3 junctions	1	2.03 (2.27)	1.54 (1.78)	1.14 (1.38)
		100	1.81 (2.05)	1.23 (1.47)	0.71 (0.95)
		1,000	1.77 (2.01)	1.20 (1.44)	0.70 (0.94)
973 K	1 junction	1	1.74 (2.08)	-	-
		100	1.39 (1.73)	-	-

	1,000	1.34 (1.68)	-	-
2 junctions	1	2.04 (2.38)	1.52 (1.86)	-
	100	1.74 (2.08)	1.12 (1.46)	-
	1,000	1.63 (1.97)	0.95 (1.29)	-
3 junctions	1	2.07 (2.41)	1.57 (1.91)	1.16 (1.50)
	100	1.90 (2.24)	1.40 (1.74)	0.94 (1.28)
	1,000	1.80 (2.14)	1.22 (1.56)	0.70 (1.04)

b) Electrical parameter variation

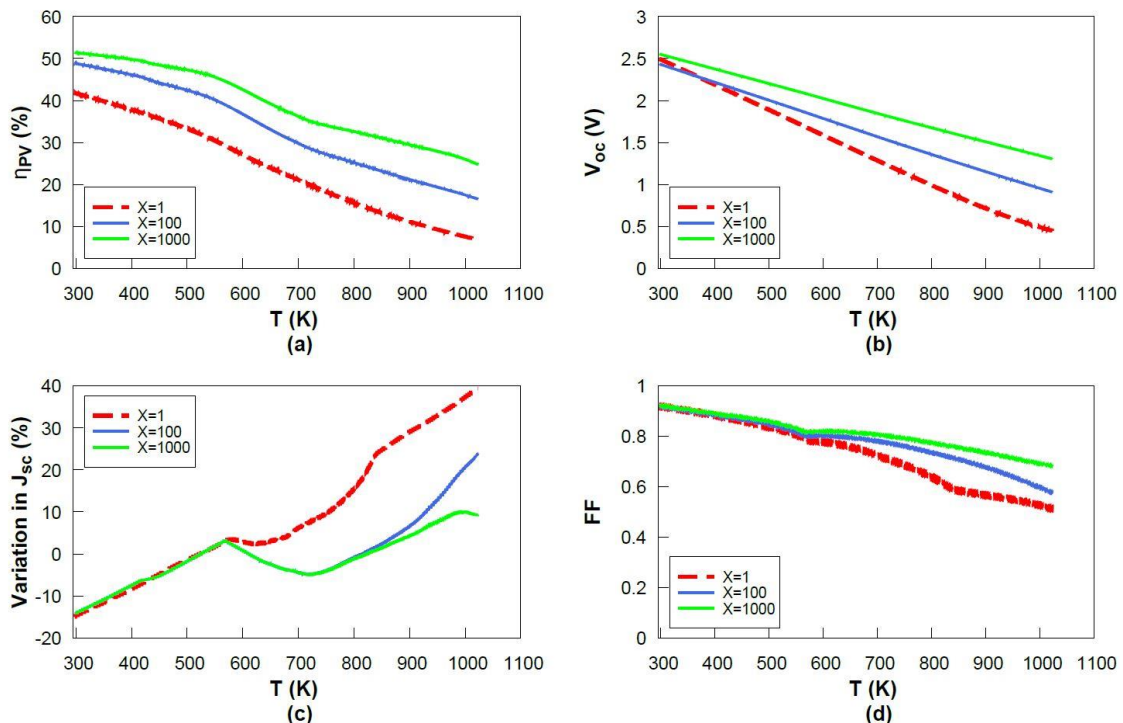


FIGURE V-10 (a) η_{PV} , (b) V_{oc} , (c) variation of J_{sc} and (d) FF, as a function of T for double-junction cells optimized at $T = 523\text{ K}$ (see Table V-6), for $X = 1, 100$ and $1,000$ suns.

Multi-junction cells, due to the current-matching constraint, are compelled to operate at the lowest current generated by the different sub-cells. As a consequence, they are more sensitive to the solar spectrum distribution than single junction cells, leading to some noticeable differences in the temperature dependence of the main electrical parameters.

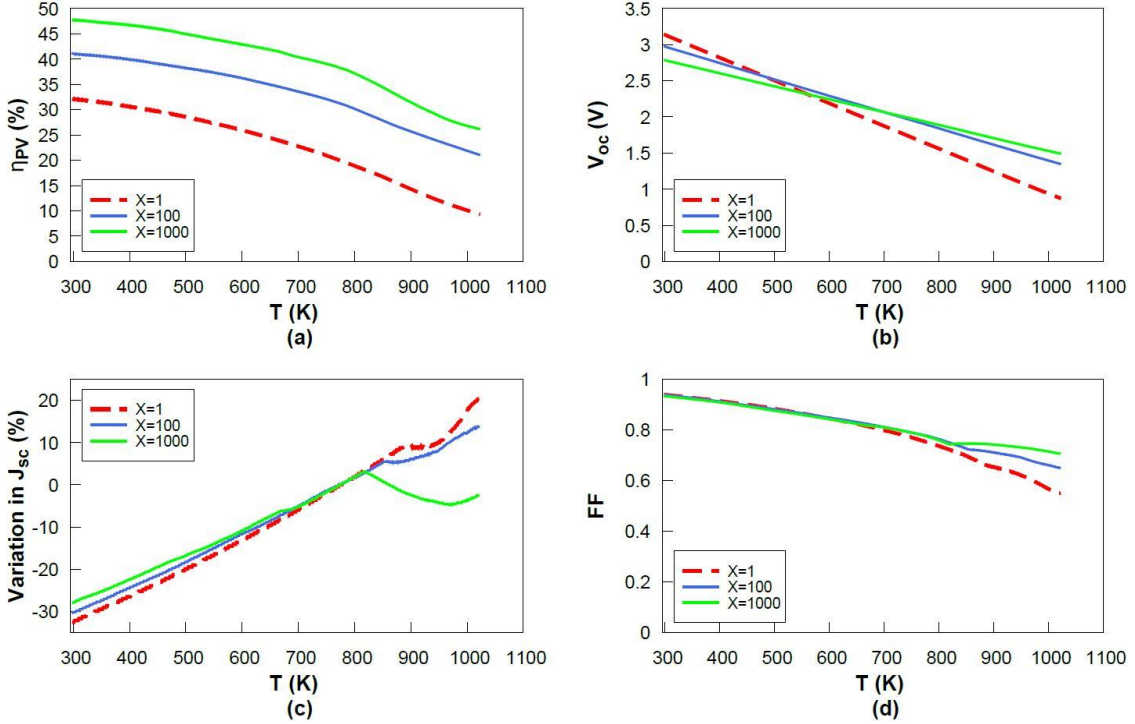


FIGURE V-11 (a) η_{PV} , (b) V_{oc} , (c) variation of J_{sc} and (d) FF, as a function of T for double-junction cells optimized at $T = 773$ K (see Table V-6), for $X = 1$, 100 and 1,000 suns.

Figure V-10 illustrates the temperature behavior of the main electrical parameters (η_{PV} , V_{oc} , J_{sc} normalized to the 523K-optimized cell value, and FF) for a double-junction cell optimized for an operating temperature of 523K. Figure V-11 illustrates the same trends for a tandem cell optimized for an operating temperature of 773K. As observed in Fig.V-10(c) and Fig.V-11(c), the short-circuit current density does not show a steady increase with increasing temperature. We observe sudden fluctuations in J_{sc} , which are particularly noticeable for 523K-optimized cells at around 573K, and also observable (even though less pronounced) for the 773K-optimized cells for temperatures exceeding 800K, particularly for 1000 suns illumination level. The decrease in the current-density occurs if the bandgap of one of the *pn* junction in the stack coincides with an absorption band in the solar spectrum: in this case, there is no additional gain in the photo-generated current associated with the bandgap shift toward lower energy. In summary, if the short-circuit current of the limiting sub-cell increases with temperature, the overall J_{sc} increases. Conversely, a decrease in the short-circuit current of the limiting sub-cell will lower the overall current of the MJ cell. In addition, stacking multiple junctions on top of each other prevents the lower sub-cells from absorbing and converting a large number of photons, resulting in an overall decrease in the short-circuit current density. The magnitude of this effect largely depends on the number of junctions used in the solar cell: the energy range that can be converted by each sub-cell is narrowed as the number of sub-cells increases in the multi-junction stack.

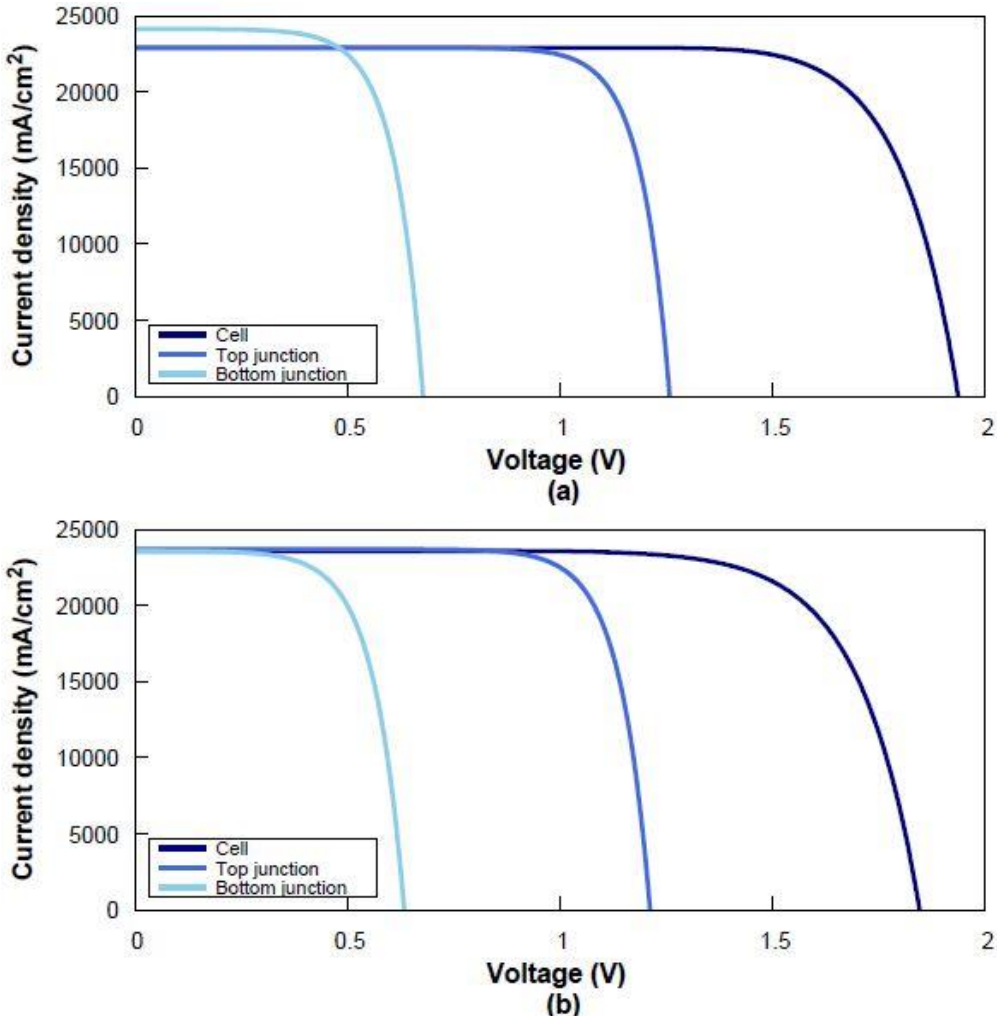


FIGURE V-12 *I-V* curve for tandem cells at 1000 suns and for cells optimized at 773K at the point of 773K (a) and 823K (b).

Similarly to single-junction solar cells, V_{oc} decreases with increasing temperature, while solar concentration reduces the negative effect of temperature. The same trends hold for conversion efficiency and fill factor, both depending on the illumination level and the temperature. Their non-monotonic behavior stems from the J_{sc} variation with temperature. As for single-junction solar cells, the fill factor decreases with increasing temperature. At the point of current-matching (i.e. when the current generated by each individual sub-cell is equal), the fill factor reaches a local minima, before further decreasing at a very high operating temperature. This behavior, which is a typical signature for MJ cells facing current-matching issues, has been largely documented elsewhere [34-36], and can be further understood from Fig.V-12.

Figure V-12 represents the top and bottom junctions *I-V* curves, together with the resulting *I-V* curve of the tandem cells optimized for an operating temperature of 773K, and at an illumination level of 1000 suns. These sets of *I-V* curves are plotted at two distinct temperatures, namely 773K (a), corresponding to the operating temperature for which the cells are optimized and 823K (b), the temperature for which the different sub-cells are current-matched (the FF being characterized by a local minimal value). If we look closer at

the different I - V curves, we notice that the point of current matching does not fall at the point of temperature optimization, which corresponds to the maximum achievable efficiency. The optimization aims at finding the point of maximal efficiency, where the power generated is the highest. This parameter depends on several variables other than the fill factor, such as the short circuit current and the open-circuit voltage. Maximizing the efficiency basically consists in optimizing these different factors. As a consequence, the point of maximum efficiency doesn't occur at the point of perfect current matching (which is reached at a slightly higher temperature). At T exceeding 823K, the current mismatch alleviates the decrease in the fill factor associated with increasing temperature.

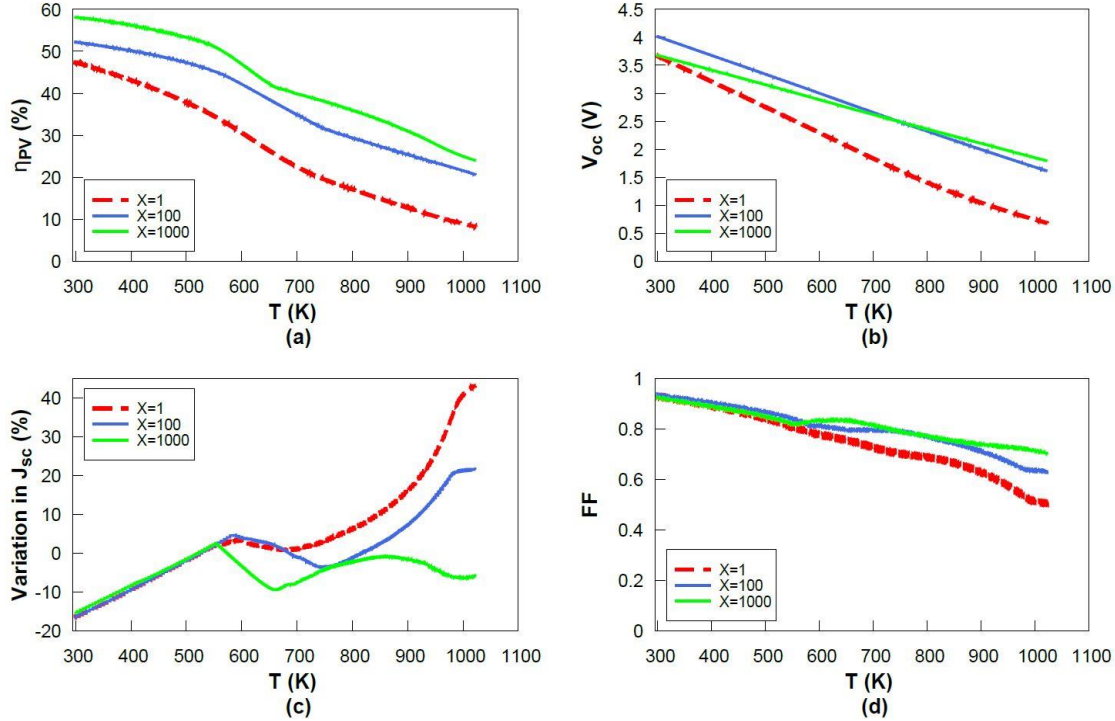


FIGURE V-13 (a) η_{PV} , (b) V_{oc} , (c) variation of J_{sc} and (d) FF, as a function of T for triple-junction cells optimized at $T = 523$ K (see Table V-6), for $X = 1$, 100 and 1,000 suns.

As for the single-junction case, conversion efficiency also decreases with temperature. Increasing the illumination level to which the cell is submitted improves the performances and lessens the temperature effect. Figure V-10 (a) shows a pronounced effect of temperature on the cell efficiency, which decreases with increasing temperature at a rate depending on the variation in the short-circuit current density. Increasing the optimization temperature minimizes this effect, as illustrated in figure V-11(a). In fact, figure V-11(a) shows that, for temperatures up to 700K, the decrease in the conversion efficiency is modest, compared to the previous case, (<10% variation). Above 800K, the cell is affected by the discontinuous nature of the solar spectrum and the conversion efficiency decreases at a faster rate.

Figures V-13 and V-14 represent the temperature dependence of η_{PV} , V_{oc} , normalized J_{sc} (relative to its optimization temperature value), and FF for triple-junction solar cells with bandgaps optimized at 523 and 773K respectively. As for the double-junction case, the current-mismatch between the different sub-cells as well as the strong sensitivity to the solar

spectrum discontinuity affect the behavior of J_{sc} with temperature, and consequently the fill factor and the conversion efficiency. The sensitivity to the solar spectrum distribution appears to worsen as the number of junctions in the cell increases.

The results described for single, double and triple junction cells, confirm the importance of using multi-junction cells to improve the cell performances, even at high temperatures. Using single-junction solar cells under 1000 suns leads to solar to electricity conversion efficiencies between 20 and 40%, depending on the temperature. In the case of tandem and triple junction solar cells, the maximum efficiency attainable shifts to 25-50% (tandem), and 30-55% (triple-junction solar cells) .

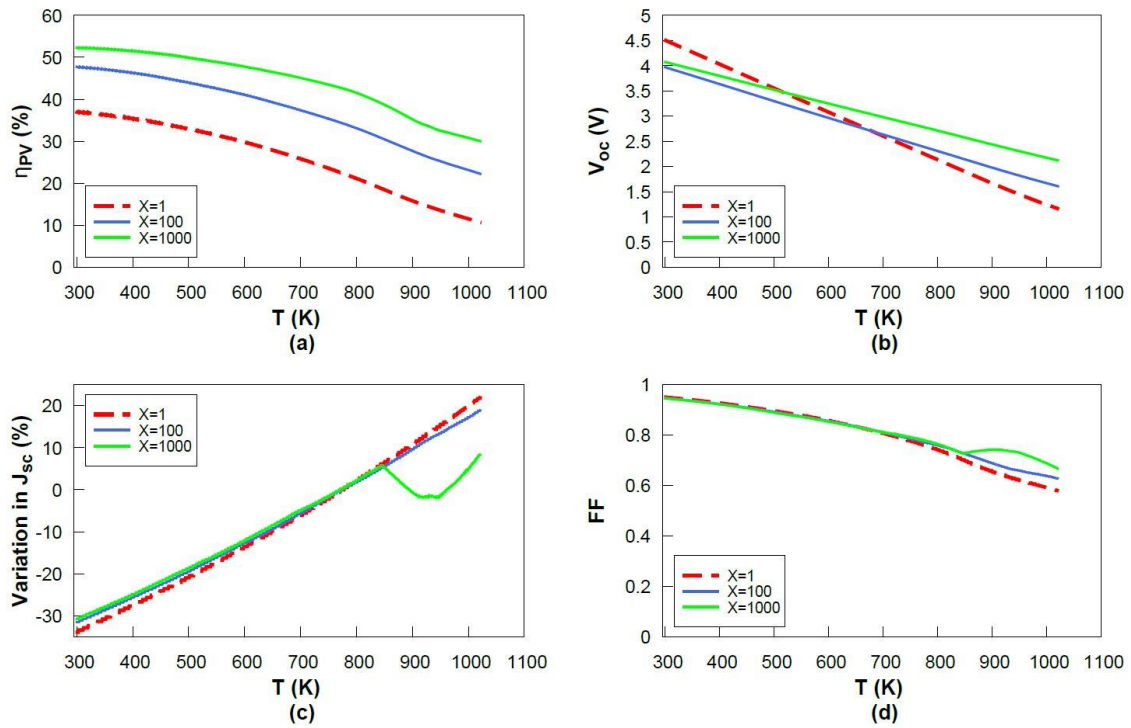


FIGURE V-14 (a) η_{PV} , (b) V_{oc} , (c) variation of J_{sc} and (d) FF, as a function of T for triple-junction cells optimized at $T = 773$ K (see Table V-6), for $X = 1, 100$ and $1,000$ suns.

The variation of the different electrical parameters for single, double and triple junction cells with bandgaps optimized at 973K are illustrated in Appendix A.

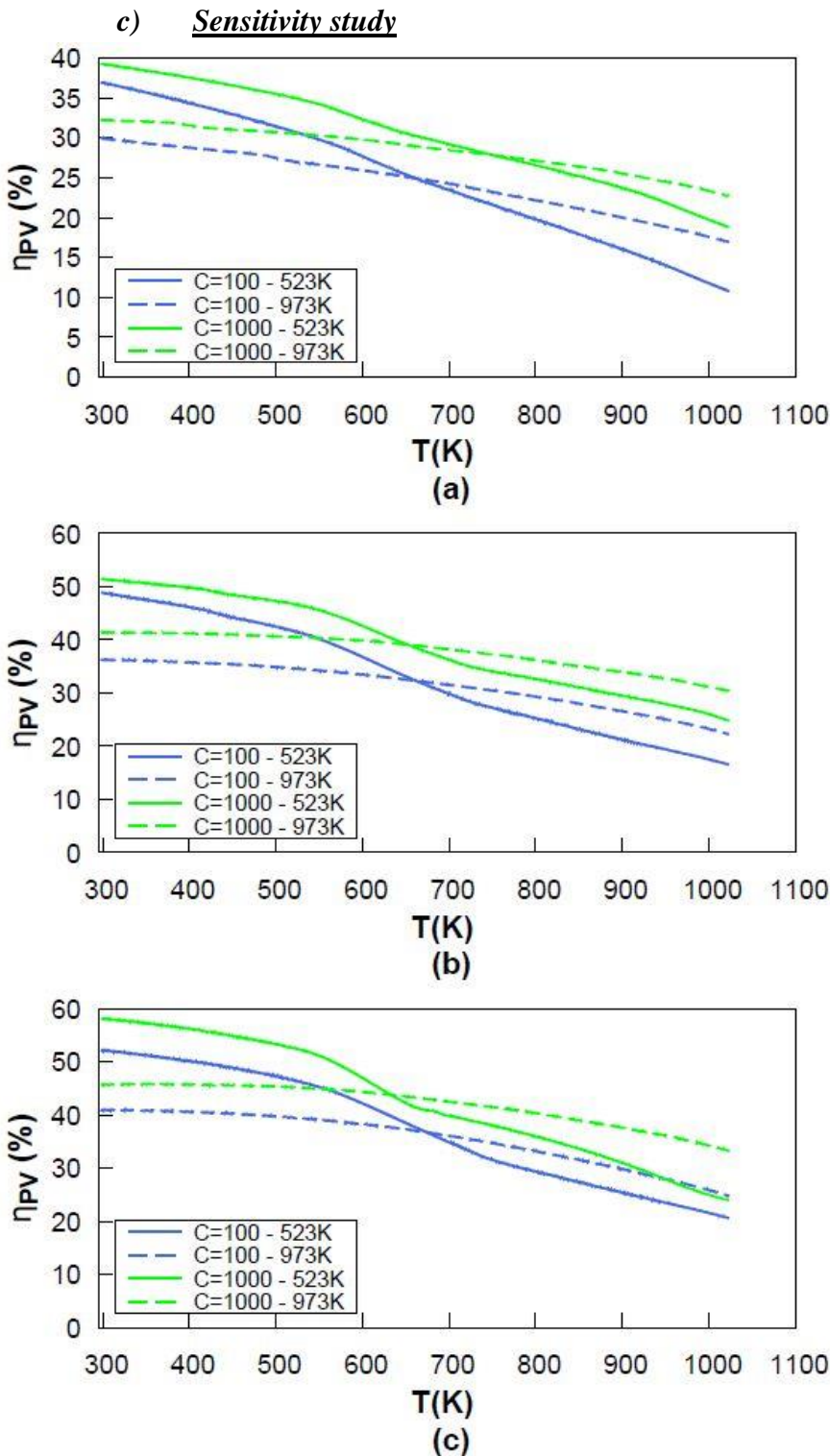


FIGURE V-15 Conversion efficiency as a function of temperature for single (a), double (b) and triple (c) junction solar cells at concentrations of 100 and 1000 suns and bandgap optimization temperatures of 523 and 973K.

To better understand the sensitivity of the results to the bandgap optimization temperature, the PV efficiency is computed as a function of temperature for single (a), double (b) and triple (c) junction cells, as illustrated in figure V-15. In each case, the solid curves represent the variation in efficiency for a PV cell optimized at 523K, while the dashed curves

show corresponding trends for a 973K-optimized cell. These 2 temperatures represent the lower and upper bounds of the temperature range considered for the high temperature approach. The bandgap combinations for each temperature and concentration are summarized in Table V-6.

The 523K optimized cells show the highest performance from ambient temperature up to 650-750K. Beyond this temperature, the 973K optimized cells are more efficient. The curves also confirm the benefit of solar concentration in counterbalancing the effect of high temperature on the conversion efficiency.

A suitable optimization temperature can be chosen as an intermediate value between the considered bounds, namely 773K. Opting for an intermediate optimization temperature ensures that the decrease in the maximum efficiency remains modest on the full range of temperature (no more than 4% in this case). This should be of particular concern if the PV cell is likely to undergo large temperature variations in real operating conditions.

The choice of the optimization temperature which should be adopted, does not depend only on the solar cells' performances, but also on the thermal efficiencies. Consequently, one should rather consider the *overall hybrid efficiency* for temperature optimization, otherwise the selected temperature should correspond to ambient. This optimization temperature strongly depends on the overall hybrid PV/CSP efficiency and, as mentioned before, on the balanced contribution of the electricity produced by PV and CSP. The following section aims to clarify this issue.

3. Hybrid system performances

The efficiency of a solar hybrid system is evaluated as a function of the receiver operating temperature using eq. (II-30). The heat transfer coefficient used to compute the convective losses is assumed equal to $20 \text{ W m}^{-2} \text{ K}^{-1}$. Systems are based on tandem junction cells where the bandgap of the different junctions is optimized at each temperature and concentration considered (no temperature coefficient is needed for these calculations), to maximize the solar cell efficiency. Thermal receiver is assumed to operate at 2/3 of the Carnot limit.

Figure V-16 illustrates the efficiencies of the solar cells and the thermal receiver (the overall hybrid efficiency being the sum of the PV and CSP efficiencies), assuming illumination levels of 100 suns (a) and 1000 suns (b) and (c), and for operating temperatures comprised between 298 and 1023K. It also shows the radiative and convective losses, as well as the heat rejection from the turbine. Figures V-16 (a) and (b) assume solar cells operating in the radiative limit whereas figure V-16 (c) accounts for a more realistic cell, with an efficiency taken equal to 2/3 of the radiative limit value.

The temperature dependence of the global conversion efficiency is different depending on the illumination level considered. Despite the fact that PV conversion efficiency decreases with increasing temperature, the overall hybrid conversion efficiency increases due to the improvement in the thermal receiver performances at high temperature.

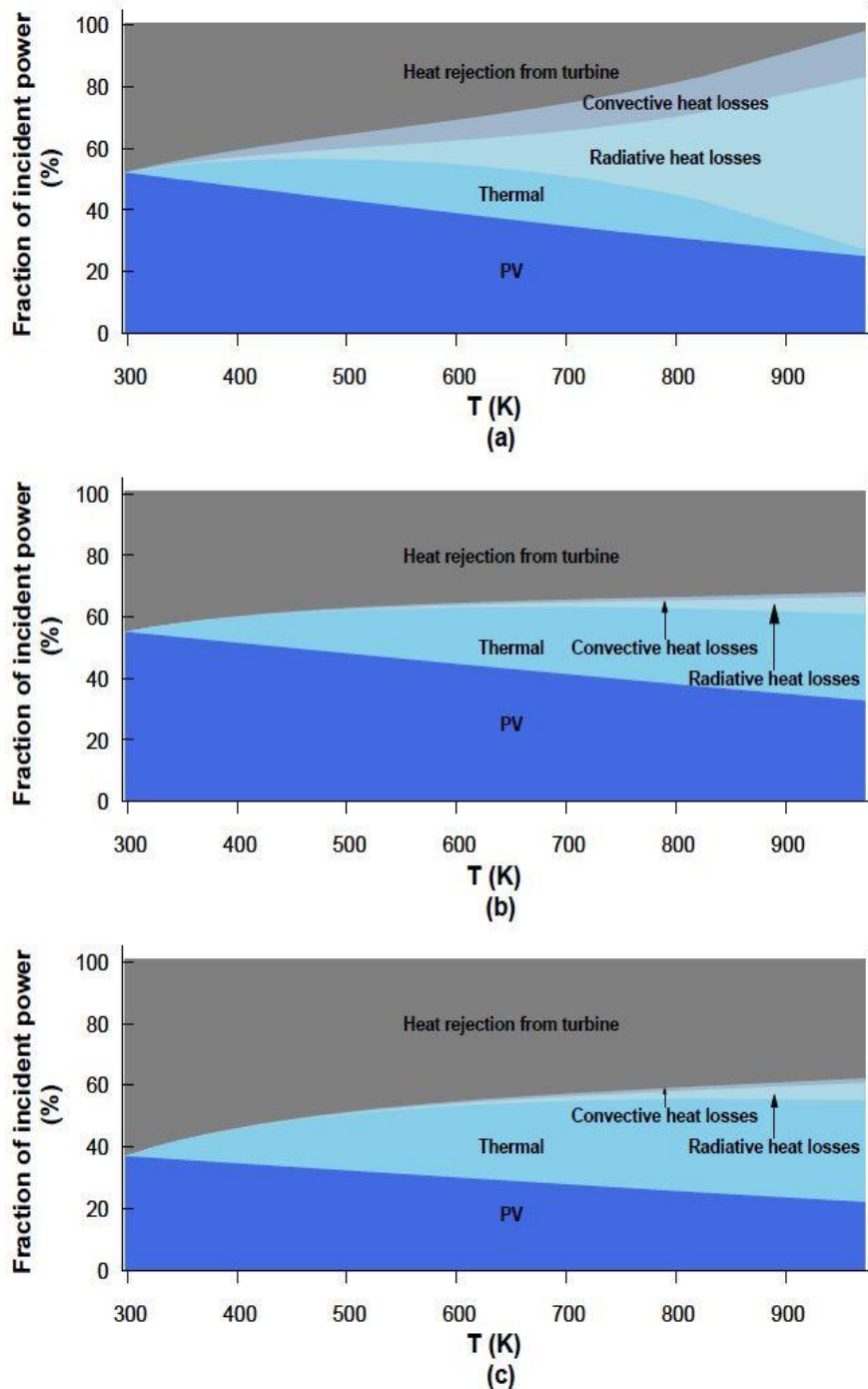


FIGURE V-16 PV, thermal and overall hybrid efficiencies as well as the associated thermal losses as a function of the operating temperature, for solar cells at the radiative limit under a concentration of 100 suns (a), at the radiative limit under 1000 suns (b) and for more realistic solar cells under 1000 suns (c).

For a concentration of 100 suns, the global efficiency increases up to $\sim 500\text{K}$. Beyond this temperature, radiative and convective losses increase dramatically leading to a strong decrease in the overall hybrid efficiency. Under an illumination of 1000 suns, the relative weight of radiative and convective losses becomes negligible. The overall hybrid efficiency increases, and then stabilizes on a broad range of temperatures (between 523 and 823K). Thermal losses increase with increasing temperature but remain negligible even at temperature approaching 1000K. Above $\sim 800\text{K}$, the efficiency decreases slowly. Thus,

increasing the solar illumination level to which the system is submitted allows 1) better system performances due to the huge decrease in the heat losses caused by radiative and convective losses 2) improved ability of the PV cells to accommodate high operating temperature 3) lower sensitivity of the overall system efficiency to temperature.

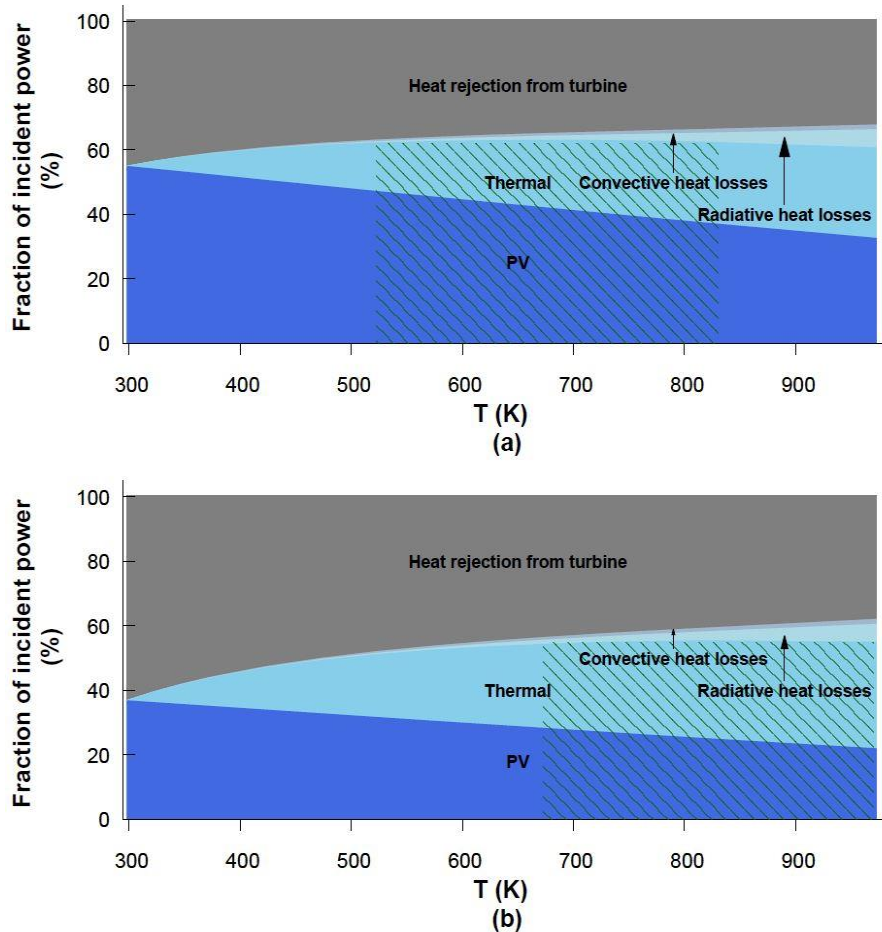


FIGURE V-17 PV, thermal and overall hybrid efficiencies as well as the associated thermal losses as a function of the operating temperature, for a concentration of 1000 suns, for solar cells at the radiative limit (a), and for more realistic solar cells (b).

Considering more realistic solar cells, similar conclusions can be drawn, however the overall maximum efficiencies achievable are slightly diminished (~55% compared to ~62% in the previous case). The peak temperature shifts toward higher values: in fact, since less photons are converted by solar cells, a greater amount of residual energy is available for the CSP converter, which increases the contribution of the thermal receiver and consequently raises the optimal operating temperatures. Compared to the ambient temperature, one can observe a significant efficiency gain (almost 20%) at the peak temperature for systems using “real” cells, in contrast to only 5% for hybrid systems with ideal solar cells. This significant gain results from the enhancement in the CSP performances with increasing temperature.

Figure V-17 allows a better comparison between ideal and more realistic cells based hybrid systems.

Even if the hybrid efficiency shows stable values on a wide range of temperatures (the green hatched region indicates the range of temperature where the system efficiency varies no more than 1% below the peak efficiency), the electricity share between PV and CSP is modified.

As mentioned earlier, an important requirement is to simultaneously ensure the highest possible overall efficiency and a balanced share between PV and thermal contributions to total electricity production. The choice of the optimal temperature should consider these two criteria, as well as the concentration level at which the system is supposed to operate. Accounting for these criteria leads to an optimization temperature between 673 and 773K in the case of “realistic” solar cells under 1000 suns: the optimal hybrid performance occurs between 673 and 1023K, with the best-balanced contributions between 673 and 773K. For hybrid systems involving “ideal” solar cells, the maximum overall efficiency appears for temperatures between 523 and 823K, whereas the best-balanced share is around 1023K.

A major conclusion one can attain in the light of these results is that achieving high solar-to-electricity conversion efficiency does not necessarily require the system to operate at very high temperatures; a temperature between 673 and 773K is sufficient, as a consequence of the trade-off between the optimal operating temperatures of PV and thermal receiver.

III. Conclusions

Hybrid PV/CSP systems have the advantages of being dispatchable, economically competitive, and generating uninterrupted power. The overall hybrid efficiency being higher than using PV or CSP alone justifies the use of such systems.

In this chapter, we compared the performances of 3 different hybrid PV/CSP approaches, the “high temperature PV”, the “spectrum splitting” and the “one-sun PV”. The evaluation is based on the ability of each strategy to fulfill two important criteria, 1) high solar to electricity conversion efficiency and 2) balanced share between the electricity produced by PV and CSP. We also assessed the use of two cut-off energies in the spectrum splitting device, for the “one sun PV” and the “spectrum splitting” strategies. The results demonstrated that the “high temperature PV” and the “one-sun PV” present similar ideal performances compared to the “spectrum splitting” approach which is less efficient. They also showed that the “high temperature PV” strategy offers the best-balanced share between the electricity produced by each sub-system. Opting for an advanced spectrum-splitting strategy (involving a second high energy cut-off) does not improve the peak efficiency since it affects mostly the low bandgap regions where *thermalization* losses are important.

These results provide upper bounds for the hybrid performances, as well as an assessment of the extent to which the most important limiting parameters (series resistance losses, non-radiative recombination) may affect these idealistic estimations. Other losses, outside the ones directly related to PV or CSP, are omitted. Optical and geometrical losses were not investigated here since they are associated with a particular concentrator type, a specific location, etc... They can equally be added to the three different approaches without

changing the comparison results but only lowering the value of the overall conversion efficiency.

In the light of these conclusions, we focused on the “high temperature PV” approach, since it leads to high overall conversion efficiencies and to the best-balanced share between the two sub-systems.

Accordingly, the temperature dependence of the cell’s main parameters was evaluated in the radiative limit at different temperatures and concentrations, for single, double and triple junction solar cells. The optimal bandgap appears to shift toward higher values at high temperature levels. The magnitude of this shift lessens with increasing concentration level. This result suggests that solar cells operating at high temperature and concentration levels probably do not require any significant modification in their architecture and optimal bandgap (in comparison with cells operating at 1 sun and ambient temperature). As a consequence, conventional materials commonly used in current CPV cells could probably still be used with no need to find new exotic ones (the optimal bandgaps left unchanged induce that the semiconductor materials remain unaltered too). Recent experimental studies using conventional materials, namely AlGaInP/GaAs tandem cells, [37,38] assert that these materials resist at high temperatures.

The temperature dependence of the main electrical parameters was investigated on a broad range of temperature (from ambient to ~1000K) and illumination levels (from 1 to 1000 suns). The detrimental effect of temperature on the operation of PV cells under extreme operating temperature was shown to be mainly associated with the increased dark current, which significantly reduces V_{oc} and, to a lesser extent, to the decrease in the cell bandgap. Increasing the concentration level reduces the sensitivity to the operating temperature and improves the performances of the solar cells. In the case of MJ solar cells, there is an additional effect associated with the discontinuous nature of the solar spectrum, which affects the short-circuit current density, and consequently the fill factor and the conversion efficiency. Because of the current-matching constraint, the magnitude of the temperature dependence at high temperature is more pronounced for multi-junction solar cells. From the different cells architectures analyzed, namely single, double and triple junctions one can conclude that increasing the number of junctions improves the performances of the cells, even at high temperatures.

For the assessment of the hybrid PV/CSP high temperature strategy, we showed that using high concentration level is beneficial to increase the overall hybrid efficiency. The overall system enhancement is not only due to improving the cell efficiency at high temperature but also to reducing the weight of the convective and radiative losses. Increasing concentration hence counterbalances the detrimental effect of increasing solar cell temperature. The optimization temperature does not necessarily need to be very high since the overall hybrid efficiency stabilizes for a wide range of temperatures. The operating temperature also affects the share between PV and CSP, higher operating temperature leading to higher CSP electricity production and degraded PV production. At the temperature of bandgap optimization, namely around 673-773K, the contribution of each sub-system of the hybrid power plant is comparable. The overall hybrid conversion efficiency, even at high

temperatures, remains higher than the best concentrator PV systems used alone, besides benefitting from excess energy storage.

To estimate the performance of “realistic” systems (in opposition to “idealized” systems operating in the radiative limit), we arbitrarily fixed a PV efficiency equal to 2/3 of the radiative limit, a realistic value for state-of-the-art solar cells at ambient temperature and at a concentration of 1000 suns [25, 26]. The ability of high-temperature cells to approach their own theoretical limits still needs to be clarified: data concerning efficiencies at very high temperature are still rare, despite the growing interest for studying and developing high temperature solar cells. The only data available nowadays shows a practical efficiency of high-temperature AlGaInP/GaAs tandem cell representing ~35% of its radiative limit at 673K and 1000 suns [37], and ~40% of its radiative limit at 673K and 345 suns [38]. Such low solar efficiencies do not change dramatically the global conclusions; they only modify the optimal operating temperature range, decrease the PV fraction and the overall hybrid efficiency, and increase the share of CSP.

IV. References

- [1] C. K. Ho and B. D. Iverson, Review of high-temperature central receiver designs for concentrating solar power, *Renew. Sust. Energ. Rev.*, 29 (2014) 835-846.
- [2] E. Batuecas, C. Mayo, R. Díaz and F.J. Pérez, Life Cycle Assessment of heat transfer fluids in parabolic trough concentrating solar power technology, *Sol. Energy Mater. Sol. Cells*, 171 (2017) 91-97.
- [3] L. Moens and D. M. Blake, Mechanism of hydrogen formation in solar parabolic trough receivers, *J. Sol. Energy Eng.*, 132 (2010) 031006.
- [4] H. Benoit, L. Spreafico, D. Gauthier, and G. Flamant, Review of heat transfer fluids in tube-receivers used in concentrating solar thermal systems: Properties and heat transfer coefficients, *Renew. Sust. Energ. Rev.*, 55 (2016) 298-315.
- [5] H.M. Branz, W. Regan, K.J. Gerst, J.B. Borak, and E.A. Santori, Hybrid solar converters for maximum exergy and inexpensive dispatchable electricity, *Energy Environ. Sci.*, 8 (2015) 3083-3091.
- [6] C.L. Schilling, O. Höhn, D.N. Micha, S. Heckelmann, V. Klinger, E. Oliva, S.W. Glunz, and F. Dimroth, Combining Photon Recycling and Concentrated Illumination in a GaAs Heterojunction Solar Cell, *IEEE J. Photovolt.*, 8 (2018) 348-354.
- [7] M. A. Green, Radiative efficiency of state-of-the-art photovoltaic cells, *Prog. Photovolt.: Res. Appl.*, 20 (2011) 472-476.
- [8] Y.P. Varshni, Temperature dependence of the energy gap in semiconductors, *Physica E Low Dimens. Syst. Nanostruct.*, 34 (1967) 149-154.
- [9] P. Geng, W. Li, X. Zhang, X. Zhang, Y. Deng, and H. Kou, A novel theoretical model for the temperature dependence of band gap energy in semiconductors, *J. Phys. D: Appl. Phys.* 50 (2017) 40LT02.
- [10] R. Pässler, Semi-empirical descriptions of temperature dependences of band gaps in semiconductors, *Phys. Stat. Sol. b* 236 (2003) 710-728.

- [11] L. Viña, S. Logothetidis, and M. Cardona, Temperature dependence of the dielectric function of germanium, *Phys. Rev. B* 30 (1984) 1979-1991.
- [12] A. Manoogian and A. Leclerc, Determination of the dilation and vibrational contributions to the energy band gaps in germanium and silicon, *Phys. Stat. Sol. b* 92(1979) K23-K27.
- [13] K.P. O'Donnell and X. Chen, Temperature dependence of semiconductor band gaps, *Appl. Phys. Lett.* 58 (1991) 2924-2926.
- [14] R. Pässler, Parameter sets due to fittings of the temperature dependencies of fundamental bandgaps in Semiconductors, *Phys. Stat. Sol. b* 216 (1999) 975-1007.
- [15] J. Bhosale and A.K. Ramdas, Temperature dependence of band gaps in semiconductors: Electron-phonon interaction, *Phys. Rev. B* 86 (2012) 195208.
- [16] I. Vurgaftman, J.R. Meyer, and L.R. Ram-Mohan, Band parameters for III-V compound semiconductors and their alloys, *J. Appl. Phys.* 89 (2001) 5815-5875.
- [17] A. Braun, E. A. Katz and J. M. Gordon, Basic aspects of the temperature coefficients of concentrator solar cell performance parameters, *Prog. Photovolt. Res. Appl.*, 21 (2013) 1087-1094.
- [18] M.R. Lorenz, G.D. Pettit, and R.C. Taylor, Band gap of gallium phosphide from 0 to 900K and light emission from diodes at high temperatures, *Phys. Rev.* 171 (1968) 876.
- [19] P.J. Dean, G. Kaminsky and R.B. Zetterstrom, Intrinsic optical absorption of gallium phosphide between 2.33 and 3.12 eV, *J. Appl. Phys.* 38 (1967) 3551-3556.
- [20] M. Panish and H. Casey Jr., Temperature dependence of the energy gap in GaAs and GaP, *J. Appl. Phys.* 40 (1969) 163-167.
- [21] J. C. Fan, Theoretical temperature dependence of solar cell parameters, *Sol. Cells* 17 (1986) 309-315.
- [22] B. Bouzazi, A. Jaouad, A. Turala, R. Arès, S. Fafard, and V. Aimez, Thermal behaviours and ageing of GaAs and InGaP solar cells for Thermal-CPV hybrid energy systems, In *AIP Conference Proceedings*, 1881 (2017) 050001.
- [23] E. E. Perl, J. Simon, J. F. Geisz, M. L. Lee, D. J. Friedman, and M. A. Steiner, Measurements and Modeling of III-V Solar Cells at High Temperatures up to 400 °C, *IEEE J. Photovolt.*, 6 (2016) 1345-1352.
- [24] Q. Guo and A. Yoshida, Temperature dependence of band gap change in InN and AlN, *Jpn. J. Appl. Phys.* 33 (1994) 2453.
- [25] A. Vossier, F. Gualdi, A. Dollet, R. Ares, and V. Aimez, Approaching the Shockley-Queisser limit: General assessment of the main limiting mechanisms in photovoltaic cells, *J. Appl. Phys.*, 117 (2015) 015102.
- [26] M. A. Green, K. Emery, Y. Hishikawa, W. Warta, E.D. Dunlop, D.H. Levi, and A.W.Y. Ho-Baillie, Solar cell efficiency tables (version 37), *Prog. Photovolt.: Res. Appl.* 19 (2011) 84-92.
- [27] M. Geyer, E. Lüpfert, R. Osuna, A. Esteban, W. Schiel, A. Schweitzer, E. Zarza, P. Nava, J. Langenkamp, and E. Mandelberg, EUROTROUGH-Parabolic trough collector developed for cost efficient solar power generation, In *Proc. of the SolarPACES 11th International Symposium on Concentrated Solar Power and Chemical Energy Technologies*, (2002) 4-6.

- [28] H.L. Zhang, J. Baeyens, J. Degrève, and G. Cacères, Concentrated solar power plants: Review and design methodology, *Renew. Sustain. Energy Rev.* 22 (2013) 466-481.
- [29] G. Smestad, H. Ries, R. Winston, and E. Yablonovitch, The thermodynamic limits of light concentrators, *Sol. Energy Mater.* 21 (1990) 99-111.
- [30] H. Cotal and R. Sherif, Temperature Dependence of the IV Parameters from Triple Junction GaInP/InGaAs/Ge Concentrator Solar Cells, in Proc. of the IEEE 4th World Conference on Photovoltaic Energy Conversion, (2006), 845 –848.
- [31] G. S. Kinsey, P. Hebert, K. E. Barbour, D. D. Krut, H. L. Cotal, and R. A. Sherif, Concentrator multijunction solar cell characteristics under variable intensity and temperature, *Prog. Photovolt. Res. Appl.*, 16 (2008) 503-508.
- [32] A. Braun, B. Hirsch, A. Vossier, E.A. Katz, and J.M. Gordon, Temperature dynamics of multijunction concentrator solar cells up to ultra-high irradiance, *Prog. Photovolt. Res. Appl.*, 21 (2013) 202-208.
- [33] S. M. Sze and K. K. Ng, Physics of Semiconductor Devices, 3rd edition, Wiley, Hoboken, New Jersey, US, 2007.
- [34] H. Cotal, C. Fetzer, J. Boisvert, G. Kinsey, R. King, P. Hebert, H. Yoon and N. Karam, III–V multijunction solar cells for concentrating photovoltaics, *Energ. Environ. Sci.*, 2 (2009) 174-192.
- [35] S. Reynolds and V. Smirnov, Modelling performance of two- and four-terminal thin-film silicon tandem solar cells under varying spectral conditions, *Energy Procedia*, 84 (2015) 251-260.
- [36] R. Adelhelm and G. La Roche, Matching of multi-junction solar cells for solar array production, In Proc. of the IEEE 28th Photovoltaic Specialists Conference (PVSC-28), (2000) 1336-1339.
- [37] M. A. Steiner, E.E. Perl, J. Simon, D.J. Friedman, N. Jain, P. Sharps, C. McPheeters, and M.L. Lee, AlGaInP/GaAs tandem solar cells for power conversion at 400C and high concentration, In AIP Conference Proceedings, 1881 (2017) 040007.
- [38] E.E. Perl, J. Simon, D.J. Friedman, N. Jain, P. Sharps, C. McPheeters, Y. Sun, Minjoo L. Lee, and M.A. Steiner, (Al)GaInP/GaAs Tandem Solar Cells for Power Conversion at Elevated Temperature and High Concentration, *IEEE J. Photovolt.*, 8 (2018) 640-645.

General Conclusions and Perspectives

Conventional solar cells are far from reaching the maximal sunlight to electricity conversion efficiency limit. Their operation is affected by different fundamental limiting mechanisms that restrict their performances to the Shockley-Queisser limit, slightly above 30%. These losses are mostly due to the inefficient conversion of the solar spectrum (*below* E_g and *thermalization* losses), as well as the asymmetry between the solid angles of absorption and emission (*Boltzmann* losses).

Different strategies are currently considered to overcome these losses and get closer to the Carnot limit. In this work, we focused on 3 different approaches aiming at mitigating these losses and improving the system performance, namely: 1) concentrator multi-junction solar cells, to reduce *Boltzmann* losses, as well as *thermalization* and *below-E_g* losses, 2) the combination of angular restriction and solar concentration to decrease the *Boltzmann* losses, and 3) hybrid PV/CSP systems to reduce the spectral losses, as well as *Boltzmann* losses in the case of systems involving sunlight concentration.

Each of these strategies is practically restricted by several limiting parameters precluding them to achieve the maximum efficiency predicted on some theoretical grounds. This thesis was articulated around two main questions: 1) to which extent the main limiting mechanisms are likely to penalize the efficiency operation of the different approaches investigated? 2) How to optimize the device architecture toward minimizing the effects of non-ideal loss mechanisms and improving the system efficiency? Our studies were conducted on different cell architectures, for single and multi-junction solar cells, and for a broad range of concentration factors.

Single and multi-junction solar cells, operating at very high concentration factors, are mostly limited by strong resistive losses. These resistive losses are function of the series resistance value and the generated electrical current, varying proportionally to the square of the current which itself increases linearly with concentration. Series resistance losses being bandgap dependent, we explored the extent to which an appropriate bandgap tuning taking into account series resistance losses may lead to enhanced cell performance when exposed to highly concentrated sunlight. We showed that bandgap optimization provides insignificant benefits for concentration levels smaller than 1000 suns, as a result of the low resistive losses.

In contrast, as the illumination or the series resistance value increases, tuning the optimal bandgap becomes very profitable: the optimal bandgap shifts toward higher values in order to reduce the short-circuit current and, in turn, to lessen resistive losses.

The bandgap combination stemming from this optimization procedure may be used by cell manufacturers to choose suitable semiconductors materials ensuring high performances. But, this choice is constrained by the necessary compatibility (in terms of lattice-matching for example) between the different materials used in multi-junction cell architectures.

These results offer upper bounds for maximum achievable efficiencies. Future studies should account for the limiting mechanisms associated with increasing bandgaps, such as lower minority carrier mobility or higher series resistance associated with the high bandgap tunnel junction. Along with these mechanisms, different cells parameters should be considered such as doping levels, materials parameters, thickness, contact geometry, etc...

However, despite the importance of bandgap tuning, this strategy, alone, is not sufficient to achieve very high performances and should be combined to appropriate cell designs and suitable optimization of the different series resistance components (such as front grid or emitter resistance). This series resistance minimization, along with the bandgap optimization, ensures the development of solar cells capable of operating at ultra-high concentration, much larger than the typical values of 500 to 1000 suns commonly implemented today.

These observations are no longer valid when considering concentration-dependent series resistances: resistive losses remain negligible since the series resistance decreases with increasing concentration level, which cancels the benefits of bandgap optimization.

Given that CPV systems are severely affected by high illumination intensities, primarily because of the high series resistance impact on the cell performances, reducing the solid angles of emission can be a suitable alternative leading to reduced *Boltzmann* losses while considering low illumination levels. Since the effect of reducing the solid angle of emission from the solar cell is essentially limited by non-radiative recombination, combining both, solar concentration and angular restriction, offers an extra degree of freedom in the quest of high conversion efficiency. The results found for conventional CPV systems remain valid for the combination of solar concentration and angular restriction: resistive losses are a major limiting mechanism whenever concentration is used, and the main loss mechanism affecting this strategy.

Considering the combined effects of the main two limiting parameters, namely series resistances and non-radiative recombination, we showed that series resistances represent the dominant limiting mechanism. In fact, the amplitude of resistive losses varies drastically with the angle of absorption, affecting the fill factor of the cell. On the other hand, non-radiative recombination decreases V_{oc} and consequently the cell performances; however, its effect remains moderate and is attenuated as the concentration ratio increases.

The best performances appear to occur for equal solid angles of absorption and emission (leading to the vanishing of *Boltzmann* losses), with the optimal angular range value depending on the amplitude of the main limiting mechanisms.

Non-radiative recombination losses are quantified by the external radiative efficiency (ERE), which was considered constant in our simulations. We did not account initially for any dependence of the non-radiative losses on the angular properties of the emission beam. Practically, this may not be the case since the ERE may vary noticeably with angular restriction: reducing the solid angle of emission may lead to increased non-radiative losses, and thus lower ERE. For a proper analysis, and to better describe the emission angle dependence of non-radiative losses, the model should account for the effect of angular confinement on the external radiative efficiency. The equation connecting these two parameters can be found using different methods, and two of them were described in this thesis. In fact, one can use the model developed by Steiner et al. [1], relating the ERE to the IRE through the probability densities of photon re-absorption and escape. Then the IRE is

linked to the minority carrier lifetime, which is dependent on the recombination rate, and this minority carrier lifetime is connected to the degree of angular restriction.

Another approach provides a direct link between the different recombination currents and the ERE value and was suggested by Rau et al. [2] and Höhn et al. [3]. The corresponding models were partially implemented, even if some inconsistencies still require to be understood and corrected, for instance regarding the radiative efficiencies for PV cells in regimes where the recombination are mainly governed by SRH. The results are in agreement with our expectations and confirm the noticeable effect of low ERE on the maximum efficiency one can achieve considering solar concentration and angular restriction simultaneously (particularly for high degrees of angular restriction). As a result, the maximum efficiency stems from a compromise between these 2 loss mechanisms and is typically observed for angles slightly exceeding maximum restriction conditions. However, resistive losses remain the dominant limiting mechanism for this strategy.

The model should be completed to account for the doping dependence before assessing the ERE variation with angular restriction. Complex cell technology, such as concentrator multi-junction solar cells, should be studied as a mean to reduce the losses related to both the inefficient solar spectrum conversion and the asymmetry between the solid angles of absorption and emission, also as a function of the angular properties, for ideal and more realistic solar cells.

The combination of solar concentration and angular restriction should also be characterized experimentally. The single and multi-junction solar cells to be tested should necessarily present high ERE, low series resistance values, close to ideal back mirror and good rear contact facilitating the current circulation. The experimental tests will allow correlating the optical properties and the cell electrical performances, as well as the amplitude of each limiting mechanism as a function of the solid angles of emission and absorption.

The observations mentioned are also valid in the case of hybrid PV/CSP systems, particularly for systems involving solar concentration. In fact, besides the series resistance impact that can affect solar cells, very high concentration factors may dramatically increase the cell temperature, an undeniable advantage when the PV cell is intended to operate as a solar receiver as well.

Hybrid PV/CSP strategies turned out to be interesting for reducing the spectral conversion losses, together with *Boltzmann* losses in the case of hybrid systems involving sunlight concentration. They could permit an economically competitive, dispatchable and uninterrupted power generation, with overall hybrid power output and conversion efficiency higher than those obtained using PV or CSP alone.

The comparison of the three different hybrid PV/CSP strategies, namely: “high temperature PV”, “spectrum splitting” and “one-sun PV” was evaluated based on two fundamental criteria: 1) the system should offer the highest conversion efficiency and 2) it should provide the best balanced share between the electricity produced by PV and by CSP. The results showed that the “high-temperature” and the “one-sun” approaches grant comparable ideal performances whereas the “spectrum splitting” approach is less efficient.

On the other hand, the “high temperature PV” strategy presents the best-balanced share between the electricity produced by each sub-system.

The use of two cut-off energies in the spectrum splitting optical device was also assessed for the “one-sun PV” and the “spectrum splitting” approaches. It was shown that this technique does not improve the peak efficiency since it only affects the system performance in the low bandgap regions (characterized by significant *thermalization* losses).

These results provide upper bounds for the hybrid performances, for ideal and practical cells accounting for series resistances or non-radiative recombination. The analysis was restricted to the losses associated with PV and CSP. Accordingly, the losses associated to each particular concentrator or to the field layout, i.e. the optical and the geometrical losses, were not considered in this analysis, since they are specific to a location and a concentrator system.

In the light of these preliminary conclusions, a detailed analysis of the “high-temperature” approach was then conducted, because of the high overall performances and the balanced share between PV and CSP this strategy allows. The temperature dependence of the cell’s main electrical parameters, namely J_{sc} , V_{oc} , FF and η , was evaluated in the radiative limit for different temperatures and concentration ratios, and for different cells architecture namely single, double and triple junction solar cells.

As the temperature increases, the optimal bandgaps appear to shift toward higher values and the extent of this shift is lessened as the illumination level to which the cell is submitted increases. Consequently, operating solar cells at high temperature and concentration does not necessarily require any modification in their architecture (compared to cells operated at ambient temperature and 1-sun illumination), thus offering the option of using conventional semiconductor materials used in current CPV cells, without the need for any new exotic materials. These conventional semiconductors seem to perform well up to temperatures of 400°C, as demonstrated recently by a NREL group that tested tandem AlGaInP/GaAs cells [4, 5].

Then, in this thesis, the main electrical parameters were evaluated for a broad range of temperatures (up to ~1050K) and concentration ratios (between 1 and 1000 suns). It was recalled that the semiconductor bandgap decreases with increasing temperature, resulting in higher short-circuit current. On the other hand, the open-circuit voltage decreases due to the dark current increase. The fill factor and the conversion efficiency decrease as well. Increasing the concentration factors reduces the sensitivity to operating temperature and enhances the cells performances. These observations still hold in the case of multi-junction cells for V_{oc} , FF , and η . However, the short-circuit current density was shown to be significantly affected by the discontinuous nature of the solar spectrum, which translates into a non-monotonous behavior of J_{sc} with increasing temperature. Because of the current matching constraint, the negative impact of temperature thus appears to be more pronounced for multi-junction solar cells, with an amplitude depending on the number of sub-cells in the stack.

It is important to stress the benefit of multi-junction cells in terms of cells performances, even for operating temperatures attaining several hundred degrees. However, the operation of multi-junction cells under such extreme conditions should be investigated more deeply. At ambient temperature, adding junctions to the cell increases the performances, having in mind that, up to a certain number of sub-cells, the gain in the energy output one can expect from those cells becomes very modest [6]. A similar study should be conducted at high temperatures and concentrations to better understand the gain in performance one can expect from the use of advanced MJ cells comprising a high number of sub-cells.

The model used in our work provides idealized limits, in the sense that several strong assumptions concerning the cell operation were formulated. Real solar cells are penalized by non-ideal absorption, non-radiative recombination, and series resistance losses. The model could be further improved to account for realistic absorption, which can modify the optimal bandgap as well as the thickness of the cell. A precise understanding of the cell behavior under extreme temperatures would also require the temperature dependence of the main recombination mechanisms to be taken into account (the model used was based on the assumption of 100% radiative recombination, independently of the temperature considered).

Another important limiting mechanism omitted in our work is related to resistive losses, which are known to dramatically alter PV cell operation under highly concentrated sunlight. How these losses vary with temperature and concentration? What are their impacts on the conversion efficiency in this case? Our model should also be improved to better account for the distributed nature of the series resistance in the cell, and to better understand the behavior of each resistance component with temperature.

As for the evaluation of the hybrid CPV/CSP system based on the “high temperature approach”, the results show the importance of operating at high concentration levels to boost the system performances, due to both the improvement in the solar cell efficiency and the reduction in the radiative and convective losses. This confirms the fact that increasing concentration counterbalances the detrimental effect of high operating temperatures. The optimal operating temperature is not necessarily very high since the overall hybrid efficiency almost reaches its maximal value for $T = 523$ K and remains almost constant over a broad range of temperatures (up to 823K). Increasing the operating temperature also affects the share between PV and CSP, since higher operating temperatures lead to higher CSP efficiency but lower solar cells performances, with a balanced share around 673-773K. In all cases, the overall hybrid efficiency remains higher than the best CPV system used alone, with an extra advantage of excess energy storage.

Considering more realistic systems (solar cells operating at 2/3 of the radiative limit) does not dramatically change the above conclusions since it only shifts the optimal temperature range toward slightly higher values, due to the decrease in the PV fraction and the increase in the CSP share. The “realistic” cell scenario was arbitrarily assumed to be corresponding to 2/3 of the Shockley-Queisser limit, a value representative of today’s state-of-the-art solar cells at ambient temperature and for a concentration of 1000 suns [7,8]. Data related to cell performances under such extreme conditions are still scarce and need to be

clarified. The only available data for tandem AlGaInP/GaAs solar cells operating at 673K and 345 suns show an efficiency corresponding to ~40% of the theoretical value [5].

For an efficient transmission of the non-absorbed photons to the CSP receiver, the cell architecture should be modified: the contacts in the rear side should be transparent to prevent reflection of low-energy photons on the back of the cell. Tailoring the cell architecture will necessarily induce some additional technological challenges, aiming for example at minimizing the additional resistive losses associated with the lateral current flow at the back of the cell.

The ability of cell manufacturers to improve the cells efficiencies at high temperatures and solar concentrations, and to get closer to the radiative limit, is a critical issue toward developing more efficient hybrid systems. This needs further understanding of the physics of semiconductors at very high temperatures, a field not much explored nowadays, as well as characterizing solar cells lifespan and degradation at high temperatures and irradiance levels, a topic which was investigated only recently [4,9]. Add to this, the need to solve the problem of long-term stability at high temperatures (with preliminary encouraging results [5]).

Subsequent to the theoretical study of PV cells operating at high temperatures, experimental studies should follow to validate the proposed theoretical models. First, conventional solar cells should be tested to see whether they withstand high operating temperatures or not. Then, single and multi-junction solar cells properly designed to operate at elevated temperature should be characterized for temperatures higher than 400°C, to investigate the cells electrical behavior. Finally, complete hybrid system (including PV+CSP) should be built and characterized, toward assessing the ability of this approach to outperform conventional PV or CSP systems.

References

- [1] M. A. Steiner, J.F. Geisz, I. García, D.J. Friedman, A. Duda, and S.R. Kurtz, Optical enhancement of the open-circuit voltage in high quality GaAs solar cells, *J. Appl. Phys.* 113 (2013), 123109.
- [2] U. Rau, U. W. Paetzold, and T. Kirchartz, Thermodynamics of light management in photovoltaic devices, *Phys. Rev. B*, 90 (2014) 035211.
- [3] O. Höhn, T. Kraus, U. T. Schwartz, B. Bläsi, Effects of angular confinement and concentration to realistic solar cells, *J. Appl. Phys.*, 117 (2015) 034503.
- [4] M. A. Steiner, E.E. Perl, J. Simon, D.J. Friedman, N. Jain, P. Sharps, C. McPheeers, and M.L. Lee, AlGaInP/GaAs tandem solar cells for power conversion at 400C and high concentration, In *AIP Conference Proceedings*, 1881 (2017) 040007.
- [5] E.E. Perl, J. Simon, D.J. Friedman, N. Jain, P. Sharps, C. McPheeers, Y. Sun, Minjoo L. Lee, and M.A. Steiner, (Al)GaInP/GaAs Tandem Solar Cells for Power Conversion at Elevated Temperature and High Concentration, *IEEE J. Photovolt.*, 8 (2018) 640-645.
- [6] A.Vossier, E. Al Alam, A. Dollet, and M. Amara, Assessing the efficiency of advanced multi-junctions solar cells in real working conditions, *IEEE J. Photovolt.*, 5 (2015) 1805-1812.

- [7] A. Vossier, F. Gualdi, A. Dollet, R. Ares, and V. Aimez, Approaching the Shockley-Queisser limit: General assessment of the main limiting mechanisms in photovoltaic cells, *J. Appl. Phys.*, 117 (2015) 015102.
- [8] M. A. Green, K. Emery, Y. Hishikawa, W. Warta, E.D. Dunlop, D.H. Levi, and A.W.Y. Ho-Baillie, Solar cell efficiency tables (version 37), *Prog. Photovolt.: Res. Appl.* 19 (2011) 84-92.
- [9] H.M. Branz, W. Regan, K.J. Gerst, J.B. Borak, and E.A. Santori, Hybrid solar converters for maximum exergy and inexpensive dispatchable electricity, *Energy Environ. Sci.*, 8 (2015) 3083-3091.

Appendices

Appendix A: Variation of the different electrical parameters for single, double and triple junction solar cells, for bandgaps optimized at 973K

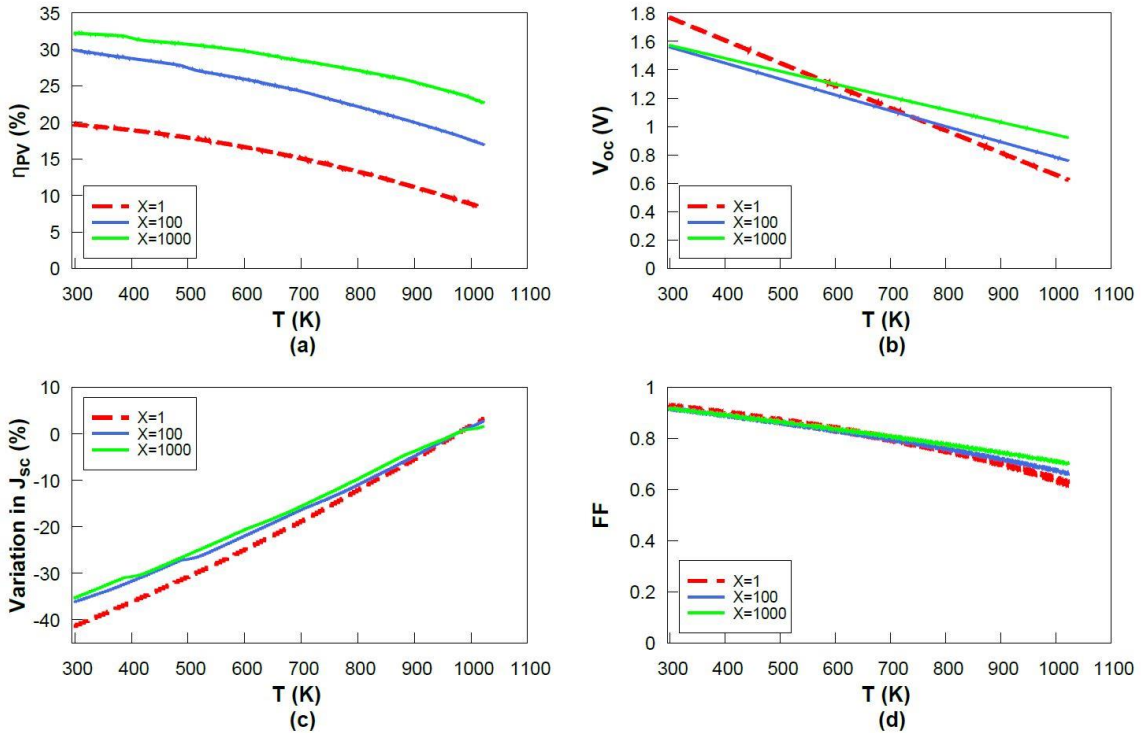


FIGURE A-1 (a) η_{PV} , (b) V_{oc} , (c) variation of J_{sc} and (d) FF, as a function of temperature for a single-junction cell optimized at $T = 973$ K (see Table V-6), for concentration factors of 1, 100 and 1,000 suns.

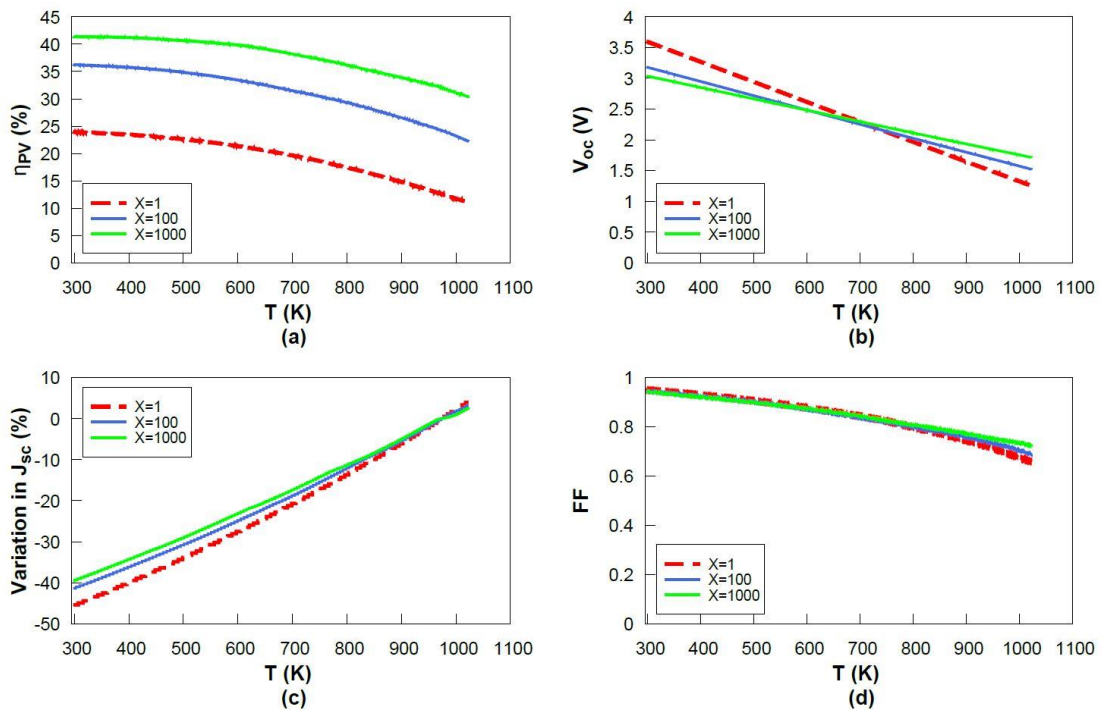


FIGURE A-2 (a) η_{PV} , (b) V_{oc} , (c) variation of J_{sc} and (d) FF, as a function of temperature for a double-junction cell optimized at $T = 973$ K (see Table V-6), for concentration factors of 1, 100 and 1,000 suns.

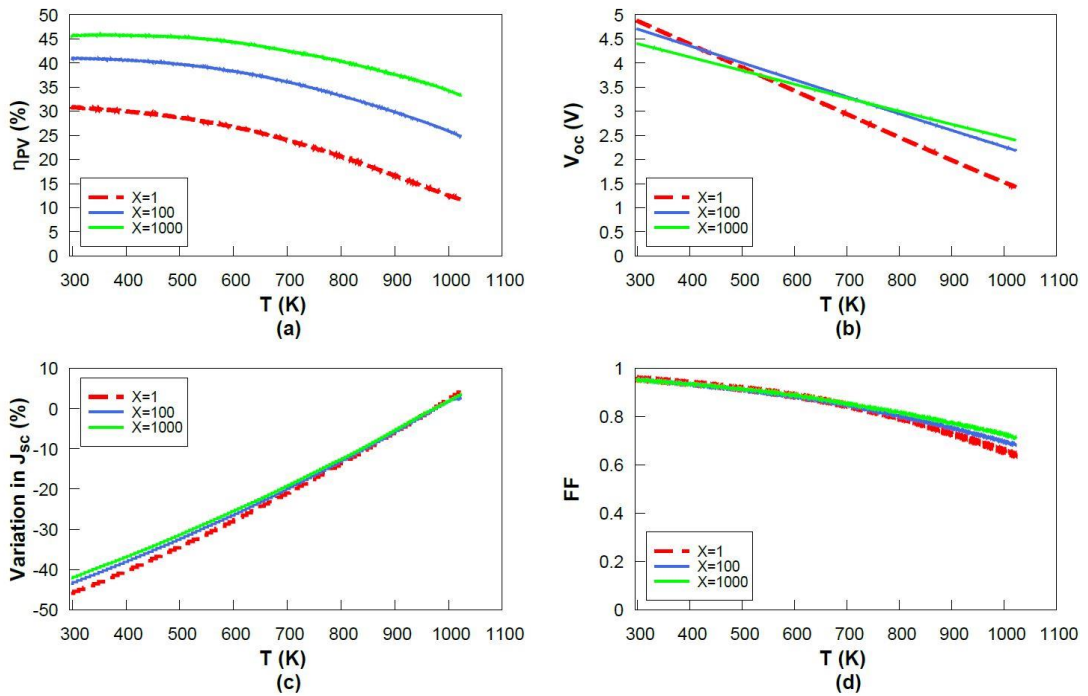


FIGURE A-3 (a) η_{PV} , (b) V_{oc} , (c) variation of J_{sc} and (d) FF, as a function of temperature for a triple-junction cell optimized at $T = 973$ K (see Table V-6), for concentration factors of 1, 100 and 1,000 suns.

Appendix B: I-V curves for single and double junction solar cells for varying temperatures and concentration levels

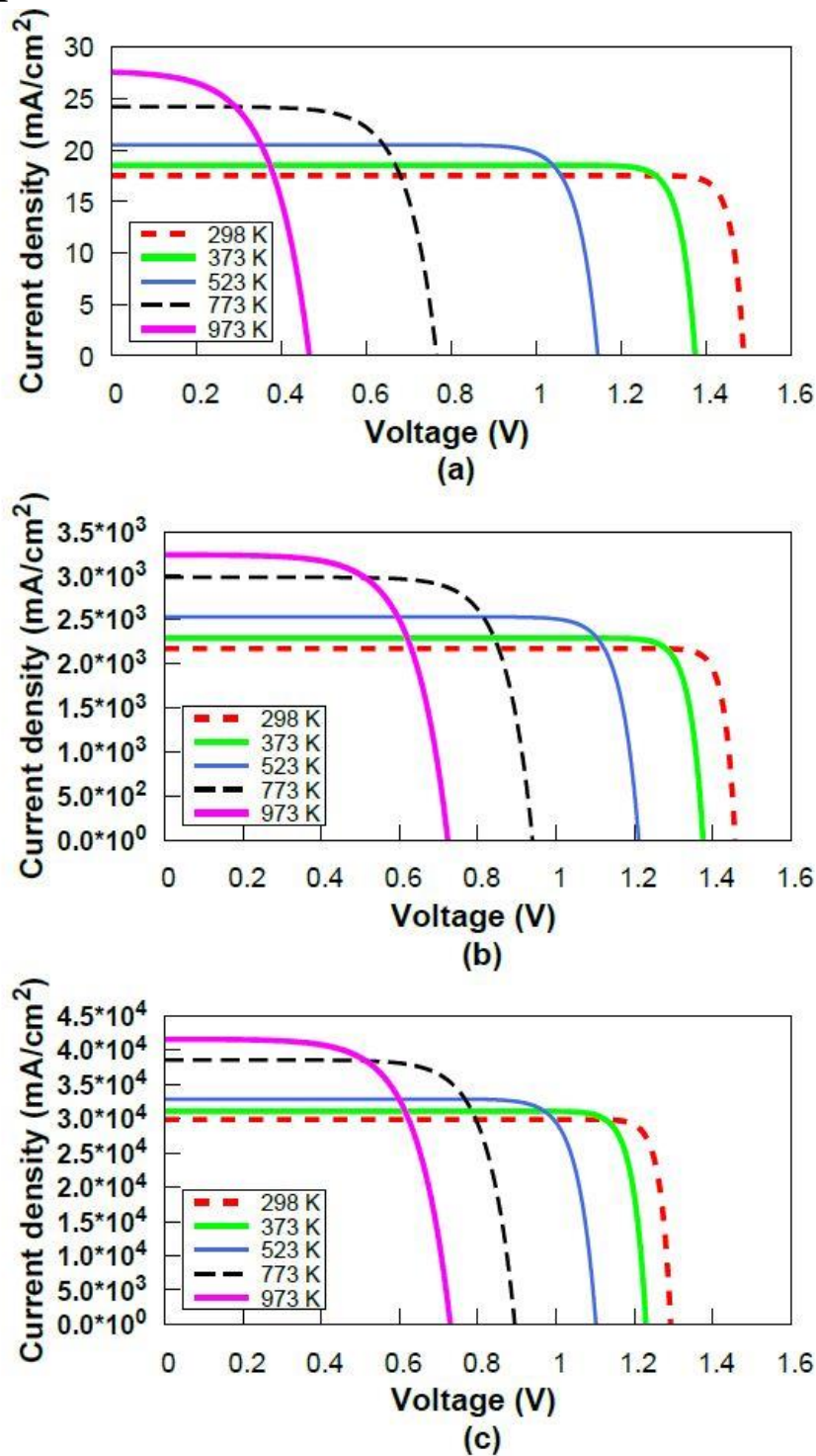


FIGURE B-1 I-V curves for single-junction solar cells for temperatures varying between 298 and 973 K and concentrations of (a) 1, (b) 100, and (c) 1000 suns.

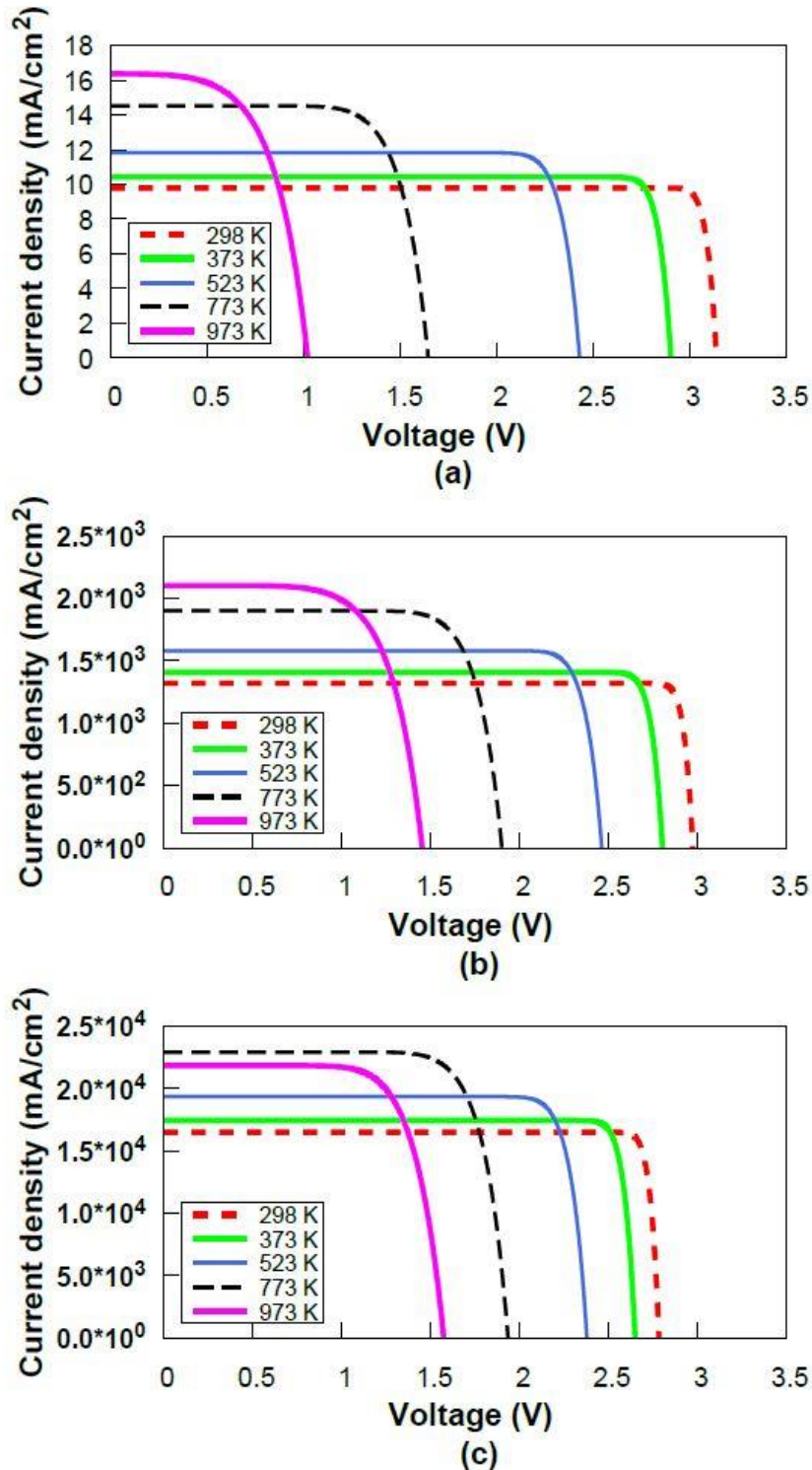


FIGURE B-2 I - V curves for double-junction solar cells for temperatures varying between 298 and 973 K and concentrations of (a) 1, (b) 100, and (c) 1000 suns.

Figure B-1 illustrates I - V curves for single-junction solar cells, for a broad range of operating temperatures varying between 298 and 973K, and for illumination levels of 1 (a), 100 (b), and 1000 (c) suns. The cells bandgaps are optimized for each concentration level considered and for a temperature of 773K. Figure B-2 represents the same I - V characteristic curves, but for double-junction solar cells with the cell bandgap combination also optimized

for each concentration, and for a temperature of 773K. These figures summarize the effect of temperature on the different electrical parameters.

In the case of single-junction solar cells, the open-circuit voltage decreases with increasing temperature, and presents less pronounced variation as the concentration increases. The same trends hold for the fill factor. Conversely, the short-circuit current increases with temperature. The voltage decrease being larger than the current increase, the cell conversion efficiency follows the open-circuit voltage variation and decreases with temperature. As for double-junction solar cells, the temperature dependence of the main electrical parameters is similar to the single-junction case in terms of open-circuit voltage, fill factor and conversion efficiency. However, the short-circuit current density shows different variations, i.e. non-monotonous fluctuations, due to the current-constraint between each individual sub-cell, making them more sensitive to the spectrum variation. In both cases, the negative effect of temperature is mitigated as the concentration level increases.

Appendix C: Experimental preliminary results on solar cells operating at high temperature

This part presents the preliminary results of the experimental tests conducted on conventional solar cells, aiming to investigate the extent to which they can handle high operating temperatures. The first tests are performed in order to study the resistance of the cell's materials to high temperatures, i.e. to determine whether or not the contacts, soldering, substrate, etc. can bear temperatures up to 400°C. Then, the main electrical parameters of the cells, namely, J_{sc} , V_{oc} , FF and η are measured for different temperatures (up to 130°C) and concentration factors, to study the effects of temperature on the cells performances.

A. Experimental set-up

The experiments are conducted in PROMES-CNRS laboratory facilities, using the 1.5kW parabolic mirror as an optical concentrator, and reaching concentration factors up to 10000 suns on average. The concentration is controlled using a flap system located between the heliostat and the parabolic mirror. The system involves a double reflection, as illustrated in Fig.C-1: the heliostat reflects direct normal solar radiation to the optical concentrator to ensure normal incidence of the direct beam onto the concentrator surface; these radiations are then reflected, focused and concentrated, at the focal point where the solar cell lies. This allows operating inside the lab contrary to systems based on simple reflection that requires outdoor installations.

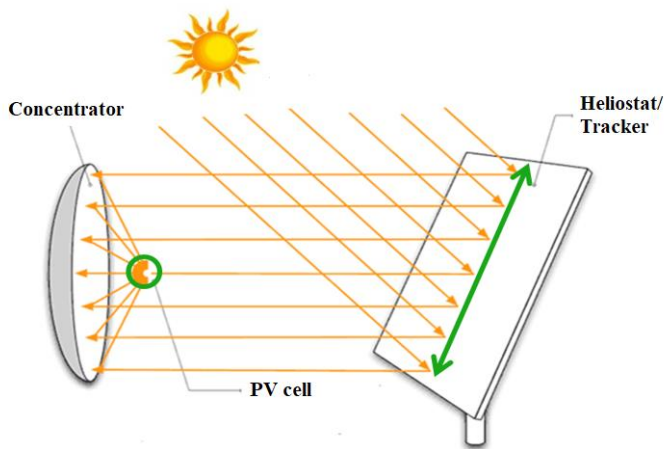


FIGURE C-1 Operating principle of the experimental set-up.

An optical fiber, characterized by a 1mm diameter and a numerical aperture (NA) of 0.66, is positioned at the concentrator focal point to transmit the concentrated light onto the cell, placed apart from the concentrator system. The fiber, and in particular the protective layer made of polymer, is not able to tolerate high operating temperature. As a result, the fiber is cooled using water active cooling systems to avoid its degradation and the melting of the polymer layer.

The Linkam HFS600E-PB4 device, manufactured by Linkam Scientific Instruments and illustrated in Fig.C-2, is used as a temperature-controlled probe system to heat the solar cells. It allows varying the temperature between ambient and 600°C, with an accuracy of

0.1°C (when the lid is closed), using a silver heating element (to ensure an optimal thermal conductivity), with the heater being a platinum resistance of 100 Ohms. A temperature sensor is integrated to the device to regulate the cell's temperature. The heating system includes 4 probes that can handle up to 300V and 4A and that are used for electrical contacts. In this experiment two of these probes are connected to a Keithley 2601 source meter, through BNC connectors, to measure the electrical characteristics of the cell. The Linkam device is connected to a computer to control the device and define the temperature profile to be applied. Indeed, it allows setting different temperature stages and delimits the temperature to be reached for each stage, the variation rate, and the resting time for the temperatures needed for cell's characterization. It also allows visualizing the temperature variation in real time. The cell, illuminated by the optical fiber, is positioned at the center of the heating plate, as represented in Fig.C-3. Since the cell is required to operate at high temperatures, no cooling system is required. On the other hand, the heating device has its own water cooling system to preserve its different electronics parts.

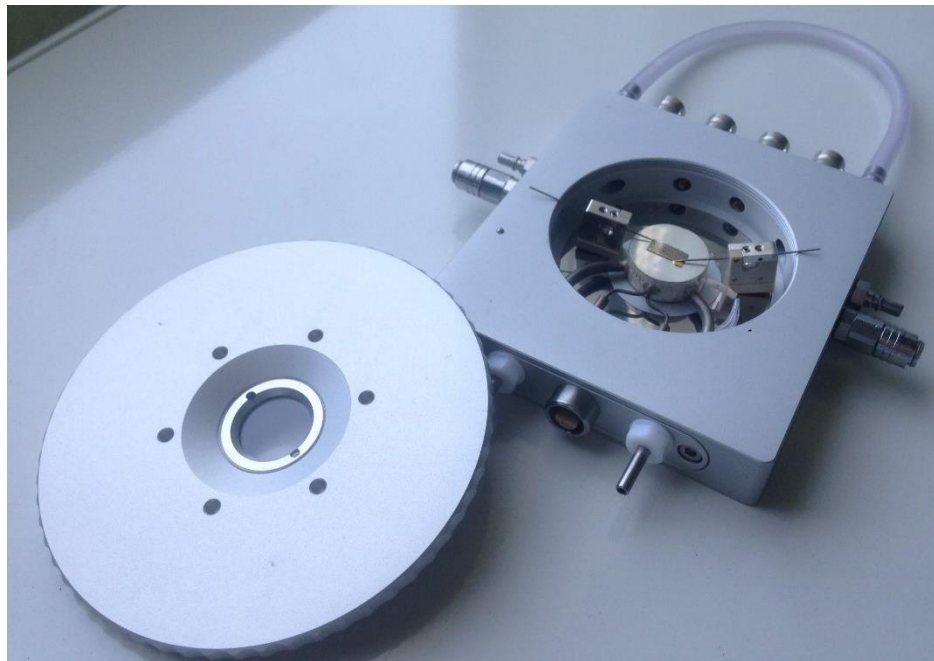


FIGURE C-2 LINKAM HFS600E-PB4 device used to control the cell temperature.

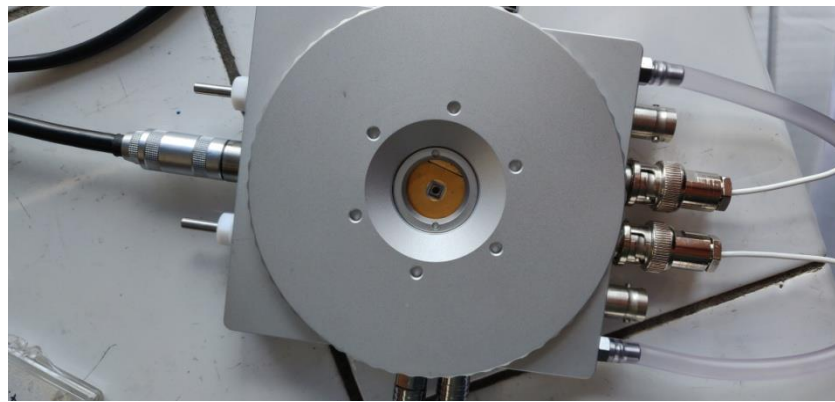


FIGURE C-3 The solar cell positioned inside the heating device.



FIGURE C-4 Experimental set-up of the high-temperature solar cells characterization (a), the temperature control system installation (b), the positioning of the solar cell on the heating plate (c), the cell illuminated by the optical fiber (d), and the Keithley 2601 (e).

The Keithley 2601 instrument is used to measure the *I-V* characteristic of the tested solar cells, for a broad range of temperatures and concentration factors, and deduce the different electrical parameters. It delivers a variable voltage to the cell and measures the generated current and voltage at the cell's terminal. Since the solar cell impedances are very low, the four-point connection is used to remove the measuring device resistances and to

improve the measurements accuracy. Figure C-4 shows the experimental setup and the different devices used for this experiment.

B. Experimental results

1. Cell design resistance to high operating temperatures

The first part of the experiment aims at evaluating the resistance of the cell design to high operating temperature, to find out whether the soldering, the substrate and the contacts withstand these extreme conditions or not. Since only the outside of the cell is tested, we first consider degraded cells. The purpose of these tests is to assess the capability of conventional CPV cells to tolerate high operating temperatures, based on a visual inspection of the cell before and after exposure to extreme test conditions.

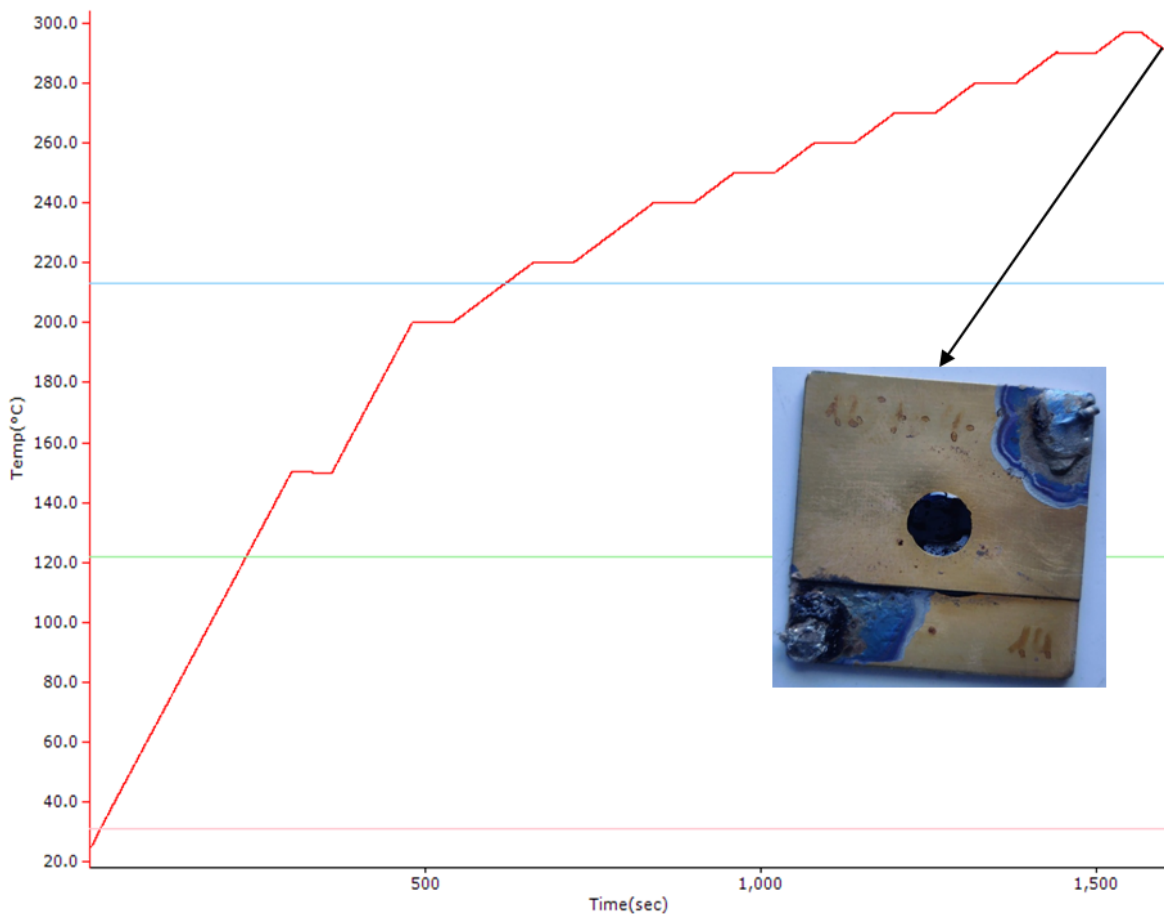


FIGURE C-5 Temperature profile and corresponding heated cell at 290°C.

The cell is positioned inside the heating device connected to the cooling system. After installing the device and connecting it to the computer, a temperature profile is established. It sets the different stop temperature levels, the increase (or decrease) temperature rate, and the stop time interval (the time at which the temperature stabilizes).

Three broken cells are tested. For the first experiment, the temperature increases rapidly up to 100°C, and after a 3min stop interval, it is set to increase up to 250°C at a slower rate. At around 170°C, the soldering starts to burn and the smoke escapes from the cell.

For the second experiment, the temperature increase rate is controlled more reasonably, since lower increasing rates are imposed. As for the previous case, the soldering starts to burn at around 170°C; however, the experiment is not stopped, and the temperature is increased up to 220°C, with many stop intervals. Then, the temperature is lowered to the ambient. At the end of the test, besides the burnt soldering, some part of the substrate (i.e. the material used between the two sheets) around the cell starts to melt and to propagate.

The same cell is resubmitted to another more intensive test, with a maximum temperature of almost 300°C (Fig.C-5 below). Above 250°C, the substrate starts melting even more and spills over the surface around the cell, and a very unpleasant smell appears. Around 270°C, the substrate turns to white, grey, and then to navy and spreads all over the cell and starts boiling, generating bubbles between both copper sheets as shown in Fig.C-6 below.

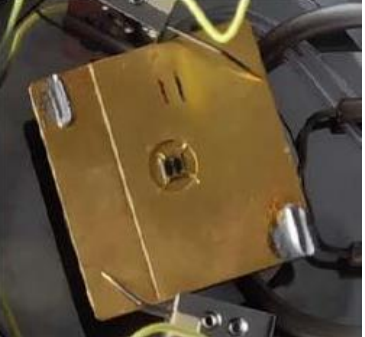


FIGURE C-6 Solar cells at 270° (left) and at 296°C (right).

The third test is run according to the profile presented in Fig.C-5. The results are identical to the previous case. The pictures of the cells showing their state before and after heating, with a mention of the temperature at which the photo is taken, are summarized in Table C-1.

These tests highlight the “physical” characteristics of solar cells, which are intended to operate under high concentrations, at high operating temperatures. As a recall, the soldering starts to burn at around 160-170°C, the substrate starts to degrade above 200°C, to melt and cover the area around the cell for temperatures above 250°C. The results show that conventional cells cannot be used at very high temperatures; they present very low resistance to high operating temperature. Thus, they are not suitable for the hybrid CPV/CSP “high temperature PV” strategy requiring solar cells capable of bearing at least 400°C without material degradation. To test the hybrid PV/CSP “high-temperature PV” approach, the cell should be carefully designed: the soldering and the substrate materials should be chosen to handle such high operating temperatures.

TABLE C-1 Properties and physical characteristics of the three tested cells before and after heating.

Properties	Before Test	After Test
Type: ?? Shape : Round Radius: 1mm	$\approx 25^\circ\text{C}$ 	$\approx 170^\circ\text{C}$ 
Type: GaAs Shape: Round Radius: 1mm	$\approx 150^\circ\text{C}$ 	$\approx 290^\circ\text{C}$ 
Type: GaAs Shape: Round Radius: 1mm	$\approx 25^\circ\text{C}$ 	$\approx 296^\circ\text{C}$ 

These first observations are of prime importance to assess the ability of the materials used to tolerate extreme operating conditions. It is also crucial to practically characterize the electrical behavior of the solar cells with increasing temperatures. Hence, since such conventional cells cannot tolerate very high temperatures, the cell's main electrical parameters were measured up to only 130°C.

2. Main electrical parameters at high operating temperatures

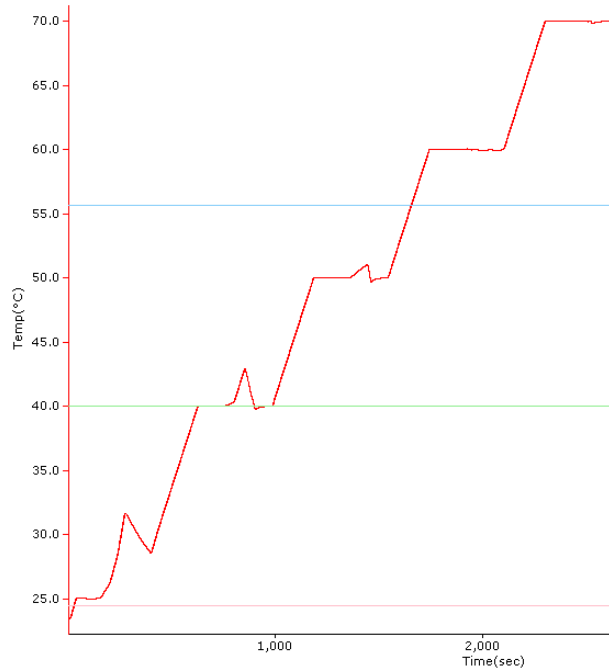


FIGURE C-7 Profile showing the effect of concentration which increases the operating temperature, up to 70°C.

The experimental set-up described earlier is designed to measure the main electrical parameters of solar cells at various temperatures. The cell is positioned inside the temperature controller and is illuminated through optical fibers. It is connected via BNC connectors to the Keithley device that measures the *I-V* characteristic curves for different temperatures and concentration factors. High concentration ratio increases the cell operating temperatures; this heating is noticeable during the stop intervals on the temperature profile for temperatures between ambient and 55°C, as shown in Fig.C-7. The temperature controller cools off the cell to maintain the required temperature level. This effect is spotted for relatively low temperatures up to 55°C. In the temperature profile presented in Fig.C-8, we don't observe any heating effect at 90 and 130°C stop temperature levels.

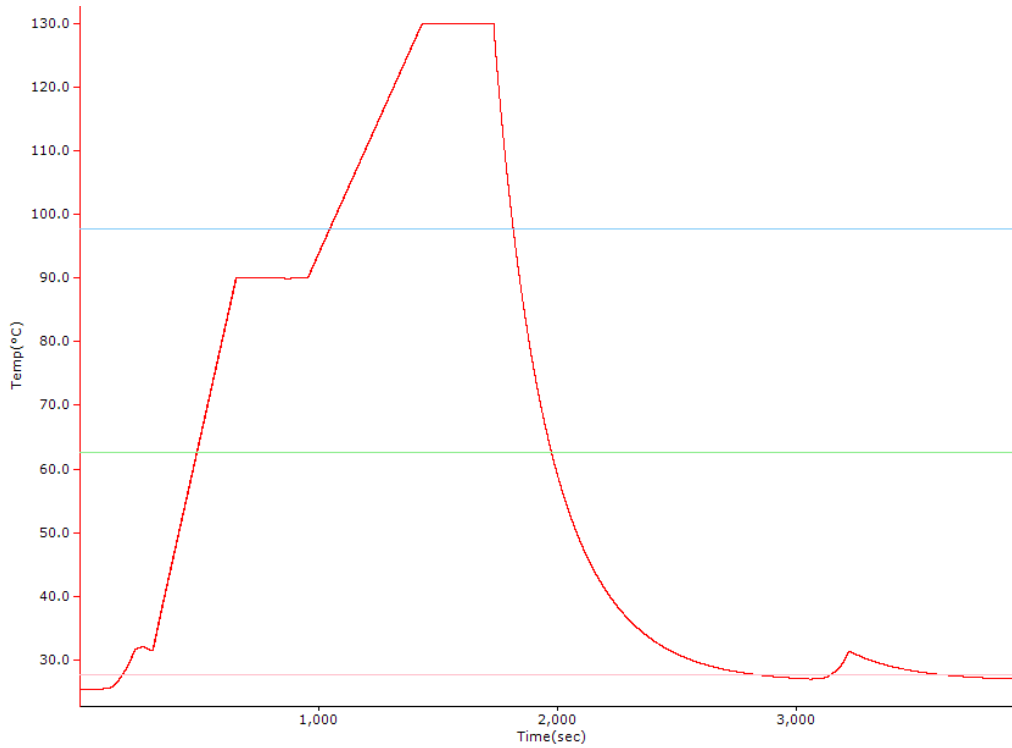


FIGURE C-8 Profile of the temperature used to measure the different cells electrical parameters.

A triple-junction solar cell is tested for temperatures varying between ambient and 130°C according to the profile shown in Fig.C-8 for concentration factors of ~500, ~1100 and ~1800 suns. The *I-V* characteristics are measured at ambient temperature, before and after heating (to ensure that the cell is not degraded due to temperature), as well as at 90°C and 130°C. Figure C-9 illustrates the different *I-V* curves plotted for varying temperatures and for concentration factors of (a) ~500 suns, (b) ~1100 suns and (c) ~1800 suns. Figure C-10 represents the variation of the open-circuit voltage (a), the fill factor (b) and the conversion efficiency (c) as a function of concentration, also for different operating temperatures. The variation of the main electrical parameters with increasing concentration factors, and for the different temperatures considered, is similar to the results described by E.E. Perl et al. [1]. V_{oc} , FF and η decreases with increasing temperature, with an amplitude function of the illumination level to which the cell is submitted. No conclusion can be drawn for the J_{sc} variation since it is directly proportional to the direct normal irradiance (DNI), which was not stable during the experiment. V_{oc} is also affected by the DNI variation but at a lower extent, since it varies with the logarithm of this parameter, the variation in this case representing 1% error rate. The experiments should be repeated in more stable environmental conditions, and additional concentrations and temperatures should be considered.

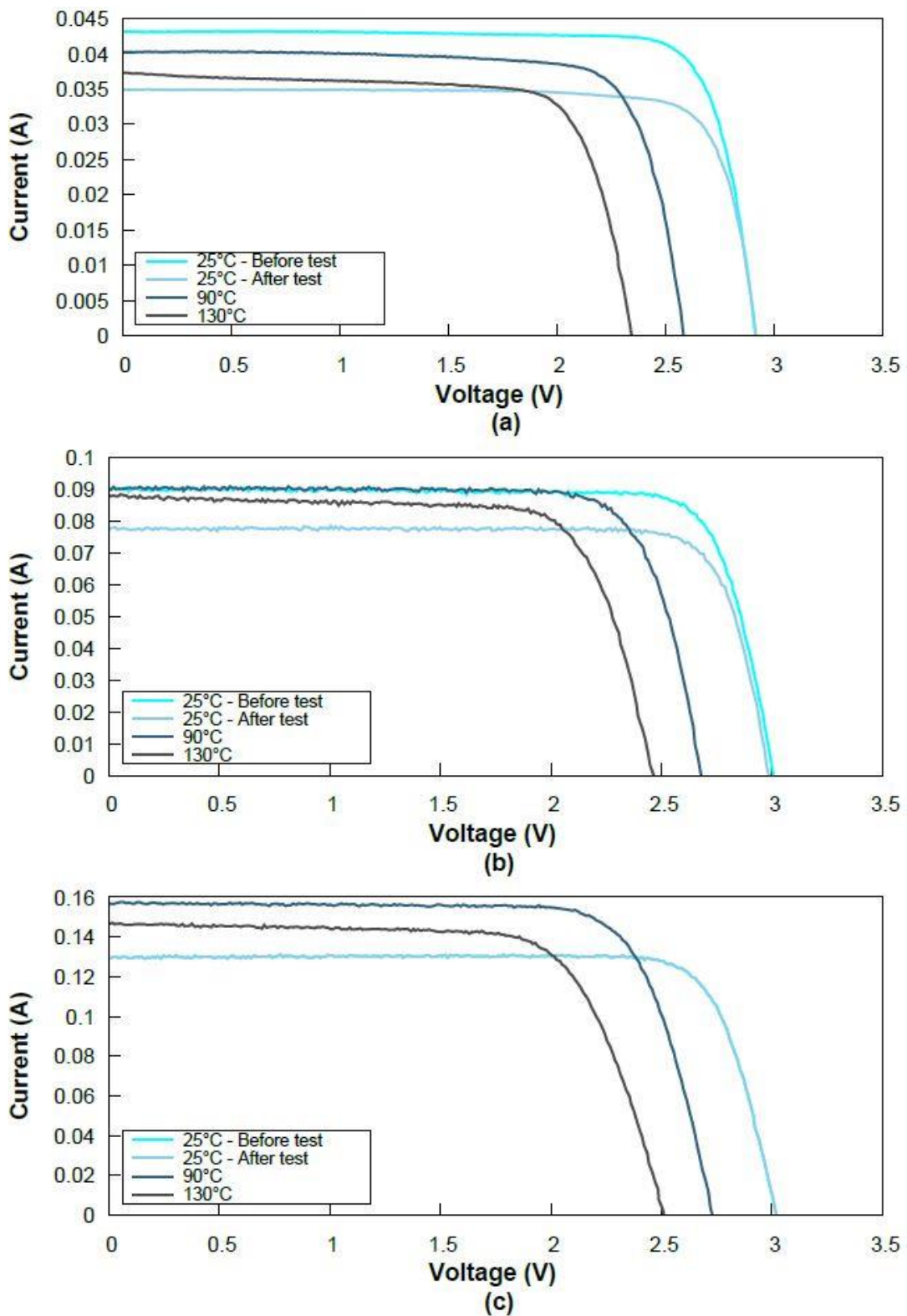
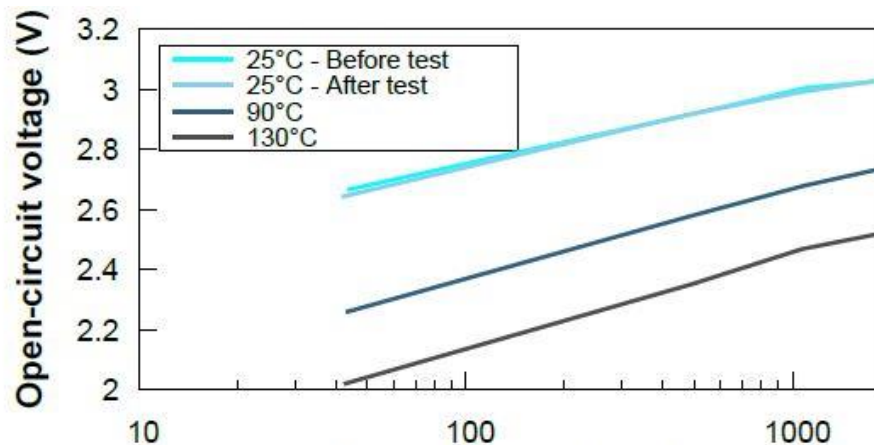
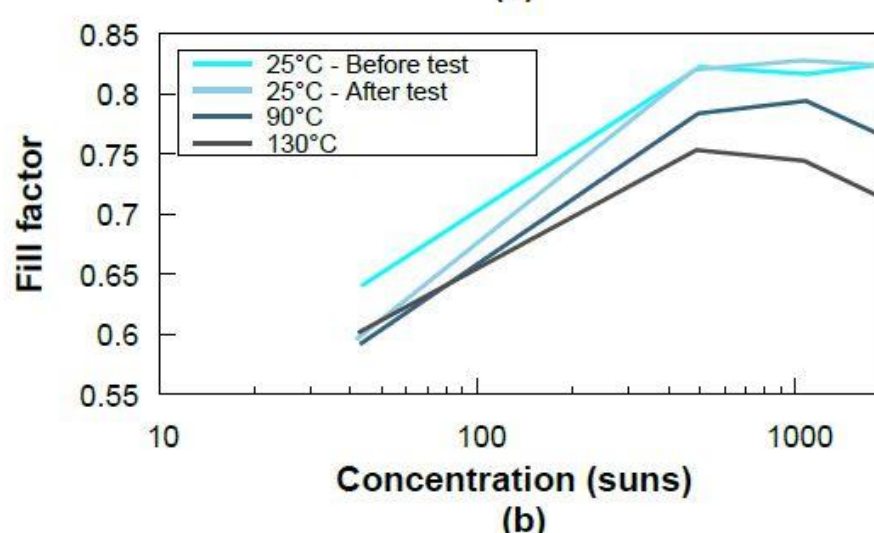


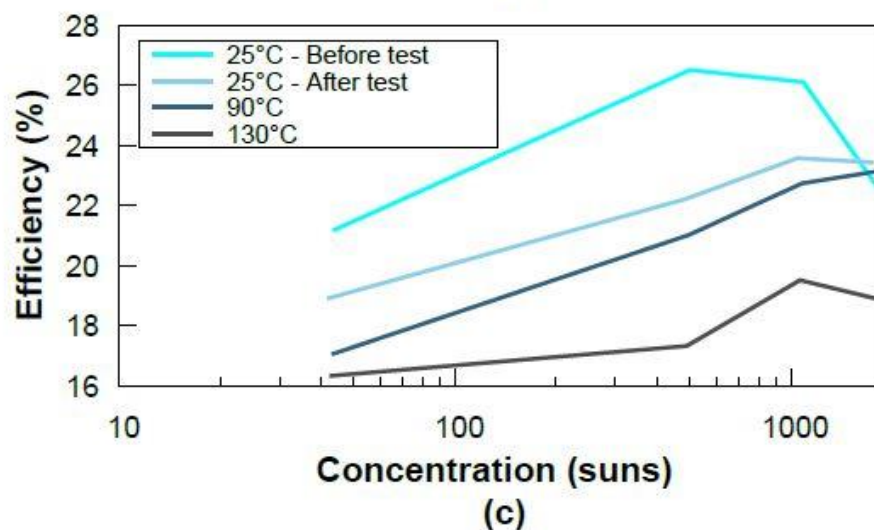
FIGURE C-9 I-V curve plotted for different temperatures and for three concentration ratios (a) 500 suns, (b) 1100 suns and (c) 1800 suns.



(a)



(b)



(c)

FIGURE C-10 V_{oc} , FF and η as a function of concentration for different operating temperatures.

In the light of the preliminary tests aiming at evaluating the ability of PV cells to tolerate extreme temperature, we couldn't risk reaching higher operating temperatures. Future experiments should consider more robust cells, to be able to test their electrical performances at temperatures exceeding 400°C, and validate the theoretical observations.

C. Reference

- [1] E.E. Perl, J. Simon, D.J. Friedman, N. Jain, P. Sharps, C. McPheeters, Y. Sun, Minjoo L. Lee, and M.A. Steiner, (Al)GaInP/GaAs Tandem Solar Cells for Power Conversion at Elevated Temperature and High Concentration, *IEEE J. Photovolt.*, 8 (2018) 640-645.

Appendix D: Résumé en Français

A. Introduction

Le solaire photovoltaïque repose sur la conversion directe de l'énergie solaire en électricité. Son efficacité théorique maximale peut être déterminée grâce au formalisme de Shockley-Queisser, qui prédit un rendement de conversion maximal de 33%. Ce formalisme [1] repose sur un certain nombre d'hypothèses, parmi lesquelles l'absence de pertes résistives et la nature des mécanismes de recombinaison mis en jeu [2]. Il considère que le courant généré par la cellule est simplement la différence entre les flux absorbés et émis par la cellule. Néanmoins, la limite de Carnot prédit un rendement de conversion solaire → électrique maximal pouvant atteindre 93%. L'écart important entre ces deux limites est dû à des pertes intrinsèques fondamentales, dont la conversion inefficace du spectre solaire, puisque les photons dont l'énergie est inférieure au gap ne sont pas absorbés, tandis que les photons plus énergétiques que le gap sont inefficacement convertis. Une troisième source de perte est liée à l'asymétrie angulaire entre les flux absorbés et émis [3].

De nombreuses approches innovantes ont été développées pour pallier ces pertes et dépasser la limite de Shockley-Queisser, dont trois développées au cours de cette thèse : 1) les cellules multi-jonctions à concentration, afin de minimiser les pertes spectrales et les pertes de *Boltzmann*, 2) la combinaison de la concentration et de la restriction angulaire, pour atténuer les pertes de *Boltzmann*, et 3) les systèmes hybrides PV/CSP pour diminuer les pertes spectrales et celles de *Boltzmann*.

Ces différentes stratégies sont limitées par des mécanismes conduisant à une détérioration des performances des cellules, telles que les résistances série, les recombinaisons non-radiatives ou les températures de fonctionnement élevées. L'objectif de cette thèse est donc d'optimiser les cellules solaires afin d'améliorer les performances de ces systèmes innovants et d'étudier l'impact de chacun des mécanismes limitant. Les largeurs de bandes interdites des cellules solaires sont optimisées pour une large plage de résistances série, de facteurs de concentration et de températures. Les propriétés angulaires des flux absorbés et émis sont également ajustées pour des cellules idéales et réelles prenant en compte les résistances série et les recombinaisons non-radiatives. Ce résumé regroupe les résultats les plus primordiaux de cette étude. L'intégral du travail et des résultats se trouvent dans la version en anglais.

B. Cellules multi-jonction à concentration

Pour réduire les pertes spectrales, l'une des technologies les plus exploitées de nos jours est le développement de cellules multi-jonctions (MJ) qui consistent en un empilement de plusieurs jonctions *p-n* caractérisées par des gaps électroniques différents permettant de convertir une plus grande fraction du spectre solaire. Les différentes jonctions étant connectées en série, la tension extraite de la cellule est la somme des tensions des différentes jonctions, tandis que le courant généré correspond à la valeur minimale du courant généré par chacune des sous-cellules de l'empilement. Les matériaux III-V sont couramment utilisés pour la fabrication des cellules MJ. En raison de leur coût très élevé, les cellules MJ sont

souvent utilisées sous concentration du flux solaire (la surface requise de cellule étant sensiblement inférieure à celle des cellules conventionnelles).

Le photovoltaïque à concentration utilise un concentrateur optique, i.e. miroirs paraboliques (système réfléchissant) ou lentilles de Fresnel (système réfractif), et une ou plusieurs cellule(s) solaire(s) placée au point focal du concentrateur. Le système est nécessairement monté sur un suiveur solaire afin d'assurer une incidence normale des rayons solaires à la surface du concentrateur optique. Le CPV offre de nombreux avantages : outre la réduction de la surface de la cellule requise, la concentration solaire permet la diminution des pertes de *Boltzmann* et donc l'accroissement du rendement de conversion. Le courant photo-généré augmente linéairement avec la concentration alors que la tension de circuit-ouvert augmente de manière logarithmique. A ce jour, le rendement record obtenu expérimentalement est de 46% pour une cellule constituée de 4 jonctions sous 508 soleils [4].

Théoriquement, le rendement de conversion photovoltaïque doit croître indéfiniment avec la concentration, ce qui constituerait une forte motivation pour développer des systèmes CPV à ultra haute concentration. Cependant, la plupart des cellules commercialisées de nos jours fonctionnent à des facteurs de concentration compris entre 500 et 1000 soleils ce qui ne constitue que 1 à 2% de la limite théorique maximale (46000 soleils) [5]. Cet écart important entre les concentrations théoriques et pratiques est principalement dû aux pertes résistives, qui sont proportionnelles au carré du courant photo-généré, et qui constituent donc un frein au développement de cellules opérant efficacement à de tels niveaux de concentration.

Il a récemment été démontré que l'amplitude avec laquelle les résistances séries affectent les performances des cellules dépend fortement du gap électronique du semi-conducteur. En conséquence, et dans le but de maximiser les performances des systèmes CPV, un premier volet de ce travail est consacré à étudier théoriquement comment les résistances série affectent les performances des cellules solaires à concentration, et comment ce paramètre modifie la combinaison optimale des bandes interdites des différentes jonctions de l'empilement.

1. Objectifs et méthodologie

a) Objectifs

La prise en compte des résistances série dans les cellules solaires modifie la combinaison optimale des gaps électroniques, en particulier pour des facteurs de concentration ou des valeurs de résistance série élevés. Nous avons étudié en premier lieu comment les résistances série affectent les performances et la combinaison optimale des gaps électroniques de cellules multi-jonction en fonction du facteur de concentration. Ensuite nous avons évalué comment l'optimisation des gaps électroniques atténue l'effet négatif des pertes résistives sur les performances des cellules.

b) Méthodologie

Pour étudier l'effet des résistances série sur la combinaison optimale des gaps électroniques, un algorithme a été développé et codé sous Matlab, basé sur la résolution de l'équation de la caractéristique courant-tension (eq. (D-1)) prenant en compte les résistances série.

$$J = J_{ph} - J_0 \left(e^{\frac{q(V+JR_S)}{nkT}} - 1 \right) \quad (\text{D-1})$$

Les courbes iso-rendements, qui illustrent les rendements de conversion en fonction des gaps électroniques des différentes jonctions de l'empilement, sont générées. Ils permettent d'évaluer l'amplitude des pertes résistives et de déterminer les rendements maximaux ainsi que la combinaison optimale des gaps permettant d'atteindre ces rendements. Les couleurs rouges représentent les rendements les plus élevés, tandis que les zones bleutées indiquent des rendements de conversion plus faibles.

Pour une cellule triple-jonction, les courbes iso-rendements sont tracées en fonction de la largeur de bande interdite des jonctions du haut et du milieu, en fixant la jonction du bas à 0.7 eV. Plus le nombre de jonctions augmente dans l'empilement et plus le nombre de gaps supposé fixe au cours de la simulation augmente, ce qui ne permet pas de déterminer correctement la combinaison optimale des gaps électroniques. Pour traiter les cellules comprenant trois jonctions et plus, la combinaison des largeurs de bandes interdites est dérivée à l'aide d'un algorithme génétique intégré dans Matlab.

2. Résultats

a) Effet de la concentration sur les cellules réelles

La figure D-1 représente les courbes iso-rendement pour des cellules solaires triple-jonction caractérisées par une résistance série de 0.01 Ω cm², en fonction des gaps électroniques de la jonction du haut et du milieu, et en fixant le gap de la jonction du bas à 0.7 eV. Ces courbes sont tracées pour différents facteurs de concentration, notamment (a) 1, (b) 1000, (c) 5000 et (d) 10000 soleils.

En observant les 4 figures, on remarque que l'augmentation du facteur de concentration entraîne une amélioration des rendements de conversion jusqu'à un niveau de concentration au-delà duquel les performances sont dégradées en raison de pertes résistives.

La concentration affecte également la combinaison optimale des gaps électroniques avec une variation modeste jusqu'à 1000 soleils (limite qui dépend de la valeur de la résistance série), et des modifications plus importantes qui tendent à décaler les gaps optimaux vers des valeurs plus élevées, au-delà de cette concentration limite. L'amplitude de ces variations est d'autant plus prononcée que la valeur de la résistance augmente.

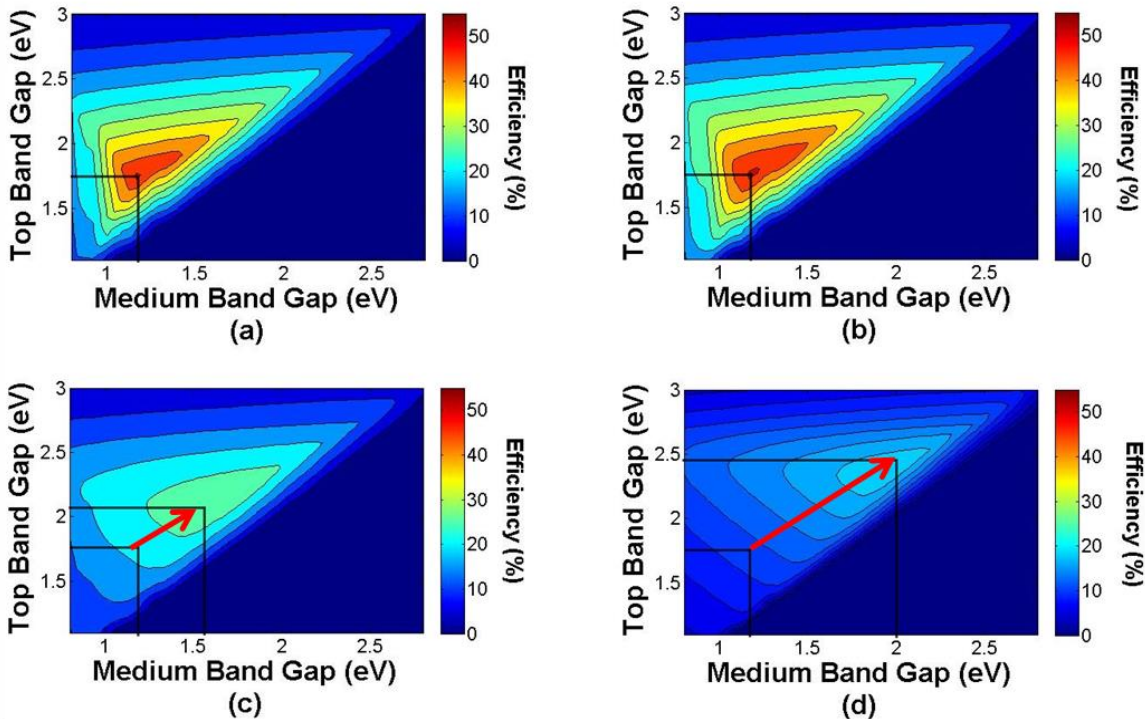


FIGURE D-1 Courbes iso-rendements pour une cellule solaire triple-jonction ayant une résistance série de 0.01 $\Omega \text{ cm}^2$, en fixant le gap de la jonction du bas à 0.7 eV, pour des facteurs de concentration de (a) 1, (b) 1000, (c) 5000 et (d) 10000 soleils.

b) Effet de la résistance série

Pour une illumination de 1 soleil, les résistances série, même étant élevées, n'affectent ni les rendements de conversion ni la combinaison optimale des bandes interdites, en raison du courant modeste traversant la cellule et impliquant des pertes résistives négligeables. Ces observations ne sont plus valables pour des facteurs de concentration élevés. La figure D-2 illustre les courbes iso-rendement pour des cellules solaires triple-jonction, soumises à une concentration de 1000 soleils, en fonction des gaps électroniques de la jonction du haut et du milieu, et en fixant le gap inférieur à 0.7 eV. Ces courbes sont représentées pour différentes valeurs de la résistance série, à savoir: a) cellule idéale, $R_s = 0 \Omega \text{ cm}^2$, (b) $R_s = 0.01 \Omega \text{ cm}^2$, (c) $R_s = 0.05 \Omega \text{ cm}^2$ et (d) $R_s = 0.1 \Omega \text{ cm}^2$.

La comparaison des différents graphes de la figure D-2 permet de montrer que l'augmentation de la valeur de la résistance série détériore les rendements de conversion photovoltaïque par rapport au cas idéal, et que cette dégradation est d'autant plus prononcée que la valeur de la résistance augmente. Il découle de la présence de pertes résistives significatives un décalage de la combinaison optimale des largeurs de bandes interdites de la cellule vers des valeurs plus élevées

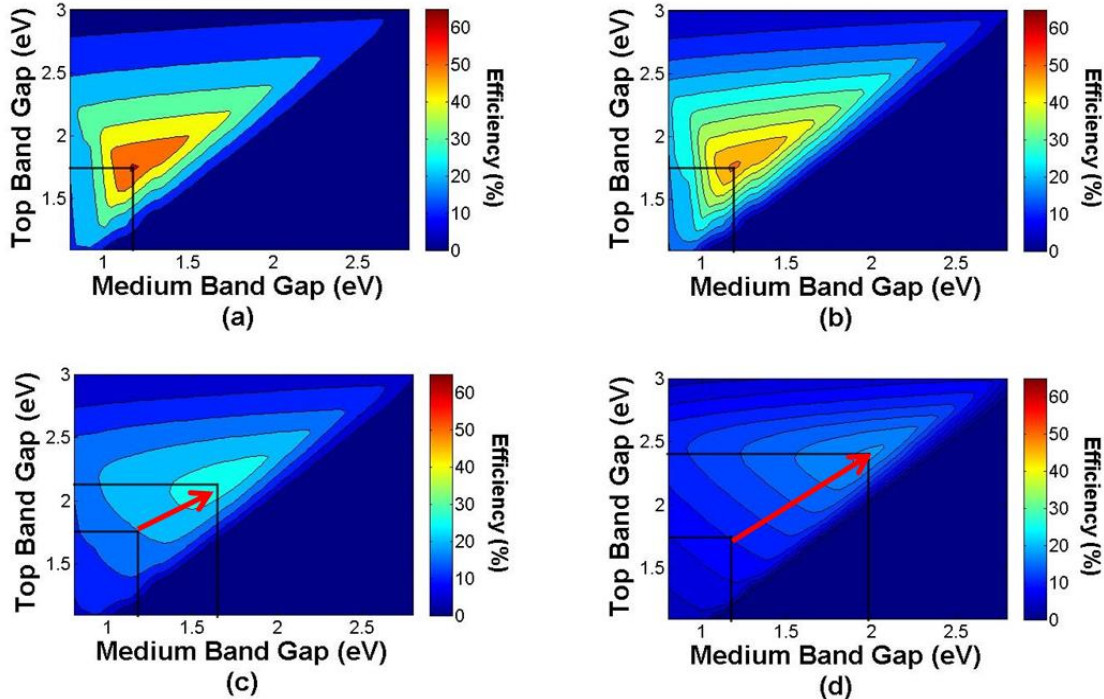


FIGURE D-2 Courbes iso-rendements pour une cellule solaire triple-jonction, en fixant le gap de la jonction du bas à 0.7 eV, pour un facteur de concentration de 1000 soleils et différentes valeurs de la résistance série : (a) 0, (b) 0.01, (c) 0.05 et (d) 0.1 $\Omega \text{ cm}^2$.

Le tableau D-1 liste la combinaison optimale des gaps électroniques pour des cellules triple-jonction ayant des résistances série de 0.01 ohm cm^2 et 0.05 ohm cm^2 , et pour des facteurs de concentration variant entre 1 et 10000 soleils. La résistance série nulle est indiquée comme référence et représente une cellule idéale, avec une combinaison optimale de $1.75/1.18/0.7 \text{ eV}$ [6]. La combinaison optimale reste inchangée jusqu'à 2500 soleils pour les faibles résistances série, et jusqu'à 1000 soleils pour les résistances élevées. Au-delà de ces concentrations, la combinaison des gaps semble changer sensiblement et la modification est d'autant plus prononcée que les concentrations ou les résistances série augmentent. Pour des valeurs élevées des résistances série et des concentrations, la combinaison optimale de matériaux semi-conducteurs n'inclut plus des matériaux à faibles gaps qui sont fondamentalement caractérisés par des pertes résistives importantes. Pour les gaps ayant des valeurs moyennes ou élevées, la cellule présente de hautes tensions et de faibles courants, ce qui conduit à une diminution des pertes résistives.

TABLEAU D-1 Combinaison optimale des gaps électroniques d'une cellule solaire triple-jonction, calculée en utilisant l'algorithme génétique, pour des facteurs de concentration compris entre 1 et 10000 soleils et des résistances série de 0.01 et 0.05 $\Omega \text{ cm}^2$

$R_s (\Omega \text{ cm}^2)$	Concentration (soleils)	Gaps Optimaux $E_{g1}/E_{g2}/E_{g3}$ (eV)
0 (Réf)	1	1.75/1.18/0.7
0.01	1	1.75/1.18/0.7
	1000	1.75/1.18/0.7
	2500	1.75/1.18/0.7
	5000	1.88/1.37/0.95
	10000	2.06/1.55/1.17
0.05	1	1.75/1.18/0.7
	1000	1.94/1.39/0.95
	2500	2.18/1.69/1.34
	5000	2.31/1.9/1.59
	10000	2.50/2.12/1.85

3. Discussion

Idéalement la concentration solaire améliore les rendements de conversion photovoltaïque. En pratique, ce n'est pas nécessairement le cas puisqu'au-delà d'un facteur de concentration « limite » (qui dépend de la cellule et de la valeur de la résistance série) les performances globales se dégradent. L'augmentation de la tension de circuit-ouvert avec la concentration est principalement responsable de l'augmentation du rendement de conversion, ce qui compense l'effet des pertes résistives. Cependant, l'effet néfaste des résistances série s'amplifie avec le facteur de concentration, jusqu'à devenir prédominant et contrebalancer l'effet positif de la concentration, ce qui réduit les rendements de conversion et décale la combinaison des gaps vers des valeurs plus élevées.

Les principaux paramètres électriques, à savoir FF , V_{oc} , J_{sc} et η , sont comparés pour diverses résistances série et facteurs de concentration, et pour des combinaisons de gaps optimisées et non optimisées. Les cellules non optimisées désignent les cellules dont les bandes interdites sont égales à 1.75/1.18/0.7 eV (qui correspond à la combinaison « optimale » d'une cellule « idéale » non affectée par les pertes résistives). Le tableau D-2 répertorie les paramètres électriques des cellules non optimisées, ainsi que des cellules optimisées en supposant une résistance série de 0.01 et 0.05 $\Omega \text{ cm}^2$, et des facteurs de concentration de 1000, 2500, 5000 et 10000 soleils. La cellule idéale ayant une résistance série nulle est mentionnée à titre indicatif. D'après les différentes valeurs, on peut observer une amélioration significative des performances de la cellule en raison de l'augmentation du

V_{oc} et du FF lorsque les bandes interdites se déplacent vers des valeurs plus élevées. Les gains en FF , V_{oc} et η sont d'autant plus remarquables que la concentration ou la résistance série augmente. Ceci démontre l'importance de l'optimisation du gap électronique.

TABLEAU D-2 Principaux paramètres électriques pour une cellule triple-jonction pour des combinaisons de gaps non-optimisées et optimisées.

Rs ($\Omega \text{ cm}^2$)	X (soleils)	Cellule non-optimisée				Cellule Optimisée			
		FF	V_{oc} (V)	J_{sc} (mA/cm ²)	η (%)	FF	V_{oc} (V)	J_{sc} (mA/cm ²)	η^* (%)
0 (Ref)	1	-	-	-	-	0.89	2.84	18.18	51.07
0.01	1000	0.86	3.37	18.18×10^3	58.18	0.86	3.37	18.18×10^3	58.18 (+0%)
	2500	0.78	3.44	4.54×10^4	54.21	0.78	3.44	4.54×10^4	54.21 (+0%)
	5000	0.66	3.49	9.09×10^4	46.54	0.74	4.03	7.5×10^4	49.6 (+3.06%)
	10000	0.45	3.55	18.18×10^4	32.04	0.71	4.63	1.12×10^5	40.54 (+8.5%)
0.05	1000	0.65	3.37	18.18×10^3	44.15	0.77	3.98	1.36×10^4	46.31 (+2.16%)
	2500	0.36	3.44	4.54×10^4	24.87	0.72	4.91	2.28×10^4	35.91 (+11.04%)
	5000	0.25	3.49	6.79×10^4	13.29	0.63	5.52	3.59×10^4	27.54 (+14.25%)
	10000	0.25	3.55	7.03×10^4	6.91	0.57	6.2	4.90×10^4	19.10 (+12.19%)

Entre parenthèse : le gain relatif en rendement par rapport à la cellule non-optimisée.

Pour mieux comprendre l'avantage de cette stratégie, le rendement de conversion est tracé en fonction de la concentration (variant entre 1 et 10000 soleils) pour des cellules triple-jonction ayant une résistance série de $0.05 \Omega \text{ cm}^2$ (Fig.D-3 (a)) avec des gaps optimisés. La variation relative du rendement, calculée comme étant la différence entre les rendements des cellules optimisées et le rendement de la cellule idéale, est également illustrée (Fig.D-3 (b)). D'après la figure D-3 (b), deux zones distinctes peuvent être identifiées : 1) une zone négative pour laquelle l'optimisation n'entraîne aucune amélioration de l'efficacité et 2) une zone positive indiquant la plage de concentration pour laquelle l'optimisation du gap conduit à une amélioration des performances des cellules.

L'optimisation du gap électronique permet d'améliorer les rendements des cellules, et ainsi de dépasser les performances des cellules conventionnelles pour des concentrations solaires supérieures à la concentration d'optimisation. Les rendements restent inférieurs aux cellules conventionnelles pour les concentrations inférieures à cette concentration. L'écart

entre les rendements des cellules optimisées et non optimisées augmentent à mesure que le facteur de concentration augmente, ce qui incite à optimiser les gaps de cellules photovoltaïques soumises à des concentrations élevées.

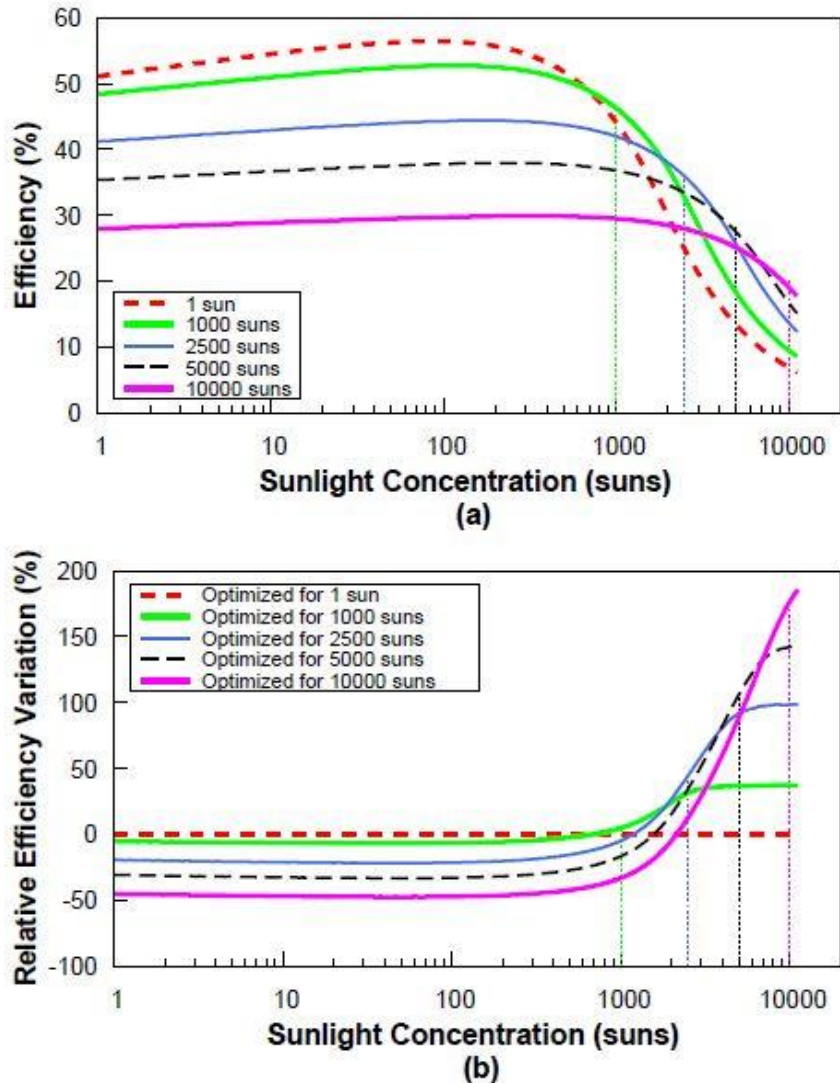


FIGURE D-3 Rendement de conversion (a) et variation relative des rendements (b) en fonction de la concentration pour une cellule solaire triple-jonction ayant une résistance série de $0.05 \Omega \text{ cm}^2$.

Les systèmes CPV permettent d'améliorer l'efficacité de conversion en diminuant l'amplitude des pertes de Boltzmann. Cette approche permet également de réduire la surface de cellule requise, et par conséquent le coût du système, mais elle est fondamentalement limitée par les pertes résistives très prononcées, qui sont particulièrement importantes pour des facteurs de concentration et des valeurs de résistance série élevées. Pour essayer de limiter ces effets négatifs, une deuxième stratégie consiste à limiter l'angle solide d'émission (affectant les photons issus des recombinaisons radiatives, et qui s'échappent de la cellule) [7-9].

C. Combinaison de la concentration et de la restriction angulaire

La restriction angulaire est une stratégie complémentaire à la concentration solaire, les deux méthodes étant thermodynamiquement équivalentes à la limite radiative. Le

confinement angulaire semble être une stratégie prometteuse dans la mesure où elle augmente les rendements de conversion, sans être affectée par les pertes résistives, puisque la concentration solaire ne rentre pas en jeu. En limitant l'angle solide d'émission, les photons émis radiativement sont recyclés et réabsorbés par la cellule, ce qui entraîne une accumulation des porteurs de charge et, une augmentation de la tension de circuit-ouvert. Cependant, cette stratégie est limitée par la faible capacité de la cellule à émettre de la lumière, qui se traduit par de faibles valeurs du rendement de fluorescence externe (ERE).

Une stratégie originale consiste donc à combiner les deux approches pour bénéficier de leurs avantages et améliorer les rendements de conversion photovoltaïque, tout en réduisant l'impact des résistances série et des recombinaisons non-radiative, principaux facteurs limitant de chaque stratégie utilisée seule. Trois volets sont étudiés dans cette partie: 1) comment cette stratégie permet d'améliorer les performances, 2) quelle est la combinaison optimale des angles solides d'absorption et d'émission et 3) comment les principaux mécanismes limitant affectent les rendements des cellules, en fonction des propriétés angulaires des flux absorbés et émis.

4. Objectifs et méthodologie

a) Objectifs

Combiner la restriction angulaire et la concentration solaire permet d'améliorer les rendements de conversion et de limiter l'impact des mécanismes limitant, notamment 1) les pertes résistives (réduisant considérablement le facteur de forme) et 2) les rendements de fluorescence externe (limitant la tension de circuit-ouvert). La combinaison des deux approches peut constituer une solution appropriée permettant un fonctionnement efficace à des concentrations et des degrés de restriction angulaire relativement faibles.

Pour étudier les avantages de cette stratégie, on a évalué la variation du rendement de conversion photovoltaïque en fonction des propriétés angulaires des flux de photons absorbés et émis. À la lumière de ces résultats, on a essayé de mieux comprendre l'ampleur des effets négatifs des mécanismes limitant sur les performances des cellules soumises simultanément à la concentration et à la restriction angulaire.

Nous avons également essayé de déterminer la combinaison optimale des angles solides d'absorption et d'émission (compromis entre le facteur de concentration et le degré de restriction angulaire) maximisant les performances pour plusieurs valeurs de résistances série et de rendements de fluorescence externe.

b) Méthodologie

Un programme a été développé sous Matlab, similaire à l'algorithme décrit précédemment (avec quelques modifications). Ce code est également basé sur la résolution de l'équation de la caractéristique courant-tension pour une cellule idéale (eq. (D-2)), et pour des cellules « réelles » tenant compte des pertes résistives (eq. (D-1)) et des recombinaisons non-radiatives (eq. (D-3)) [2].

$$J = J_{ph} - J_0 \left(e^{\frac{qV}{nkT}} - 1 \right) \quad (\text{D-2})$$

$$J = J_{ph} - \frac{J_{0,rad}}{ERE} \left(e^{\frac{qV}{nkT}} - 1 \right) \quad (\text{D-3})$$

Dans les premiers calculs, l'ERE est supposé fixe et varie entre 1% (valeur typique des cellules solaires efficaces de nos jours [10]) et 100% (cellules solaires idéales).

Afin de tenir compte de l'effet combiné des pertes résistives et des recombinaisons non-radiatives, l'équation devient :

$$J = J_{ph} - \frac{J_{0_rad}}{ERE} \left(e^{\frac{q(V+JR_s)}{nkT}} - 1 \right) \quad (\text{D-4})$$

La restriction angulaire permet d'accroître la tension de circuit-ouvert grâce à la diminution du courant de saturation, comme décrit par les équations (D-5) et (D-6) :

$$s = \frac{1}{(\sin(\theta_{em}))^2} \quad (\text{D-5})$$

$$J_{0_s} = \frac{J_0}{s} \quad (\text{D-6})$$

Les paramètres électriques des cellules solaires sont étudiés pour une large gamme d'angles d'absorption et d'émission. Les courbes iso-rendements, représentant l'efficacité avec laquelle l'énergie solaire est convertie en fonction des angles solides d'absorption et d'émission, sont ensuite générées pour des cellules idéales et pour différents cas de cellules réelles. Ils permettent de déterminer la combinaison angulaire optimale basée sur l'efficacité maximale tout en prenant en compte les principaux mécanismes limitants. Pour toutes les courbes iso-rendement, la région située en dessous de la ligne $x=y$ (zone colorée en noir) représente une région angulaire interdite, car les angles d'absorption doivent nécessairement être égaux ou inférieurs aux angles d'émission, pour ne pas enfreindre la seconde loi de la thermodynamique.

5. Résultats

a) Cellules Solaires Idéales

Idéalement, à la limite radiative, les meilleures performances des cellules sont obtenues à chaque fois que les angles solides d'absorption et d'émission sont égaux, indépendamment de leur valeur, conduisant à la suppression des pertes de *Boltzmann*.

Les résultats de la simulation montrent que pour tous les angles égaux d'absorption et d'émission, les performances sont maximales avec des valeurs de 42%, un V_{oc} de 1.4 V et un FF de 0.918.

b) Effet des résistances série

Les résistances série sont des mécanismes affectant négativement les cellules solaires, particulièrement sous très fortes concentrations solaires, ou pour des valeurs de résistances série élevées. En revanche, on s'attend à ce que la combinaison de la concentration et de la restriction angulaire aboutisse à une combinaison optimale à chaque fois que les angles solides d'absorption et d'émission sont égaux et faibles.

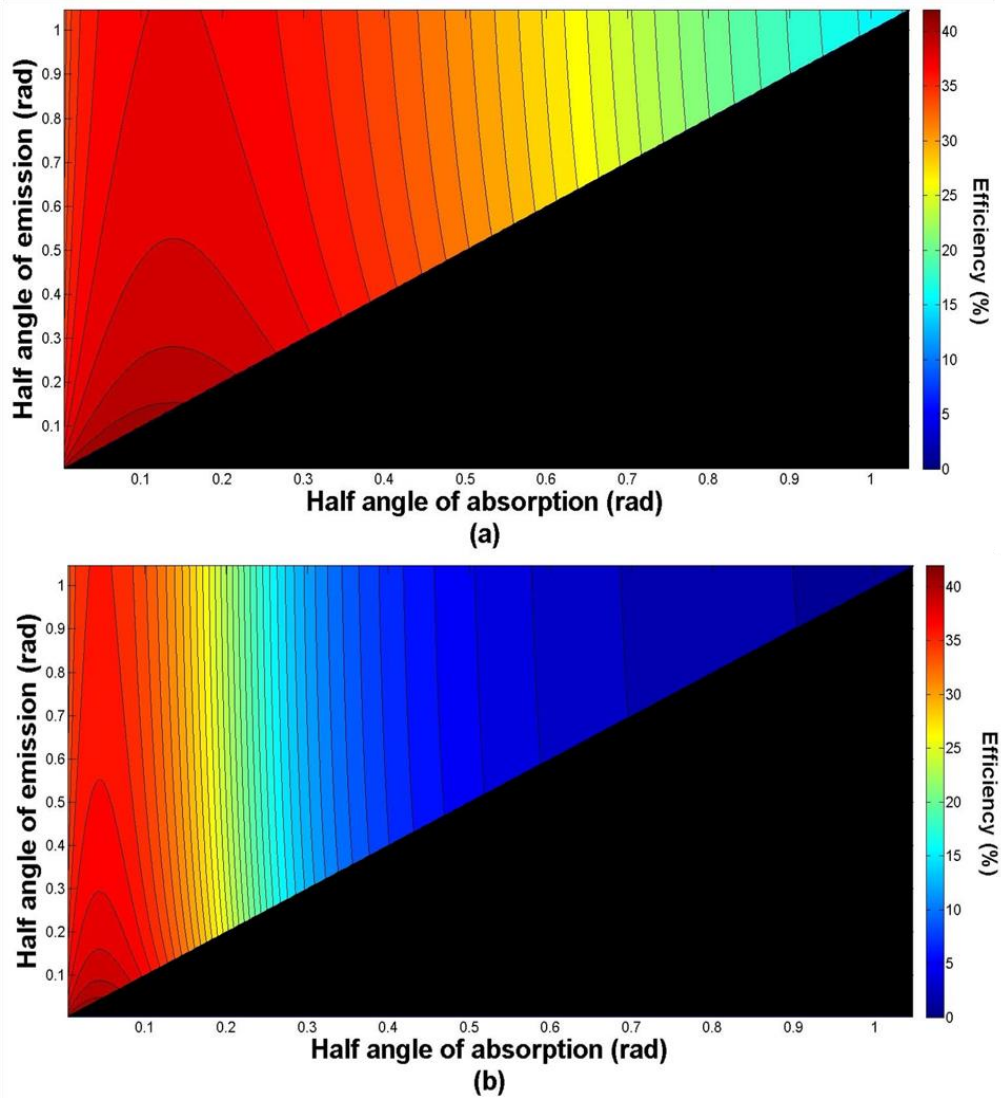


FIGURE D-4 Courbes iso-rendement pour une cellule solaire simple-jonction ayant un gap électronique de 1.4 eV en fonction des angles solides d'absorption et d'émission, en supposant des recombinaisons 100% radiatives et des résistances série $0.001 \Omega \text{ cm}^2$ (a) et $0.01 \Omega \text{ cm}^2$ (b).

La Figure D-4 représente des courbes I-V pour une cellule simple jonction ayant un gap électronique de 1.4 eV, des recombinaisons 100% radiatives, et des résistances série de $0.001 \Omega \text{ cm}^2$ (a) et $0.01 \Omega \text{ cm}^2$ (b) en fonction des angles solides d'absorption et d'émission. En comparant les deux graphes on peut clairement voir l'amélioration des performances de la cellule lorsque la concentration augmente, jusqu'à une valeur seuil de concentration au-dessus de laquelle les pertes résistives deviennent importantes, entraînant ainsi une diminution du rendement de conversion. Les pertes résistives deviennent de plus en plus notables pour des résistances série croissantes, ce qui se traduit par une dégradation prononcée des performances (perceptible en comparant les graphes des Fig.D-4 (a) et D-4 (b)). En revanche, l'efficacité maximale atteinte reste identique ($\sim 40\%$) et correspond à des angles solides d'absorption et d'émission comparables, et faibles (une région pour laquelle les pertes résistives restent négligeables). La zone angulaire pour laquelle les performances sont optimales se contracte (sans affecter la valeur d'efficacité maximale) avec l'accroissement des valeurs de résistance série.

c) **Effet des recombinaisons non-radiatives**

En tenant compte des recombinaisons non-radiatives, qui augmentent le courant de saturation et diminuent par conséquent la tension de circuit-ouvert, on prévoit théoriquement des performances idéales pour des combinaisons d'angles égaux et élevés, puisque l'effet des recombinaisons non-radiatives est, à priori, davantage accentué pour de forts degrés de restriction angulaire.

La Figure D-5 représente les courbes iso-rendements pour une cellule solaire simple jonction en fonction des angles solides d'absorption et d'émission, pour un gap de 1.4 eV, des pertes résistives nulles et des rendements de fluorescence externe de 1% (a) et 30% (b). Les résultats démontrent que la diminution du ERE dégrade les performances. La cellule solaire caractérisée par un ERE de 1% (Fig.D-5(a)) présente un V_{oc} maximal de 1.29 V et un rendement optimal d'environ 38% alors qu'une cellule ayant un ERE de 30% (Fig.D-5(b)) présente un V_{oc} de 1.38 V et une efficacité maximale de ~ 41%. Contrairement à nos attentes, les performances optimales sont observées pour des angles égaux, quelle que soit leur valeur.

Il est également important de souligner l'effet de la concentration sur les performances des cellules soumises à la restriction angulaire, ce qui démontre que la combinaison des deux approches atténue les effets néfastes des recombinaisons non-radiative. Par exemple, en supposant une cellule ayant un ERE de 1%, une illumination d'1 soleil ($\theta_{abs} = 4.65$ mrad) et un angle d'émission de $\pi/5$ (ou 36°), le V_{oc} est d'environ 1.05 V et le rendement atteint ~ 30%. La même cellule soumise cette fois à une concentration d'environ 16000 soleils (correspondant à un angle d'absorption égal à l'angle d'émission de $\pi/5$ rad) révèle un V_{oc} de 1.3 V et un rendement d'environ 38%.

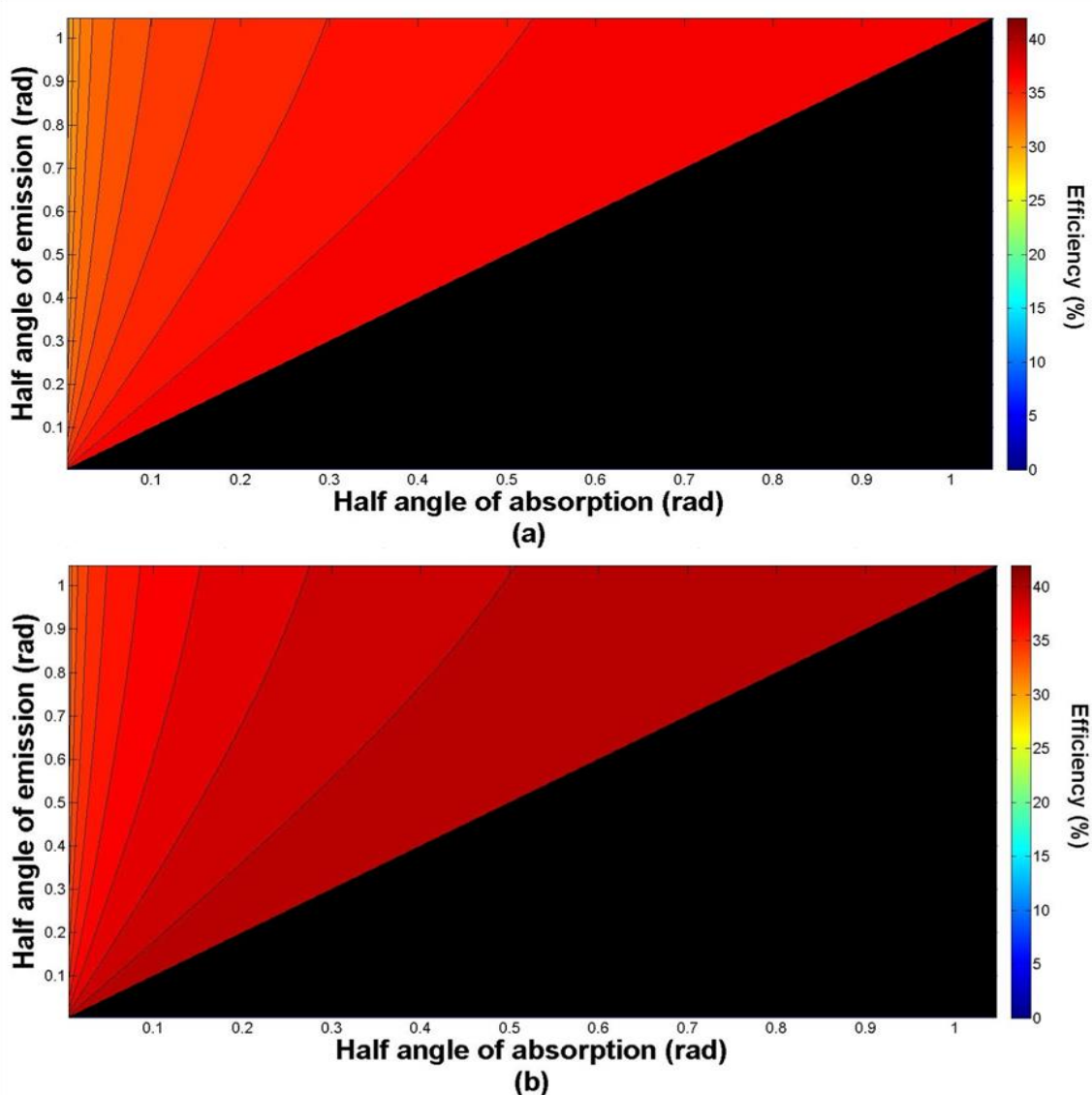


FIGURE D-5 Courbes iso-rendement pour une cellule solaire simple jonction ayant un gap électronique de 1.4 eV en fonction des angles solides d'absorption et d'émission, en supposant des résistances série nulles et des recombinaisons radiatives de 1% (a) et 30% (b).

d) Effet des pertes résistives et des recombinaisons non-radiatives

En considérant simultanément les pertes résistives et les recombinaisons non-radiatives, on peut s'attendre à ce que l'effet de chacun des mécanismes limitant soit visible sur les courbes iso-rendement, et donc à ce que la combinaison optimale des angles solides d'absorption et d'émission soit atteinte pour les angles égaux mais de valeurs moyennes, pour limiter les pertes associées aux deux stratégies.

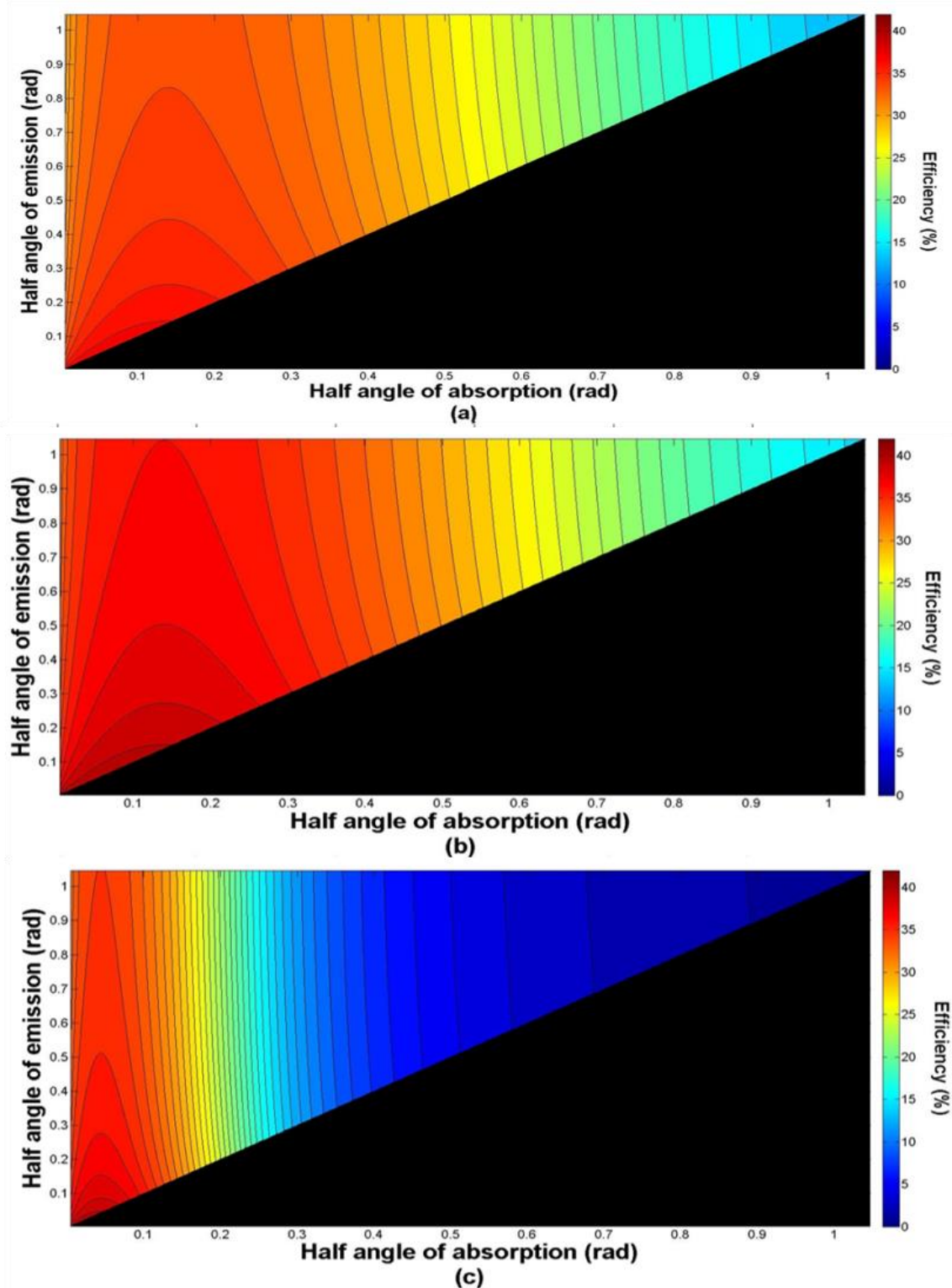


FIGURE D-6 Courbes iso-rendement pour une cellule solaire simple jonction ayant un gap électronique de 1.4 eV en fonction des angles solides d'absorption et d'émission, en supposant un ERE de 1% et $R_s 0.001 \Omega \text{ cm}^2$ (a) ERE de 30% et R_s de $0.001\Omega \text{ cm}^2$ (b) et un ERE de 30% et R_s de $0.01\Omega \text{ cm}^2$ (c).

La Figure D-6 représente les courbes iso-rendement pour une cellule solaire simple jonction ayant un gap de 1.4 eV, en fonction des angles solides d'absorption et d'émission, et pour différentes combinaisons de résistances série et d'ERE : un ERE de 1% et R_s de 0.001Ω

cm^2 (a), un *ERE* de 30% et R_s de $0.001\Omega \text{ cm}^2$ (b) et un *ERE* de 30% et R_s de $0.01\Omega \text{ cm}^2$ (c). Ces graphes résument ce qui a déjà été souligné :

- 1- Des valeurs plus élevées de ERE améliorent les performances des cellules.
- 2- Des valeurs élevées des résistances série entraînent une dégradation des performances des cellules.

D'après ces graphes, et contrairement à nos attentes, la combinaison optimale correspond à des angles d'absorption et d'émission égaux et faibles, ce qui est comparable au cas tenant compte des pertes résistives uniquement.

L'effet des pertes résistives semble donc être le principal mécanisme limitant affectant la combinaison de la restriction angulaire avec la concentration, provoquant des pertes plus importantes que les faibles valeurs du ERE.

En fait, les pertes résistives sont fonction de la valeur de la résistance série mais aussi du courant photo-généré qui augmente linéairement avec la concentration. Les pertes résistives sont donc modifiées à chaque fois que l'angle d'absorption varie, ce qui explique pourquoi elles constituent le mécanisme limitant dominant. Inversement, les pertes associées aux recombinaisons non-radiatives dépendent uniquement du ERE, qui est considéré constant tout au long de la simulation. Cette hypothèse peut être incorrecte puisqu'on s'attend à ce que le confinement angulaire modifie la fraction de recombinaison non-radiative. Il est donc important de trouver un modèle capable de considérer l'effet de la restriction angulaire sur le rendement de fluorescence externe.

D. Systèmes hybrides PV/CSP

Une troisième stratégie envisagée afin de réduire les pertes spectrales et de *Boltzmann* (si les systèmes CPV sont considérés), est l'utilisation de systèmes hybrides PV/CSP, qui permettent de mieux exploiter le spectre solaire et de stocker l'excès d'énergie sous forme de chaleur, facilitant la production d'électricité à bas coût toute la journée. Ces systèmes reposent sur l'utilisation de deux sous-systèmes : le PV et le CSP, séparés ou connectés. Une partie des photons incidents est absorbée par le système PV (ou CPV), le reste étant utilisé par le système thermique CSP qui les convertit directement, ou stocke leur énergie sous forme de chaleur, selon le besoin. Différentes approches existent pour construire de tels systèmes, et sont classées en trois groupes: l'approche « PV 1 soleil », l'approche de « division spectrale » et l'approche « PV haute température ».

Cette partie aborde deux volets importants pour aboutir à des systèmes hybrides très performants : 1) une comparaison est nécessaire entre les différentes stratégies de systèmes hybrides basée sur deux critères : a) les rendements de conversion solaire et b) l'équilibre entre les fractions d'électricité produites par le PV et par le CSP. 2) L'approche haute température implique l'utilisation de cellules photovoltaïques capable de fonctionner efficacement dans des conditions extrêmes de température et de concentration. L'architecture des cellules doit donc être optimisée pour plusieurs valeurs de température et de concentration, et la variation des différents paramètres électriques doit également être étudiée en fonction de la température.

1. Comparaison des performances des différentes approches

a) Objectifs et méthodologie

i. Objectifs

Un système hybride performant doit simultanément satisfaire deux critères importants : 1) avoir un rendement de conversion de l'énergie solaire élevé et 2) présenter un équilibre satisfaisant entre les fractions d'électricité produites par le PV et par le CSP, afin de garantir une production continue d'électricité à faibles coûts. Ces deux critères sont évalués en fonction de la largeur de bande interdite pour des cellules idéales, puis pour des cellules « réelles » en prenant en compte les pertes résistives et les recombinaisons non-radiatives [11,12]. L'étude est ensuite élargie pour évaluer l'intérêt d'utiliser des dispositifs de division spectrale ayant 2 énergies de coupure.

ii. Méthodologie

La comparaison des différents systèmes hybrides est réalisée à l'aide de Matlab. Le programme résout l'équation de la caractéristique $I-V$ pour des cellules solaires idéales simple jonction (eq. D-2) et en tenant compte des résistances série (eq. (1)) et des recombinaisons non-radiatives (eq. D-3) pour différentes valeurs de température et de concentration. Les pertes radiatives et convectives sont calculées d'après les équations (D-7) et (D-8) :

$$P_{\text{rad}} = \varepsilon\sigma \times (T^4 - T_a^4) \quad (\text{D-7})$$

$$P_{\text{conv}} = h \times (T - T_a) \quad (\text{D-8})$$

La puissance générée par la turbine est calculé par :

$$P_{\text{turbine}} = (P_{in} - P_{PV} - P_{rad} - P_{conv}) \frac{2}{3} \times (1 - \frac{T_a}{T}) \quad (\text{D-9})$$

Et finalement la puissance globale est la somme des puissances générées par le PV et par le CSP (puissance générée en sortie de la turbine).

$$\eta_{\text{turbine}} = \frac{P_{PV} + P_{CSP}}{P_{in}} \quad (\text{D-10})$$

iii. Hypothèses

L'approche « PV 1 soleil » repose sur l'utilisation de cellules solaires qui recouvrent la surface d'un concentrateur optique et qui fonctionnent à température ambiante et sous une illumination d'1 soleil. Ces cellules peuvent convertir le rayonnement direct et diffus puisqu'elles ne sont pas soumises au flux concentré. Cette stratégie implique une division spectrale des photons incidents: une fraction du spectre est transmise vers le PV et le reste réfléchi vers le CSP, selon l'énergie des photons incidents [13-15].

L'approche de « division spectrale » consiste à utiliser un dispositif de division spectrale, ayant 1 ou 2 énergies de coupure, pour rediriger les photons du flux solaire concentré vers le PV ou le CSP, selon leur énergie. Les deux sous-systèmes étant physiquement séparés, ils peuvent fonctionner à des températures et des concentrations différentes [12,16-19].

L'approche « PV haute température » repose sur l'utilisation d'un récepteur intégré, le CPV étant connecté thermiquement à un récepteur thermique capable d'absorber les photons

non absorbés ainsi que la chaleur résiduelle dégagée par le CPV. Les deux sous-systèmes doivent fonctionner obligatoirement aux mêmes conditions extrêmes de température et de concentration, ce qui nécessite un système CPV fonctionnant efficacement à très haute température. Contrairement aux deux autres approches, cette stratégie ne requiert aucun dispositif de division spectrale [11,12,16,20].

Pour les trois approches considérées, on suppose que le système thermique fonctionne à 2/3 de la limite de Carnot (une valeur communément observée sur une large gamme de systèmes CSP). Des températures de fonctionnement de 666 et 823K, et des concentrations de 25, 50, 1000 et 2000 soleils sont évaluées.

b) Résultats

Les graphes de la figure D-7 représentent les rendements de conversion hybrides globaux (gauche) et la fraction d'électricité générée par le PV (droite) pour les différentes approches de systèmes hybrides, et pour un récepteur thermique opérant à 666K et 1000 soleils. Les croix indiquent la fraction PV correspondant au point de rendement maximal, tandis que les parties colorées représentent les fractions inférieures ou égales à 0.5.

Dans le cas d'une cellule idéale (Fig.D-7(a)), les différentes stratégies considérées montrent des tendances similaires en ce qui concerne la variation du rendement en fonction des gaps électroniques, les rendements maximaux se situant entre 1,1 et 1,5 eV. Les approches «PV hautes températures» et «PV 1 soleil» démontrent les performances les plus élevées, avec une efficacité maximale de 42%, contre 39% pour l'approche basée sur la division spectrale. Des différences peuvent être observées dans la contribution de chaque sous-système: pour les stratégies «PV 1 soleil» et «division spectrale», la fraction PV diminue à mesure que la bande interdite augmente, avec des systèmes à dominance photovoltaïque au point de rendement maximal. Pour l'approche « PV hautes températures », les fractions sont beaucoup plus équilibrées, surtout au voisinage du point de rendement optimal.

La prise en compte des facteurs limitant, telles que les résistances série (Fig.D-7(b)) et les recombinaisons non-radiatives (Fig.D-7(c)) altère ces observations. Les rendements maximaux restent les plus élevés pour l'approche « PV 1 soleil », tandis que la stratégie «PV haute température» continue de présenter le meilleur équilibre entre les fractions de PV et de CSP.

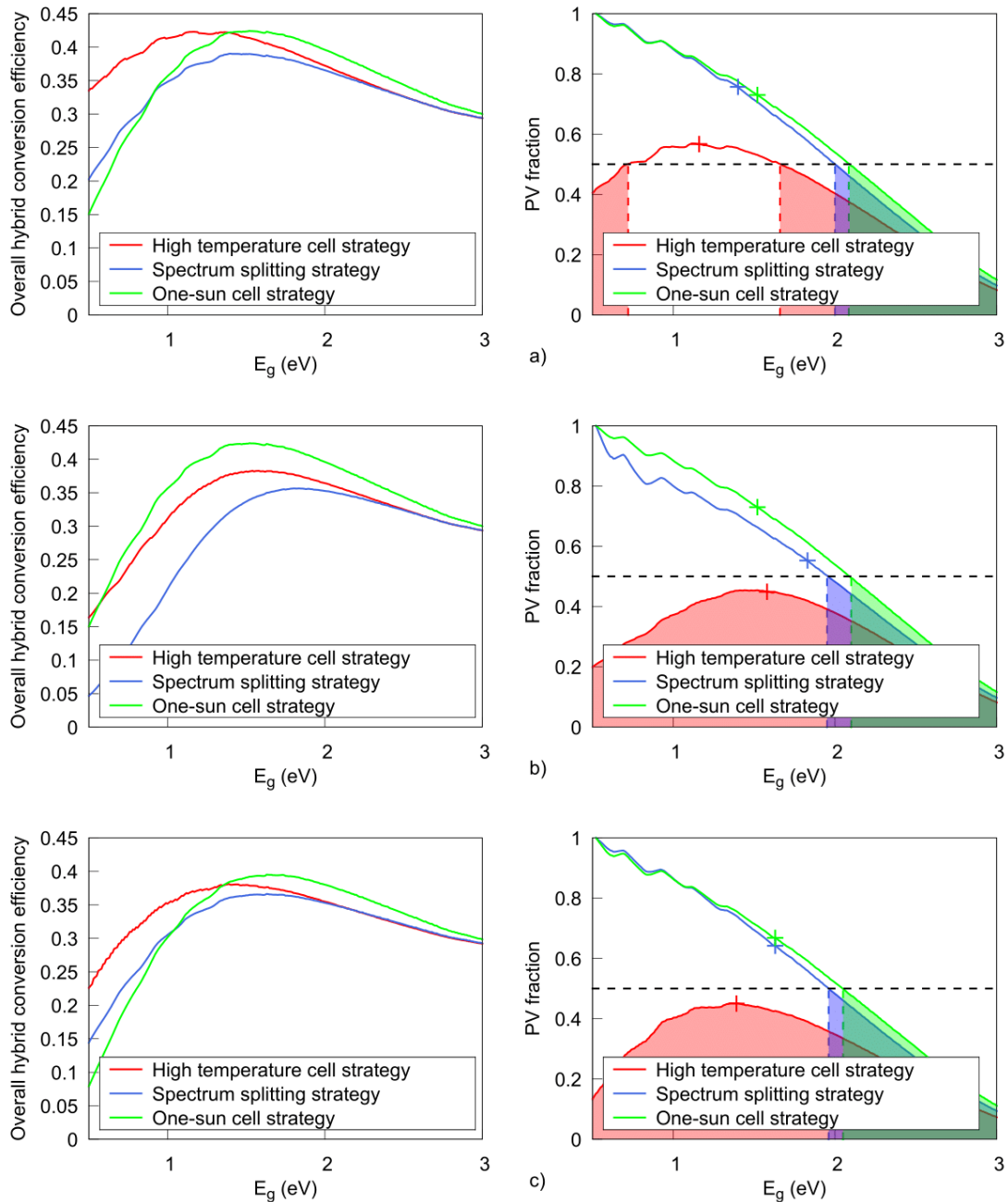


FIGURE D-7 Rendement de conversion hybride global (gauche) et contribution du PV à la production de l'électricité totale générée (droite) en fonction du gap électronique pour les trois approches étudiées. Les graphes supposent une concentration de 1000 soleils, et sont tracés pour des cellules solaires idéales (a) des cellules ayant des pertes résistives de 0.01 Ohm cm^2 (b) et un ERE de 1% (c).

L'ajout d'une 2^{nde} énergie de coupure (dans le cas des approches « division spectrale » et « PV 1 soleil ») améliore les performances et l'équilibre entre chacun des sous-systèmes, mais uniquement pour les faibles gaps, ce qui ne conduit pas à une amélioration des performances optimales du système.

En conclusion, l'approche « PV haute température» présente des rendements de conversion comparables à l'approche 1 soleil, mais se caractérise également par un meilleur

équilibre entre les fractions d'électricité produites par le PV et le CSP, ce qui nous a poussé à l'étudier plus en détail.

2. Approche PV haute température

a) Objectifs et Méthodologie

i. Objectifs

L'approche « PV haute température » implique le fonctionnement de cellules solaires à des niveaux de températures très élevées, ce qui soulève deux questions fondamentales: 1) dans quelle mesure des cellules photovoltaïques fonctionnant à des températures de plusieurs centaines de degrés Celsius sont-elles susceptibles de convertir efficacement la lumière du soleil en électricité ? 2) Comment adapter l'architecture des cellules « haute température » afin de garantir des performances maximales ?

L'objectif principal est donc d'évaluer la capacité des cellules photovoltaïques à fonctionner à des températures élevées, dans le but d'atteindre des rendements hybrides globaux élevés, tout en assurant une répartition équilibrée entre les énergies produites par le PV et par le CSP. Pour répondre à ces questions, les gaps électroniques de cellules simples et multi-jonctions sont optimisées afin de maximiser l'efficacité de conversion photovoltaïque. Les principaux paramètres électriques, à savoir V_{oc} , J_{sc} , FF et η , sont ensuite évalués pour une large gamme de températures et de concentrations. Une fois les limites supérieures des performances photovoltaïques établies, nous avons analysé les rendements hybrides globaux en fonction de la température pour différents facteurs de concentration et d'idéalité de la cellule.

ii. Méthodologie

Le programme utilisé pour étudier les effets de la température sur les principaux paramètres électriques (V_{oc} , J_{sc} , FF et η) est similaire à celui décrit dans la section CPV basé sur la résolution de l'équation de la caractéristique $I-V$ à la limite radiative. Les gaps électroniques sont optimisés en utilisant l'algorithme génétique et les cellules simples et multi-jonctions sont étudiées à la limite radiative, en supposant des gaps électroniques ayant des coefficients de température de -0.5 meV/K.

Les rendements hybrides sont calculés en utilisant les équations (D-7) à (D-10) pour plusieurs valeurs de températures et de concentrations, et pour des systèmes hybrides basés sur des cellules tandem dont le gap électronique a été optimisé à chaque température, de manière à maximiser le rendement photovoltaïque. Les récepteurs thermiques sont supposés fonctionner à 2/3 de la limite de Carnot.

b) Résultats

i. Cellules solaires simple-jonction

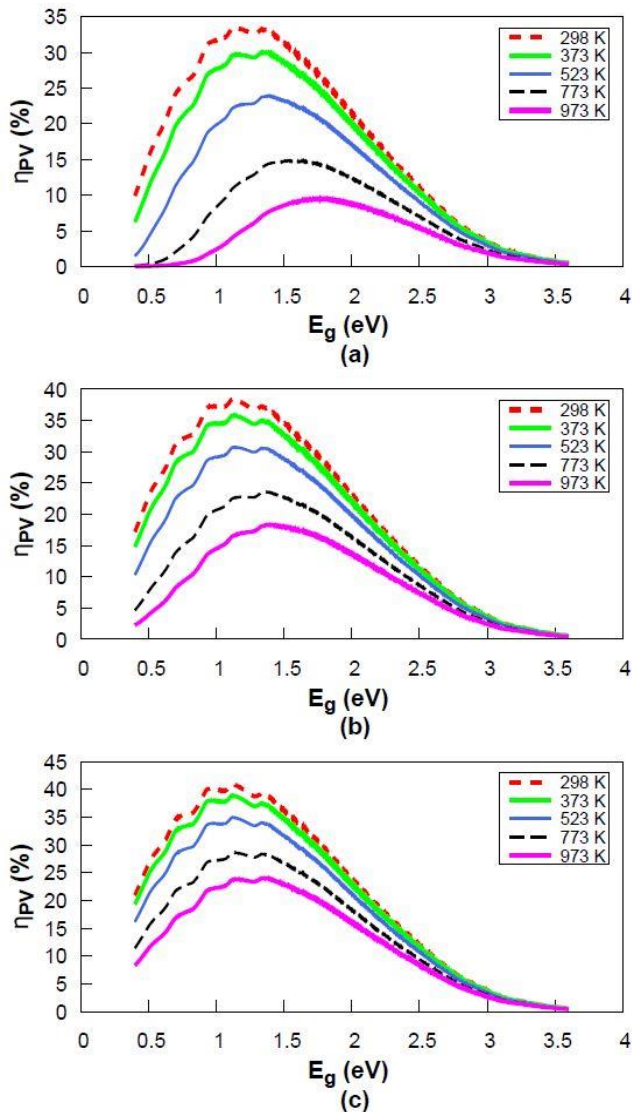


FIGURE D-8 Rendement théorique maximal pour une cellule solaire simple-jonction en fonction du gap électronique, pour des températures comprises entre 298 et 973K et pour des concentrations de (a) 1 soleil, (b) 100 soleils (c) 1000 soleils.

La figure D-8 représente les performances des cellules solaires simple-jonction à la limite radiative en fonction des gaps électroniques, pour des températures comprises entre 298 et 973K et des facteurs de concentration de (a) 1 soleil, (b) 100 soleils et (c) 1000 soleils. On remarque que les rendements diminuent avec l'augmentation de température. Pour les faibles concentrations, les gaps électroniques optimaux tendent à se décaler vers des valeurs plus élevées avec l'augmentation de la température. Augmenter la concentration du flux solaire diminue les effets de la température : la différence entre les courbes correspondant à différentes températures devient plus petite, et le décalage vers des largeurs de bandes interdites plus élevées est moins prononcé. La concentration aide donc à contrebalancer l'effet négatif de la température.

La Figure D-9 représente la variation des paramètres électriques principaux, η (a), V_{oc} (b), la variation de J_{sc} (c) et FF (d), en fonction de la température pour des cellules simples jonctions optimisées pour une température de 773 K, et pour des facteurs de concentration de 1, 100 et 1000 soleils. La densité de courant de court-circuit augmente avec l'augmentation de température. Ceci découle de la diminution du gap électronique avec la température, qui conduit à l'absorption d'un nombre plus élevé de photons. Le degré de variation de J_{sc} n'est pas constant à cause de la nature discontinue du spectre solaire AM1.5D, et ces variations dépendent fortement de la valeur du gap électronique à la température considérée.

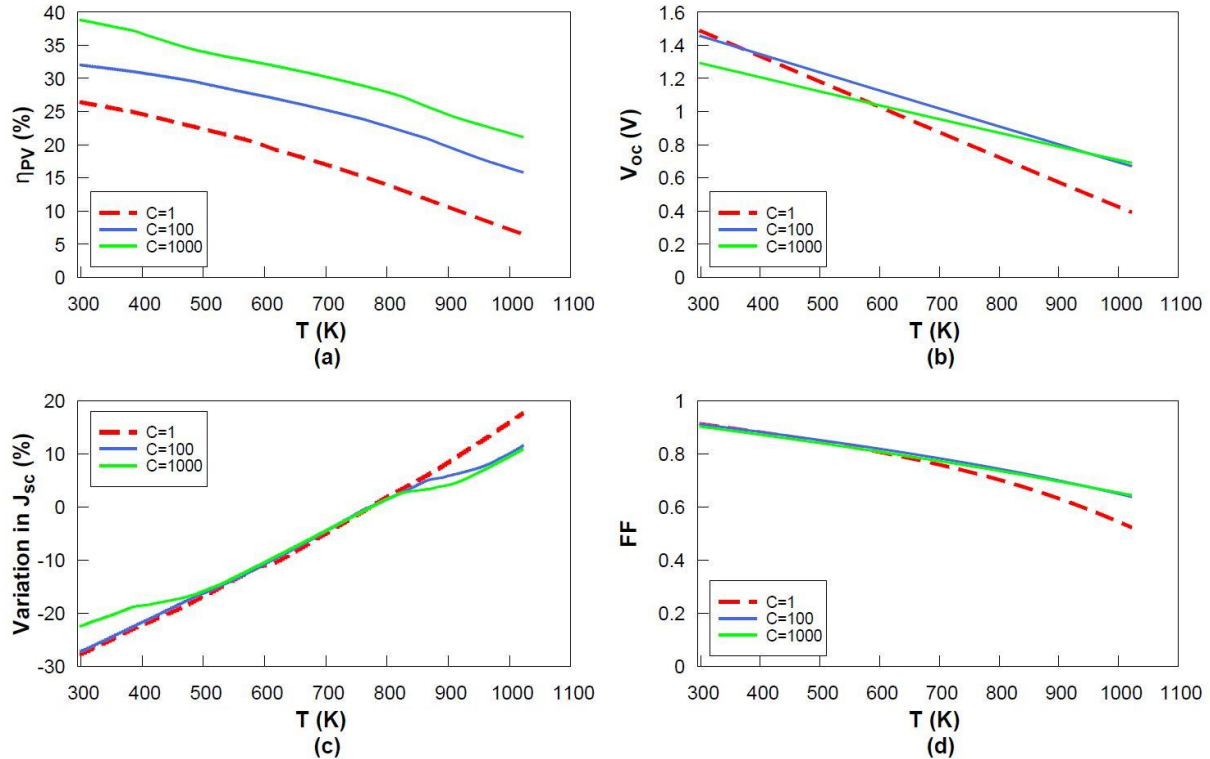


FIGURE D-9 (a) η_{PV} , (b) V_{oc} , (c) variation du J_{sc} et (d) FF , en fonction de la température pour une cellule simple-jonction optimisée pour $T=773K$, et pour des concentrations de 1, 100 et 1000 soleils.

Contrairement à J_{sc} , V_{oc} est une fonction décroissante de la température. Le comportement de V_{oc} découle de deux facteurs concurrents: la dépendance de J_0 à E_g et à la température (proportionnellement au cube de la température), et la dépendance de J_{ph} à E_g et à la concentration solaire. En conséquence, et pour une concentration donnée, V_{oc} décroît linéairement avec l'augmentation de la température. L'effet néfaste de la température sur ce paramètre est considérablement atténué par l'augmentation du facteur de concentration. Les mêmes tendances s'appliquent au facteur de forme et au rendement de conversion, la concentration réduisant l'effet négatif de la température sur ces paramètres.

ii. Cellules Multi-jonctions

L'optimisation du gap électronique pour les cellules double et triple jonctions aboutit aux mêmes conclusions: à mesure que la température augmente, l'efficacité diminue et la combinaison optimale de E_g se déplace vers des valeurs plus élevées. La concentration

permet d'améliorer l'efficacité et de réduire le décalage des largeurs de bandes interdites par rapport à la combinaison optimale à 298K.

A cause de la contrainte en courant imposée aux cellules multi-jonction, ces cellules sont plus sensibles que les cellules simple-jonction aux variations du spectre solaire, ce qui entraîne des différences notables au niveau de la variation des paramètres électriques en fonction de la température.

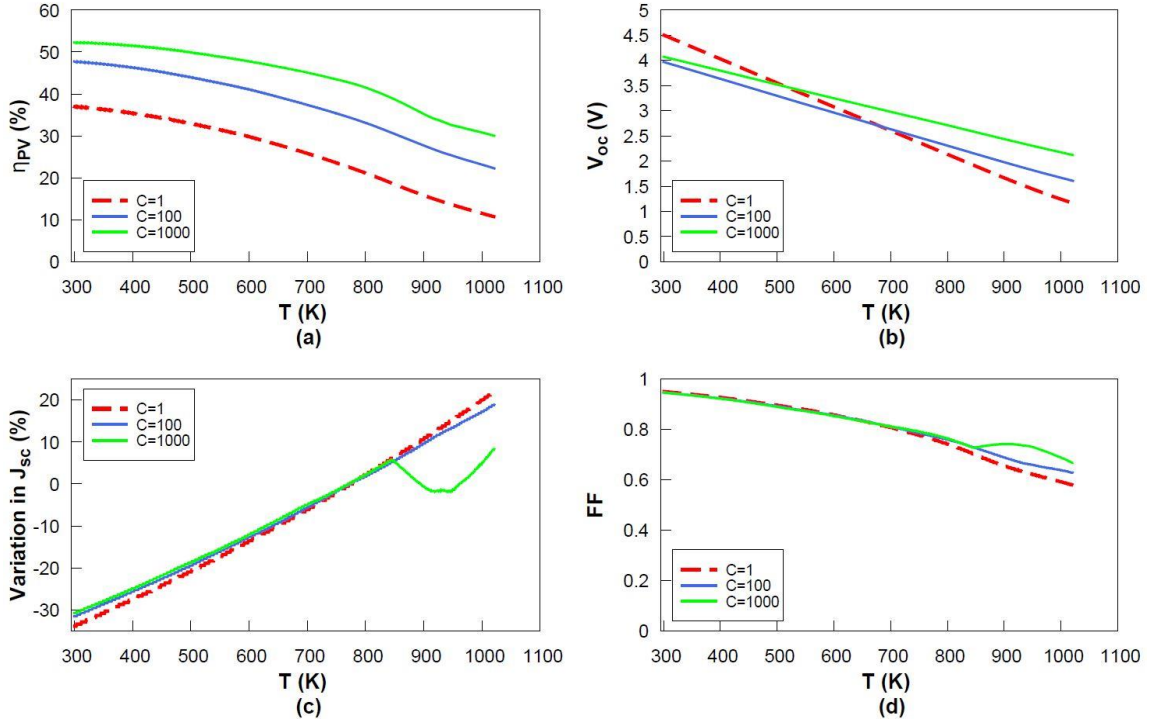


FIGURE D-10 (a) η_{PV} , (b) V_{oc} , (c) variation du J_{sc} et (d) FF, en fonction de la température pour une cellule triple-jonction optimisée pour $T=773K$, et pour des concentrations de 1, 100 et 1000 soleils.

La figure D-10 représente les principaux paramètres électriques η (a), V_{oc} (b), la variation de J_{sc} (c) et FF (d), en fonction de la température pour des cellules triple-jonction optimisées pour une température de 773 K et des facteurs de concentration de 1, 100 et 1000 soleils. À l'instar des cellules simple-jonction, la tension de circuit-ouvert, le facteur de forme et le rendement de conversion diminuent avec la température, et la concentration contrebalance l'effet de la température. En contrepartie, la densité de courant de court-circuit ne montre pas une augmentation monotone avec la température, elle diminue si E_g de l'une des jonctions de l'empilement coïncide avec une bande d'absorption du spectre solaire.

iii. Systèmes hybrides

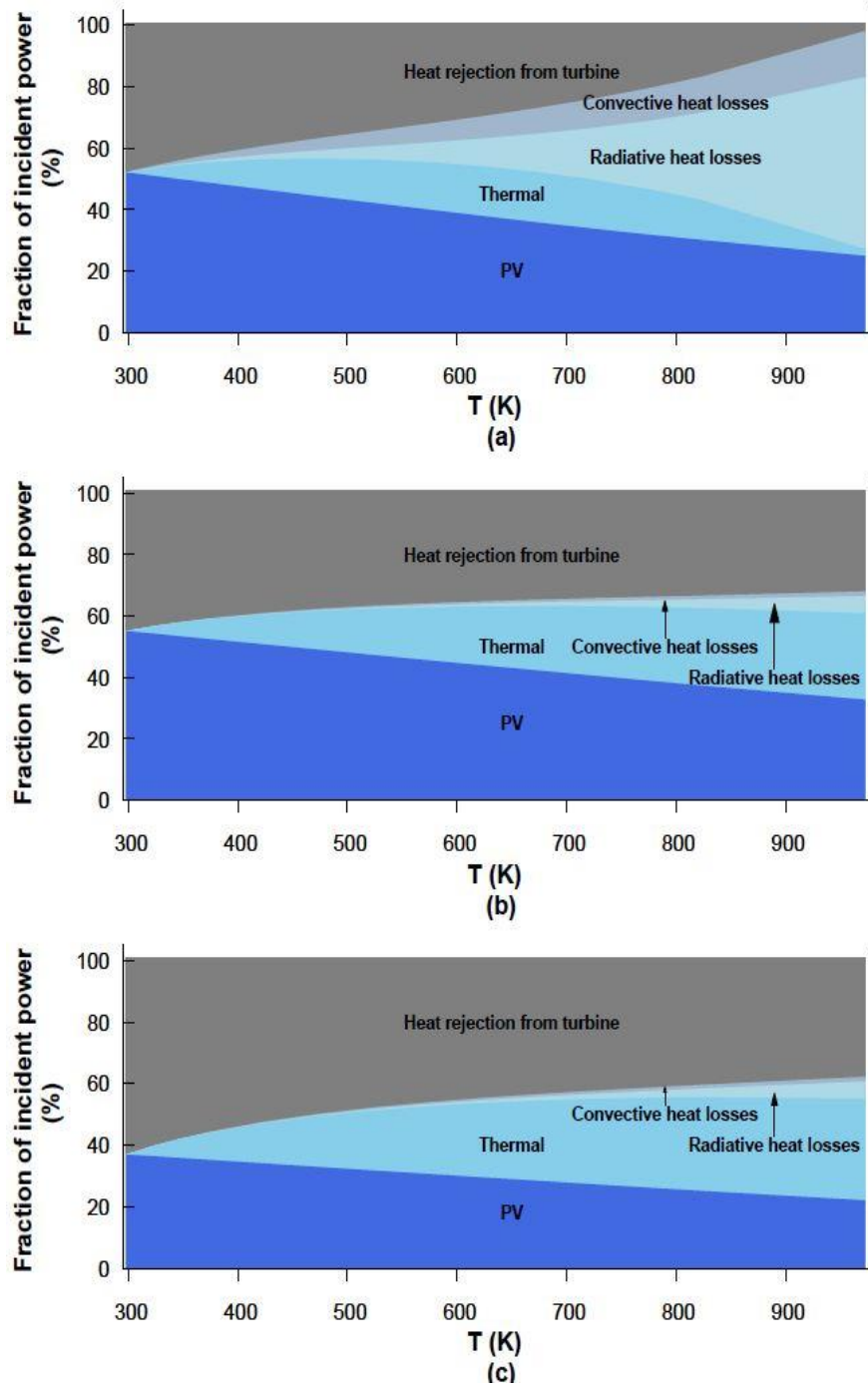


FIGURE D-11 Rendements de conversion PV, thermique et hybride en fonction de la température de fonctionnement ainsi que les pertes thermiques associées pour des cellules fonctionnant à la limite radiative sous une concentration de 100 soleils (a), à la limite radiative sous 1000 soleils (b) et pour des cellules solaires « réelles » sous 1000 soleils (c).

La figure D-11 illustre les rendements photovoltaïques et thermiques (le rendement global hybride étant la somme des rendements PV et CSP), pour des concentrations de 100 soleils (a) et 1000 soleils (b) et (c) et pour des températures de fonctionnement comprises entre 298 et 1023K. Les pertes radiatives et convectives associées sont également représentées ainsi que les pertes liées à la turbine. Les figures D-11 (a) et (b) supposent des

cellules solaires fonctionnant à la limite radiative alors que la figure D-11 (c) représente une cellule opérant à 2/3 de la limite radiative.

La variation du rendement en fonction de la température dépend fortement du facteur de concentration considéré. Même si l'efficacité du PV diminue avec la température, le rendement hybride continue à augmenter en raison de l'amélioration des performances du CSP à haute température.

Pour une concentration de 100 soleils, l'efficacité globale augmente jusqu'à environ 500 K. Au-delà de cette température, les pertes par rayonnement et par convection augmentent considérablement, ce qui entraîne une forte diminution du rendement. Sous une illumination de 1000 soleils, le poids relatif des pertes radiatives et convectives devient négligeable. L'efficacité hybride augmente avec la température, puis se stabilise sur une large gamme de températures (entre 523 et 823K). Les pertes thermiques restent négligeables même à une température proche de 1000K. Au-dessus de ~800K, le rendement commence à diminuer lentement. La concentration permet donc d'améliorer les performances des cellules photovoltaïques et du système hybride, de diminuer les pertes thermiques, ainsi que la sensibilité du système à la variation de température. Considérer des cellules solaires « réelles » (c'est-à-dire affectées par des mécanismes limitant et présentant des rendements de conversion inférieurs à ceux prédicts par le formalisme de Shockley-Queisser) conduit à des conclusions similaires, avec des rendements plus faibles et des températures optimales décalées vers des valeurs plus élevées. Dans les deux cas, même si le rendement se stabilise pour une large gamme de températures, la variation de la température permettra de modifier la contribution du PV et du CSP à l'énergie totale produite.

E. Conclusions

Trois différentes stratégies ont été étudiées pour améliorer les performances des systèmes photovoltaïques capables de convertir l'énergie solaire en électricité, et diminuer l'amplitude des principales sources de pertes. Ce projet a permis d'optimiser les différents systèmes en tenant compte de la nature « idéale » ou « réelle » des cellules, qui considèrent ou non les pertes résistives ou les recombinaisons non-radiatives. Les résultats montrent l'importance de l'optimisation du gap pour les fortes concentrations et résistances série, la nécessité d'adapter les propriétés angulaires d'absorption et d'émission de la cellule, et l'utilité d'utiliser la concentration pour contrebalancer l'effet négatif de la température sur les cellules solaires.

Les cellules multi-jonctions opérant à des concentrations élevées sont limitées par les fortes pertes résistives qui affectent les performances des cellules. L'effet de l'optimisation des gaps est important pour les concentrations supérieures à 1000 soleils et tend à décaler la combinaison de E_g vers des valeurs plus élevées, dans une zone où le courant généré est plus faible et le V_{oc} plus élevé (conduisant à une réduction notable des pertes résistives).

A cause de ces pertes, les systèmes CPV ne peuvent pas atteindre des concentrations très élevées. Une stratégie alternative est de restreindre l'angle d'émission des photons mais elle est limitée par l'inefficacité de la cellule à émettre de la lumière. Une solution originale est de combiner les deux approches afin que les cellules fonctionnent à des niveaux de

concentrations et de confinement angulaire acceptables. Pour cette stratégie, les effets des pertes résistives et des recombinaisons non-radiatives sur les performances des cellules ont été étudiés, ainsi que l'influence des propriétés angulaires des flux de photons absorbés et émis. Les pertes résistives représentent le facteur limitant dominant à cause de sa dépendance au carré du courant photo-généré, qui est proportionnel à la concentration. L'effet des recombinaisons non-radiatives reste minime. Les meilleurs rendements ont été observés pour des angles solides d'absorption et d'émission égaux.

Dans le cas des systèmes hybrides PV/CSP, il a été démontré que l'approche « PV haute température » présente des rendements de conversion comparables à l'approche « PV 1 soleil » tout en offrant un meilleur équilibre entre les contributions du PV et du CSP à l'énergie totale générée. En conséquence, on a étudié cette stratégie en détail et on s'est principalement focalisé sur l'effet de la température sur les différents paramètres électriques de la cellule, pour plusieurs facteurs de concentration, et pour des cellules simple et multi-jonction. L'augmentation de température modifie l'agencement optimal des gaps électroniques en les décalant vers des valeurs plus élevées.

Le gap électronique diminue avec la température, entraînant une augmentation du courant photo-généré, qui varie de manière non-monotone à cause de la nature discontinue du spectre solaire. V_{oc} , FF et η diminuent avec la température. Les mêmes conclusions sont observées dans le cas de cellules multi-jonctions, même si ces dernières présentent une sensibilité accrue au spectre solaire, dû à la contrainte en courant imposée aux différentes jonctions.

On a également souligné l'importance de la concentration solaire afin de garantir un fonctionnement optimal des systèmes hybrides, et de diminuer l'amplitude des pertes radiatives et convectives. La température de fonctionnement optimale ne doit pas être nécessairement très élevée, puisque le rendement hybride se stabilise sur une large gamme de températures. La température caractéristique du système peut en revanche servir de variable d'ajustement entre les fractions PV et CSP et contribuer à garantir un équilibre convenable entre les 2 sous-systèmes, en assurant la production continue d'électricité solaire à faible coût.

F. Références

- [1] W. Shockley and H. J. Queisser, Detailed balance limit of efficiency of pn junction solar cells, *J. Appl. Phys.*, 32 (1961) 510-519.
- [2] A. Vossier, F. Gualdi, A. Dollet, R. Ares, and V. Aimez, Approaching the Shockley-Queisser limit: General assessment of the main limiting mechanisms in photovoltaic cells, *J. Appl. Phys.*, 117 (2015) 015102.
- [3] L. C. Hirst and N. J. Ekins-Daukes, Fundamental losses in solar cells, *Prog. Photovolt: Res. Appl.*, 19 (2011) 286–293.
- [4] M. A. Green, Y. Hishikawa, E. D. Dunlop, D. H. Levi, J. Hohl-Ebinger and A. W.Y. Ho-Baillie, Solar cell efficiency tables (version 51), *Prog. Photovolt. Res. Appl.*, 26 (2018) 3-12.
- [5] S.P. Philips, A.W. Bett, K. Horowitz and S. Kurtz, Current status of concentrator photovoltaic (CPV) technology, Fraunhofer Institute for Solar Energy Systems ISE,

Freiburg, Germany and National Renewable Energy Lab. (NREL), Golden, Colorado, US, Tech. Rep. NREL/TP-5J00-65130), December 2015.

- [6] A. Vossier, E. Al Alam, A. Dollet, and M. Amara, Assessing the Efficiency of Advanced Multijunction Solar Cells in Real Working Conditions: A Theoretical Analysis. *IEEE J. Photovolt.*, 5 (2015) 1805-1812.
- [7] E.D. Kosten, J.H. Atwater, J. Parsons, A. Polman, and H.A. Atwater, Highly efficient GaAs solar cells by limiting light emission angle, *Light: Sci. App.*, 2 (2013) e45.
- [8] J.N. Munday, The effect of photonic bandgap materials on the Shockley-Queisser limit, *J. Appl. Phys.* 112 (2012) 064501.
- [9] M. Peters, J.C. Goldschmidt, and B. Bläsi, Angular confinement and concentration in photovoltaic converters, *Sol. Energ. Mater. Sol. Cell.*, 94 (2010) 1393-1398.
- [10] M.A. Green, Green, M. A. (2012). Radiative efficiency of state-of-the-art photovoltaic cells, *Prog. Photovolt. Res. Appl.*, 20 (2012) 472-476.
- [11] ARPA-E, Full-Spectrum Optimized Conversion and Utilization of Sunlight (FOCUS), FOCUS Program Overview, United States Department of Energy, Funding Opportunity Announcement, 2013.
- [12] X. Ju, C. Xu, Y. Hu, X. Han, G. Wei, and X. Du, A review on the development of photovoltaic/concentrated solar power (PVCSP) hybrid systems, *Sol. Energ. Mater. Sol. Cell.*, 161 (2017) 305-327.
- [13] T.P. Otanicar, S. Theisen, T. Norman, H. Tyagi, and R. A. Taylor, Envisioning advanced solar electricity generation: Parametric studies of CPV/T systems with spectral filtering and high temperature PV, *Appl. Energ.*, 140 (2015) 224-233.
- [14] Y.V. Vorobiev, J. Gonzalez-Hernandez, and A. Kribus, Analysis of potential conversion efficiency of a solar hybrid system with high-temperature stage, *J. Sol. Energ. Eng.*, 128 (2006) 258-260.
- [15] Y. Vorobiev, J. Gonzalez-Hernandez, P. Vorobiev, and L. Bulat, Thermal-photovoltaic solar hybrid system for efficient solar energy conversion, *Sol. Energ.*, 80 (2006) 170-176.
- [16] H.M. Branz, W. Regan, K.J. Gerst, J.B. Borak, and E.A. Santori, Hybrid solar converters for maximum exergy and inexpensive dispatchable electricity, *Energy Environ. Sci.*, 8 (2015) 3083-3091.
- [17] Y. Ji, A. Ollanik, N. Farrar-Foley, Q. Xu, L. Madrone, P. Lynn, V. Romanin, D. Codd, and M. Escarra, Transmissive Spectrum Splitting Multi-junction Solar Module for Hybrid CPV/CSP System, In Proc. of the 42nd IEEE Photovoltaic Specialist Conference (PVSC-42), (2015).
- [18] M. Orosz, N. Zweibaum, T. Lance, M. Ruiz, and R. Morad, Spectrum-splitting hybrid CSP-CPV solar energy system with standalone and parabolic trough plant retrofit applications, In AIP Conference Proceedings, 1734 (2016) 070023.
- [19] D.M. Bierman, A. Lenert, and E.N. Wang, Spectral splitting optimization for high-efficiency solar photovoltaic and thermal power generation, *Appl. Phys. Lett.*, 109 (2016) 243904.
- [20] E. E. Perl, J. Simon, J. F. Geisz, M. L. Lee, D. J. Friedman, and M. A. Steiner, Measurements and Modeling of III-V Solar Cells at High Temperatures up to 400 °C, *IEEE J. Photovolt.*, 6 (2016) 1345-1352.

Appendix E: List of publications and communications

A. Publications

Journal Papers

- 1- J. Zeitouny, A. Dollet and A. Vossier, “Angular confinement in PV cells: a critical review”, In preparation, to be submitted to Renewable and Sustainable Energy Reviews.
- 2- J. Zeitouny, A. Dollet and A. Vossier, “Effect of series resistance and non-radiative recombination on the combination of concentration and angular restriction”, In preparation, to be submitted to Journal of Applied Physics.
- 3- A. Vossier, J. Zeitouny, E. A. Katz, A. Dollet, G. Flamant and J. M. Gordon, “Performance bounds for hybrid solar photovoltaic/thermal electricity-generation strategies”, Sustainable Energy and Fuels, 2, 2018, pp. 2060-2067.
- 4- J. Zeitouny, N. Lalau, G. M. Gordon, E. A. Katz, G. Flamant, A. Dollet and A. Vossier, “Assessing high-temperature photovoltaic performance for solar hybrid power plants”, Solar Energy Materials and Solar Cells, 182, 2018, pp.61-67.
- 5- J. Zeitouny, E. A. Katz, A. Dollet and A. Vossier “Band gap engineering of multi-junction solar cells: effects of series resistances and solar concentration”, Scientific Reports, 7, 2017, 1766.

Conference Proceedings

- 1- J. Zeitouny, N. Lalau, E. A. Katz, A. Dollet and A. Vossier, “On the potential of solar cells to efficiently operate at high temperature”, In Proc. 13th International Conference on Concentrator Photovoltaic System (CPV13) – May 1-3, 2017, Ottawa – Canada.
- 2- J. Zeitouny, A. Dollet and A. Vossier, “Combining sunlight concentration and angular confinement: studying the effects of series resistance and external fluorescence efficiency”, In Proc. 12th International Conference on Concentrator Photovoltaic System (CPV12) – April 25-27, 2016, Freiburg – Germany.
- 3- J. Zeitouny, A. Dollet and A. Vossier, “Effects of non-ideal losses on the optimal bandgap arrangement of multi-junction solar cells comprising up to 5 sub-cells”, In Proc. 11th International Conference on Concentrator Photovoltaic System (CPV11) – April 13-15, 2015, Aix les Bains – France.

B. Conferences

- 1- J. Zeitouny, A. Vossier, E. A. Katz, A. Dollet, G. Flamant and J. M. Gordon, “On the efficiency of hybrid PV/CSP systems”, Poster Presentation in the 14th International Conference on Concentrator Photovoltaic System (CPV14) – April 16-18, 2018, Puertollano – Spain.
- 2- J. Zeitouny, E. A. Katz, J. M. Gordon, G. Flamant, A. Dollet and A. Vossier, “Sur l’efficacité des systèmes hybrides PV/CSP”, Oral Presentation in Journée Nationale du Photovoltaïque (JNPV 2017) – December 5-8, 2017, Dourdan – France.
- 3- J. Zeitouny, E. A. Katz, G. Flamant, A. Dollet and A. Vossier, “On the potential of combining PV and CSP”, Oral Presentation in the 13th SOLLAB Doctoral Colloquium – May 15-17, 2017, Berlin – Germany.

- 4- J. Zeitouny, N. Lalau, E. A. Katz, A. Dollet and A. Vossier, “On the potential of solar cells to efficiently operate at high temperature”, Oral Presentation in the 13th International Conference on Concentrator Photovoltaic System (CPV13) – May 1-3, 2017, Ottawa – Canada.
- 5- J. Zeitouny, E.A. Katz, A.Dollet and A. Vossier, “Le photovoltaïque peut-il fonctionner efficacement à hautes températures ? ”, Oral Presentation in Journée Nationale du Photovoltaïque (JNPV 2016) – November 29-December 2, 2016, Dourdan – France.
- 6- J. Zeitouny, E. A. Katz, A. Dollet and A. Vossier, “Nouvelles architectures de cellules solaires : influence de la température et des pertes résistives ”, Oral Presentation in Congrès des Doctorants de l’UPVD – November 18-19, 2016, Perpignan – France.
- 7- J.Zeitouny, A.Dollet, A. Vossier, “Combining sunlight concentration and angular confinement: studying the effects of series resistance and external fluorescence efficiency”, Poster Presentation in the 12th International Conference on Concentrator Photovoltaic System (CPV12) – April 25-27, 2016, Freiburg – Germany.
- 8- J. Zeitouny, A. Dollet and A. Vossier, “Nouvelles architectures de cellules multi-jonction: influence des pertes résistives et du contenu spectral de la lumière”, Invited Oral Presentation in Journée Nationale du Photovoltaïque (JNPV 2015) – December 1-4, 2015, Dourdan – France.

Abstract

The maximum efficiency limit attainable with a single-junction PV cell is $\sim 33\%$ according to the detailed balance formalism (also known as Shockley-Queisser model), which remains far from the Carnot limit, predicting a solar to electricity efficiency upper value of 93%. The large gap between both limits is due to intrinsic loss mechanisms, including the inefficient conversion of the solar spectrum and the large discrepancy between the solid angles of absorption and emission. To overcome these losses and get closer to the Carnot limit, three different strategies are considered in this thesis: concentrated multi-junction solar cells, the combination of solar concentration and angular confinement, and hybrid PV/CSP systems. Each strategy is inherently limited by several loss mechanisms that degrade their performances. The objective of this thesis is, hence, to better understand the extent to which these strategies are likely to be penalized by these losses, and to tailor the cell properties toward maximizing their efficiencies. To address these questions, a detailed-balance model of PV cell accounting for the main loss mechanisms was developed. A genetic-algorithm optimization tool was also implemented, aiming at exploring the parameter space and identifying the optimal operation conditions. We demonstrate the uttermost importance of tailoring the electronic properties of the materials used with both multi-junction solar cells undergoing significant series resistance losses, and PV cells operating at temperature levels exceeding ambient temperature. We also investigate the extent to which series resistances losses and non-radiative recombination are likely to affect the ability of PV cells simultaneously submitted to concentrated sunlight and angular restriction of the light emitted by band-to-band recombination.

Keywords: Concentrated photovoltaic (CPV), solar concentration, multi-junction solar cells, angular confinement, radiative limit, hybrid PV/CSP systems, resistive losses, external radiative efficiency (ERE), high temperature.

Résumé

La limite théorique de rendement des cellules photovoltaïques simple-jonction est de l'ordre de 33% d'après le modèle de Shockley-Queisser, ce qui reste éloigné de la limite de Carnot, prédisant une limite maximale de conversion énergie solaire \rightarrow électricité de 93%. L'écart important entre ces deux limites découle des pertes intrinsèques, essentiellement liées à la conversion inefficace du spectre solaire et à la disparité entre les angles solides d'absorption et d'émission. Pour surmonter ces pertes et se rapprocher de la limite de Carnot, trois stratégies sont envisagées dans cette thèse : les cellules multi-jonction à concentration, la combinaison de la concentration et de la restriction angulaire et les systèmes hybrides PV/CSP. Chacune de ces stratégies est limitée par des mécanismes qui dégradent leur performance. L'objectif de cette thèse est donc de comprendre dans quelle mesure les différents mécanismes limitants sont susceptibles d'affecter les performances des différentes stratégies étudiées, et d'optimiser l'architecture des cellules dans le but d'accroître leur efficacité de conversion. Dans ce but, un modèle détaillé de cellule solaire tenant compte des principaux mécanismes limitant a été développé. Un outil d'optimisation par algorithme génétique a également été mis au point, afin d'explorer l'espace des différents paramètres étudiés pour identifier les conditions d'opération optimales. Nous démontrons l'importance majeure que revêt l'adaptation des propriétés optoélectroniques des matériaux utilisés aux conditions opératoires, que ce soit dans le cas des cellules solaires à concentration endurant des pertes résistives significatives, ou encore dans le cas de cellules solaires fonctionnant à des niveaux de températures très supérieurs à l'ambiante. Enfin, nous avons déterminé l'effet des principaux facteurs limitant que constituent les pertes résistives et les recombinaisons non-radiatives sur les cellules solaires simultanément soumises au flux solaire concentré et à la restriction angulaire du rayonnement émis.

Mots-clés: Photovoltaïque concentré (CPV), concentration solaire, cellules solaires multi-jonctions, confinement angulaire, limite radiative, systèmes hybrides PV/CSP, pertes résistives, rendement de fluorescence externe (ERE), haute température.